Towards Nanophotonic All-optical Image Processing

Lukas Wesemann

ORCID: 0000-0001-9142-1342

A thesis presented for the degree of
Doctor of Philosophy

February 2021

in the
School of Physics
Faculty of Science

THE UNIVERSITY OF MELBOURNE

Submitted in total fulfilment of the requirements
of the degree of Doctor of Philosophy

THE UNIVERSITY OF MELBOURNE

Abstract

Doctor of Philosophy

Towards Nanophotonic All-optical Image Processing

Lukas Wesemann

The processing of spatial information, including images, is fundamental in modern scientific, industrial and medical applications. Some imaging techniques rely on amplitude information contained in a wavefield and permit conversion of optical information into electronic signals through conventional integrated photodetector technology and subsequent digital processing. The ever increasing complexity and volume of data that often needs to be processed in real-time and with low energy consumption in applications such as satellite imagery, autonomous vehicles or object and face recognition pushes current electronic systems to its limits. Other situations utilize the extraction of polarization or phase information from a wavefield which commonly requires the use of optical image processing technology. The visualization of phase information underpins for example widely employed techniques to enhance image contrast in live biological cells. Conventional optical processing approaches, however, typically involve expensive and bulk-optical components thereby limiting their potential to be involved in next-generation compact optical systems.

These constraints on current electronic and optical processing technology require the development of new solution approaches. Ultra-compact, analogue optical solutions that enable real-time processing of spatial information carry potential to circumvent conversion of optical to electronic signals and the associated digital computation while simultaneously avoiding bulk-optical components. The significant progress in micro- and nanofabrication over the last decades has enabled researchers to create artificial materials with unprecedented optical characteristics including photonic crystals, thin-film systems and optical metasurfaces. Recently these systems have gained considerable scientific attention for the implementation of analogue spatial computation devices and have been applied to all-optically perform mathematical operations including differentiation and integration on optical images. In particular approaches that enable accessing and manipulating the Fourier content of a wavefield in the object-plane carry vast potential for the development of flat optical image processing solutions.

The main objective of this work is to further our understanding of ultra-compact all-optical image processing in general, and to develop specific implementation approaches utilizing nanophotonic structures. Here the conception, modelling, fabrication and characterization of three fundamentally different approaches to nanophotonic image processing in the object plane are presented for the first time. Firstly, metal-insulator-metal thin-film absorbers are investigated for the first time as reflective image processing devices. Secondly, the excitation of subradiant modes on plasmonic trimer metasurfaces is exploited to perform all-optical spatial frequency filtering in reflection. Finally, plasmonic resonant waveguide gratings are investigated as compact transmitting spatial frequency filters. The implemented solutions are applied as high-pass spatial frequency filters to demonstrate all-optical edge-detection in amplitude images and the visualization of phase gradients in optical wavefields. Furthermore proof-of-concept application of the investigated structures to image processing of biological samples is demonstrated. The results of this thesis contribute to the advancement of our understanding of nanophotonic systems for the processing of spatial information and demonstrate their significant potential to be integrated in next-generation optical systems.

Declaration of Authorship

I, Lukas Wesemann, declare that this thesis titled, 'Towards Nanophotonic All-optical Image Processing' and the work presented in it are my own. I confirm that:

- The thesis comprises only my original work towards the Doctor of Philosophy (PhD) except where indicated in the preface;
- due acknowledgement has been made in the text to all other material used; and
- the thesis is fewer than the maximum word limit in length, exclusive of tables, maps, bibliographies and appendices as approved by the Research Higher Degrees Committee.

Signed:

Date: Melbourne, Australia - 04.02.2021

Preface

This thesis was submitted as a requirement for the achievement of the degree of Doctor of Philosophy (PhD) in the School of Physics, Faculty of Science at The University of Melbourne. The research presented in this thesis was performed under the supervision of Prof. Ann Roberts, Prof. Kenneth Crozier and Dr. Evgeniy Panchenko. Some of the figures included in this work have been taken from other publications. In these cases the source has been cited in the respective figure caption to acknowledge the original authors.

All samples investigated in this thesis were fabricated at the Melbourne Centre for Nanofabrication (MCN). Dr. Evgeniy Panchenko undertook early sample preparation before I was licencensed to operate the electron-beam lithography tool (EBL), the electron beam evaporator (EBPVD) and the chemical vapour deposition tool (PECVD) at the Melbourne Center for Nanofabrication. The samples fabricated by him were initial samples for the investigation of subradiant resonances on plasmonic metasurfaces and metal-insulator-metal (MIM) thin-film absorbers (see chapters 4 and 5). Dr. Timothy D. James, Kalpana Singh and Panji Achmari carried out foundational work on subradiant mode excitation on plasmonic metasurfaces (see chapter 5) prior to the commencement of the authors PhD research. Dr. Jingchao Song performed electron beam evaporation on a sample of metallic resonant wave guide gratings (RWG) investigated for the work presented in chapter 6. Dr. Enrico Della Gaspera from RMIT University in Melbourne has assisted in obtaining angular reflectance spectra from the fabricated MIM absorbers (see section 4.3.1). The remainder of the sample fabrication and characterization were performed independently by the author of this thesis. Prof. Timothy J. Davis and Prof. Daniel E. Gómez are acknowledged for their expert advise on numerical modeling and experimental characterization of nanostructures.

The PhD candidature of the author was supported by the Melbourne International Fee Remission Scholarship (MIFRS) and the Melbourne International Research Scholarship (MIRS). Conference participations were additionally supported by travel grants from The Optical Society (OSA) and the Laby foundation. Project costs were covered by Australian Future Fellowship (Grant No. FT140100514) and ARC Discovery Project grants (Grant No. DP160100983). Several journal articles, conference proceedings and a provisional patent application are based on the research in this work and summarized below.

List of Publications

JOURNAL PUBLICATIONS RELATED TO PhD THESIS

- **Lukas Wesemann**, Evgeniy Panchenko, Kalpana Singh, Enrico Della Gaspera, Daniel E. Gómez, Timothy J. Davis, and Ann Roberts. ”Selective near-perfect absorbing mirror as a spatial frequency filter for optical image processing.” *APL Photonics*, 4(10):100801, 2019.
- **Lukas Wesemann**, Panji Achmari, Kalpana Singh, Evgeniy Panchenko, Timothy D. James, Daniel E. Gómez, Timothy J. Davis, and Ann Roberts. ”Metasurfaces, dark modes, and high NA illumination.” *OSA Continuum*, 1(2):727-735, 2018.
- Charlene Ng, **Lukas Wesemann**, Evgeniy Panchenko, Jingchao Song, Timothy J. Davis, Ann Roberts, and Daniel E. Gómez. ”Plasmonic Near-Complete Optical Absorption and Its Applications.” *Advanced Optical Materials*, 14(7):1801660, 2019.
- **Lukas Wesemann**, Timothy J. Davis, Ann Roberts. ”Metasurface Enhanced Coverslip.” *In preparation*
- **Lukas Wesemann**, Ann Roberts, and Timothy J. Davis. ”Review: Meta–optical devices and systems for all-optical information processing.” *In preparation*

PATENT APPLICATIONS RELATED TO PhD THESIS

- Ann Roberts, Timothy J. Davis, and **Lukas Wesemann**. ‘Electromagnetic Filter Device and Method of Use.’ *Australian Provisional Patent Application*, no. 2019904670, in the name of The University of Melbourne, December 2019.

CONFERENCE PRESENTATIONS AND ABSTRACTS RELATED TO PhD THESIS

- **Lukas Wesemann**, Timothy J. Davis, and Ann Roberts. ”On-chip optical image processing with plasmonic metasurfaces” *14th Pacific Rim Conference on Lasers and Electro-Optics - CLEO Pacific Rim*, Sydney, Australia, 2020.
- **Lukas Wesemann**, Evgeniy Panchenko, Kalpana Singh, Daniel E. Gómez, Timothy J. Davis, and Ann Roberts. ”Plasmonic Metasurfaces for Information Processing.” *SPIE Micro + Nano Materials, Devices, and Applications*, pp. 112010F, 2019.

- **Lukas Wesemann**, Kalpana Singh, Evgeniy Panchenko, Daniel E. Gómez, Timothy J. Davis, and Ann Roberts. ”Nanophotonic Approaches to Optical Information Processing.” *Integrated Photonics Research, Silicon and Nanophotonics*, pp. IW2B-1. Optical Society of America, 2018.
- **Lukas Wesemann**, Evgeniy Panchenko, Kalpana Singh, Daniel E. Gómez, Timothy J. Davis, and Ann Roberts. ”Towards Plasmonic Metasurfaces for Information Processing.” *15th International Conference on Near-Field Optics, Nanophotonics and Related Techniques - NFO*, Troyes, France 2018.
- **Lukas Wesemann**, Evgeniy Panchenko, Kalpana Singh, Daniel E. Gómez, Timothy J. Davis, and Ann Roberts. ”Towards plasmonic metasurfaces for phase sensing applications.” *International Conference on Nanoscience and Nanotechnology - ICONN*, Wollongong, Australia 2018.

OTHER PUBLICATIONS

- Evgeniy Panchenko, **Lukas Wesemann**, Daniel E. Gómez, Timothy D. James, Timothy J. Davis, and Ann Roberts. ”Ultracompact Camera Pixel with Integrated Plasmonic Color Filters.” *Advanced Optical Materials*, 7(23):1900893, 2019.
- Kalpana Singh, Evgeniy Panchenko, Babak Nasr, Amelia Liu, **Lukas Wesemann**, Timothy J. Davis, and Ann Roberts. ”Cathodoluminescence as a probe of the optical properties of resonant apertures in a metallic film.” *Beilstein Journal of Nanotechnology*, 9(1):1491-1500, 2018.
- Evgeniy Panchenko, **Lukas Wesemann**, Timothy J. Davis, Daniel E. Gómez, and Ann Roberts. ”Metasurface-integrated Fully CMOS-compatible Phase Gradient Photodetector.” *CLEO: Applications and Technology*, pp. AW4O-5. Optical Society of America, 2018.
- Evgeniy Panchenko, Jasper J. Cadusch, Timothy D. James, **Lukas Wesemann**, and Ann Roberts. ”Differential Polarisation-sensitive Photodetectors Design Utilising Plasmonic Metasurfaces.” *Frontiers in Optics - FiO*, pp. JW3A-75. Optical Society of America, 2017.
- Jörg Imbrock, **Lukas Wesemann**, Sebastian Kroesen, Moussa Ayoub and Cornelia Denz. ”Waveguide-integrated three-dimensional quasi-phase-matching structures” *Optica*, 7(1):28-34, 2020.

Acknowledgements

Firstly, I would like to express my sincere gratitude to my principle supervisor Prof. Ann Roberts for offering me the opportunity to undertake the research that has led to this thesis, and for her continuous support and guidance throughout my studies. Her encouragement, input and feedback have been invaluable and have made this research project possible. Furthermore, I would like to thank my other supervisors and the members of my PhD committee, Prof. Kenneth Crozier, Prof. Jeffrey McCallum and Dr. Evgeniy Panchenko for their insightful comments and constant support along the journey. I would also like to thank my collaborator on various research projects, Prof. Timothy J. Davis. His experience in the field of nanophotonics, and the stimulating discussions of our research have added great value to this work. My sincere thanks also goes to Prof. Daniel E. Gómez for providing access to the research facilities at RMIT University that were crucial for the experimental results in this thesis. A heartfelt thanks goes out to everyone at the School of Physics at the University of Melbourne for the warm welcome into their community. Living and studying in Melbourne for the last few years has been a highlight of my life, and they have been a large part of that.

I wish to acknowledge the University of Melbourne and the Australian Government for supporting me through the Melbourne International Research Scholarship, which has enabled me to live and study in Australia. I would also like to acknowledge the Australian Research Council for its contribution to the funding of this research. I also wish to express my gratitude to the Laby Foundation for their financial support, which has allowed me to attend an international conference in Europe and participate in a truly unique research experience - a flight over Antarctica.

From the bottom of my heart I would like to thank all my colleagues, labmates and friends that have made the last years a very memorable time. Faris, Niken, Kelvin, Jon, Laura, Giel and Jingchao - without our coffee meetings and lab marathons the hard times would have been a lot tougher. Kiall, thank you for constantly involving me in your quest for philosophical enlightenment, which has never failed to broaden my perspective. The team of the OSA student chapter also deserves credit for continuously reminding me of all the fun that science has to offer. Thank you all for the great times we had together. Finally, and most importantly, I need to thank my family for their unrelenting support and inspiration. My mother, father and grandmother for believing in me at every step, and my little brother for never failing to make me laugh. Jessica, you have been there for the good times and the bad. Without your patience and love, this manuscript would not exist.

Contents

List of Figures

List of Tables

Chapter 1

Introduction

Images have been a pivotal medium of information storage and transmission for humans since the earliest traces of cave art over $60,000$ years ago to the digital images of the present day [1]. The processing of spatial information, including images, plays a paramount role in every area of modern technology and begins with the extraction of the relevant features from an optical wavefield. In some cases the amplitude provides sufficient information, while other applications also require the extraction of polarization state and phase. Conventional photodetector technology permits conversion of the optical amplitude into an electronic signal that can subsequently be processed through digital computation [2]. In applications where relevant information is contained in the polarization or phase, however, alternative strategies usually involving optical processing are required [3–8]. Currently available electronic and optical image processing approaches are confronted with multifaceted challenges and require the development of novel solutions.

As a consequence of the rapid development of electronic systems over the past decades, computational power and efficient algorithms are broadly available in most situations where digital processing is possible [9]. However, the constantly increasing volume and complexity of data has pushed state-of-the art digital processing technology to its limits. These include extremely data intensive imaging applications as diverse as remote sensing through satellite imagery for environmental monitoring [10–12] and the prediction of the spread of diseases [13], data driven agricultural farming [14, 15] and security concerns such as face recognition [16]. For remote data collection in particular, as for instance in nanosatellites [17], computational power, transmission bandwidth and power consumption generate significant challenges for current electronic systems.

A prominent example that requires evaluation of information beyond the amplitude of a wavefield is the characterization of transparent objects such as biological cells. These cells usually generate insufficient amplitude contrast to visualize important details of their internal structure. Enhancing cell images through chemical staining and fluorescence labeling is therefore common practice in biology and medical diagnostics but inherently implies changing, and in some cases damaging or even destroying, the cell environment [18, 19]. Due to the thickness and refractive index profile of a cell, relevant spatial information is, however, contained in the phase of a wavefield that has passed through the cell. Label-free visualization of these phase-gradients has been a major driver in the development of optical microscopy and image processing technology [20].

Approaches to all-optical spatial information processing, including phase-visualization, usually rely on sensing or manipulating the Fourier content of a wavefield. Classically, methods employed in this field range from accessing the Fourier spectrum through a lens and filtering with spatial masks [21, 22], to interference based systems. Zernike phase contrast microscopy [5], Differential Interference Constract (DIC) [7] or laser based set-ups are widely used for the visualization of optical phase. Non-interferometric approaches for example based on Shack-Hartmann (SH) sensors [23] or the Transport of Intensity Equation (TIE) [4] have also been demonstrated. However, the above methods either rely on costly, bulk-optical components or are indirect and require computational post-processing (TIE, SH). For these reasons their capacity for subwavelength miniaturization and their integration into next-generation compact optical imaging devices is limited.

These limitations of current electronic and optical processing technology for spatial information motivate the development of novel solution approaches. Ultra-compact, analogue optical solutions for real-time processing in particular, represent a promising platform that simultaneously bypasses the requirement of conversion of optical to electrical signals for processing, the associated digital computation or the macroscopic footprint of bulk-optical components [24]. The progress in micro- and nanofabrication technology throughout the last decades has enabled the fabrication of synthetic subwavelength-structured materials, so called optical metamaterials, that gather unusual properties from their morphology rather than their chemical composition. These artificial materials are composed of three-dimensional arrangements of subwavelength building blocks and enable selective light matter interactions within spatial dimensions below or comparable to the wavelength of light [25]. This is in stark contrast to conventional optical components that rely on the effects of refraction, diffraction and propagation over distances that far exceed the wavelength of light. Optical metamaterials have received significant attention in the scientific community owing to their unusual optical properties including negative refractive index [26], perfect optical absorption [27] or giant circular dichroism [28]. However, the development of most metamaterials is hampered by the implied complex three-dimensional fabrication schemes [29]. As a subclass of optical metamaterials, optical metasurfaces circumvent this limitation by reducing the dimensionality of the approach. The principle of metasurface design is to arrange two-dimensional arrays of tailored optical scatterers [30]. The excitation of coherent charge oscillations on metallic nanoparticles and surfaces, so called surfaces plasmon resonances, as well as resonances on dielectric scatterers have been widely used [29, 31]. This has enabled the development of planar optical components with subwavelength thickness [32] such as flat lenses [33, 34], waveplates [35, 36] and holograms [37, 38]. In combination with other micro- and nanophotonic systems which predated the rise of optical metamaterials, such as photonic crystals and thin-film devices, the scientific community today has promising platforms for the miniaturization of optical technology at their disposal.

Leveraging these nanophotonic systems for spatial analogue optical information processing has recently drawn significant scientific attention [39]. The approaches can generally be divided into two categories. The first category comprises approaches that change between Fourier- and object plane through conventional lenses or lens-like elements (Graded Refractive Index (GRIN) elements) and manipulate the Fourier content by placing a tailored metasurface in the Fourier plane. The second category describes systems that directly manipulate the Fourier content of an impinging wavefield in the object plane without the need of transformation between object- and Fourier plane. Since object-plane approaches do not require bulk-optical lenses or GRIN elements, which typical have thicknesses of several wavelengths and require associated propagation distances, they carry vast potential for the development of subwavelength size all-optical image processors. In principle, any compact optical structure that exhibits a sensitivity of its reflection or transmission coefficient to the angle of incidence carries potential to access and manipulate the Fourier content of a wavefield in the object plane. Prior to the recent escalation of interest, initial demonstrations of object-plane spatial-frequency filtering date back to the 1970 and 80's using volume hologram filters [40, 41] as well as interference filters [42] but scientific interest in their development declined with the rise of digital computers. The idea has only recently regained popularity with approaches exploiting a large spectrum of nanophotonic structures and mechanisms ranging from phase-shifted Bragg gratings [43, 44], the excitation of surface plasmon polaritons [45], the Brewster-effect [46] and the Spin-Hall effect of light [47] to resonant waveguide gratings [48, 49], photonic crystals [50, 51] and the excitation of subradiant plasmonic modes [52, 53]. A particular focus has been set on exploiting above structures to optically perform spatial differentiation and edge-detection on phase and amplitude images. In the following chapter these and other approaches will be reviewed in detail. It should be noted that a significant number of the associated articles were published during the course of this research.

Despite the variety of suggested approaches, some of which have been experimentally demonstrated, significant challenges remain. Firstly, the experimental realization of some strategies is yet to be demonstrated owing to the implied fabrication complexity. These include the various thin-film devices with a large number of stacked layers and little tolerance to irregularities in layer thicknesses or refractive indices as acknowledged in [54]. The development of robust approaches is therefore crucial. Secondly, while some imaging applications might require processing in one spatial dimension, others will rely on processing in two-dimensions. Although several studies have numerically investigated approaches for two-dimensional processing [50, 53, 55–57], it has only been experimentally demonstrated by two studies [51, 58]. Thirdly, previous studies have focused on the detection of sharp edges in amplitude and phase images but the visualization of non-abrupt phase-gradients in optical wavefields has received scant attention [57] and has only been experimentally demonstrated by one study which focussed on wavefront sensing [59]. Finally, the experimental application of object-plane spatial frequency filters for the edge-detection of biological images has only been demonstrated in one study to the present day [51]. It is therefore the central goal of this thesis to further our understanding of nanophotonic image processing systems and to implement novel approaches that address the limitations of existing solutions. Here we investigate, for the first time, metal-insulator-metal (MIM) thin-film absorbers, subradiant modes (or bound modes in the continuum) on plasmonic nanotrimer metasurfaces and plasmonic resonant waveguide gratings as all-optical, two-dimensional spatial frequency filters. The underlying optical mechanisms will be introduced in detail in the following chapters.

1.1 Thesis Goals and Contribution to Knoweledge

Above we have discussed the need for compact optical information processing platforms as part of next generation image processing devices. The primary objective of this thesis is to leverage nanophotonic approaches to design and implement specific image processing devices with subwavelength thickness. In order to achieve this, the cornerstones of this research are to:

- Establish an in-depth understanding of the potential and limitations of nanophotonic analogue optical computation in the spatial domain with a focus on image processing including phase-visualization.
- Develop numerical models to describe and optimize the capacity of nanophotonic structures to perform all-optical spatial-frequency filtering inlcuding edge-detection and phase-visualization.
- Design and fabricate novel optical nanostructures for spatial frequency filtering in reflection and transmission based on numerical results.
- Characterise implemented structures using custom built setups and perform all-optical image processing including contrast enhancement in biological samples.

The research outcomes that state the contribution to knowledge by this work in relation to the above formulated goals are listed in detail below.

- Demonstration of metal-insulator-metal (MIM) thin-film absorbers as reflective spatial frequency filters with subwavelength thickness.
  ⟶ ([60], chapter 4).
- Investigation of the angular sensitivity in the excitation of subradiant modes (SRM) on plasmonic metasurfaces and their potential and limitations for all-optical image processing in reflection.
  ⟶ ([61], chapter 5)

- Development of plasmonic resonant waveguide gratings (RWG) capable of performing high-pass spatial frequency filtering on transmitted wavefields.
  ⟶ ([62], chapter 6).
- Performing of numerical and experimental edge detection in amplitude images via MIM absorbers, SRM excitation and via RWGs.
  ⟶ ([60, 63], chapters 4-6)
- Numerically and experimentally demonstrating the capacity of MIM absorbers and RWGs to visualize phase-gradients in reflected and transmitted wavefields respectively.
  ⟶ ([60], chapters 4 and 6).
- Performing experimental contrast enhancement in images of biological samples through reflection from MIM absorbers and transmission through RWGs.
  ⟶ ([60], sections 4.3.4 and 6.3.4).

In the following section an overview of the structure of this thesis that enables the achievement of these cornerstones is presented.

1.2 Thesis Structure

This thesis is structured as follows. In chapter 2 the theoretical fundamentals required for the understanding and description of spatial optical information processing are discussed. Initially the relevant fundamentals of Fourier-optics are introduced and related to space-invariant linear optical systems. Using this framework the concept of spatial-differentiation through filtering of Fourier components is reviewed and its application to the processing of amplitude images as well as the visualisation of phase-gradients in wavefields discussed. Subsequently optical metasurfaces and thin-film approaches are introduced as promising nanophotonic platforms to implement compact imaging devices. Finally, recent progress in optical analogue computation in the spatial domain including image processing is reviewed and related to the research in this thesis. The following chapter 3 is concerned with the introduction of the numerical- and nanofabrication methods that enable this work. In particular we review the Finite Element Method (FEM) as a versatile tool for the modelling of nanophotonic structures and introduce the operational principle of fabrication and characterisation techniques including Electron Beam Lithography (EBL), thin-film deposition methods and Scanning Electron Microscopy (SEM). Based on the introduced fundamentals and methods, the following chapters focus on three different approaches for nanophotonic image processing.

In chapter 4 we investigate thin-film metal-insulator-metal absorber structures as subwavelength thickness spatial-frequency filters. Subsequently, the excitation of subradiant modes on plasmonic metasurfaces is investigated as a second avenue for all-optical image processing in chapter 5. Both of these approaches rely on operation in reflection while for many imaging applications, particularly biological applications, operation in transmission is preferred. For this reason, chapter 6 investigates plasmonic resonant waveguide gratings as transmitting spatial-frequency filters and its application to image processing. Finally, in the final chapter of this thesis the key outcomes of this research are summarized and conclusions drawn. Furthmore specific extensions of the presented approaches are discussed and put into the context of the general outlook on further developments in the field of nanophotonic all-optical image processing.

Chapter 2

Fundamentals and Literature Review

This section is concerned with the fundamentals of image processing and its nanophotonic implementation. Firstly an introduction to Fourier optics as the fundamental theoretical framework for spatial analogue optical computing will be given. Subsequently the interaction between metals and electromagnetic waves at optical frequencies will be discussed as an introduction to the enabling effects of nano-plasmonics. The concept of optical metasurfaces as a platform to implement optical analogue computing concepts will then be introduced. Finally recent progress in the field of nanophotonics enabled optical computation in the spatial domain will be reviewed in detail.

2.1 Fundamentals of Image processing

The objective of this thesis is the development of nanophotonic approaches enabling all optical image processing. In the following, the mathematical fundamentals underpinning common image processing approaches are elucidated and the connection with phase-sensing methods is drawn. These represent a brief summary of a more comprehensive discussion given in [22].

The degree of optical coherence of a light source is an important property of an imaging system. Optical coherence refers to a constant relationship in the phase of an optical wavefield between two different points in space and time. As part of this, temporal coherence describes a constant relationship between a wavefield at a fixed point in space at two different instances in time and is inversely proportional to the spectral bandwidth of the light source. Spatial coherence on the other hand describes a constant relationship in the phase of an optical wavefield between two different points in space at fixed instance in time and depends on the spatial size of a lightsource and its angular spectrum. In the following deductions we confine the discussion to monochromatic, i.e. temporally coherent, and spatially coherent imaging systems.

2.1.1 The two dimensional Fourier transform

The basis of image processing methods in this thesis lie in manipulating the spatial frequency content of an image or wavefield. An understanding of the fundamentals of two-dimensional signal processing forms the foundation of these methods for which the relevant theoretical framework will be introduced in a first step. It is assumed here that the reader is familiar with the characteristics of the Fourier transformation of functions of a single variable $f(x)$ and we begin by expanding the concept to functions of two variables $f(x, y)$.

We define the two-dimensional Fourier transform $\mathcal{F}\big(f(x,y)\big) = F(k_x, k_y)$ of the complex valued function $f{:}\mathbb{R} \times \mathbb{R} \to \mathbb{C}$ as

$$F(k_x, k_y) = \iint\limits_{-\infty}^{+\infty} f(x,y) e^{-i2\pi(xk_x + yk_y)}\, dx\, dy \tag{2.1}$$

and the inverse two dimensional Fourier transform $\mathcal{F}^{-1}\big(F(k_x, k_y)\big)$ by

$$f(x,y) = \iint\limits_{-\infty}^{+\infty} F(k_x, k_y) e^{i2\pi(xk_x + yk_y)}\, dk_x\, dk_y \tag{2.2}$$

It should be noted that the existence of the integrals in equations (2.1) and (2.2) puts requirements on the function $f(x, y)$. One set of sufficient conditions states that f has to be (A) absolutely integrable over the infinite x, y plane, (B) can only have a finite number of discontinuities and a finite number of maxima and minima in any finite rectangle and (C) f cannot have infinite discontinuities. Functions such at $f(x,y) = 3$ or $f(x,y) = sin(x)$ do not fulfill these conditions because they are not (A) absolutely integrable over the infinite x, y plane. Without embarking on a detailed discussion, the solution to finding meaningful transforms for those functions is usually to represent them by a series of transformable functions that have the original function as their limit. The so called *generalized Fourier transform* is then the limit of of the transforms of this series of functions. For the purposes of this thesis the distinction between both transforms can be neglected and we will refer to the generalized Fourier transform whenever the function under investigation does not possess a Fourier transform that strictly satisfies conditions (A)-(C).

Following the principle of the one dimensional case, the two dimensional Fourier transform thus decomposes a function into orthogonal basis functions $e^{-i2\pi(xk_x+yk_y)}$ with k_x and k_y taking the role of frequencies. A series of those basic functions are depicted in Fig.2.1. We briefly discuss some fundamental properties of the two dimensional Fourier transform that we will refer to later within the description of image processing applications. As for the one-dimensional case, the two-dimensional Fourier transform is a linear operation for which

$$\mathcal{F}\big[af(x,y) + bg(x,y)\big] = a\mathcal{F}\big[f(x,y)\big] + b\mathcal{F}\big[g(x,y)\big] \tag{2.3}$$

With $a, b \in \mathbb{C}$ constants. Furthermore the property of similarity states that

$$\mathcal{F}\big[f(ax,by)\big] = \frac{1}{|ab|}F\left(\frac{k_x}{a}, \frac{k_y}{b}\right) \tag{2.4}$$

The two dimensional Fourier transform also holds the useful property of turning a convolution of two functions $f(x,y)$ and $g(x,y)$ in the space domain into a multiplication of their respective Fourier transforms $F(k_x,k_y)$ and $G(k_x,k_y)$:

$$\mathcal{F}\left[\iint\limits_{-\infty}^{+\infty} g(\alpha,\beta)f(x-\alpha,y-\beta)\,d\alpha\,d\beta\right] = G(k_x,k_y)F(k_x,k_y) \tag{2.5}$$

We will utilize this property below in the context of linear space-invariant optical systems. Finally, the Parseval-Rayleigh theorem states that

$$\iint_{-\infty}^{+\infty} |f(x,y)|^2 \, dx \, dy = \iint_{-\infty}^{+\infty} |F(k_x,k_y)|^2 dk_x \, dk_y \tag{2.6}$$

Interpreting $f(x,y)$ as a signal, the left hand side of the equation takes the form of the energy contained in the signal $f(x,y)$ giving rise to the interpretation of $|F(k_x,k_y)|^2$ as the energy density in the spatial spectra. Hence the theorem states that the energy of the signal in real and in frequency space must be equal.

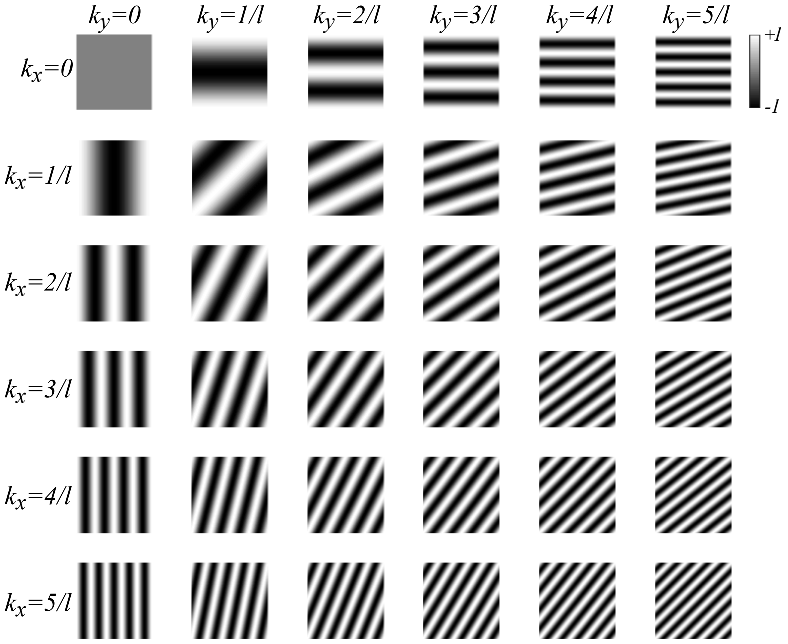

Figure 2.1: Visualization of the real part of the orthogonal basis functions $A = e^{-i2\pi(xk_x+yk_y)}$ for a plane of size $l \times l$. Shown is real(A) for spatial frequencies k_x, k_y ranging from 0 to $5/l$.

Application of the considerations above to numerical or experimental data will always mean discretization of the input function $f(x,y)$ as well as its corresponding frequency spectrum $F(k_x,k_y)$. A two dimensional sample of the function $f(x,y)$ of m data points in x-direction and n data points in y-direction can be expressed as a series $f_{j+1,k+1}$ where j runs from 0 to $(m-1)$ and k from 0 to $(n-1)$. From this discretized representation of f we can calculate a discretized Fourier transform (DFT) $F_{p+1,q+1}$ defined by

$$F_{p+1,q+1} = \sum_{j=0}^{m-1}\sum_{k=0}^{n-1} e^{\frac{-2\pi ijp}{m}} e^{\frac{-2\pi ikq}{n}} f_{j+1,k+1} \tag{2.7}$$

where p and q run from 0 to $(m-1)$ and $(n-1)$ respectively. The DFT is usually calculated via one of several algorithms collectively referred to as the fast Fourier transform (FFT) as for instance implemented in MATLAB R2018b - R2020a and used throughout this thesis. Equivalently the discrete inverse Fourier transformation is given by

$$f_{p+1,q+1} = \frac{1}{m}\sum_{j=0}^{m-1}\frac{1}{n}\sum_{k=0}^{n-1} e^{\frac{2\pi ijp}{m}} e^{\frac{2\pi ikq}{n}} F_{j+1,k+1} \tag{2.8}$$

Discretization of a function raises the question what the sampling requirements are in order for the sampled data to be an adequate representation of the original function. In the following we will summarize the Whittaker-Shannon Sampling Theorem for the case of two dimensional functions that makes a statement about this.

2.1.2 Whittaker-Shannon Sampling Theorem

Assuming a regular sampling of the function f in a two dimensional lattice with spacing X (Y) in x-direction (y-direction) yields a sampled function

$$f_s(x,y) = \mathrm{comb}\left(\frac{x}{X}\right)\mathrm{comb}\left(\frac{y}{Y}\right)f(x,y) \tag{2.9}$$

that consist of regularly spaced δ functions weighted with the respective value of the function f. It can be shown that for a certain class of functions, so called bandlimited functions, and a sufficiently dense sampling X, Y the resulting sampled function $f_s(x,y)$ is not only a good but an exact representation of the original function $f(x,y)$. A bandlimited function is a function that is non-zero only over a finite region R_{bl} of the frequency space and zero outside of that region. We denote the length and width of the smallest rectangle that fully contains the region R_{bl} as B_x and B_y respectively. The Whitaker-Shannon Sampling Theorem then states that for

$$X \leq \frac{1}{B_x} \,\text{and}\, Y \leq \frac{1}{B_y} \tag{2.10}$$

the sampled function f_s equals the original function f. It is thus important to choose adequate sampling whenever we apply the Fourier transform to discretized data. Undersampling, i.e. sampling where eq. (2.10) is not fullfilled, results in artifacts in the sampled function.

2.1.3 Invariant Linear Optical Systems

For the purpose of this thesis it is convenient to describe the nanophotonic devices developed for all-optical image processing as invariant linear systems. In the following we will introduce the basic concepts behind this class of system. We define a system as a mapping of a set of input functions to a set of output functions. In the particular case of interest here, which are optical imaging systems, the input and output variables are real valued intensities $I(x, y)$ or complex-valued field amplitudes $E(x, y)$ over a two dimensional spatial plane. In the following we will therefore elucidate the relevant concepts with regard to the optical realm.

We describe our system by an operator $S\{\,\}$ such that

$$E_{\text{out}}(x_2, y_2) = S\{E_{\text{in}}(x_1, y_1)\}. \tag{2.11}$$

Our system is then referred to as linear if the following relation holds for all input functions $E_1(x, y)$, $E_2(x, y) : \mathbb{R} \times \mathbb{R} \to \mathbb{C}$ and all constants $a, b \in \mathbb{C}$:

$$S\{aE_1\} + S\{bE_2\} = aS\{E_1\} + bS\{E_2\}. \tag{2.12}$$

Given this linearity the response of the system to an arbitrary input signal can always be expressed as the combined response of the system to elementary functions into which we can decompose the input. It can be shown that the response of the system to delta-Dirac functions located at any position in the infinite x, y plane enables to determine the output of the system for any arbitrary input:

$$E_{\text{out}}(x_2, y_2) = \iint\limits_{-\infty}^{+\infty} E_{\text{in}}(\alpha, \beta) S\{\delta(x_1 - \alpha, y_1 - \beta)\}\, d\alpha\, d\beta. \tag{2.13}$$

Here we introduce the *point-spread function* h which characterizes the impulse response of our system

$$h(x_2, y_2; \alpha, \beta) = S\{\delta(x_1 - \alpha, y_1 - \beta)\} \tag{2.14}$$

Which yields a compact version of equation (2.13) for the system output

$$E_{\text{out}}(x_2, y_2) = \iint\limits_{-\infty}^{+\infty} E_{\text{in}}(\alpha, \beta) h(x_2, y_2; \alpha, \beta)\, d\alpha\, d\beta. \tag{2.15}$$

So far we have investigated *linear* systems. An *invariant linear* system, in the case of an optical imaging system, requires the additional characteristic that its point-spread function depends only on the distance between excitation and response point but not on the absolute position, that is

$$h(x_2, y_2; \alpha, \beta) = h(x_2 - \alpha, y_2 - \beta). \tag{2.16}$$

Hence for linear-invariant systems using equation (2.16), equation (2.15) simplifies to

$$E_{\text{out}}(x_2, y_2) = \iint\limits_{-\infty}^{+\infty} E_{\text{in}}(\alpha, \beta) h(x_2 - \alpha, y_2 - \beta)\, d\alpha\, d\beta. \tag{2.17}$$

The output of the system is thus determined by a two-dimensional convolution of the input field E_{in} with the point-spread function of the system h. Recalling the characteristic of the Fourier transform to convert a convolution in the spatial domain into a multiplication in the spectral domain as discussed in equation (2.5), we obtain the central result of this chapter

$$\tilde{E}_{\text{out}}(k_x, k_y) = H(k_x, k_y)\tilde{E}_{\text{in}}(k_x, k_y) \tag{2.18}$$

with $\tilde{E}_{\text{in}}$, $\tilde{E}_{\text{out}}$ the Fourier transforms of the input and output field respectively and H the Fourier transform of the point-spread function h referred to as the *optical transfer function* of the system. It is thus possible, for an invariant-linear optical system, to determine the output field for any given input field by Fourier transforming the input field, multiplying by with the optical transfer function H and inverse Fourier transforming.

$$E_{\text{out}}(k_x, k_y) = \mathcal{F}^{-1}\Big[H(k_x, k_y)\tilde{E}_{\text{in}}(k_x, k_y)\Big] \tag{2.19}$$

We will make extensive use of the result shown in equation (2.19) throughout this thesis whenever the predicted output for an image processing device is calculated. In particular, high-pass spatial-frequency filtering will be performed using this equation. The optical transfer function of a system is given by its complex reflection and transmission coefficients $r(k_x, k_y)$ and $t(k_x, k_y)$ for reflecting and transmitting devices respectively. The corresponding reflectance and transmittance of the system as a function of spatial-frequency are then given by $R(k_x, k_y) = |r|^2$ and $T(k_x, k_y) = |t|^2$.

For the sake of simplicity we have neglected polarization of the electric field in the above discussion. This is a valid approach as long as the system has a transfer function that is independent of polarization. If this is not the case the optical transfer function becomes a tensor

$$\begin{pmatrix} \tilde{E}_{p,\text{out}}(k_x, k_y) \\ \tilde{E}_{s,\text{out}}(k_x, k_y) \end{pmatrix} = \begin{pmatrix} H_{pp}(k_x, k_y) & H_{sp}(k_x, k_y) \\ H_{ps}(k_x, k_y) & H_{ss}(k_x, k_y) \end{pmatrix} \begin{pmatrix} \tilde{E}_{p,\text{in}}(k_x, k_y) \\ \tilde{E}_{s,\text{in}}(k_x, k_y) \end{pmatrix}. \tag{2.20}$$

where the subscripts p and s refer to $p-$ and $s-$polarization respectively. For structures that do not cross-polarize light, i.e. do not convert between p- and s-polarized light, we find that $H_{ps} = H_{sp} = 0$.

2.1.4 Spatial differentiation in Fourier space

In the following we will discuss different transfer functions $H(k_x, k_y)$ and their effect on the system input. Of particular interest are transfer functions that correspond to first- and second order spatial derivatives. We recall the definition of the two-dimensional Fourier transform from equation (2.1) and consider the gradient operator

$$\nabla f(x,y) = \left(\frac{\partial f}{\partial x}, \frac{\partial f}{\partial y}\right). \tag{2.21}$$

Its components are calculated from the first-order partial spatial derivatives in x and y direction respectively. Being a linear operation, first-order partial differentiation after one of the spatial variables x, y yields

$$\begin{aligned} \frac{\partial f}{\partial x} &= \iint\limits_{-\infty}^{+\infty} F(k_x,k_y) e^{i2\pi(xk_x+yk_y)} \big(i2\pi k_x\big)\, dk_x\, dk_y \\ \frac{\partial f}{\partial y} &= \iint\limits_{-\infty}^{+\infty} F(k_x,k_y) e^{i2\pi(xk_x+yk_y)} \big(i2\pi k_y\big)\, dk_x\, dk_y \end{aligned} \tag{2.22}$$

where we define $H_1(k_x, k_y) = i2\pi k_x$ and $H_2(k_x, k_y) = i2\pi k_y$ as the transfer functions. It is apparent from equations (2.22) that a transfer function linear in k_x or k_y corresponds to an operation proportional to first order differentiation in the respective spatial direction. Equivalently, applying the Laplace operator

$$\nabla^2 f(x,y) = \frac{\partial^2 f}{\partial x^2} + \frac{\partial^2 f}{\partial y^2} \tag{2.23}$$

we obtain again using equation (2.1)

$$\nabla^2 f(x,y) = \iint\limits_{-\infty}^{+\infty} F(k_x,k_y) e^{i2\pi(xk_x+yk_y)} \Big(-(2\pi)^2 (k_x^2 + k_y^2)\Big)\, dk_x\, dk_y \tag{2.24}$$

with $H_3(k_x, k_y) = -(2\pi)^2(k_x^2 + k_y^2)$ demonstrating that taking the second order derivative (Laplacian) in real space is equivalent to a transfer function quadratic in k_x and k_y, except for a constant multiplicative factor. The central result of this section is thus that one can perform mathematical operations, particularly spatial differentiation, on a wavefield by engineering a system with a suitable optical transfer function. The deductions above can be generalized to n-th order differentiation in x-direction, or in analogous fashion in

y-direction, via a transfer function H with

$$H = (2\pi i k_x)^n \tag{2.25}$$

It should be noted that for non-integer values of n, eq. (2.25) describes a transfer function that performs fractional derivatives as for example reviewed in [64]. Performing fractional derivatives generally produces complex system outputs and we will refer to this below when we discuss ringing artifacts in processed images. It is convenient to express a transfer function as a complex function

$$H(k_x, k_y) = |H| e^{i \cdot \arg(H)} \tag{2.26}$$

such that the amplitude contribution abs$(H) = |H|$ and phase contribution arg(H) can be considered independently. For optical applications spatial frequencies are usually normalized by divison through the wavenumber $k_0 = 1/\lambda$ of the light in use[1]. In the following we will refer to these as normalized spatial frequencies. Normalized spatial frequencies larger than one then correspond to evanescent waves.

In Fig.2.2 the amplitude and phase of transfer functions H_1 and H_2 corresponding to first and second order differentiators respectively are plotted along the line $k_y = 0$. Their linear and quadratic dependence on spatial frequency are apparent in the amplitude contributions in Fig.2.2(a,c) respectively. Importantly, while the second order differentiator exhibits a constant zero phase contribution, the phase contribution of a first-order differentiator has a π phase-shift at $k_x = 0$. This discontinuity renders the transfer function of a first-order differentiator asymmetric while a second-order differentiator is a symmetric function about $k_x = 0$.

---

[1] If angular frequencies are considered, and the definition of the Fourier transform in eq.(2.1) and (2.2) is adapted accordingly, then the angular wavenumber $k_0 = 2\pi/\lambda$ is used to normalize spatial frequencies.

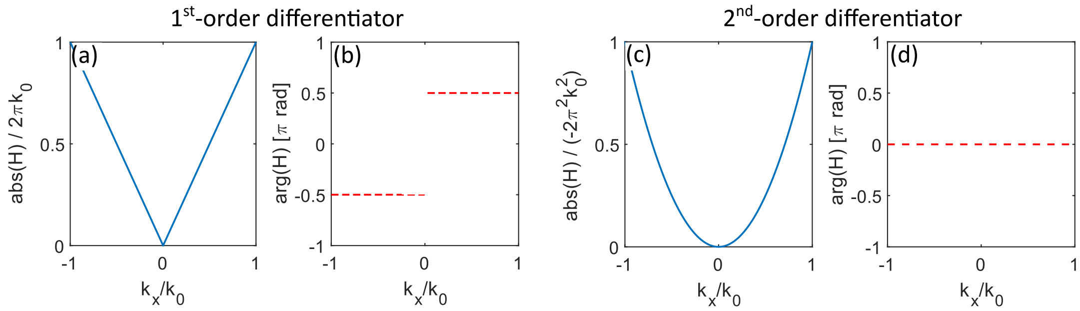

Figure 2.2: Transfer function H of an ideal first- (a,b) and second-order (c,d) differentiator. Shown are the amplitude contribution abs(H) (a,c) and the phase contribution arg(H) (b,d) respectively.

Fig.2.3 shows examples of differentiation of a scalar electric field with a Gaussian shaped amplitude modulation as depicted in Fig.2.3(a). While here the magnitude of the electric field is shown, in experimental situations the intensity I which is proportional to the square of the electric field magnitude $|E|^2$ is measured. It is apparent that applying a linear optical transfer function results in a system output that is proportional to the first order spatial differentiation in either the $x-$direction (Fig.2.3(c)) or the $y-$direction (Fig.2.3(f)). Applying a quadratic optical transfer function yields a field distribution proportional to $\nabla^2 E_{\text{in}}$ (Fig.2.3(i)).

One application of spatial differentiation is the enhancement of edges in an image. Edges refer to abrupt changes of the intensity value in an image between two regions and their recognition plays a key role in image processing applications such as object and face recognition [2]. While homogenous areas of an image are associated with low spatial frequencies, sharp edges and corners are associated with higher spatial frequencies. By filtering the low spatial frequency content of an image it is thus possible to remove homogenous areas of an image and extract the edges and regions dominated by high spatial frequencies.

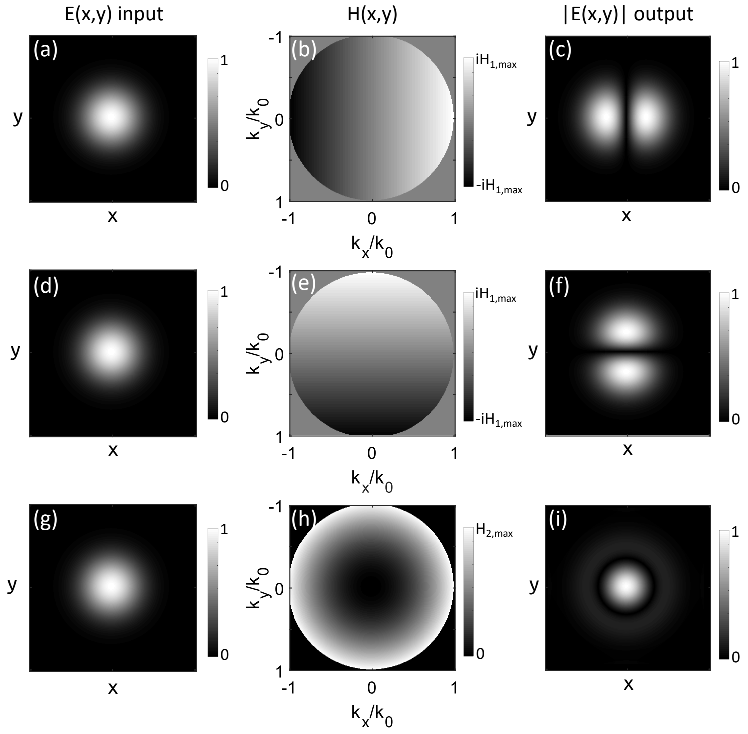

Figure 2.3: Numerical demonstration of first- and second-order spatial differentiation of an amplitude image of arbitrary size, significantly larger than the wavelength λ of the employed light. Shown are the cases of a Gaussian shaped input field (first column), linear and quadratic transfer functions with evanescent waves excluded (second column) and their respective output fields (third column). All field amplitudes are normalized to the maximum values of the respective image. The transfer functions shown are H_1 (b), H_2 (e) and H_3 (h) as defined above with the scaling factors $H_{1,\max} = 2\pi k_0$ and $H_{2,\max} = 2\pi^2 k_0^2$.

In Fig. 2.4 we show edge enhancement in an amplitude image applying the three different transfer functions H_1,H_2 and H_3 shown in Fig.2.3(b),(e) and (h). It is apparent that first order differentiation in $x-$ and $y-$direction in Fig.2.3(b) and (c) yields an image with highlighted edges in the respective differentiation direction while homogenous areas of the image appear dark. Applying the quadratic transfer function results in a processed images with highlighted edges in all spatial directions due to the rotational symmetry of the transfer function as depicted in Fig.2.3(d). This process is also referred to as *edge enhancement* or *edge detection.*

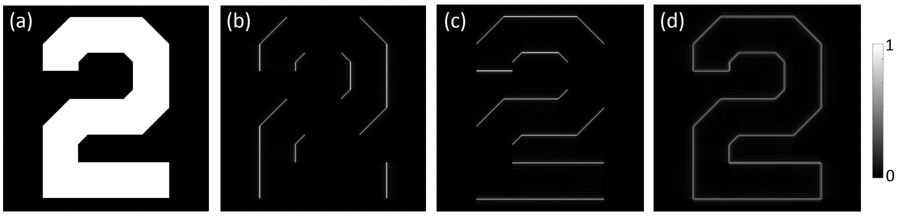

Figure 2.4: Numerical demonstration of edge detection in an amplitude image of arbitrary size significantly larger than the wavelength λ of light for a figure '2' through first- (b,c) and second-order differentiation (d). Input amplitude E_{in} is shown in (a) with the output amplitude in (b)-(c). Optical transfer functions are H_1 (b), H_2 (c) and H_3 (d).

A key difference between edge-detection through first- and second-order differentiation is the resulting single or double-peak in the intensity at the location of the edge in the original image. In order to illustrate this, Fig.2.5(a) shows the example of a smooth edge with the resulting amplitude for first- and second-order differentiation. The width and separation of the peaks depends on the steepness of the edge. For fractional derivatives, which commonly arise from nonlinear transfer functions, we can generally expect multiple local intensity maxima in the vicinity of an edge. Closely related to this is the observation of 'ringing' artifacts originating from the limited bandwidth, usually referred to as the numerical aperture (NA), of an optical system. This is also referred to as 'Gibbs-Wilbraham phenomenon' [65] and illustrated in Fig.2.5(b) at the example of a sharp edge (red) and the resulting intensity distribution for limited spatial bandwidth representation (blue) with the typical 'overshoot' apparent at the edge. Together these effects contribute to the occurrence of ringing artifacts in optical systems with complex, non-linear transfer functions and limited spectral bandwidth. Examples of first- and second-order differentiation through a system with limited spatial bandwidth are shown in Fig.2.5(c,d) respectively. In section 2.6 we will review nanophotonic approaches that enable image processing including edge detection. These approaches commonly generate ringing artifacts as for example apparent in [66] and we will refer to ringing in various calculations and measurements throughout this thesis.

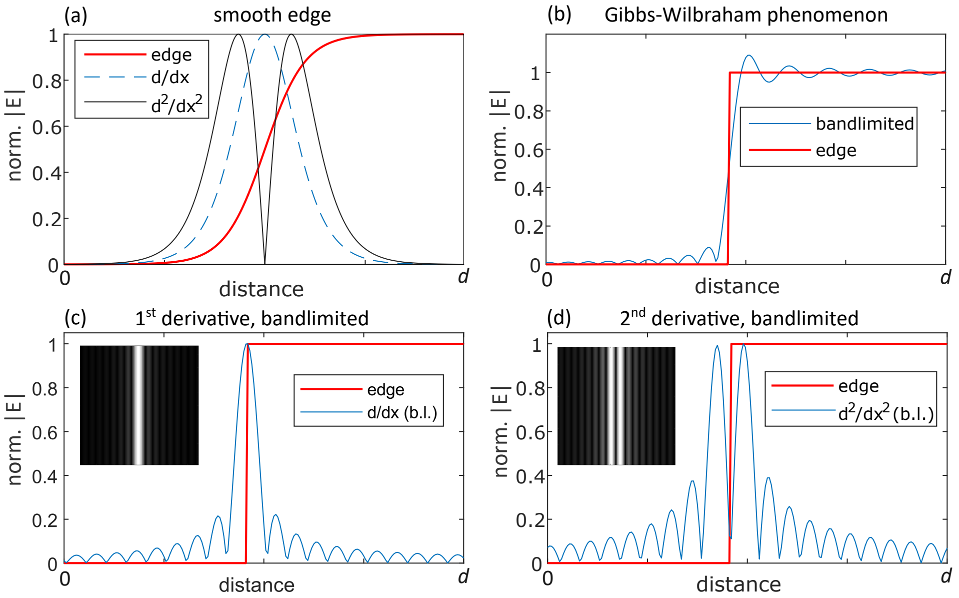

Figure 2.5: Detection of a smooth edge in an amplitude image with input amplitude shown in red and output from first- (blue) and second-order differentiation (black). (b) Ringing effects for system with limited spatial bandwidth due to the Gibbs-Wilbraham phenomenon. Shown is a sharp edge (red) with corresponding Fourier approximation for limited bandwidth (blue). Ringing effects for edge detection through (c) first- and (d) second-order spatial differentiation in a system with limited bandwidth. Insets show two-dimensional amplitude distribution indicating ringing around the edges. In (b-d) the bandwidth is limited to 10% of the Nyquist-frequency.

More advanced edge detection operators, that are commonly used in electronic computation, but have been implemented in bulk-optical systems as well include the Sobel, Prewitt and Roberts edge detection operator [67]. Here we focus on optical edge detection through high-pass spatial frequency filtering including spatial differentiation as discussed above.

While edge detection in pure amplitude images can be achieved through suppression of low-spatial frequency content with generally low dependence on the particular mathematical operations associated with the transfer function, this doesn't hold true for images containing phase-gradients. Below we will discuss the complex dynamics involved in phase-visualization through spatial frequency filtering.

2.1.5 Phase gradients and spatial differentiation

Conventional photodetector technology can directly detect the intensity of an optical wavefield while its phase remains invisible. Spatial differentiation enables conversion of phase gradients in a wavefield into intensity modulations, usually referred to in its most general sense as phase-visualization.

We assume a field $E(x, y) = e^{i\phi(x,y)}$ with a phase modulation $\phi(x, y) : \mathbb{R} \times \mathbb{R} \rightarrow \mathbb{R}$ and constant amplitude $|E(x, y)| = 1$. Considering first order spatial differentiation we obtain for the intensity of the differentiated field

$$\left|\frac{\partial E(x,y)}{\partial x}\right|^2 = \left|e^{i\phi(x,y)}\frac{\partial \phi(x,y)}{\partial x}\right|^2 = \left|\frac{\partial \phi(x,y)}{\partial x}\right|^2 \tag{2.27}$$

$$\left|\frac{\partial E(x,y)}{\partial y}\right|^2 = \left|e^{i\phi(x,y)}\frac{\partial \phi(x,y)}{\partial y}\right|^2 = \left|\frac{\partial \phi(x,y)}{\partial y}\right|^2 \tag{2.28}$$

Using first-order differentiation, we are therefore able to extract phase information from the wavefield with the output intensity of the system being the square of the phase gradient. As an example we use a light field with a Gaussian shaped phase-profile as described in eq.(2.29).

$$\phi(x, y) = \phi_{\max} e^{-\left((\frac{x}{\sqrt{2}\sigma})^2+(\frac{y}{\sqrt{2}\sigma})^2\right)} \tag{2.29}$$

Applying first order differentiation in either the x- or the y-direction to this phase-modulation with a width of $\sigma = l/2$ where l is the size of the image as shown in Fig.2.6, we obtain an intensity distribution that highlights regions of high phase gradient as expected from eq.(2.29).

We will see in the following that, counter intuitively, application of the Laplace operator does not yield an intensity variation purely related to the second order differentiation but a complex function of first and second order derivative of the phase modulation. A non-linear intensity response to phase-modulations in a wavefield is common in conventional phase-visualization methods as we will discuss at the end of this section.

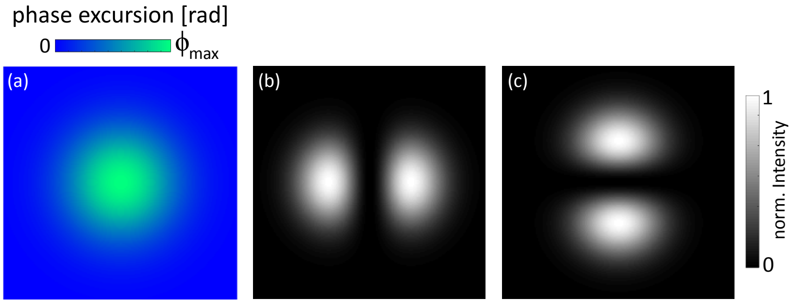

Figure 2.6: Calculated output Intensity of a first order differentiator applied to a wavefield with Gaussian shaped phase modulation $\phi(x,y)$ as described in eq. (2.29). The phase modulation is shown in (a) with $\sigma = l/6$ and $l \times l$ the size of the image. (b,c) Output intensity normalized to the brightest pixel for first-order differentiation along x- and $y-$ direction respectively.

Applying the Laplace operator ∇^2 we obtain

$$\left|\nabla^2 E(x,y)\right|^2 \tag{2.30}$$

$$=\left|\frac{\partial^2 E(x,y)}{\partial x^2}+\frac{\partial^2 E(x,y)}{\partial y^2}\right|^2 \tag{2.31}$$

$$=\left|\frac{\partial}{\partial x}\frac{\partial E(x,y)}{\partial x}+\frac{\partial}{\partial y}\frac{\partial E(x,y)}{\partial y}\right|^2 \tag{2.32}$$

$$=\left|e^{i\phi}\left[\frac{\partial\phi(x,y)}{\partial x}\right]^2+e^{i\phi}\frac{\partial^2\phi(x,y)}{\partial x^2}+e^{i\phi}\left[\frac{\partial\phi(x,y)}{\partial y}\right]^2+e^{i\phi}\frac{\partial^2\phi(x,y)}{\partial y^2}\right|^2 \tag{2.33}$$

$$=\left|\underbrace{\left[\frac{\partial\phi(x,y)}{\partial x}\right]^2}_{\text{1st order}}+\underbrace{\frac{\partial^2\phi(x,y)}{\partial x^2}}_{\text{2nd order}}+\underbrace{\left[\frac{\partial\phi(x,y)}{\partial y}\right]^2}_{\text{1st order}}+\underbrace{\frac{\partial^2\phi(x,y)}{\partial y^2}}_{\text{2nd order}}\right|^2. \tag{2.34}$$

From eq. (2.34) it is apparent that the second order derivative enables us to extract phase modulations from the wavefield and convert them into intensity variations. However, the presence of terms corresponding to first and second-order derivatives indicates a complex system output. Fig.2.7 shows the intensity output of a system that applies the Laplace operator to a wavefield with a Gaussian shaped phase modulation. It is apparent that the functional form of the intensity modulation now changes as a function of the absolute phase excursion ϕ_{max} in contrast to first-order differentiation considered above. Hence, for the purpose of phase extraction, a first-order optical transfer function is generally required. However, as long as we assume the phase variation $\phi(x,y)$ to be such that it can be approximated by a Taylor-expansion around a point (x_0, y_0) as a linear deviation from a constant phase background with

$$\phi(x,y) \approx \phi(x_0,y_0) + \frac{\partial\phi(x_0,y_0)}{\partial x}(x-x_0) + \frac{\partial\phi(x_0,y_0)}{\partial y}(y-y_0) \tag{2.35}$$

applying the Laplace operator yields

$$\left|\nabla^2 E(x,y)\right|^2 = \left|\left[\frac{\partial\phi}{\partial x}\right]^2 + \left[\frac{\partial\phi}{\partial y}\right]^2\right|^2. \tag{2.36}$$

In this case an intensity variation that is a function of only the phase-gradients $\frac{\partial\phi}{\partial x}, \frac{\partial\phi}{\partial y}$ in both spatial directions is produced. We can thus conclude that a system with a quadratic, and more generally a non-linear, transfer-function will convert a given phase modulation into a complex intensity modulation. Within the limits of near-linear phase-modulations this can still be employed for phase-gradient visualization.

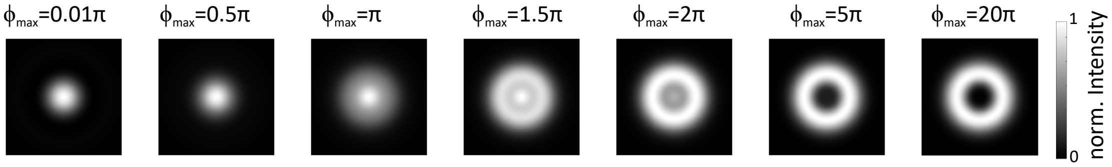

Figure 2.7: Calculated output intensity arising from the application of the Laplace operator ∇^2 applied to a wavefield with Gaussian shaped phase modulation $\phi(x,y)$ as described in eq. (2.29). Shown is the resulting intensity for varying maximum phase modulations $\phi_{\max}$ and $\sigma = l/5$ with $l \times l$ the size of the image.

As outlined in chapter 1, the visualization of phase-variations has been a major driver in the field of microscopy due to its importance for the visualization of mostly transparent objects like biological cells. A non-linear intensity response to phase-variations as discussed above is common in most conventional phase-visualization techniques including dark field micropscopy [68], differential interference microscopy (DIC) [7] and Schlieren microscopy [69, 70] as discussed in chapter 8 of [22]. Zernike phase-contrast microscopy was historically the first method that can generate intensity contrast that is linearly related to the phase profile of a wavefield for phase-shifts that are small compared to 2π radians [5]. The method was considered to be of such importance to the field of microscopy that its inventor Frits Zernike received the Nobel prize in 1953 [71]. In the following chapters we will investigate various novel nanophotonic approaches that permit filtering of Fourier components and discuss their capacity and limitations for the visualization of phase gradients.

2.1.6 All-optical Spatial Frequency Filtering

While the mathematical considerations of linear-invariant systems above were formulated in terms of an optical system, they are valid for linear electronic systems as well. In the introduction to this thesis the potential of optical systems to outperform electronic information processing systems in terms of speed and energy consumption were outlined but pathways to achieve this have not yet been discussed in detail. In the following we will review the fundamentals of traditional optical image processing and contrast it with the general approach for spatial frequency filtering in this thesis. The following review is based on deductions in [22].

2.1.6.1 Fourier transforming property of thin lenses

Thin optical lenses possess the ability to optically compute the Fourier transform of a wavefield. In order to understand the origin of this property we will review how a thin lens transforms an incident wavefield. A lens is referred to as 'thin' if light rays passing through it enter and exit the lens at the same lateral position with negligible translation inside of the lens. It can be shown that the phase transformation performed by a thin lens centered on the optical axis ($x = y = 0$) is given by

$$t_{\text{lens}}(x, y) = e^{-i\frac{\pi}{f\lambda}(x^2+y^2)} \tag{2.37}$$

with λ the wavenumber and f denoting the focal length of the lens defined by its curvature parameters and the refractive index of the material of which it is composed. This expression assumes that only parts of the wavefront that lie near the optical axis are considered. We now consider the situation of a flat object placed at a distance d in front of a lens L_2 as illustrated in Fig 2.8a. For illumination of the object with a monochromatic, planar wave of wavelength λ propagating parallel to the optical axis we denote the amplitude distribution directly behind the object as $E_0(x, y)$ and its Fourier transform as $\tilde{E}_0(k_x, k_y)$. In order to propagate the optical field through free space, we can use the Fresnel diffraction approximation. It assumes that only small angles of diffraction are considered and is therefore also referred to as the ‘paraxial approximation’. In this approximation propagation of a field over a distance d through free space can be performed via multiplication of its Fourier transform with a phase factor $\Delta\phi$ where

$$\Delta\phi = e^{-i\pi\lambda d(k_x^2+k_y^2)}. \tag{2.38}$$

For the Fourier spectrum of the field incident on the lens $\tilde{E}_{\text{in}}(k_x, k_y)$ we therefore obtain

$$\begin{align} \tilde{E}_{\text{in}}(k_x, k_y) &= \tilde{E}_0(k_x, k_y)\Delta\phi \tag{2.39} \\ &= \tilde{E}_0(k_x, k_y)e^{-i\pi\lambda d(k_x^2+k_y^2)} \tag{2.40} \end{align}$$

Using the phase transformation of the lens given in eq.(2.37) we obtain for the field E_{out} directly behind the lens

$$E_{\text{out}}(x, y) = E_{\text{in}}(x, y)t_{\text{lens}}(x, y) \tag{2.41}$$

where $E_{\text{in}} = \mathcal{F}^{-1}\big(\tilde{E}_{\text{in}}\big)$. Again exploiting the Fresnel diffraction formula it can then be shown that in the back focal plane of the lens L_2, i.e. at a distance f behind the lens, the intensity distribution $E_{\text{f}}(x, y)$ is given by

$$E_{\text{f}}(x, y) = \underbrace{\frac{e^{i\frac{k}{2f}(1-d/f)(x^2+y^2)}}{i\lambda f}}_{\text{quad. phase term}} \times \underbrace{\iint\limits_{-\infty}^{+\infty} E_0(\alpha, \beta)e^{-i\frac{2\pi}{\lambda f}(x\alpha+y\beta)}\,d\alpha\,d\beta}_{\text{Fourier transform}}\,. \tag{2.42}$$

From eq.(2.42) it is apparent that the amplitude and phase of the light at lateral coordinates (x, y) in the back focal plane are related to the amplitude and phase of the Fourier spectrum of the input field $E_0(x, y)$ at spatial frequencies $(k_x = x/\lambda f, k_y = y/\lambda f)$. The quadratic phase factor preceding the integral disappears for $d = f$, i.e. when the object is placed one focal length in front of the lens L2. In this situation the field produced in the back focal plane is proportional to an exact Fourier transformation.

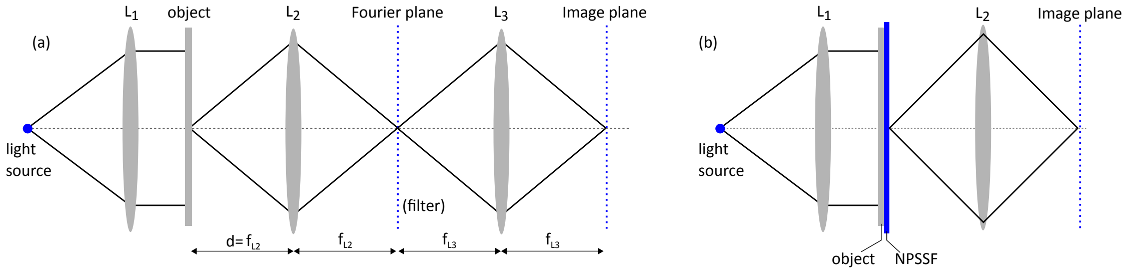

Figure 2.8: Conventional Fourier plane- and meta-optical object-plane spatial frequency filtering approach. (a) Conventional optical setup enabling access to the Fourier plane of an Image and filtering its spatial frequency content by placing a spatial filter in the Fourier plane. (b) Meta-optical approach for directly accessing and filtering the spatial frequency content of a wavefield.

With the Fourier transform of the wavefield E_0 being formed in the back focal plane of lens L_2, it enables filtering of the spatial frequency content by manipulating parts of the beam in the Fourier plane through tailored filters with varying amplitude and phase. This permits implementation of a range of useful filtering operations such as a high- or low-pass edge filters through the use of a blocking disc in the center of the beam or a pinhole respectively. Filtering of low- and high-spatial frequencies underpins for example widely used image processing applications such as object and face recognition [72] as well as previously discussed conventional approaches to phase visualization like Zernike phase-contrast microscopy, DIC imaging and Schlieren imaging [5, 7, 69]. More advanced filtering operations like blocking of a particular non-zero spatial frequency can be achieved using for example ring shaped beam-blockers. While traditionally these filters were binary masks, recently nanophotonic devices with engineered local amplitude and phase response have been demonstrated as potential pathways for advanced Fourier-plane spectral filtering in the domain of analogue optical computing as we will refer to below. However, these methods inherently rely on additional, usually macroscopic, building blocks allowing to access Fourier- and object plane respectively which implies limitations for their minituarization and integration into future optical devices.

2.1.6.2 Nanophotonic all-optical spatial frequency filtering

Traditional image- and information processing methods relying on accessing the Fourier plane and manipulating the spectral content through spatial filters are referred to as *Fourier-plane filtering* methods in the following. These approaches rely on at least two lensing elements, which can be either conventional lenses or more compact graded index (GRIN) elements, as well as a spatially structured filter element reshaping the Fourier content of a wavefield [22, 39]. While traditionally macroscopic apertures and beam-blockers were used [3] more recently nanophotonic approaches have drawn attention. Two-dimensional nanophotonic structures referred to as plasmonic metasurfaces were for example spatially tailored to perform differentiation when placed in the Fourier plane of an imaging system [73]. We will introduce optical metasurfaces in detail below in section 2.5.

This is in contrst to methods that enable accessing and filtering the Fourier content of a wavefield in the object plane thereby avoiding the requirement for bulky lenses or lens-like elements. We will refer to this type of filtering methods as *object-plane filtering* methods even though the devices could be positioned at other locations in the optical path [40]. In Fig.2.8(b) the working principle of such a method is illustrated for a transmitting filter. However, reflective filters are possible as well. In section 2.6 a review of implementation approaches for object-plane filtering methods will be given. These include metasurfaces, gratings, photonic crystals and thin-film based approaches. While methods requiring bulky or non-subwavelength elements have limited potential for miniaturization, the use of subwavelength nanophotonic elements operating in the object plane opens up significant potential for ultra-compact integrated optical filters that can perform passive all-optical information, and particularly image processing operations in real time.

2.1.7 High-pass Fourier filter performance

The focus of this work is on high-pass spatial frequency filtering. Various transmitting and reflecting devices are numerically investigated and experimentally implemented throughout this thesis. It is therefore natural to define a set of parameters that can be used to quantify the characteristics and performance of the respective high-pass spatial frequency filters. Here we define the numerical aperture NA and the standard filtering contrast C_s of a filtering function as follows. We assume a system with a two dimensional scalar optical transfer function $H(k_x, k_y)$ and define NA and C_s as system specific quantities for a given spatial direction, usually along one of the coordinate axes. The system characteristics along the x-direction would for example be deduced from $H(k_x, k_y = 0)$. Fig.2.9a shows an exemplary high-pass filter as a function of the normalized spatial frequency component k_x/k_0. We define the NA of the filtering function as the highest normalized spatial frequency up to which $|H(k_x, k_y)|^2$, i.e. the transmittance, for transmitting devices, or reflectance, for reflecting devices, increases monotonically. In the provided example we obtain NA= 0.67. Furthermore we define the standard contrast as

$$C_s = \frac{I_\mathrm{m} - I_0}{I_\mathrm{m} + I_0} \tag{2.43}$$

with I_m and I_0 the transmittance or reflectance at the NA and $k_x = 0$ respectively. From the definition in eq.(2.43) we obtain a filtering contrast of $C_s = 0.78$.

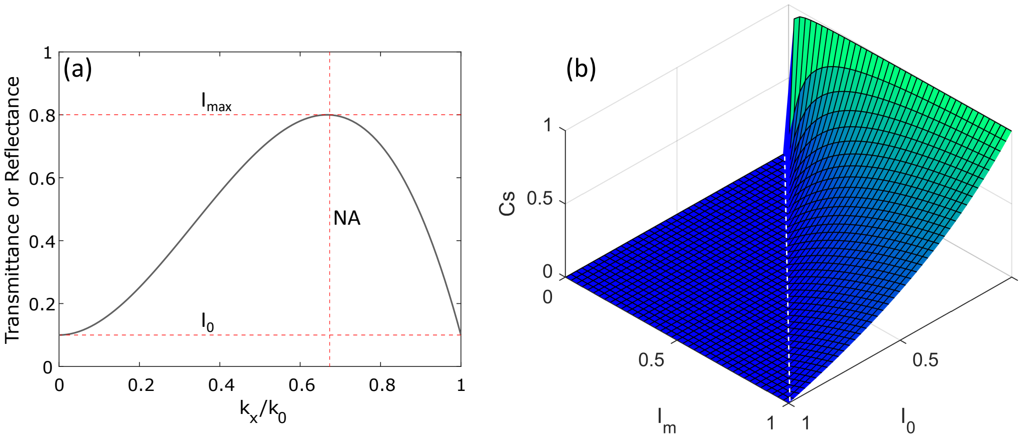

Figure 2.9: Characterisation of a high-pass spatial frequency filter. (a) Exemplary high-pass filtering function with red lines indicating numerical aperture (NA), zero-offset I_0 and maximum value I_m within the NA of the system. (b) Plot of the standard filtering contrast C_s for all possible combinations of I_m and I_0.

The majority of the spatial frequency filters investigated in this thesis exhibit a near-quadratic optical transfer function in at least one spatial direction. For this reason we will on several occasions compare them with an ideal second-order differentiator. As a measure we will fit the quadratic function

$$H_2\left(\frac{k_x}{k_0}\right) = a_1\left(\frac{k_x}{k_0}\right)^2 + a_2 \tag{2.44}$$

to the transmission coefficient t or reflection coefficient r of the respective devices along $k_y = 0$ and equivalently for the perpendicular direction. The fitting parameters a_1 and a_2 indicate the proportionality and zero-offset compared to an ideal second order differentiator with $a_1 = -4\pi^2 k_0^2$ and $a_2 = 0$.

2.2 Optical Response of Stratified Media

Tailored stacks of homogenous optically thin films have gained considerable attention as devices for nanophotonic image processing and we will review relevant work on the topic in section 2.6.1. In this thesis an approach to utilize simple three layer stacks in the form of metal-insulator-metal (MIM) absorbers is investigated. Below we will review the fundamentals that permit modelling of the optical response from stratified media made of homogenous layers and will here be used to describe MIM absorbers. The following is a summary of the relevant aspects of more extensive theoretical deductions of light - thin-film interactions by Macleod in chapter 2 of [74].

Initially we are considering the cases of a single thin film on top of a substrate as well as an extension to two or more films stacked on top of each other supported by a substrate as illustrated in figure 2.10. A film is considered optically thin when interference effects are observable in light reflected by- or transmitted through the film. This is equivalent to the condition that all waves propagating within a thin film stack exhibit a well defined phase relation between each other. Due to the in-plane isotropy of thin-film stacks they can be well described analytically. From Maxwell's equations it follows that at any optical boundary between two media with different refractive indices, the electric field component tangential to the boundary must be continuous. For the following derivation it is convenient to introduce the concept of the oblique admittance $\eta = H_t/E_t$ relating the tangential components E_t and H_t of the electric and magnetic field in a medium with refractive index N for propagation at an angle θ to the normal of a boundary. Depending

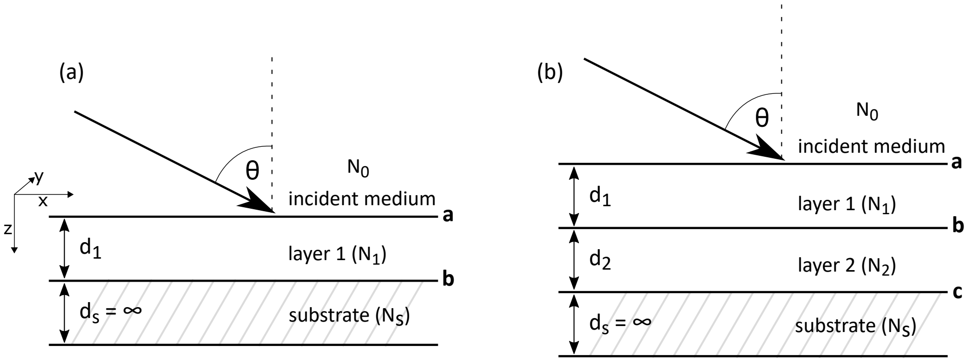

Figure 2.10: Numerical model of stacks of optically thin films. A number of partially transparent films of thicknesses (d_i) consisting of materials with dielectric properties (N_i) are stacked on top of each other supported by a semi-infinite substrate. Shown are examples of a one-layer (a) and two-layer system (b).

on the polarization state η is then given by

$$\eta = \eta_0 N \cos\theta \qquad \text{for s} - \text{polarization} \tag{2.45}$$

$$\eta = \eta_0 N / \cos\theta \qquad \text{for p} - \text{polarization} \tag{2.46}$$

with η_0 the free space admittance. Based on this we are now going to elaborate on the interaction of linearly polarized incident light with a single film of refractive index N_1 and thickness d_1 covering a semi-infinite substrate with refractive N_s as shown in Fig. 2.10a. Due to the presence of two interfaces in this system, a number of beams will be propagating simultaneously and their superposition will yield the reflection and transmission from and through the arrangement. Here we consider a plane wave incident on the single film structure. In the following we will denote forward going waves (in the positive z-direction) with the symbol '+' and backward going waves with the symbol '-'. In the superstrate as well as in the thin-film layer, forward and backward going waves will be present simultaneously while the substrate will accommodate only a forward going wave due to the lack of an underlying reflection layer.

At the boundary between the film and the substrate (boundary b) the tangential components E_b and H_b of the electric and magnetic field then satisfy

$$E_b = E_b^+ + E_b^- \tag{2.47}$$

$$H_b = \eta_1 E_b^+ - \eta_1 E_b^- \tag{2.48}$$

with η_1 the oblique admittance of the thin film layer 1. From equations (2.47),(2.48) we directly obtain expressions for the tangential field components of the forward and backward going waves.

$$E_b^+ = (H_b/\eta_1 + E_b)/2 \tag{2.49}$$

$$E_b^- = (-H_b/\eta_1 + E_b)/2 \tag{2.50}$$

$$H_b^+ = (H_b + \eta_1 E_b)/2 \tag{2.51}$$

$$H_b^- = (H_b - \eta_1 E_b)/2 \tag{2.52}$$

In order to deduce the fields at the other interface (boundary a) from equations (2.49)-(2.52) at a point with identical x and y coordinates, one has to propagate the wave by multiplying the fields with a phase factor $e^{\pm i\delta}$ that corresponds to the effective layer thickness δ with

$$\delta = \frac{2\pi N_1 d_1 \cos\theta_1}{\lambda} \tag{2.53}$$

for light propagating at an angle θ_1 within the layer, where λ is the free space wavelength. Here the propagation angle θ_1 can be a complex number indicating a potentially evanescent field. Introducing this phase factor into equations (2.49)-(2.52) yields

$$E_a^+ = E_b^+ e^{i\delta} = \frac{1}{2}(H_b/\eta_1 + E_b)e^{i\delta} \tag{2.54}$$

$$E_a^- = E_b^- e^{i\delta} = \frac{1}{2}(-H_b/\eta_1 + E_b)e^{i\delta} \tag{2.55}$$

$$H_a^+ = H_b^+ e^{i\delta} = \frac{1}{2}(H_b + \eta_1 E_b)e^{i\delta} \tag{2.56}$$

$$H_a^- = H_b^- e^{i\delta} = \frac{1}{2}(H_b - \eta_1 E_b)e^{i\delta}. \tag{2.57}$$

From this we obtain a set of equations relating the tangential field strengths at boundary a to those of boundary b

$$E_a = E_a^+ + E_a^- = E_b \cos\delta + H_b \frac{i \sin\delta}{\eta_1} \tag{2.58}$$

$$H_a = H_a^+ + H_a^- = i E_b \eta_1 \sin\delta + H_b \cos\delta. \tag{2.59}$$

Equations (2.58),(2.59) can most conveniently be expressed as a matrix equation

$$\begin{bmatrix} E_a \\ H_a \end{bmatrix} = \begin{bmatrix} \cos\delta & i\sin\delta/\eta_1 \\ i\sin\delta\eta_1 & \cos\delta \end{bmatrix} \begin{bmatrix} E_a \\ E_b \end{bmatrix} \tag{2.60}$$

To obtain the overall optical response of the thin film, it is convenient to define the admittance Y of the system as

$$Y = H_a/E_a. \tag{2.61}$$

From the system admittance Y and the admittance of the incident medium η_i the reflection coefficient r as well as the reflectance R is then calculated using

$$r = \left(\frac{\eta_i - Y}{\eta_i + Y}\right) \tag{2.62}$$

$$R = rr^* = |r|^2 \tag{2.63}$$

The experiments performed in this thesis include thin film systems with three layers as depicted in Fig. 2.10b. It can be shown that repeating the derivation above leads to an extension of eq. (2.60) describing stacks of thin films with an arbitrary number of layers. For a stack of $q-1$ films on top of a substrate the tangential field components are then described by

$$\begin{bmatrix} B \\ C \end{bmatrix} = \prod_{r=1}^{q} \begin{bmatrix} \cos(\delta_r) & i\sin(\delta_r)/\eta_r \\ i\sin(\delta_r)\eta_r & \cos(\delta_r) \end{bmatrix} \begin{bmatrix} 1 \\ 1/\eta_m \end{bmatrix} \tag{2.64}$$

where $B = E_a/E_b$, $C = H_a/E_b$, η_m the admittance of the substrate, and η_r the admittance of the r-th layer. The system admittance is then given by $Y = C/B$ and the optical response can again be calculated from eq. (2.62),(2.63).

We will conclude the fundamental consideration of thin film stacks at this point. In chapter 4 we will model metal-insulator-metal (MIM) thin-film absorbers using the framework above and draw conclusions about their spatial-frequency filtering capabilities. In the following we will move our focus to the interaction between light and subwavelength sized metallic particles and their relevance for meta-optical imaging systems.

2.3 Metals at optical frequencies

In the radio frequency regime the interaction between electromagnetic waves and metals can be well described by the approximation that metals behave as perfect conductors. Hence at any time the free electrons in the metal instantaneously arrange in such a way that an external electric field is screened out and thus cannot penetrate into the metal. In this case all incident fields decay exponentially beneath the surface. However as frequencies approach the optical spectral range, the assumption of a perfect conductor is no longer appropriate for metals and fields begin to penetrate into the metal. In the following we will discuss the consequences of this based on more detailled discussions provided in [75]. In contrast to the charge carriers in a perfect conductor, the electrons now acquire characteristics of a strongly dispersive plasma. This behavior can be observed at frequencies around and above the near-infrared spectral range for most metals. Techniques, as for instance ellipsometry, permit determining the complex dielectric function of metals

$\epsilon(\omega) = \epsilon_1 + i\epsilon_2$ by reflectivity studies at optical frequencies. However a deeper understanding requires a theoretical model for $\epsilon(\omega)$. For this reason we will make some fundamental assumptions about the properties of conduction electrons in metals that finally lead to a general equation for the dielectric function.

2.3.1 The Free Electron Gas Model of Metals

Some optical properties of metals are well described by the assumption that the conduction electrons of a metal are a gas of negatively charged particles (an electron plasma) moving in front of a positively charged background, which represents the ion cores of the metal. Structural details of the potential of the crystal lattice and collisions between electrons are neglected in this assumption. The model following from these assumptions is referred to as the *'free-electron gas model'* or *'Drude-Sommerfeld model'*. We consider an electron that is driven by the electric field **E** of an incident EM wave and damped by collisions with positively charged ion cores and obtain the equation of motion for an electron in this gas:

$$m\ddot{\mathbf{x}} = -e\mathbf{E} - m\gamma\dot{\mathbf{x}} \tag{2.65}$$

where m is the effective mass of an electron and γ denotes the frequency at which electrons collide with the positive ion cores. For a harmonic time dependance of the electric field **E** it can be shown that the macroscopic polarization **P** following from the electron displacement described in eq. (2.65) holds

$$\mathbf{P} = -\frac{ne^2}{m(\omega^2 + i\gamma\omega)}\mathbf{E}. \tag{2.66}$$

Equation (2.66) yields the dielectric function of the free-electron gas with

$$\epsilon(\omega) = 1 - \frac{\omega_p^2}{\omega^2 + i\gamma\omega}, \tag{2.67}$$

where $\omega_p^2 = \frac{ne^2}{\epsilon_0 m}$ is the plasma frequency of the metal with electron density n.

The main factors resulting in a disagreement between the free electron model and experimentally determined dielectric functions are interband transitions and highly polarized environments caused by filled bands in the vicinity of the Fermi surface. While we do not have to take these effects into account for alkali metals, where the free electron gas model yields good results up to the UV range, they occur already between near-infrared and optical frequencies for noble metals such as gold and silver. In order to take the strongly polarized environments occurring due to the electronic band structure in noble metals into account, the term $\mathbf{P}_\infty = \epsilon_0(\epsilon_\infty - 1)\mathbf{E}$, with ϵ_∞ a dielectric constant, is added to the dielectric displacement. This yields a modified dielectric function with

$$\epsilon(\omega) = \epsilon_\infty - \frac{\omega_p^2}{\omega^2 + i\gamma\omega}. \tag{2.68}$$

In Fig.2.11 the dielectric function of the extended free-electron gas model from eq. (2.68) was fitted to the measured dielectric data for gold [76]. It is apparent that while the experimental data is well represented at lower energies, the prediction of the free-electron gas model deviates significantly from experimental data at visible wavelengths due to interband transitions as observable in ϵ_2. The free-electron gas model provides important insight into the origin of the dispersive nature of the interactions between metals and electromagnetic waves at optical wavelengths. However, for quantitative analysis we will resort to literature values of experimentally determined dielectric functions to model plasmonic resonances in this thesis. As we will discuss when the relevant experimental results are presented in following chapters, these values depend on the particular fabrication process of a material. In particular for optically thin films fabricated through evaporation processes, deviations in the dielectric function from the literature values are found and commonly lead to spectral shifts and broadening of resonances.

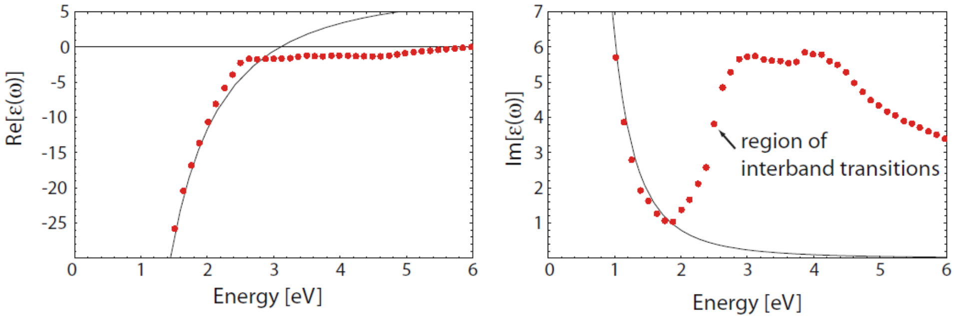

Figure 2.11: Complex dielectric function of gold. Left: Real part ϵ_1, Right: Imaginary part ϵ_2. Shown is a comparison between the free-electron gas model (solid line) and experimentally measured data for gold [76] (dotted line). Figure taken from [75][2].

---

[2] Reprinted by permission from Springer Nature Customer Service Centre GmbH: Springer Nature, 'Plasmonics: Fundamentals and Applications - Electromagnetics of Metals' by S.A. Maier, 2017.

2.4 Plasmonic Resonances

In the previous section the dispersive characteristics of the electron gas in metals at optical frequencies was reviewed. Based on the above discussion we will now progress to review resonant excitations of the electron gas in metals as they are broadly exploited in meta optics. Quantized oscillations in the electron gas density are generally referred to as plasmons. For the field of meta-optics two different kinds of coherent plasmonic excitations that occur as a result of the interaction between a driving electromagnetic field and the electron plasma are of relevance - surface plasmon polaritons (SPP) and localized surface plasmons (LSP). We will introduce both excitations as elucidated in detail in [75] in the following before we proceed to their application in the field of plasmonic metasurfaces.

2.4.1 Surface Plasmon Polaritons (SPP)

Surface plasmon polaritons (SPP) are propagating collective charge oscillations that can be excited at an interface between a metal and a dielectric or a semiconductor and a dielectric. Here the term SPP refers to the charge oscillation (plasmon) as well as the related electromagnetic field (polariton) decaying exponentially perpendicular to the surface as illustrated in Fig. 2.12a,b. An incident electromagnetic wave can excite an SPP on a planar surface if both momentum and energy are conserved. Propagation of surface plasmon polaritons at planar interfaces can be fully deduced from Maxwell's equations and is analytically well understood. From this the propagation constant β_{SPP} of an SPP excited by light with wavenumber k_0 at the interface of a dielectric with dielectric constant ϵ_a and a metal with dielectric constant ϵ_b can be derived as

$$\beta_{\mathrm{SPP}} = \sqrt{\frac{\epsilon_a \epsilon_b}{\epsilon_a + \epsilon_b}} k_0. \tag{2.69}$$

Equation (2.69) is valid for conductors without and with ohmic losses, i.e. real and complex dielectric function. In the case of a complex propagation constant the SPP decays exponentially along the surface. From eq.(2.69) it is apparent that the propagation constant of the SPP is greater than the absolute value of the wavenumber of the incident light inside the adjacent dielectric. This momentum mismatch prohibits direct excitation of an SPP and additional phase-matching techniques are required. Among others the most prominent excitation methods for surface plasmon polaritons exploit prism coupling in Kretschmann or Otto configuration, grating coupling or near-field excitation. Since the vast majority of the work discussed in this thesis is based on plasmonic excitations on confined subwavelength-sized particles instead of planar interfaces, the reader will be referred to [75] for a more detailed review of SPP excitation and we will focus on localized surface plasmons.

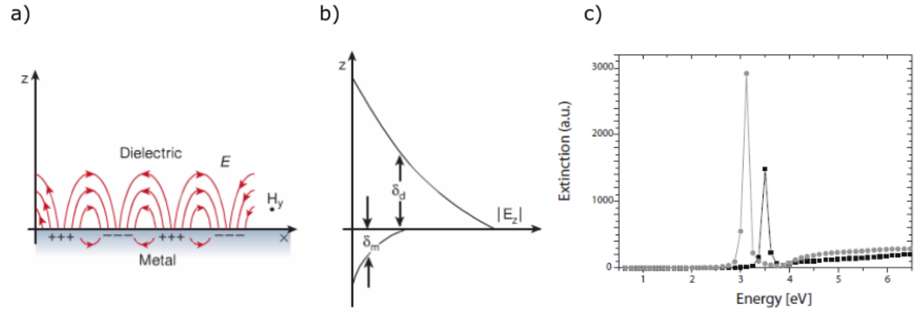

Figure 2.12: Surface Plasmon Polaritons and Localized Surface Plasmons. a) Collective charge oscillations and associated electric field of a Surface Plasmon Polariton b) The electric field strength decays exponentially into the metal and the dielectric for non-radiative SPPs enabling strong field confinement. c) Calculated LSP resonances for a gold sphere in air (black) and silica (gray). a) and b) taken from [77][3] and c) taken from [75][4].

2.4.2 Localized Surface Plasmons (LSP)

The second plasmonic excitation of interest in the context of this work are localized surface plasmons (LSP). SPP's were introduced above as dispersive propagating electromagnetic waves associated with charge oscillations at material interfaces. On the other hand LSP's are non-propagating dispersive excitations of the electron plasma on subwavelength sized conductive particles immersed in an ambient dielectric and coupled to an electromagnetic field. In the optical realm, these particles are usually referred to as metal nanoparticles. Upon interaction with an incident electromagnetic wave the forces acting on the electron plasma in the nanoparticle displace the electrons from their median position. Following this displacement restoring forces from Coulombic attraction between electrons and the positively charged nuclei as well as charge accumulations on the nanoparticle result in a dispersive oscillation of the electron cloud. For a combination of nanoparticle shape,

---

[3] Reprinted by permission from Springer Nature Customer Service Centre GmbH: Springer Nature, Nature, 'Surface plasmon subwavelength optics', William L. Barnes et al., 2003

[4] Reprinted by permission from Springer Nature Customer Service Centre GmbH: Springer Nature, 'Plasmonics: Fundamentals and Applications - Localized Surface Plasmons' by S.A. Maier, 2017.

size, material and dielectric environment, this oscillation can go into resonance with an incident electromagnetic wave of given frequency. This resonance is referred to as a localized surface plasmon resonance (LSPR). For nanoparticles consisting of metals such as gold and silver, LSPR can occur at visible wavelengths resulting in bright color effects in transmitted and reflected light historically used for example in remarkably colourful, stained glass windows. A second characteristic of localized surface plasmons are strongly enhanced electric fields in the direct vicinity of the surface, an effect referred to as near field enhancement. These strong electric fields offer the potential for sensing applications [78, 79] including surface enhanced Raman scattering (SERS) and near field microscopy, improvements in the efficiency of nonlinear optical effects [80] and the excitation of zero net-dipolar moment modes as discussed below. For this reason considerable scientific effort has been directed to the fabrication of nanoparticles with tailored spectral responses. Nanoparticles with shapes including for instance cubes [81], rods [82], prisms [83] and core-shell structures [84] have been investigated. Control over their spectral response by geometry adjustments and sensitivity to changes in the ambient dielectric have for instance been demonstrated in disordered layers of ring-shaped structures [85].

The particular set of resonances that can be excited on a nanoparticle depends on a complex interplay of its shape, material, dielectric environment [81–84] and, as we will see below, the illumination conditions. For a very limited number of cases an analytic expression for the LSP resonances can be deduced while other cases require numerical treatment. However, analytic treatment of the problem provides a fundamental understanding of the resonance phenomenon for which we here review the case of a plane wave incident on a metallic sphere placed in an ambient dielectric as an example.

2.4.2.1 Plasmonic Resonance of a Conductive Sphere

In the case that the radius a of the particle under consideration is small compared to the wavelength λ of an incident electromagnetic wave, i.e. $a \ll \lambda$, one can assume that the phase of the electromagnetic field is constant over the entire volume of the particle. This is referred to as the *quasi-static approximation* and allows us to model the particle response in a static electric field $\mathbf{E} = E_0 \mathbf{e}_z$ and add the harmonic time dependance after solving for the field distribution. This approximation well describes the optical response of nanoparticles with sizes of up to approximately 100 nm. Further below we will discuss numerical ways to model nanoparticles for which the quasi-static approximation fails. The derivation of the optical response of the nanoparticle thereby simplifies to solving the Poisson equation $\nabla^2\phi = 0$ for the given boundary conditions with ϕ the electric potential. Due to the symmetry of the problem it can be shown that the general solution to this problem is of the form

$$\phi(r,\theta) = \sum_{l=0}^{\infty} \left[A_l r^l + B_l r^{-l-1}\right] P_l(\cos\theta) \tag{2.70}$$

with A_l, B_l the coefficients to be determined, $P_l(\cos\theta)$ the Legendre polynomials of order l and θ describing the angle between the position vector $\mathbf{r}$ and the z axis of the coordinate system. Applying the boundary conditions at $r = \infty$ and $r = a$ permits a derivation of the potential outside of the particle ϕ_{out} as a superposition of the applied field and the field of a dipole situated at the center of the sphere given by

$$\phi_{\text{out}} = -E_0 r\cos\theta + \frac{\mathbf{p}\cdot\mathbf{r}}{4\pi\epsilon_0\epsilon_m r^3} \tag{2.71}$$

$$\mathbf{p} = 4\pi\epsilon_0\epsilon_m a^3 \frac{\epsilon-\epsilon_m}{\epsilon+2\epsilon}\mathbf{E_0}. \tag{2.72}$$

Here ϵ and ϵ_m denote the dielectric functions of the dielectric and the metal. For the field of the dipole $\mathbf{p}$ we can define the polarizability α as

$$\alpha = 4\pi a^3 \frac{\epsilon-\epsilon_m}{\epsilon+2\epsilon_m}. \tag{2.73}$$

It is apparent that α exhibits a resonant maximum when $|\epsilon + 2\epsilon_m|$ is minimized. This is fulfilled for the so called 'Fröhlich condition', real$(\epsilon) = -2\epsilon_m$, in the case of a slowly varying imaginary part of the metallic dielectric function. As the essential result of this deduction, eq.(2.73) shows the existence of a resonant response of a metallic nanosphere upon interaction with an incident field. The mode associated with this resonance is the dipole surface plasmon of the metallic sphere. From this result characteristic resonances in the absorption and scattering cross section can be deduced. Exemplary numerical calculations for a gold particle in air and silica in Fig.2.12(c) illustrate their resonance at optical wavelengths. While the analytic derivation above enables a fundamental understanding of the origin of LSP resonances, more complex nanoparticle shapes as well as larger particles for which the quasi-static approximation fails, generally have to be treated numerically. This involves in particular higher-order multipolar modes on complex shaped nanoparticles which will be discussed in the context of subradiant modes below. In this thesis we employ the finite element method (FEM) to model plasmonic resonances on metallic nanostructures as introduced in section 3.1.1.

2.4.3 Plasmon Hybridization and Subradiant Resonances

The discussion above revolved around resonances on isolated, individual nanoparticles and we will now extend our considerations to nanoparticle ensembles. In close proximity, the behavior of nanoparticles can vary significantly from their individual response to light due to interparticle coupling effects [75, 86]. This can be described as bonding and antibonding combinations of the individual particle plasmons resulting in a modal hybridization analogous to molecular orbital interaction as described by Prodan et al. [87]. The effect is spectrally observable as a splitting of the individual resonances into the hybridized resonances as the coupling strength between the particles increases. Although higher order multipoles on the participating particles contribute to the hybridization, to first approximation the response of the ensemble can be described by coupling between the lowest order modes, the dipole plasmons of the individual particles. For instance, in the simple case of two adjacent nanodiscs, a so called *dimer*, a bonding mode of lower energy and an antibonding mode of higher energy arise [88]. The strength of the modal hybridization of the dimer increases with decreasing interparticle separation. Investigation of the phenomenon with a range of nanoparticle geometries and ensembles has received

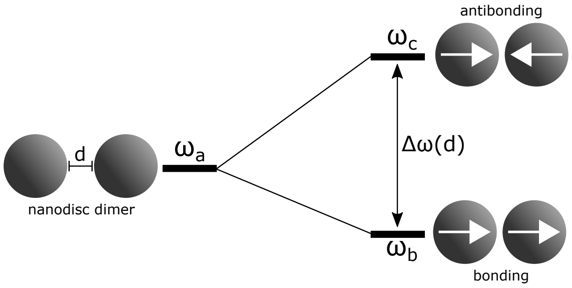

Figure 2.13: Modal hybridization on nanodisc dimer in dipole approximation as desribed in [88]. For small separation d of the nanodiscs, resonance hybridizes from the resonance ω_a of the individual disc into ω_b for the bonding mode and ω_c for the antibonding mode. The degree of hybridization $\Delta\omega$ is a function of the particle separation.

considerable attention. Complex and symmetry broken nanoparticle ensembles in particular exhibit interesting hybridization effects [79, 89]. In order to systematically study the emerging hybridizations on nanostructures, symmetry arguments from group-theory can be exploited. This was for example demonstrated using the example of nanodisc trimers as illustrated in Fig.2.14(a) [90]. In this case a set of orthonormal modes, consisting of different combinations of dipole modes on the individual discs, was derived.

While the fundamental resonance of a nanoparticle or nanoparticle ensemble is its electric dipole mode, various structures support higher-order modes with zero net-dipolar moment. These modes are referred to as subradiant modes and are an example of bound modes in the continuum (BIC) [91, 92]. As we consider individual nanoparticles, subradiant modes refer to higher-order multipole resonances such as quadru- or octupolar modes that exhibit zero electric dipole moment. On the other hand modal hybridization in nanoparticle ensembles as discussed above can also result in resonances with a zero-net electric dipole moment of the ensemble. Due to their vanishing dipole moment these modes cannot couple to, or only weakly couple to, normally incident, linearly polarized light for which they were also coined *dark modes*. Consequently, in order to excite dark modes, one needs to introduce either a symmetry breaking in the geometry of the nanostructure or employ alternative excitation schemes [79, 89, 93, 94]. These include for instance: excitation by focussed electron beams [95], evanescent near field excitation [96], off-normal incidence [79, 97] and subwavelength phase-engineered beams [98]. Compared to their electric dipole counterparts these modes suffer reduced radiative damping and thus enable more efficient energy storage in nanoparticle structures and exhibit a reduced resonance linewidth [92, 93]. In this work we will confine our considerations to light based excitation schemes. The central result of the research discussed above for the purposes of this work is the angular sensitivity of the optical excitation of these subradiant modes. While here we discuss the fundamental resonant characteristics of dark modes, in the following section 2.6.2 we will review how meta-optical approaches can exploit this effect to perform all-optical spatial-frequency filtering.

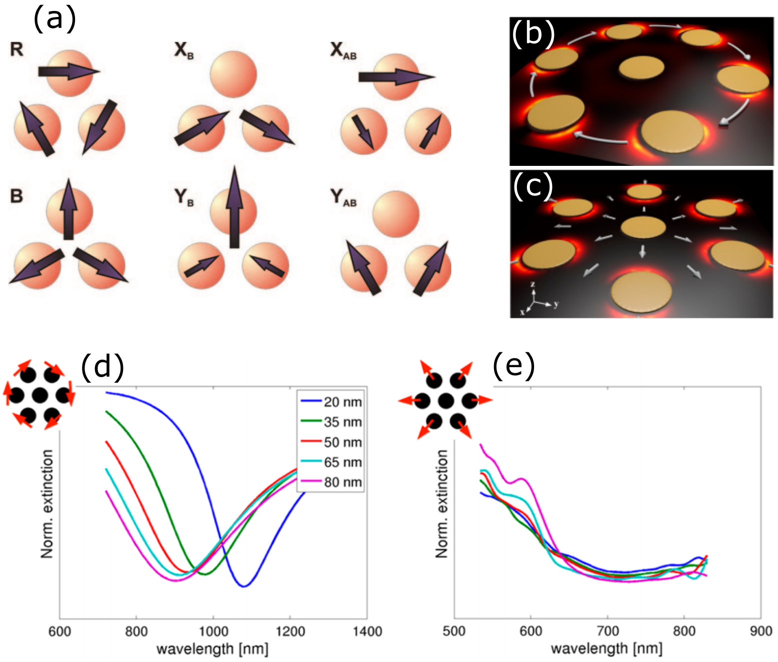

Figure 2.14: Subradiant modes on nanoparticle ensembles. (a) Orthonormal set of modes of a disc trimer arrangement deduced from group theory considerations taken from [90][5] , (b,c) Oligomer nanodisc ensemble in breathing and rotation mode with corresponding calculated spectral response for excitation with azimuthally polarized light (d) and radially polarized light (e) as a function of nanodisc separation. (b-e) reprinted with permission from [99][6].

We will conclude this section by reviewing some relevant examples of subradiant resonances on plasmonic nanostructures. Various studies have employed a broken geometric symmetry for the excitation of resonances with subradiant character. Examples for such geometries are the non-concentric ring disk cavity [79] or its three dimensional equivalent, the core-shell particle with an offset core [89]. The concentric ring disk cavity (CRDC) consists of a metallic disk concentrically surrounded by a metallic ring. Fao and coworkers have demonstrated excitation of higher order modes in this structure through off normally incident light as well as through the systematic introduction of a geometric asymmetry in the form of an off-centered disk [79]. Symmetric arrangements of rods and disks have also received increased attention with regard to their subradiant mode characteristics. Examples are the oligomer geometry (*cf.* Fig. 2.14(b-e)) consisting of five circularly arranged metallic discs with an additional central disc [99] as well as plasmonic trimers consisting

---

[5] Reprinted with permission from 'Plasmonic Properties of Silver Trimers with Trigonal Symmetry Fabricated by Electron-Beam Lithography', Joan Alegret, Tomas Rindzevicius, Tavakol Pakizeh, et al., J Phys Chem C, vol. 112, no. 37, pp. 14313–17. Copyright 2008 American Chemical Society

[6] Reprinted with permission from 'Near- and far-field properties of plasmonic oligomers under radially and azimuthally polarized light excitation.', Avner Yanai, Meir Grajower, Gilad M. Lerman, et al., Acs Nano, vol. 8, no. 5, pp. 4969–74. Copyright 2014 American Chemical Society

of discs [90] (*cf.* Figure 2.14(a)) or rods [93] arranged on the vertices of a triangle. As an example, two subradiant modes of a nanodisc oligomer as illustrated in Figure 2.14(b-e) are considered. The modes can be categorised as a 'rotation mode' and a 'breathing mode' according to the corresponding energy density distributions. It should be noted that out-of-plane dipole moments were neglected here. One way to excite a particular mode such as the breathing or rotation mode in this nanostructure is to choose a polarization state of the incident light that matches the structural symmetry of the dipolar displacements. The excitation of the different modes is apparent from the extinction spectra with the lower energy rotational mode (*bonding*) appearing at longer wavelengths compared to the higher energy breathing mode (*anti-bonding*).

To summarize we have reviewed localized plasmonic resonances of nanoparticles and near-field coupling effects in nanoparticles ensembles above and stated their relevance for historical and modern optical applications. We will now transition to a review of recent work on repetitive arrays of nanostructures, so called *optical metasurfaces*, and particularly their relevance as ultra-compact all-optical image processing platforms.

2.5 Introduction to Optical Metasurfaces

Classical optics employs components that rely on the effects of refraction, diffraction and light propagation over distances longer than the wavelength of light in naturally occurring materials. This enables control over the amplitude, polarization and phase distribution of an optical wave in bulky components like classical lenses and waveplates [100]. Recent advances in nanofabrication technology however have enabled the fabrication of artificially structured materials, termed metamaterials, that obtain their physical properties from their designed morphology rather than their chemical composition. Metamaterials have been demonstrated to enable control over optical, microwave, radio frequency, acoustic and heat transfer response not attainable with naturally occurring materials [32]. Photonic metamaterials have received enormous attention in the scientific community owing to their unusual optical properties. These include, for instance, metamaterials with negative refractive indices due to negative permittivity and permeability, impedance matched zero-reflection materials, perfect optical absorbers or materials exhibiting giant circular dichroism [25].

Meta materials generally consist of three-dimensional arrangements of fundamental building blocks, coined meta-atoms, that act as tailored optical resonators. Unfortunately the implementation of three-dimensional structures naturally requires complex fabrication and design methods in order to stack several layers of meta-atoms [29]. Approaches such as direct laser writing [101], templating approaches and lithographic techniques such as membrane projection lithography have been considered to enable fabrication of thin metamaterials [25]. The complex fabrication and limited compatibility of three-dimensional meta materials with planar optical chip-designs hence elicits a demand for two dimensional counterparts with similar properties.

2.5.1 Operational principle of optical metasurfaces

A subclass of metamaterials with reduced dimensionality, so called metasurfaces, are of particular interest for overcoming these limitations due to their ability to enable highly specialized optical devices with reduced fabrication complexity and without the need for macroscopic light propagation. Their designs are based on arrays of dielectric or metallic optical scatterers as illustrated in Fig.2.15 [32]. These are commonly combined with untextured optically thin films. Owing to their mostly two dimensional nature and typically subwavelength thickness, metasurfaces are suitable for on-chip photonic devices for next generation information technology, imaging and sensing applications. The principle of metasurface design is to arrange fundamental scatterers with varying geometric orientations or shapes in order to create a desired, potentially spatially varying, optical response

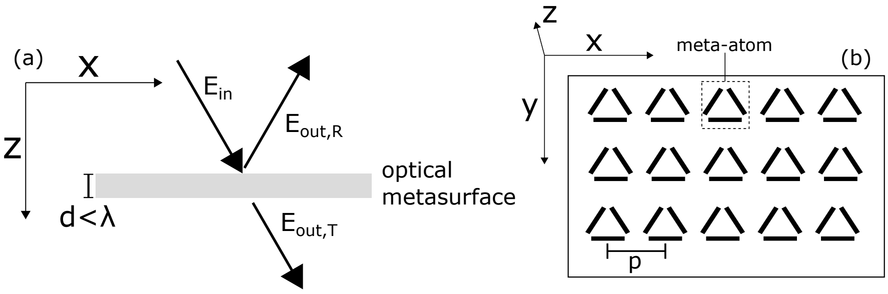

Figure 2.15: Operational principle of optical metasurfaces. (a) Photonic structures of commonly subwavelength thickness process an incident optical field with the output contained in the reflected and transmitted field. (b) Optical Metasurfaces consist of arrays of optical scatterers (meta-atoms).

to an incident field. In turn the collective scattering of these arrays results in modification of amplitude, phase and polarization of the reflected or transmitted field [29]. Based on this approach optical wavefronts can either be moulded into a desired shape [32, 100] or information carried by them can be extracted [102]. In the following we will briefly review applications of optical metasurfaces in general before we proceed to a detailed review of their role in approaches for analogue optical computation.

In addition to the geometry and other properties of the unit cell, the operational nature of optical metasurface arrays depends precisely on the separation of the meta atoms which can be divided into three regimes [29]. Firstly, as the distance between neighbouring meta atoms is comparable to the resonance wavelength of the structure, diffractive far field interactions can lead to collective modes referred to as surface lattice resonances. In the second regime, the separation of the meta atoms is large enough to neglect near field interactions but smaller than the resonance wavelength and thus disables the collective modes mentioned above. Phase-gradient meta surfaces that enable wave front shaping are of this category and will be discussed below. Thirdly, as meta atoms are placed in close proximity, near field-interactions dominate their optical response as discussed above in section 2.4.3.

2.5.2 Plasmonic and Dielectric Metasurfaces

A particularly promising platform to implement optical metasurfaces are plasmonic resonances. Plasmonic metasurfaces are composed of arrays of metallic meta atoms and exploit localized surface plasmon resonances [29] as discussed in detail in the previous section. These metallic meta-atoms exhibit an effective electric and, under certain circumstances, magnetic polarizability and can be as simple as antenna rods or exhibit more complex geometries inspired from common shapes in the radiofrequency realm [103]. In accordance with Babinet's principle [104] apertures in metallic films can also be considered to be plasmonic meta-atoms.

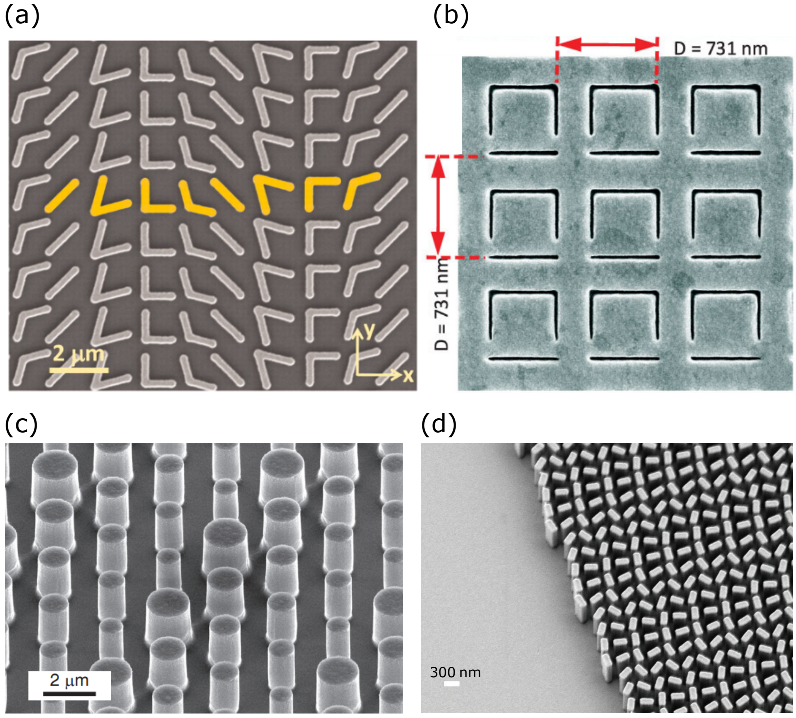

Figure 2.16: Scanning electron microscopy (SEM) images of exemplary plasmonic and dielectric metasurfaces. (a) array of V-shaped antennas to generate out-of plane reflection and refraction (b) Babinet inverted meta-atom as slits in a gold film to enhance nonlinear effects in carbon nanotubes (c) Dielectric resonator array for infrared flat lenses (d) Dielectric antenna array implementing a metalens at visible wavelengths. Images reprinted with permission from (a)[105][7], (b) [106][8], (c) [107][9]and (d) [108][10].

While initially research on optical metasurface has mainly exploited plasmonic resonances, recently dielectric metasurfaces have gained considerable attention as alternative pathways [30]. An overview of exemplary plasmonic and dielectric metasurface architectures is provided in Fig.2.16. The motivation for using resonances on dielectric nanoparticles, rather than metallic ones, originated from the additional degrees of freedom available with magnetic resonances as well as reduced losses [31]. Plasmonic nanoantennas in their basic rod form are limited to inducing phase shifts of π on an incident wavefield and require hybrid solutions involving resonant phase shifts and engineering of the geometric phase to cover

---

[7] From 'Light propagation with phase discontinuities: Generalized laws of reflection and refraction', N. Yu, P. Genevet, M. A. Kats, F. Aieta, J. Tetienne, F. Capasso, and Z. Gaburro, *Science*, vol. 334, no. 6054, pp. 333 – 337, 2011. Reprinted with permission from AAAS.

[8] Reprinted figure with permission from A. E. Nikolaenko, F. De Angelis, S. A. Boden, N. Papasimakis, P. Ashburn, E. Di Fabrizio, and N. I. Zheludev, *Physical review letters*, vol. 104, p. 153902, 2010. Copyright (2010) by the American Physical Society.

[9] Reprinted with permission from OSA publishing, taken from [107].

[10] From 'Metalenses at visible wavelengths: Diffraction-limited focusing and subwavelength resolution imaging', M. Khorasaninejad, W. T. Chen, R. C. Devlin, J. Oh, A. Y. Zhu, and F. Capasso, *Science*, vol. 352, no. 6290, pp. 1190 – 1194, 2016. Reprinted with permission from AAAS.

the entire 2π range as we will discuss further in the following section. This particularly limits the design of metasurfaces for wavefront control. Dielectric nanoparticles on the other hand support strong dielectric and magnetic resonances thereby enabling full 2π phase-coverage [109]. While magnetic resonances can be exploited in certain plasmonic nanoparticles, so called *Huygens resonators*, as well, they imply complex fabrication and high optical losses. Dielectric nanoparticles offer lower losses at optical wavelengths and have therefore become a popular platform for wavefront shaping metasurfaces [31]. However, we argue that for the particular case of spatial frequency filtering metasurfaces considered here, high losses from plasmonic resonances can aid the suppression of light reflection or transmission and are, therefore, of considerable interest. For this reason, the research presented in this thesis focuses exclusively on approaches based on plasmonic resonances. To facilitate an adequate overview of the field, plasmonic and dielectric metasurface approaches will be discussed together in the following section.

Below we will review relevant theoretical and experimental work on optical metasurfaces. Initially we will provide a brief overview of various kinds of metasurfaces and their fields of application. Due to the tremendous speed at which the research in this field has developed over the last decades a full review is out of the scope of this thesis and representative work will be discussed instead. We then proceed to a detailed review of metasurfaces that are able to manipulate the spatial frequency content of an optical field, which is the central point of interest of this thesis. It is exactly this category of metasurfaces that can perform all-optical computing including image processing and holds potential to facilitate ultra-compact phase-imaging for biological applications.

2.5.3 Overview of Metasurface Applications

Major fields in which optical metasurfaces find applications are wavefront shaping, biological and chemical sensing, the generation of structural colour, energy harvesting and photodetection as well as analogue optical computation. We will provide a brief introduction to the first four categories here and, owing to its relevance for this thesis, review the latter in detail in the following sections.

2.5.3.1 Wavefront control with optical metasurfaces

As a broad term wavefront control metasurfaces describes metasurfaces that allow the reshaping of an incident wavefront manipulating its intensity and polarization distribution. It should be noted that, in opposition to metasurfaces discussed in the following section, we here refer to metasurfaces that are not designed to sense properties of the incident field, such as its phase profile. Among other applications of optical metasurfaces they possess particular potential for next generation imaging systems as ultra compact equivalents to conventional bulk optical components.

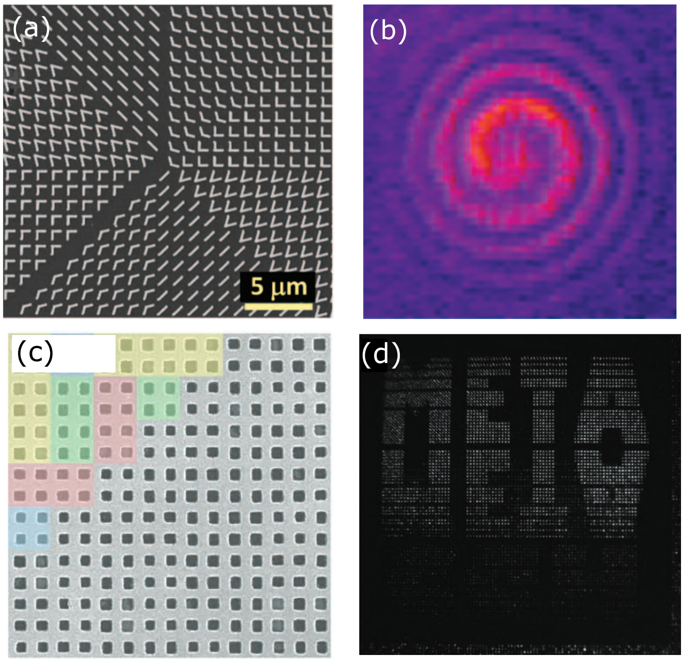

Figure 2.17: Examples of wavefront control metasurfaces. (a) SEM capture of phase gradient metasurface for the generation of vortex beams with (b) the generated vortex beam upon interference with a Gaussian beam (c) SEM image of plasmonic metasurface array with generated hologram shown in (d). Images reprinted with permission from (a,b) [105][11]and (c,d) [37][12].

For this reason a review of their underlying principles is of importance for the presented work. According to the Huygens principle, the secondary waves emitted from different scatterers interfere such that their envelopes form a modified wavefront. Via engineered

---

[11] From 'Light propagation with phase discontinuities: Generalized laws of reflection and refraction', N. Yu, P. Genevet, M. A. Kats, F. Aieta, J. Tetienne, F. Capasso, and Z. Gaburro, *Science*, vol. 334, no. 6054, pp. 333 – 337, 2011. Reprinted with permission from AAAS.

[12] Reprinted with permission from B. Walther, C. Helgert, C. Rockstuhl, F. Setzpfandt, F. Eilenberger, E.B. Kley,F. Lederer, A. Tünnermann, and T. Pertsch, 'Spatial and spectral light shaping with metamaterials', *Advanced Materials*, 2012, copyright 2012 WILEY-VCH Verlag GmbH & Co. KGaA, Weinheim.

introduction of spatially varying discrete phase-changes $\Delta\phi(x, y)$ and potentially amplitude changes $\Delta E_0(x, y)$ on a surface one can thus create arbitrarily shaped wavefronts upon interaction of an incident wavefield with the metasurface. For this purpose meta-atoms that are able to induce a tailored phase shift in the range of $\Delta\phi = [0 - 2\pi]$ between the scattered and the incident light are required. We can distinguish between meta-atoms generating phase shifts based solely on their resonance curve, meta-atoms generating phase differences solely due to their geometric shape and orientation (Pancharatnam-Berry Phase) and those employing a combination of both [30, 110]. As discussed in the previous section, a simple plasmonic antenna oscillator cannot cover the entire phase range and approaches based on geometric phase engineering are required. Due to their favorable amplitude conserving characteristics particularly V-shaped plasmonic antennas consisting of two rod antennas connected at an angle α have received scientific attention [105]. Spatially varying orientations of the V-shaped antenna allow implementation of phase-control metasurfaces on the basis of resonant features in combination with the Pancharatnam-Berry phase. These modal properties of V-shaped antennas enable extended control over the amplitude, phase and polarization of the radiated light. Furthermore V-shaped antennas usually achieve large scattering amplitudes for a broad wavelength range due to their high radiative losses and their two eigenmodes enabling the design of broadband optical components [100]. It is worth noting that a variety of alternative approaches for introducing phase-shifts with metasurfaces have also been proposed. These include for instance gap surface plasmon resonances [111] and nanoparticle clusters. More recently high-index dielectric, rather than plasmonic, resonators have gained attention for the engineering of phase gradient metasurfaces. As outlined in the previous section dielectric meta-atoms can cover the full 2π phase-shift range without relying on geometric phase engineering by manipulating their electric and magnetic resonances. Their additional low losses at optical wavelengths have made them the platform of choice for wavefront shaping metasurfaces [31, 109]. The artificially engineered phase-gradients on a metasurface can result in unusual anomalous refraction and reflection effects not occurring at conventional optical interfaces such as out-of-plane refraction and the existence of two angles for total internal reflection [105, 112].

Phase-gradient meta surfaces have received great attention as potential replacements for bulk optical components by chip-compatible equivalents [110], particularly flat lenses [33, 34, 113, 114] and waveplates [35, 36, 115]. Ni et al. for instance have used circular arrays of Babinet inverted V-shaped antennas to achieve extremely strong focusing at visible wavelengths on length scales below 10 µm [116]. Yu et al. have created a broadband quarter-wave plate to change the polarization state of transmitted light from linear to circular in the far-infrared regime [36]. Finally various groups have demonstrated the ability of phase-gradient metasurfaces to generate and manipulate vector beams [105, 117, 118] and implement holograms [37, 38, 119–122]. Representative examples in Fig.2.17 show the generation of a vortex beam upon transmission through a metasurface and a metasurface producing holograms at infrared wavelengths.

2.5.3.2 Other Applications of Optical Metasurfaces

Other prominent applications of optical metasurfaces relate, for instance, to enhancements in chemical and biological processes, near-perfect absorption and the generation of structural colour. Here we include a limited selection of examples to emphasize the astonishing number of potential applications of optical metasurface approaches.

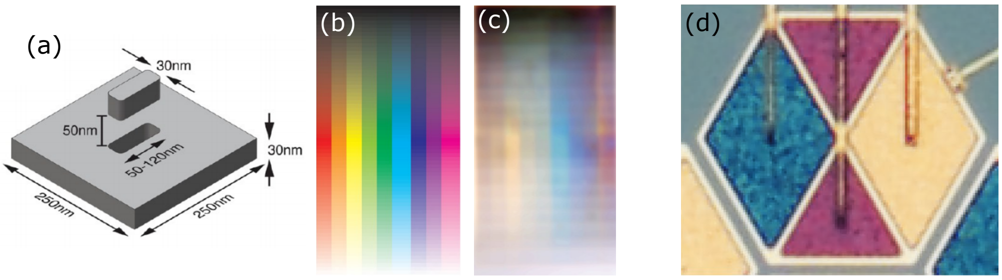

Figure 2.18: Structural colour from plasmonic metasurfaces. (a) Floating metal dipole unit cell as a platform for the generation of structural colour pixels (b) colour mixing test pattern and (c) metasurface reproduction using the floating dipole architecture (d) colour camera pixel using metasurface colour filters instead of conventional dye based filters for reduced spatial footprint and colour cross talk. Images reprinted with permission from (a-c) [123][13], (d) [124][14].

Within chemical and biological applications particularly surface enhanced Raman spectroscopy (SERS) has received enormous attention as a high resolution molecular sensing technique [125–127]. SERS is based on the enhancement of Raman scattering from

---

[13] Reprinted with permission from 'The plasmonic pixel: large area, wide gamut color reproduction using aluminum nanostructures', T. D. James, P. Mulvaney, and A. Roberts, *Nano Letters*, vol. 16, no. 6 , pp. 3817–3823, 2016. Copyright 2016 American Chemical Society

[14] Reprinted with permission from E. Panchenko, L. Wesemann, D. E. Gómez, T. D. James, T. J. Davis, and A. Roberts, 'Ultracompact camera pixel with integrated plasmonic color filters', *Advanced Materials*, 2019, copyright 2019 WILEY-VCH Verlag GmbH & Co. KGaA, Weinheim.

molecules on a structured surface by orders of magnitude ($\approx 10^{10} - 10^{11}$) such that single molecule detection becomes accessible and biological analysis is enhanced [128, 129]. Both plasmonic and dielectric nanostructures have been demonstrated to facilitate the SERS approach [130, 131].

A broad area of research focuses on optical metasurfaces for the generation and filtering of colour through nanostructuring [132–135]. The approach is usually referred to as *structural colouration* since the formation of colour stems from the nanostructure of the surface rather than its chemical composition. Through engineering of the absorption spectrum of electric and magnetic resonators as well as thin-film stacks, full color representation has been achieved [123, 136–138]. Fig.2.18 shows examples of structural colour generation through a floating dipole architecture together with a metasurface colour filter for ultra-compact camera pixels. Structural colour mechanisms are often inspired by biological environments [139] and have potential applications in the coloration of consumer products [140, 141], as optical document security features and as optical spectral filters [124] among others.

Related to the generation of structural colour are metasurfaces designed for near-perfect absorption that find applications for example as efficiency enhancements in optoelectronics and photocatalysis [142]. A full summary of the above topics lies outside of the scope of this work and the reader is referred to comprehensive reviews on the topics [137, 143–145].

2.6 Nanophotonic Spatial-Frequency Filtering in the Object-plane

Optical computation can take place in the temporal or spatial domain. While there is a large area of research focused on engineering approaches in the temporal domain [146–151] here we focus exclusively on spatial domain approaches. In section 2.1.6.2 we have introduced the concept of all-optical analogue computation in the object-plane. In principle any nanophotonic structure exibiting a transmission or reflection that is a function of the angle of incidence has the capacity to perform object-plane spatial frequency filtering on an incidence wavefield. The first implementations of the approach were initially demonstrated in the 1970 and 80's using thick grating structures [40, 41] as well as using interference filters [42]. With the rise of digital computation, however, scientific interest in the development of these optical approaches declined and has only recently regained attention owing to the advances in nanofabrication technology and concepts emerging from studies of metasurfaces. This section is dedicated to a review of recent progress in nanophotonic approaches for all-optical computation in the object plane. The emerging approaches fall into two different categories: devices based on stacks of non-structured optical thin-films and approaches incorporating one or several layers textured on the nanoscale. In the following we will review recent work on both approaches and discuss their relevance for analogue optical computation including optical image processing. It should be noted that a significant number of the articles reviewed below have been published in parallel to the research carried out in this thesis.

2.6.1 Thin-film absorbers

While the approaches for all-optical spatial frequency filtering reviewed in the following section rely on structures with one or more layers textured on the nanoscale, first we discuss devices consisting of stacks of non-structured optically thin films. Structured optical metasurfaces usually require complex fabrication techniques including lithography [152, 153]. Uniform thin-film structures on the other hand are commonly fabricated by thermal or electron beam evaporation or sputtering methods, thus enabling scalability due to low-cost, large area fabrication of devices [74].

One approach that has recently gained attention as a platform for analogue optical computing and was investigated in various theoretical studies are phase-shifted Bragg gratings (PBSG) [43, 44, 154] (*cf.* Fig.2.19(a)). Optical Bragg gratings are periodic modulations of the refractive index of a transparent material, such that near-complete reflection occurs for a particular wavelength [155, 156]. PSBG's in their simplest form consist of two consecutive Bragg gratings with a defect layer between them introducing a phase-shift. Owing to this additional phase-shift a Fabry-Pérot type cavity is formed between the first and the second Bragg grating resulting in ultra narrow absorption bands [157] and enabling optical computation in the temporal domain [158]. Subsequent to these results it was theoretically demonstrated that PBSG's also enable analogue optical computation in the spatial domain due to a steep change in the interference condition as a function of angle of incidence. In particular it was shown that a PBSG can perform first-order spatial differentiation in reflection for a wavefront incident under a device specific angle θ_0 and compute the Laplace operator of the incident field for normally incident light [43, 44]. It should be noted that these results demonstrate the possibility of the approach to engineer devices with both odd- and even optical transfer functions. Additionally, the potential of PBSG to perform all-optical integration of a transmitted wavefront was theoretically investigated [154]. As pointed out in [44] the quality of the computation as well as the energy efficiency are determined by the total number of layers in the Bragg gratings for which a case-dependent compromise is required. In the above study devices with a total number of layers between 13 and 21 were considered. At the time of writing these devices had yet to be experimentally demonstrated.

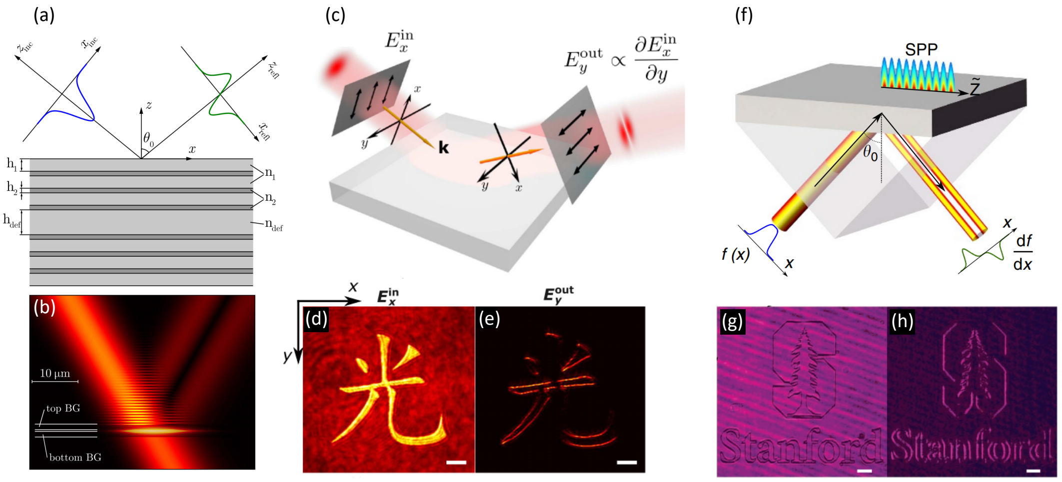

Figure 2.19: Object plane spatial-frequency filtering using optical thin-films. (a,b) Phase shifted Bragg gratings (PSBG) as reflective optical differentiators with differentiated Gaussian beam (electric field amplitude) [43][15], (c-e) Spatial differentiation upon interface reflection based on spin-hall effect (SHE) of light [47][16]with edge detection in amplitude images (f-h) Surface Plasmon Polariton (SPP) excitation on metal thin-films for spatial differentiation upon reflection [45][17]with edge detection in phase-image. Scalebars are 50 μm (d,e) and 100 μm (g,h). Figures reprinted with permission from provided references.

A recent theoretical study has investigated how a more general thin-film stack consisting of alternating layers of Si and SiO$_2$ can be tailored to optically perform a custom linear

---

[15] Reprinted with permission from OSA publishing, taken from [43].

[16] Reprinted with permission from American Physical Society.

[17] Reprinted with permission from Springer Nature (Creative Commons CC BY license).

operation on a reflected wave front [54]. Using an optimization algorithm the optical transfer function of a thin-film stack with a given layer number is fitted to the optical transfer function corresponding to the desired linear operation. The technique is used to design devices that can perform second order spatial differentiation. Requirements for total numbers of layers are discussed in terms of the width of the spatial frequency spectrum they are designed to process. The examples investigated in the study include between 5 and 20 layers for processing of narrower and broader spectra respectively and have not yet been experimentally demonstrated.

Another thin-film enabled concept for analogue optical computing that has been studied numerically is that of dielectric slab waveguides. The concept operates on the distinct angular sensitivity of modal coupling in the vicinity of the excitation angle of the modes of a dielectric slab waveguide. One study demonstrated that for a specific angle of incidence reflection from a slab waveguide can enable spatial differentiation in reflection [159]. A second study using this concept demonstrated spatial integration for transmitted wavefields [160]. In both studies the authors use Si on SiO_2 for numerical case studies. As more compact versions of the investigated concept both studies propose and calculate an example based on graphene sheets with engineered surface conductivities instead of dielectric layers forming the slab wavguide. Various approaches discussed in the following section of this review also exploit the angular sensitivity in the excitation of slab waveguide modes but utilize grating-type coupling mechanisms.

Neither of the previously discussed thin-film stack approaches have yet been experimentally demonstrated. As acknowledged in [54] nanometer precision in thin-film deposition thickness as well as high-requirements regarding deviations of the refractive indices imply complex fabrication schemes for devices requiring a large number of layers. Additionally the large number of layers required for the above described approaches usually results in devices thicker than the wavelength of the light they are designed for thus rendering the approaches non ultra-compact.

The excitation of surface plasmon polaritons (SPP) on thin metallic films has also been proposed for optical computation and was initially investigated in a theoretical study [161]. The approach exploits the angular dispersion in the excitation of SPP resonances on metallic thin-films for the computation of the first spatial derivative in one dimension. Furthermore the study points out the potential of the structure to act as an optical integrator when an additional pump beam incident from the back of the film is used. To the present day, only the differentiator functionality has been experimentally demonstrated. The approach requires the use of a prism in Kretschmann configuration and reflection of the wavefield from the film under an angle that ensures matching of the lateral wavenumbers of incident light wave and SPP which in turn depends on the material and thickness of the film. The first experimental demonstration of of this device was provided by Vohnsen and Valente who employed a thin gold film on a glass prism to perform wavefront sensing through spatial differentiation [59]. In a subsequent study Zhu. et al. demonstrated first-order spatial differentiation using a thin silver film on a glass prism [45] (*cf.* Fig.2.19(f)). This was employed by the authors to perform experimental edge detection in a reflected amplitude and a phase image with sizes of several hundred micrometers. While the thin-films in these studies had subwavelength thicknesses of approximately 50 nm, the requirement for a macroscopic glass-prism prevents device integration of the method in its current form. The authors of [45] suggest using a two-dimensional grating coupler in order to extend the device's functionality to differentiation in both directions as well as eliminating the requirement for a macroscopic prism element. A seperate study has numerically investigated this alternative approach for SPP excitation on graphene at Terahertz wavelengths [162]. By placing a graphene film on top of a silicon grating, supported by a reflective gold substrate, the authors achieve second order differentiation in reflection at normal incidence.

Two studies have investigated single planar optical interfaces as a simple platform for optical analogue computation. The first study proposes exploiting the Brewster effect that occurs for TM-polarized light reflected at an optical interface [46]. The study numerically demonstrates that first order differentiation is performed on a wavefield reflected from a planar surface at the material specific Brewster angle. A second approach was recently proposed and experimentally demonstrated exploiting the spin-hall effect (SHE) of light [47] (*cf.* Fig.2.19(c)). The approach is based on the principle that a linearly polarized beam refracted at a surface is spatially split into its left- and right-circularly polarized components [163]. Using a second, perpendicular polarizer as an analyzing element the effect can be used for spatial differentiation. The authors employ the approach to demonstrate edge detection in an amplitude and a phase image with sizes of several hundred micrometers reflected from an air-glass and from an air-gold interface. While the SHE vanishes for normally incident light, no specific angle of reflection is required for which the authors were able to perform differentiation for light incident onto the surface at angles ranging from 25° to 65°.

While the multilayer thin-film structures discussed in the beginning of this section commonly require large numbers of layers, in this thesis an approach based on three layer metal-insulator-metal (MIM) absorber structures is demonstrated to enable all-optical spatial frequency filtering in reflection [60].

2.6.2 Metasurfaces, Gratings and Photonic Crystals

Following the introduction of plasmonic and dielectric metasurfaces we will now review nanophotonic approaches for analogue optical image processing that incorporate one or several layers textured on the nanoscale. These include gratings, photonic crystals and metasurfaces. Subwavelength gratings, including resonant diffraction gratings (RWG), have received considerable attention as object plane spatial frequency filters. RWG refer to a class of nanostructures incorporating subwavelength gratings that support leaky guided modes along the grating as reviewed in [164]. Among other configurations they consist, for example, of a shallow grating on top of a slab waveguide layer such that the grating enables coupling of incident light into resonant modes supported by the slab waveguide. Based on the angular dispersion of this coupling mechanism, the structure enables analogue optical computation in reflection and transmission. RWG should be distinguished from high-contrast gratings (HCG) that rely on the excitation of vertical Bloch modes in deep grating grooves rather than guided modes traveling in horizontal direction. Initial theoretical work has derived a differential equation describing the spatial transformation of a two dimensional beam upon diffraction by a resonant wave guide grating [48]. The study establishes a framework in which conditions for a resonant waveguide grating to operate as an optical integrator and differentiator are given. The model approximates transmission and reflection from the structure in the vicinity of a resonance in terms of the respective non-resonant optical coefficients and propagation constants of the eigenmodes of the structure. In an explicit numerical example of an aluminium arsenide grating on a silica layer the differentiation of a transmitted Gaussian beam is demonstrated. It should be noted that the approach requires operation at oblique incidence in order to achieve first-order differentiation.

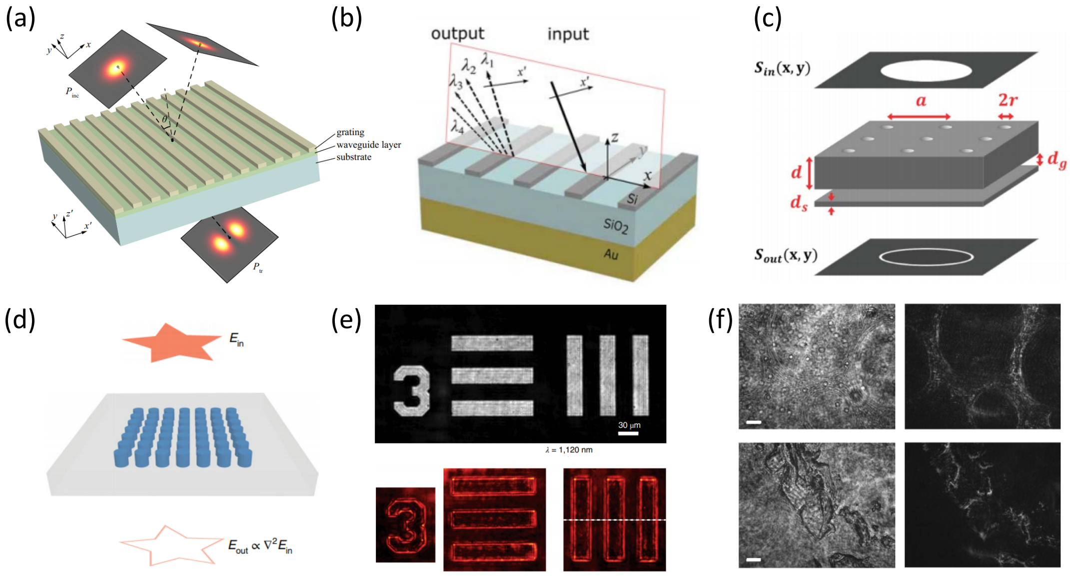

Figure 2.20: Object plane spatial-frequency filtering through gratings, metasurfaces and photonic crystals. (a) Resonant waveguide grating (RWG) for first-order differentiation in transmission [49][18](b) Wavelength multiplexed differentiation with RWG in reflection [165][19](c) Photonic crystal slab resembling a transmitting optical Laplace operator [50][20](d) Photonic crystal implementing a Laplace-like operator in transmission [51][21]enabling (e) Edge detection of amplitude images and (f) contrast enhancement in Biological samples. Shown are the examples of a pumpkin stem (top) and a pig motor nerve (bottom) for imaging without (left) and with the photonic crystal (right). Scalebars are 50 μm. Images adapted with permission from provided references.

Several studies have experimentally implemented the proposed design for differentiation along one spatial direction. Bykov et al. have used a structure consisting of a TiO$_2$ layer and a ERP40 electron resist grating operating in the visible wavelength range [49] (*cf.* Fig.2.20(a)). The study demonstrates differentiation of a Gaussian beam upon transmission. The same principle was exploited to realize a one-dimensional structure consisting of a silicon grating on a quartz thin-film for near-infrared operation [166]. An extension of

---

[18] Reprinted with permission from OSA publishing, taken from [49].

[19] Reprinted with permission from OSA publishing, taken from [165].

[20] Reprinted with permission from OSA publishing, taken from [50].

[21] Reprinted by permission from Springer Nature Customer Service Centre GmbH: Springer Nature, Nature Photonics, vol. 14, pp. 316 – 323, 'Flat optics for image differentiation', Y. Zhou, H. Zheng, I. I. Kravchenko, and J. Valentine, Copyright 2020.

the resonant wave guide grating design for wavelength-multiplexed spatial differentiation in reflection was suggested in a theoretical study [165] (*cf.* Fig.2.20(b)). The design is based on a silicon grating on top of a SiO_2 slab and a reflecting Au substrate operating at telecommunication wavelengths and oblique incidence. By storing each image at a different wavelength in the input field and diffracting them under a wavelength dependent output angle, the device enables demultiplexing of the processed output. As an example edge detection is performed on four different images stored within a spectral bandwidth of approximately 260 nm. A plasmonic subwavelength grating operating without a waveguide layer was recently demonstrated for operation in the visible wavelength regime using a gold grating on a quartz substrate [167]. The approach exploits excitation of surface plasmon polaritons (SPP) on the grating surface at a particular angle of incidence. Furthermore this study demonstrated the ability of the device to perform edge detection on transmitted images. While the above studies focus on one-dimensional spatial-frequency filtering, a numerical study has investigated how a two-dimensional silicon nitride grating embedded in a SiO_2 slab can extend this functionality to two-dimensional operation [55]. The study demonstrates high-pass spatial frequency filtering and edge detection for transmitted amplitude images. The authors acknowledge the anisotropy and complexity of the optical transfer function as a limiting factor for uniform edge detection in all directions. This also prevents the device from performing 'clean' first- or second order differentiation. In chapter 6 of this thesis plasmonic RWG consisting of subwavelength silver gratings on a TiO_2 waveguide layer are investigated. Two-dimensional object-plane filtering in transmission using a plasmonic RWG will be investigated for the first time.

The concept of engineering guided mode structures has further been extended to exploit Fano-type resonances and leaky modes in photonic crystals. A theoretical study by Kwon et al. proposes engineering of arrays of resonant particles with a superimposed periodic spatial- or dielectric modulation such that interference between particle resonances and guided surface modes results in narrow Fano-type resonances [56]. The authors demonstrate, using the example of an array of split ring resonators with varying dielectric constant of the gap material, that the resulting angular response of the device enables first- and second-order differentiation of transmitted wavefields in one dimension. Using an extended design, the authors also demonstrate the ability of the approach to implement a device performing the Laplace operator and apply it to numerically demonstrate two-dimensional edge detection on a transmitted image. Subsequent work numerically and experimentally demonstrated how gratings consisting of dielectric nanobeams with suitable parameters can be engineered to support narrow-band Fano-resonances [66]. Using this structure first- and second-order differentiation in one spatial dimension were numerically demonstrated. An experimentally implemented silicon nanobeam grating was subsequently proven to enable one-dimensional second order differentiation at near-infrared wavelengths. Two dimensional photonic crystal slabs have also been proposed as a platform for all-optical analogue computing [50]. In a theoretical study Guo et al. demonstrate that the band structure of a photonic crystal slab, consisting of a hole array and a homogenous dielelectric layer interrupted by an air gap, can be engineered to perform the Laplace operator on a transmitted wavefield. Edge detection upon transmission through the photonic crystal slab was also numerically demonstrated. The most extensive study based on a guided-mode metasurface to the present day has recently experimentally demonstrated performing the Laplace operator on a transmitted wavefield using a two dimensional photonic crystal [51]. The design consists of an array of Silicon nanorods on top of a SiO_2 slab operating at near-infrared wavelengths. By engineering the geometry such that leaky-modes are excited in the silica slab and interfere with directly transmitted light to form Fano-type resonances the authors obtain a device with quadratic optical transfer function. Experimental edge detection of amplitude images as well as contrast enhancement in images of several biological samples including onion epidermis, pumpkin stems and pig motor nerves was demonstrated. As an extension of the proposed design the authors combine the photonic crystal with a metalens forming a bilayer system that can directly be placed on top of an image sensor to perform edge detection. Centimeter sized test-objets were sucessfully processed using this compound device.

Another physical mechanism that has been suggested as a platform for all-optical analogue computing is the excitation of subradiant modes of resonant particles as introduced in detail above in section 2.4.3. While the electromagnetic response of a nanoparticle or ensemble thereof is usually dominated by its electric or magnetic dipole resonance, weaker and spectrally narrower higher order modes with zero net-dipolar moment can be excited under specific circumstances [168]. These modes are usually referred to as subradiant- or dark modes as well as bound modes in the continuum (BIC). The excitation of subradiant modes of plasmonic metasurfaces has received considerable attention [93, 169]. Owing to their zero electric net-dipole moment these higher-order modes do not couple to normally incident, linearly polarized light. However, off-normally incident light introduces a phase-difference across the particle or particle ensemble thereby enabling excitation of subradiant modes. This angular sensitivity in their excitation provides a platform for all-optical spatial frequency filtering, particularly edge detection and phase visualization, as theoretically described by Roberts et al. [53, 57] within the framework of angular sensitive metasurface modes. The framework is based on the electrostatic eigenmode approximation which considers a limited number of dipole resonances of each particle within a unit cell and from their interaction constructs higher-order electromagnetic responses of the metasurface. Furthermore the model assumes perfectly conducting elements (PEC). It was numerically demonstrated how various arrangements of three nanoantennas per unit cell enable excitation of subradiant modes for oblique incidence . The appearance of ultra-narrow Fano resonances as a consequence of interference between dipole and dark modes is also discussed [53]. Numerical case studies were carried out demonstrating edge detection and phase-visualization upon transmission through arrays of coaxial ring apertures [57].

A particular structure that has been investigated by several studies as a platform for all-optical analogue computation through subradiant mode excitation are dolmen-shaped rod arrangements [52, 58, 170]. The structure is also referred to as a 'plasmonic Wheatstone bridge'. In an initial numerical study a dolmen structure consisting of two parallel rods and a third perpendicular arm centered above was proposed as a reflective and transmissive method for phase visualization along one spatial dimension based on the spatial frequency filtering ability of the structure [52]. The structure operates on the principle that phase differences in the dipole LSP oscillations on the parallel rods excite an oscillation on the third rod. It should be noted that the approach requires input that is linearly polarized along the two parallel rods and generates cross-polarized output for which a polarizer before, and an analyzer behind the metasurface are required. An extension of the structure for two-dimensional spatial frequency filtering has later been proposed and experimentally implemented [58]. Recently a related structure has been numerically engineered to perform second-order spatial differentiation on a transmitted wavefield in one direction [170].

Asymmetric optical transfer functions, as discussed in section 2.1.4, are essential to perform mathematical operations including first order differentiation. Kwon et. al have argued that these can only be generated from two-dimensional structures by breaking the symmetry in horizontal and vertical direction [56]. However, Davis et al. have subsequently theoretically demonstrated that, if polarization is taken into account, an asymmetric metasurface response can be generated without breaking the up-down mirror symmetry of the metasurface [171]. Using the example of a plasmonic Wheatstone bridge the authors provided experimental evidence to support this claim.

Another nanoplasmonic structure that drew attention as a platform for spatial-frequency filtering based on subradiant mode excitation are plasmonic radial rod-trimers [93]. As part of this thesis ordered arrays of radial rod-trimers are investigated as reflective object plane filters in Chapter 5. The excitation of electrical and magnetic subradiant modes will be investigated and inter-unit cell coupling discussed as a reason for the emergence of complex optical transfer functions [61]. Furthermore the capacity of the structure to perform edge-detection on amplitude images and limitations of the approach due to high sensitivity towards deviations in the trimer geometry will be investigated [63].

2.7 Summary and Conclusion

The first part of this chapter was dedicated to the introduction of fundamental mathematical and physical concepts underpinning analogue optical computation in the spatial domain including optical image processing. Relevant aspects of Fourier optics were discussed and their relationship to spatial differentiation, edge-enhancement in amplitude images and visualization of phase gradients were elucidated. The significance of these processes for biological imaging applications has been emphasized. Following the concepts of Fourier- and object plane spatial frequency filtering were introduced. Developing nanophotonic approaches that enable manipulation of the Fourier content of a wavefield in the object plane was stated as the central goal of this thesis. The approaches for all-optical image processing in this thesis employ optical metasurfaces and stacks of optically thin films. Their underlying mechanisms were introduced beginning with the mathematical description of the optical response of stratified media which provides an analytical model for the description of metal-insulator-metal absorber in chapter 4. Subsequently the interaction between electromagnetic waves at optical frequencies and metallic nanostructured was reviewed and the concept of optical metasurfaces was introduced. The significance of optical metasurfaces was underpinned by an exemplary review of their broad range of applications. In chapter 5 and 6 we will use the concept of optical metasurfaces as object plane spatial frequency filters. In the final part of this chapter a detailed review of existing nanophotonic approaches to spatial analogue optical computation were reviewed and the research chapters of this thesis motivated in their context.

Chapter 3

Modelling and Nanofabrication Methods

This chapter is concerned with the numerical modelling and experimental fabrication and characterisation methods on which this thesis relies. We will first introduce the Finite Element Method (FEM) as a useful tool for quantitative modeling of nanophotonics structures. In the second part of this chapter the nanofabrication techniques of Electron Beam Physical Vapour Deposition (EBPVD), Electron Beam Lithography (EBL) and Chemical Vapour Deposition (CVD) will be discussed. Finally, Scanning Electron Microscopy (SEM) will be introduced as an essential characterization method in nanophotonic research.

3.1 Numerical Methods

The fabrication and characterization of prototype photonic nanostructures is a time consuming and costly process. For this reason, computational methods, that permit time efficient simulation of the interaction of light with matter in complex geometries, are crucial [172, 173]. This section is dedicated to a brief general introduction to commonly used methods in numerical electrodynamics while the focus will be on the Finite Element Method (FEM). The following review is based on chapter 2 and 4 of [174].

The interaction of electromagnetic waves with matter is described by Maxwell's equations, which represent a set of partial differential equations that are subject to problem-specific boundary conditions. Apart from a very limited number of electromagnetic field problems, these equations cannot be solved analytically and one needs to resort to numerical methods to find an approximate solution.

The core principle of any numerical method aiming to solve partial differential equations is to transfer the operator equations into a discretized and approximate algebraic matrix equation, which can then be solved by standard methods. In developing such a procedure, one should carefully consider two major aspects. First of all one should assess how well the simplified model describes the actual physical state of the system. This consideration will provide crucial information about the value and accuracy of any solution to be obtained from this numerical model. Secondly, the economical usage of computing power has to be taken into account. In particular, numerical calculations for electromagnetic field problems can require enormous computing capacity. Thus a balance between accuracy and required computation time needs to be found. Two of the most commonly used numerical methods to simulate electromagnetic field problems are the Finite Difference Time Domain method (FDTD) [175] and the Finite Element Method [174]. While these methods offer a high degree of generality, other approaches such as Rigorous Coupled Wave Analysis (RCWA) [176, 177] are more problem specific but can offer higher computational efficiency. Comparison of different numerical techniques in terms of flexibility, efficiency and accuracy is a matter of ongoing research and generally highly problem specific [178–180].

Historically one of the earliest class of methods to emerge were the ‘finite difference methods’ [174]. While its principles date back to the 1910s, its development advanced rapidly in the 1930s and has been used to solve a broad spectrum of engineering problems ever since. The FDTD method belongs to the class of finite difference methods. Its principle of operation is to divide the solution domain into a regular grid and replacing the differential space- and time derivatives in Maxwell’s equations by discrete difference quotients. The solutions for the electric and magnetic field are then represented by the discrete values obtained at the grid nodes from solving these algebraic equations [175]. Due to its operation in the temporal domain, the method permits calculation of the optical response of a structure for a wide frequency spectrum in a single computational run which commonly enables time-efficient calculation of spectral data. Furthermore it permits direct simulation of nonlinear optical phenomena including four wave mixing [181–183]. However, a major limitation of the method is the requirement for a regular grid in its standard formulation which does not allow locally increased spatial resolution where required. In particular, complex geometries with feature sizes varying over a wide range, common in nanophotonics, need to be discretized with a fine grid over the entire solution domain. This significantly increases the computational overhead. Alternative formulations of the FDTD method to overcome this limitations by introducing non-uniform discretization approaches have been proposed, but usually require the introduction of complex, problem specific modifications into a numerical model as reviewed in chapter 11 of [175].

The finite element method later gained popularity in the 1950s for solving problems in structural mechanics and about a decade later was applied to solve electromagnetic field problems [174]. In contrast to the FDTD method, the FEM enables discretization of the solution domain into elements with varying size and shape in its standard formulation and thus overcomes its major drawback. The FEM method therby offers better modelling of curved surfaces and dispersive materials [178]. For this reason the finite element method is selected to solve the considered electromagnetic field problems in this thesis. We use the COMSOL 5.3a and 5.4 software package with the RF-module for CAD design and FEM analysis of nanophotonic metasurfaces.

3.1.1 The Finite Element Method (FEM)

In the following we will review the fundamentals of the finite element method. Since a rigorous derivation of the method's complex mathematical background has been extensively published elsewhere - see for example [184–186], we will focus on a brief overview of the fundamental steps of the method.

3.1.1.1 Fundamentals of the finite element method

One of the essential steps in the finite element method is the conversion of the differential equation under consideration into an algebraic matrix equation. Here we assume a partial differential equation of the form

$$\hat{O}u(x, y, z) = f \tag{3.1}$$

where $\hat{O}$ is a differential operator, u is the solution function we seek and f is an arbitrary known function. In a first step, the solution function u is approximated by a linear combination of N so called '*shape functions*' ψ_k such that

$$u \approx \sum_{k=1}^{N} u_k \psi_k \tag{3.2}$$

so that eq. (3.1) becomes

$$\hat{O}\left(\sum_{k=1}^{N} u_k \psi_k\right) = f \tag{3.3}$$

It will be discussed further below that the FEM method also requires discretization of the solution domain. Each shape function ψ_k is usually non-zero over only a small number of discretization elements. At this point there are two common approaches to convert the obtained partial differential equation (3.3) into a matrix equation. The first one is the *'variational approach'* and the second one, which we will follow here, is the *'method of weighted residuals'*, most commonly the *'Galerkin method'*. The concept is to multiply the residual R following from eq. (3.3) with

$$R = \hat{O}\left(\sum_{k=1}^{N} u_k \psi_k\right) - f \tag{3.4}$$

by appropriate shape functions ψ_j and integrating over the domain under consideration G so that we obtain

$$\int_G \left[\hat{O}\Big(\sum_{k=1}^{N} u_k \psi_k\Big) - f\right] \psi_j \, dG = 0 \tag{3.5}$$

$$\sum_{k=1}^{N} u_k \int_G (\hat{O}\psi_k)\psi_j \, dG = \int_G f \psi_j \, dG \tag{3.6}$$

for $j = \{1..N\}$. If one now defines $A = \int_G (\hat{O}\psi_k)\psi_j \, dG$ as well as $\mathbf{f} = \int_G f\psi_j \, dG$ and $\mathbf{u}$ as the column vector containing the coefficients u_i then eq.(3.6) can be expressed as an algebraic matrix equation

$$A\mathbf{u} = \mathbf{f}. \tag{3.7}$$

The solution $\mathbf{u}$ can then be obtained by solving this matrix equation under consideration of problem specific boundary conditions. While, in principle, inverting matrix A solves the problem, in practice there are usually more efficient approaches due to mathematical details evolving around the sparse nature of A with most elements being zero. This is discussed in more detail below.

The FEM method as implemented in the RF module of COMSOL Multiphysics 5.3a and 5.4 and used throughout this thesis solves the inhomogenous Helmholtz equation (3.8) for the electric field **E** for given boundary conditions

$$\nabla \times (\frac{1}{\mu_r}\nabla \times \mathbf{E}) - k_0^2\epsilon_r\mathbf{E} = 0 \tag{3.8}$$

where μ_r and ϵ_r denote the relative magnetic permeability and electric permittivity respectively and k_0 the free space wavenumber. In the problems discussed in this thesis the relative magnetic permittivity is set to $\mu_r = 1$ due to the vanishing magnetic susceptibility of the investigated materials at optical frequencies.

3.1.1.2 Discretization and termination of the solution domain

The FEM operates on the principle of discretizing the solution domain and computing values of the solution function u at the nodes of the discretization elements. This process is commonly referred to as *'meshing'* due to the decomposition of the entire domain into a complex mesh of varying geometric shapes, so called '*finite elements*'. An example of a three dimensional mesh for a nanophotonic structure is given in Fig. 3.1. Usually the algorithms involved in this process take into account requirements for locally increased

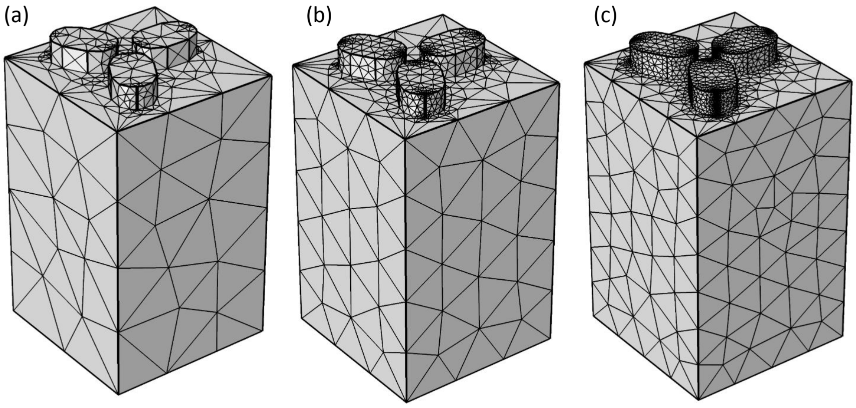

Figure 3.1: Example of three dimensional domain discretization ('meshing') as step of the finite element method (FEM). Shown is a nanophotonic silver rod-trimer geometry in a dielectric environment for increasing mesh density from coarser in (a) to finer in (c). The mesh density is locally increased at the silver rods compared to the dielectric environment in all cases.

resolution as it is the case for instance at metallic interfaces and corners in electrodynamic problems. It should be noted that the resolution of the meshing directly impacts the convergence and accuracy of the solution. Hence, the precise choice of the meshing is crucial. As a rule of thumb for the initial set up of a model, the meshing resolution for problems in electrodynamics can be taken as a fifth of the considered wavelength inside the investigated medium. However, certain geometries or parameter configurations can require even higher resolution to ensure appropriate sampling of the geometry. On the other hand, increased meshing resolution usually implies longer computation times. It is thus crucial to balance mesh resolution with consumption and availability of computational resources in the design process of an FEM model.

The geometry defined in any FEM model has to be spatially terminated at some point. Boundary conditions are essential in terminating the geometry without yielding unphysical results. In this thesis two different types of boundary conditions were used to model infinite arrays of plasmonic metasurfaces: *port boundary conditions* and *periodic boundary conditions*. For the lateral boundaries of any model, periodic boundary conditions, implementing Floquet boundary conditions, were chosen thus modeling the infinite repetition of the defined unit cell. For this particular case, identical meshing on opposing boundaries was implemented since it has shown to reduce numerical artifacts and improve solution convergence. The upper and lower boundaries of the model were terminated by port boundaries. Port boundaries prevent unphysical backreflections of plane waves travelling in specified directions that correspond to propagating diffracted orders of periodic structures. At the same time they facilitate the calculation of important secondary quantities such as transmittance and reflectance via S-parameters from electronic system theory.

3.1.1.3 Solving the global matrix equation

For the final solution step to solve the global matrix equation of the model, COMSOL provides a range of solver packages each of which provides advantages in certain situations [187]. We will briefly review the different solver options at this point to justify choices made in upcoming investigations. The different solvers can generally be classified as either *direct* (e.g. MUMPS, PARDISO, SPOOLES) or *iterative* methods. All direct methods are based on variations of the principle of LU-decomposition, which expresses a matrix as a product of a lower and an upper triangular matrix. Even though all direct methods will arrive at the same solution for well conditioned problems, they exhibit differences in their relative speed, use of memory, capacity for out-of-core storage of the problem on the hard disk as well as cluster computing features. In contrast to direct solvers, iterative solvers arrive at a solution in multiple steps rather than in one computational run. The methods available in COMSOL are mostly based on adaptions of the conjugate gradient method. The major advantage of iterative solver methods is the lower requirement for memory compared to direct solvers. However, depending on the problem, the convergence towards a defined error threshold can be monotonic or exhibit an oscillatory behavior implying extensive computation time. It can generally be said that direct solvers are to be preferred if memory permits, since they tend to be more robust compared to iterative solvers. In this thesis only direct solvers were employed. Once the approximate solution for the function u has been obtained, post processing allows extraction of secondary quantities that are derived from u. In the case of FEM simulations for electromagnetic problems the method would solve for the electric field $\mathbf{E}$ or the magnetic field H from which secondary quantities such as reflectance, transmittance etc. can be extracted.

The FEM simulations in COMSOL Multiphysics in this thesis were carried out on a high performance computer with 32 2.5 GHz Intel Xenon E5-2650 CPUs and 256 GB of RAM.

3.2 Nanofabrication and characterization methods

We have so far discussed the potential applications of optical metasurfaces in chapter 2 and the means to numerically model their optical properties above but disregarded potential approaches to enable their experimental implementation. This section is thus concerned with a review of suitable fabrication methods for nanostructures and discusses their applicability for high resolution fabrication, prototyping and rapid throughput, low-cost mass production.

3.2.1 Electron Beam Physical Vapour Deposition (EBPVD)

The fabrication of nanophotonic devices in this thesis relies on the deposition of metallic and dielectric thin films. Electron beam physical vapour deposition (e-beam evaporation) is a nanofabrication method that enables deposition of metallic and dielectric films with thicknesses commonly ranging from 1 nm to 1 µm and is commonly used in nanophotonics [188]. The method relies on the heating of a material through an electron beam resulting in the transition of the material into the gas phase and subsequent deposition of the vapour onto a target substrate. A typical e-beam tool setup is shown in Fig.3.2.

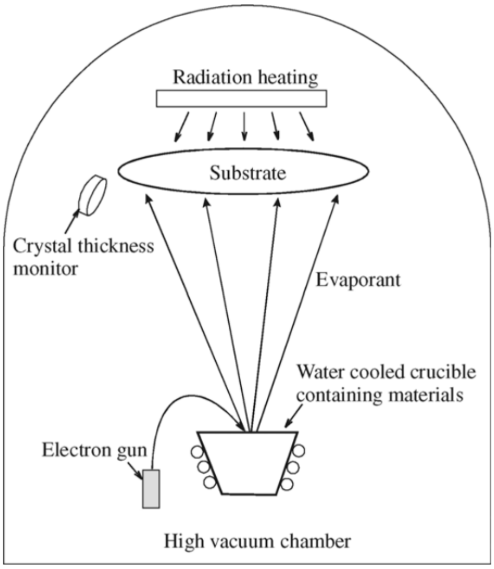

Figure 3.2: Schematic illustrating the operational principle of a high-vacuum EBPVD tool. Image reprinted with permission from [189][22].

The evaporation chamber is kept under high vacuum during the deposition process and in some devices the target substrate can be heated. The electron gun emits a beam of electrons that is directed to the material to be evaporated which forms the anode. Above the anode the material deposits on the target substrate thus growing the thin film. The deposition process is monitored and controlled via crystal type film thickness sensors and a mechanical shutter that screens the target from the crucible. For the device fabrication in this thesis an Intlvac NanoChrome II e-beam evaporator was used. Prior to deposition, the tool pumps down to a pressure of approximately 7×10^{-5} Torr. The evaporation takes place at a rate defined by the user and depends on the material in use. Based on empirically determined values dielectric materials including SiO_2 and TiO_2 are evaporated at slower rates below 0.5 Å/s to ensure high film quality while metals such as Al, Ag and Au can be evaporated at higher rates between approximately 0.6 Å/s and 1 Å/s.

---

[22] Reprinted from Materials Science and Engineering: R: Reports, vol. 48, no. 2-5, N. Xu and S. E. Huq, 'Novel cold cathode materials and applications', pp. 47 – 189, Copyright (2005), with permission from Elsevier.

3.2.2 Chemical Vapour Deposition (CVD)

For the deposition of thin films of dielectric materials, chemical vapour deposition (CVD) represents an alternative fabrication method to electron beam evaporation [190, 191]. The technique has distinct advantages over EBPVD in some cases as will be discussed below. For the work carried out in this thesis CVD is employed for the time efficient deposition of SiO_2 thin films.

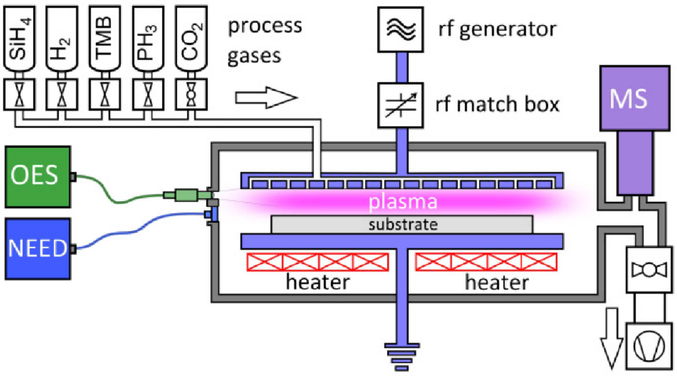

Figure 3.3: Typical plasma enhanced chemical vapour deposition (PECVD) setup for the fabrication of SiO_2 thin films. Image reprinted with permission from [192][23].

We will briefly outline the basic working principle of CVD based on an extensive review given in [193]. CVD works on the principle of chemicals in the gas phase reacting in a controlled environment thereby yielding a solid byproduct that forms a thin film on a substrate. While CVD systems are commonly designed for particular deposition processes, a CVD setup usually involves a supply system for chemical vapour precursors, a CVD reaction chamber and an effluent gas handling system. The principle setup is shown in Fig.3.3. The supply system provides chemical precursors for the intended reaction and delivers them to the CVD chamber. Depending on whether the required precursors are provided in gas, liquid or solid form different components are required in the supply system. It should be noted that the precursors involved can be toxic which implies a potential health hazard which is a clear disadvantage of CVD over EBPVD. The CVD reaction chamber is the place where the chemical precursors react to yield the solid byproduct that forms the thin film of dielectric material on top of the substrate. In order to facilitate the

---

[23] Reprinted from [192] with permission from The European Physical Journal under the Creative Commons Attribution License.

reaction, the chamber is kept under vacuum and is heated. An advanced version of CVD, so called plasma enhanced chemical vapour deposition (PECVD), a plasma is formed in the chamber in order to lower the required reaction temperature thereby avoiding phase transitions of the thin films [194]. The presence of a plasma furthermore usually enhances the achievable deposition rate as well as film density. In the particular case of SiO_2 typical deposition rates of approximately 100 Å/s can be achieved [195] which significantly exceeds those typical for EBPVD. The basic reaction for the formation of SiO_2 from gaseous precursors in CVD is the reaction of silene (SiH_4) and oxygen (O_2) forming silica (SiO_2) and hydrogen (H_2). Subsequently undesired byproducts and residues from the reaction inside the chamber are transported out of the chamber via gasflow into the effluent gas handling section. Throughout this thesis CVD is performed using an Oxford Instruments PLASMALAB 100 PECVD tool operating at temperatures below $350°C$. The tool has a load lock which enables fast pumping and venting thereby considerably reducing the fabrication times compared to EBPVD.

3.2.3 Electron Beam Lithography (EBL)

A versatile non-optical method for the fabrication of nanophotonic structures is Electron Beam Lithography (EBL) [196]. The fabrication of optical metasurfaces in particular takes extensive advantage of patterning through this nanolithography technique [100, 110, 197]. We will shortly review the technology based on a more elaborate introduction given in [198]. Optical lithography reaches its limits as a nanofabrication technique in the regime of feature sizes approaching approximately $30 - 50$ nm due to issues evolving around focal depth near the diffraction limit and the unavailability of optical components and photoresists that arises with decreasing wavelength. EBL utilizes focused beams of electrons instead to create two dimensional, or in some cases three dimensional, patterns in electron sensitive films, so called EBL resists, coated on substrates. As a result of the smaller wavelength of electrons compared to visible light, the technique operates beyond the optical diffraction limit. The method allows the creation of nanostructures with a resolution finer than 5 nm in commercially available resists for which it is a common prototyping technique in current research and development. Electron beam lithography refers to two different fabrication approaches, the variable-shape beam type and the point-beam type. With only the point-beam type offering the required precision for the optical nanostructures fabricated in this thesis, we focus on this approach and refer the reader to secondary literature on variable-shape EBL [199]. The principle of point-shape EBL is to scan the surface point-by-point with a focussed electron beam, thus inducing tailored chemical changes in the electron resist according to a previously determined pattern. It should be noted that due to the serial nature of this approach, long fabrication times can occur so it is not suitable for rapid throughput, mass production applications. The achievable resolution of an EBL is mainly hampered by electron scattering processes in the resist and the substrate. A complex interplay of the electron energy, the resist and the substrate governs this scattering process, and thus the lower resolution limit. The precise choice of the writing parameters for a particular setting is therefore crucial. Quantitative data supporting this choice is commonly deduced employing Monte Carlo simulations of the scattering process and from experimental data for similar settings.

3.2.3.1 Setup of an electron beam lithography tool

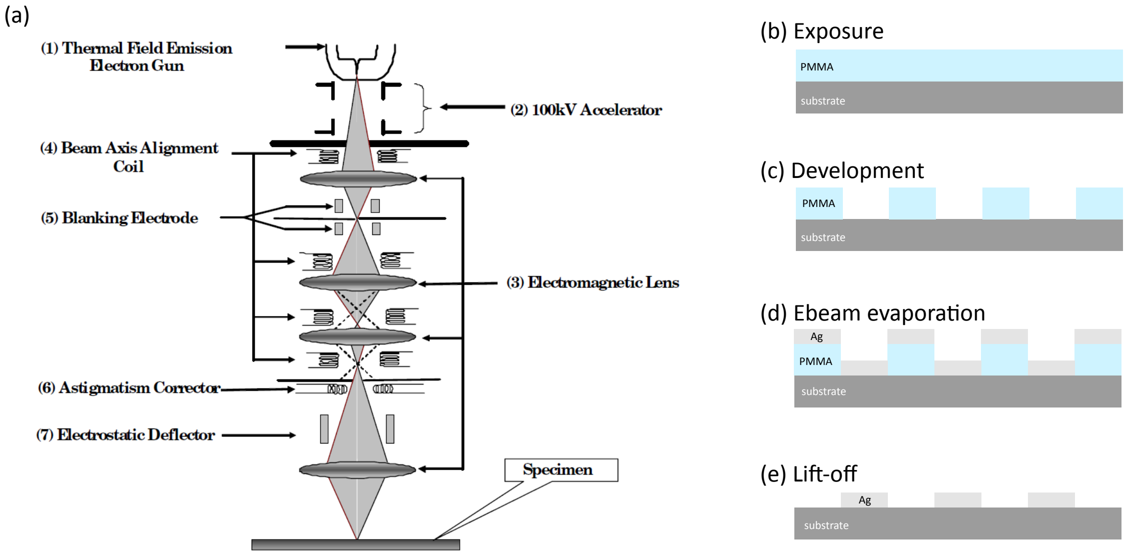

Figure 3.4: Electron Beam Lithography (EBL) for fabrication of optical and electronical nanostructures. (a) Schematic of an EBL tool reprinted with permission from [198][24], (b)-(e) Typical fabrication steps of an EBL process in PMMA resist for the fabrication of a Ag nanostructure.

An EBL device consists of an electron emission unit, a subsequent accelerator, and a focussing unit as illustrated in more detail in figure 3.4a. The thermal field emission gun provides free electrons based on the quantum mechanical tunnelling effect that occurs

---

[24] Copyright 2010 Wu CS, Makiuchi Y, Chen CD. Published in [198] under CC BY 3.0 license. Available from: http://dx.doi.org/10.5772/8179.

when a strong electric field is applied to the surface of a metal. These electrons are subsequently accelerated by voltages of the order of 100 kV towards the specimen. A set of electromagnetic lenses finally enables focusing and directing of the beam towards the desired locations on the surface of the specimen.

The EBL tool used for fabrication of samples in this thesis is a Vistec EBPG 5000+ device with an accelating voltage of 100 kV. The setup enables a minimum beam spot size of 2 nm at an electron beam current between 50 pA and 100 nA using beam apertures with diameters ranging from 200 µm to 400 µm. Automatic astigmatism- and sample tilt correction are implemented in the EBL tool. The EBL system is used together with a commercial software package called 'BEAMER' [200] that converts CAD designs into control sequences understandable by the EBL. The data preparation process for pattern design is as follows. Patterns are initially designed as GDSII files in a software called Klayout and subsequently have to be converted into production files interpretable by the EBL tool. This conversion is carried out using the BEAMER software and a software called CJOB provided by the tool manufacturer. During this conversion process details about the exposure conditions including beam step size, beam spot size and dosage are specified and communicated to the tool. The BEAMER software also includes algorithms for proximity error correction (PEC) compensating for inevitable charge accumulations. While fabrication steps vary, depending on the device to be implemented, we here review a common device fabrication process using Electron Beam Lithography. Whenever devices are fabricated throughout this thesis, more detailled specifications are provided in the relevant section.

3.2.3.2 Typical EBL fabrication process

A typical EBL fabrication process, following the above data preparation, is depicted in Fig. 3.4(b)-(e). A substrate, usually silica or silicon, is cleaned with isopropanol and acetone. A layer of resist, in this thesis PMMA or HSQ, is spincoated onto the substrate with a thickness controlled by the rotational speed of the spincoater.

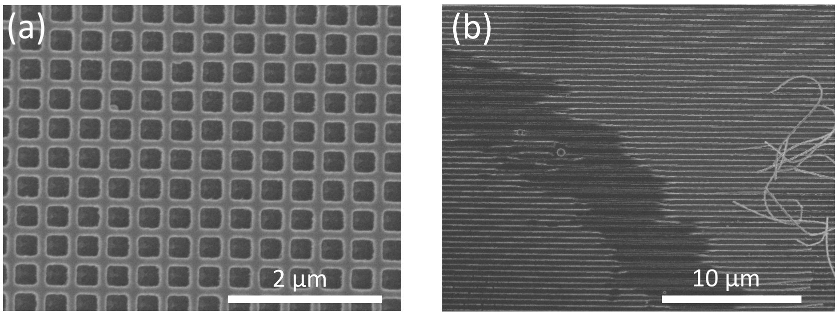

Figure 3.5: SEM images of typical nanopatterns fabricated using an EBL process in PMMA as outlined above. (a) successful fabrication of a two-dimensional subwavelength Au grating and (b) non successful fabrication of a one-dimensional Au grating due to local overexposure without PEC.

Typically, the resist thickness is chosen to be four times as thick as the structure to be fabricated. The resulting thin layer of resist is subsequently hard baked by placing the sample on a hot plate. In the case of non-conductive substrates such as Silica a thin layer of approximately 30 nm of chromium is sputtered onto the resist to avoid charge accumulation before the EBL exposure is carried out. Following the exposure, the chromium layer is removed using chromium etchant and the pattern is developed in a mixture of methylisobutylketone (MIBK) and isopropanol (IPA) and rinsed in IPA. Subsequently the sample is metalized using electron beam evaporation. Finally, a lift-off step removes the remaining resist by placing the sample in acetone. For some metals, particularly aluminium, heating the acetone and placing the sample in an ultrasonic bath can be required in order to perform this step successfully. Other metals, such as silver or gold, commonly have lower adhesion and one runs the risk of destroying the structure by applying ultrasonication. SEM images of two typical Au nanostructures fabricated using an EBL process are shown in Fig. 3.5. While Fig. 3.5(a) indicates successful fabrication, Fig. 3.5(b) shows a typical result of a failed fabrication due to local overexposure arising from not having performed adequate proximity error correction (PEC).

3.2.4 Scanning Electron Microscopy (SEM)

Visualizing photonic nanostructures requires an image resolution well beyond the diffraction limit of light. Scanning electron microscopy (SEM) is a technique that utilizes electron-matter, instead of light-matter, interactions for the visualization of samples which enables operation beyond the optical diffraction limit due to the shorter wavelength of electrons compared to photons [201, 202]. SEM imaging has been demonstrated to enable resolutions of up to 0.4 nm [203]. In the following we briefly review the working principle of an SEM [204]. An SEM operates on the principle of accelerating electrons emitted by a thermionic, Schottky or field-emission electron gun by an applied bias and focusing them onto the surface of a sample with a magnetic lens systems. The SEM operates in a vacuum chamber in order to avoid collisions between electrons and air molecules. There are several modes of operation in which an SEM can subsequently evaluate the interaction of the incident electron beam with the sample in order to obtain an image of its topology. While the most common method is the detection of secondary electrons emitted by the sample, others exploit the detection of backscattered electrons, X-rays or cathodoluminescence among others.

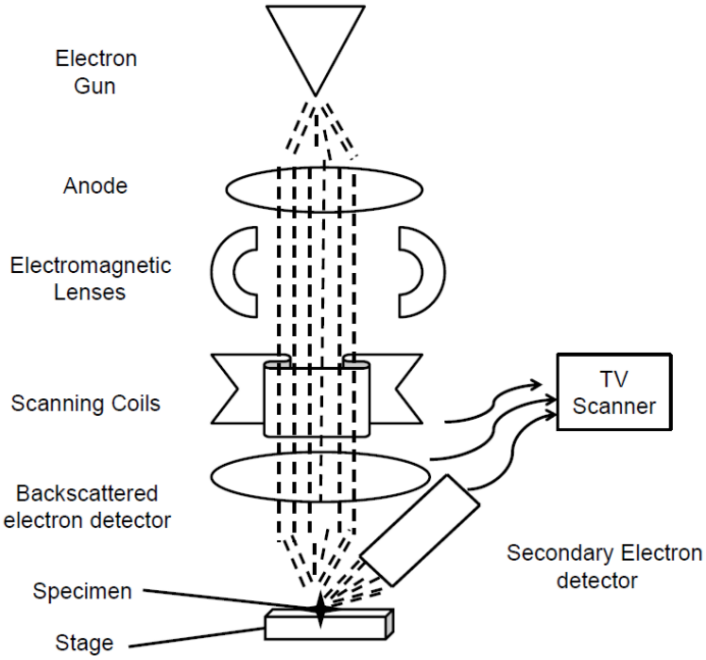

Figure 3.6: Schematic of the setup of a scanning electron microscope (SEM) reprinted with permission from [205][25]. The device chamber is kept under a deep vacuum.

For the characterization purposes in this thesis, SEM imaging is carried out in secondary electron detection mode. The electron beam is scanned in a raster pattern over the surface of the sample so that an image is obtained. In this thesis a FEI NovaNanoSEM-430 microscope was used operating under a vacuum below 10^{-4} Torr and an accelerating voltage

---

[25] Reprinted with permission from [205]. Available from https://ecommons.udayton.edu/bio_fac_pub/158/.

between $3-5\,\mathrm{kV}$ at beam currents of up to $360\,\mathrm{pA}$. SEM analysis of EBL fabricated samples in this thesis provided a means of validation of a successful fabrication process as well as providing geometric information of fabricated structures and potential deviations from nominal values. Examples of typical SEM images of a successful and a failed fabrication of Au nano gratings through electron beam lithography are shown in Fig.3.5 above.

3.3 Summary and Conclusions

This chapter was dedicated to the introduction of relevant methods for numerical modeling and nanofabrication. Initially the finite element method (FEM) was discussed as a powerful numerical approach to model plasmonic metasurfaces by solving the inhomogeneous Helmholtz equation for a given set of boundary conditions. In this thesis the method, as implemented in COMSOL Multiphysics with the Radiofrequency (RF) module, is used. Secondly the nanofabrication and characterization methods employed in this thesis were introduced. These include techniques for thin-film deposition (EBPVD, PECVD), Nanolithography (EBL) and electron microscopy (SEM). The introduced set of methods enable modelling and fabrication of plasmonic metasurfaces and thin-film absorbers as investigated in this thesis and additional details about modeling and fabrication procedures will be provided where necessary.

Chapter 4

Image processing via thin-film near-perfect absorbers

In section 2.6.1 we reviewed the recent scientific interest in untextured optical thin-film devices as analogue optical computation platforms. In this chapter the potential of metal-insulator-metal (MIM) near-perfect absorber (NPA) structures as ultra-compact solutions for all-optical information processing is investigated for the first time. The initial part of this chapter reviews recent developments in the field of optical MIM absorbers and motivates their potential for all-optical spatial-frequency filtering in the object plane. Subsequently, the information processing capacity and limitations of MIM type absorbers are investigated in a numerical study employing the numerical framework previously introduced in section 2.2. Finally, in the last part of this chapter we experimentally demonstrate all-optical information processing in the visible region of the spectrum through the use of ultra-compact MIM absorbers. The material discussed in this chapter is partly covered in the following publications.

L. Wesemann, E. Panchenko, K. Singh, E. Della Gaspera, D. E. Gómez, T. J. Davis, and A. Roberts. "Selective near-perfect absorbing mirror as a spatial frequency filter for optical image processing." *APL Photonics*, 4(10):100801, 2019.

C. Ng, L. Wesemann, E. Panchenko, J. Song, T. J. Davis, A. Roberts, and D. E. Gómez. "Plasmonic Near-Complete Optical Absorption and Its Applications." *Advanced Optical Materials*, 14(7):1801660, 2019.

4.1 Introduction to thin film NPA structures

Near-perfect absorption through Fabry-Pérot type cavities has recently received increased attention. The underlying concept is inspired by the Salisbury screen for radio frequency waves patented in the 1950s [206]. An optical Salisbury screen as shown in Fig.4.1 consists of a transparent dielectric layer of approximately a quarter-wavelength thickness between a semi-transparent thin metallic film and a fully reflective metal substrate. This three-layer thin-film stack can act as a wavelength selective and angle-dependent near-perfect absorber [207–210]. Near-perfect absorption in this metal-insulator-metal (MIM) structure has been physically explained using interference theory [211]. The near-perfect absorption originates from destructive interference between reflection from the air-metal interface and multiple reflections within the quarter-wave cavity. We denote the phase accumulation of the light propagating through the dielectric layer with β, the phase-shift upon reflection from the substrate with ϕ_s and the phase shift after transmission through the absorbing cover layer with ϕ_c. Destructive interference then occurs if the total phase accumulation compared to the light reflected at the air-metal interface is a multiple of 2π,

$$\phi_s + 2\beta + \phi_c = n2\pi \tag{4.1}$$

with n beiing an integer number. The absorption wavelength of the MIM absorber is mainly determined by its spacer layer and can therefore be engineered through choice of the layer thickness and dielectric material. As discussed in section 2.3 however, metals cannot be considered as perfect conductors at optical wavelengths which results in non-trivial phase changes different from 0 or π upon reflection from the substrate and transmission through the cover layer [208, 212, 213]. This effect alters the condition for destructive interference and thus needs to be taken into account in the design of MIM absorbers.

Several experimental studies have demonstrated near-perfect absorption using MIM absorbers. Li et al. have for example demonstrated that a Ag/SiO$_2$/Ag stack enables near perfect absorptance of 97% of the incident light at wavelengths in the visible spectrum [213]. Another study concluded that other metals such as Au, Ag and Cu are also suitable for MIM absorbers with resonances at optical wavelengths [208]. The concept, however, does not rely on metallic reflectors and dielectric Bragg-reflectors have been demonstrated to offer similar absorption performance [214]. While the focus of this thesis is based on operation in the visible spectrum, it is worth noting that the concept of MIM near-perfect absorbers can be extended into the near- and mid infrared. Through doping of silicon, characteristics of noble metals in the visible spectrum, particularly high cavity confinement and low loss, become available at infrared wavelengths [215]. MIM absorber as described above are designed to operate at a specific angle of incidence and polarization state. Near-perfect absorption through destructive interference in MIM absorbers commonly relies on a particular angle of incidence and polarization. Changing the angle of incidence or polarization thus alters the interference conditions and thereby the absorptance efficiency. In conventional MIM absorbers the absorption wavelength blue-shifts when the angle of incidence is increased [213]. It is particularly this characteristic that enables spatial frequency filtering using MIM absorbers which make them a suitable candidate for research carried out in this thesis. We will elucidate the absorption and spatial frequency filtering characteristics of Salisbury screen type devices extensively with the support of numerical calculations in the following section.

An alternative approach to near-perfect absorption using thin-film stacks made of only two layers should be noted here: a metal film under a thin dielectric film with large optical losses (i.e. with a complex part of its refractive index comparable to that of its real part). In this case, reflection of light is suppressed by the non-trivial phase shifts taking place during propagation and at the mirror and dielectric-air interface, which can lead to values not limited to 0 or π, resulting in strong suppression of reflectance (high absorption), which can take place for dielectric film thickness far below the quarter-wave condition as it is the case for Salisbury screen type absorbers (*cf.* equation (4.1)). While in conventional MIM structures losses are considered an undesired perturbation, this design particularly exploits high losses. The principle was experimentally demonstrated by Kats *et al.* [216] using thin 7 to 25 nm thick Ge films on top of Au mirrors. The demonstrated absorbers exhibited experimental absorption efficiencies of up to approximately $80\% - 97\%$ at wavelengths in the visible to near infrared. However, due to the relatively thin dielectric layer with regard to the wavelength of light, phase accumulation during propagation is relatively low compared to interface phase-shifts resulting in significantly lower angular sensitivity than exhibited by the previously discussed Salisbury-type absorbers. For this reason, although beneficial for some applications, ultra-thin film systems of this kind are not suitable as spatial frequency filters.

In summary, Salisbury screen (MIM) type absorbers offer strong absorption paired with angular sensitivity in reflection while requiring comparably low complexity in fabrication. For this reason the following chapter investigates the potential of Salisbury type absorbers for all-optical information processing including image processing and phase imaging.

4.1.1 Implementation of a numerical thin film model

A numerical model based on the thin film theoretical framework introduced in section 2.2 has been developed. The simulation implements equation (2.64) based on input parameters d_r for the layer thicknesses, dielectric functions $\epsilon_r(\lambda)$ for the layer materials, the wavelength λ and the angle of incidence θ. From this the effect of variations in dielectric functions of deposited materials, fabrication inaccuracies in layer thicknesses and the impact of finite spectral linewidth can be investigated. Furthermore the model enables the determination of the optical transfer function (OTF) for a given thin film stack via calculation of its complex reflection coefficient $r(\lambda, \theta)$ as a function of wavelength λ and angle of incidence θ for different polarization states. From this its spatial frequency filtering capability can be assessed. While a qualitative explanation for the occurrence of absorption in MIM absorbers has been given in the introduction of this chapter, we will now investigate its quantitative absorption characteristics employing the numerical model outlined above.

4.2 Numerical Results

In the following we investigate a thin film absorber in the classical Salisbury three-layer configuration. Gold (Au) is chosen as the thin partly reflecting layer and the substrate layer while SiO_2 (silicon dioxide) serves as the dielectric spacer layer as illustrated in Fig.4.1(a). We will refer to this device as ‘SBS1’ for Salisbury screen 1. From Fig.4.1(b) the absorbing effect of a typical three layer stack is apparent. At $\lambda_{\mathrm{a}} = 631\,\mathrm{nm}$ at normal incidence the reflectance of the film drops to approximately 0.2% with an absorption bandwidth (FWHM) of $\Delta_{\mathrm{abs}} = 35\,\mathrm{nm}$, rendering the device a narrowband near-perfect absorber at this wavelength and angle of incidence. As expected a phase-shift of approximately π in the amplitude of the reflected field is apparent from Fig.4.1(c) as the

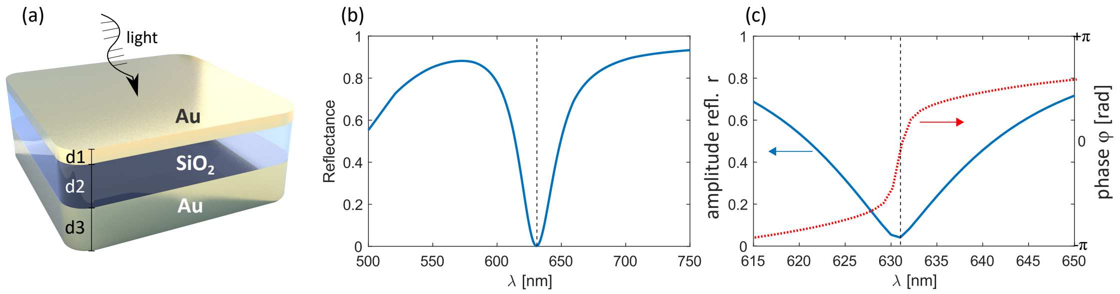

Figure 4.1: Numerical simulation of reflection from a three layer thin film stack at normal incidence. A layer of SiO_2 on top of a Au substrate is covered by a thin layer of Au as indicated in (a). The reflectance spectrum is shown in (b) and the magnitude (blue) and the complex argument (phase shift $\Delta\varphi$, red) of the amplitude reflection coefficient are shown in (c). Layer thicknesses are $d_1 = 30\,\text{nm}$ and $d_2 = 155\,\text{nm}$ with the underlaying Au-layer as the substrate ($d_3 = \infty$). Sources for dielectric functions of SiO_2 and Au are taken from [217], [76]. (a) Reprinted with permission from [60], licensed under a Creative Commons Attribution (CC BY) license.

wavelength is tuned through the resonance. As demonstrated before in [210, 213], the spectral position of the absorption maximum of MIM absorber structures is primarily defined by the thickness of the dielectric spacer layer, in this case the SiO_2 layer. In Fig. 4.2 the tunability of the spectral position of the absorption maximum is numerically demonstrated. Within the limitations of the chosen fabrication method and the reproducibility of the optical properties of the materials, this enables precise design of highly specialized spatial filtering devices at optical wavelengths.

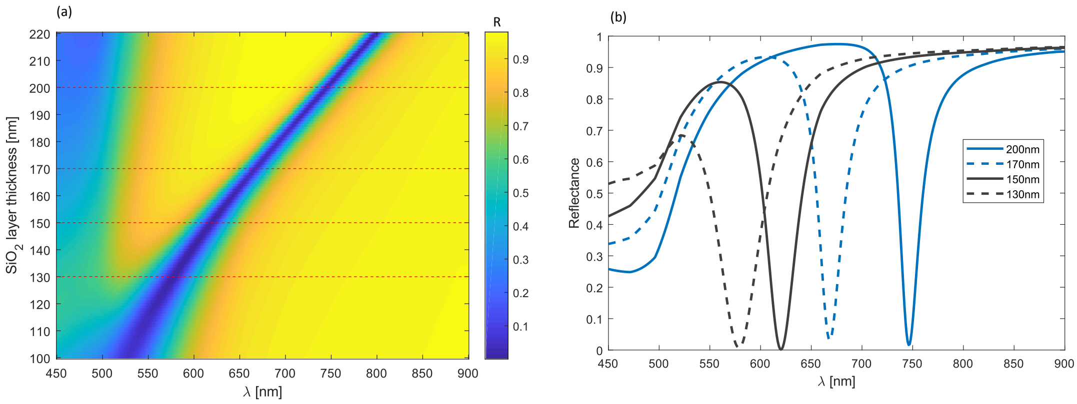

Figure 4.2: Numerical simulation of the reflection spectrum of the three layer thin film SBS1 for normally incident light with adjusted thickness of the SiO_2 spacer layer (a). Exemplary line plots for devices with SiO_2 layer thicknesses ranging from 130 nm to 200 nm.

From Figure 4.2(b) it is apparent that the different simulated absorber structures reach different maximum absorption efficiencies. For this reason, in order to maximize absorption at a particular wavelength, fine tuning of the thickness of the semitransparent metallic layer (Au) is crucial. Typical results of a calculation of the reflectance from the SBS1 device with fixed SiO_2 layer thickness and varying thickness of the top Au layer is shown in Fig. 4.3. The result indicates that only a layer thickness of around 31 nm (red circle) yields strong absorption in this configuration. We will use a thickness of 31 nm for the thin Au layer for further considerations. For smaller and larger thicknesses different reflectance and induced phase shifts at the upper layer diminish the capacity of the device to suppress reflection through destructive interference. A ±10% deviation in evaporation thickness is a typical value for an electron beam evaporation process. For the investigated device this corresponds to a range of $28-34$ nm for the superstrate thickness for which the reflectance of the device is still below 3% based on the calculations presented in Fig.4.3.

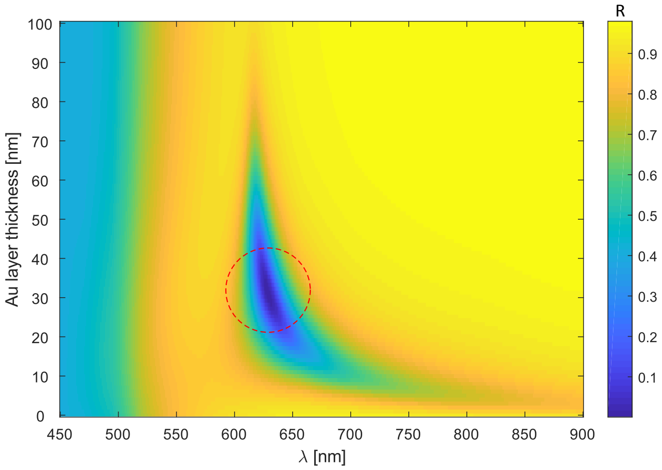

Figure 4.3: Numerical simulation of reflectance from device SBS1 for varying thickness of the Au superstrate. The red circle indicates the suitable working point for this configuration.

Experimentally, dielectric functions of metals and dielectrics can differ from values obtained from the literature due to a range of reasons. Firstly, differences can occur due to the fabrication method that can have an impact on the porosity of evaporated films [218]. Secondly deviations appear due to inherent differences between dielectric functions for bulk material and in optically thin films. The potential impact of typical small deviations in refractive index in the SiO_2 spacer layer and the gold superstrate have been investigated numerically with the results shown in in Fig. 4.4. We choose a range of ±5%

as a typical variation between bulk gold and thin-film gold as well as between different film thicknesses of gold [76, 219]. It is apparent that the absorption maxima shift by up to approximately ±30 nm for in each case. For this reason deviations from the design absorption wavelength are to be expected in experimental demonstrations.

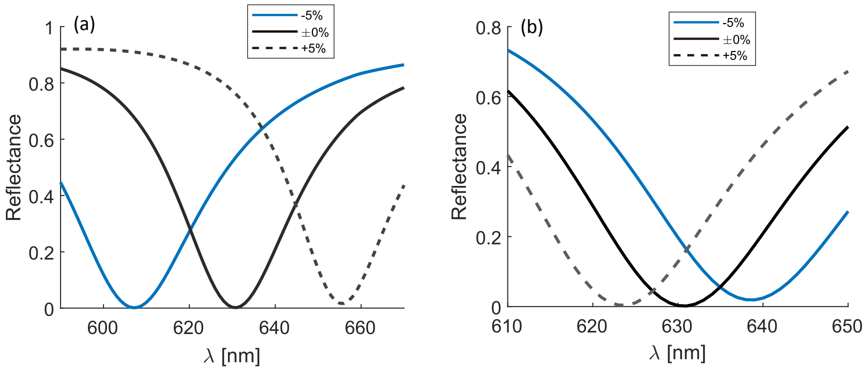

Figure 4.4: Numerical demonstration of impact of small deviations (±5%) in refractive index of (a) the SiO_2 layer (b) the Au superstrate for the SBS1 configuration described above.

4.2.1 Angular filtering with MIM absorbers

In order to employ this MIM absorber for image processing applications, it is relevant to investigate its spatial frequency filtering capability, i.e. its reflectance as a function of the incidence angle $R(\theta)$ for different polarizations. For this reason we will now move our focus towards the angular sensitivity of MIM absorber structures. Fig.4.5 (a),(b) show the reflectance of the device SBS1 as a function of angle of incidence for p- and s-polarized light respectively. In line with the qualitative explanation above the plot confirms that the absorption wavelength of the thin film stack shifts towards the blue as the angle of incidence θ increases. For this reason, the reflectivity at $\lambda_a = 631\,\text{nm}$ increases towards $R = 1$ for θ approaching 90°. Hence, the device under consideration only represents a near-perfect absorber at λ_a under illumination at normal incidence, while a large fraction of the incident light is reflected at higher angles. It is particularly this characteristic that is the key to the spatial-frequency filtering capability of MIM absorbers. The respective lineplots in Figures 4.5 (b),(d) show the reflectance as a function of normalized spatial-frequency for both polarization states at the absorption wavelength. Owing to the fact that the device has no lateral surface structure, reflection from the absorber

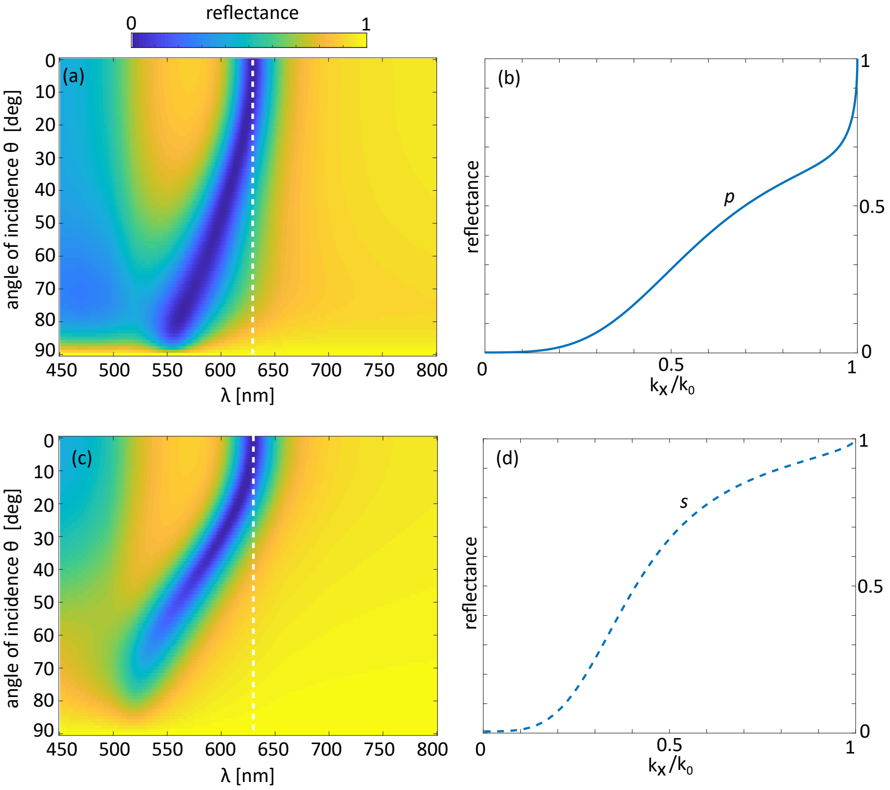

Figure 4.5: (a),(c) Numerical simulation of reflectance from device SBS1 as a function of angle of incidence. (b),(d) Reflectance $R = |r|^2$ as a function of spatial frequency at the wavelength $\lambda_a = 631\,\text{nm}$ indicated by dashed lines with $k_x/k_0 = \sin\theta$. Reprinted with permission from [60], licensed under a Creative Commons Attribution (CC BY) license.

is independent of the polar angle. While minor differences in the sensitivity of the reflectance toward angle of incidence between p- and s- polarization are evident, both follow the same pattern and enable high-pass spatial frequency filtering. For some applications the remaining sensitivity of the reflectance to polarization might represent a challenge. However, it also offers a prospect for switching between different optical transfer functions of the device through an adjustable polarizer in the beam path. As introduced in section 2.1.7, the filter function of the device exhibits a numerical aperture of NA= 1 for both $p-$ and $s-$polarization with a filtering constrast of $C_s = 0.997$ for both polarization states. Low pass spatial frequency filtering is possible at wavelengths shorter than the absorption wavelength where maximum absorption is achieved at off-normal incidence.

In the fundamentals chapter of this thesis it was discussed that the shape of the optical transfer function, in this case the reflection coefficient r, determines the mathematical operation performed by the system. While for edge-detection applications suppression of low spatial frequencies is sufficient, other applications including phase-visualization, are highly dependent on the particular shape of the transfer function. For this reason Fig.4.6 shows the amplitude- abs(r) and phase contribution arg(r) of absorber SBS1 at its absorption wavelength λ_a. From the device symmetry it follows that its optical transfer function must be symmetric for which it is relevant to compare it with the quadratic transfer function H_2 of a second order differentiator as given in eq.(2.44). The corresponding fitting parameters are summarized in table A.2 in the appendix. The amplitude coefficient of absorber SBS1 exhbits a near-quadratic dependence on spatial frequency for normalized spatial frequencies up to about 0.4 while the phase transfer function shows considerable deviation from the flat phase contribution of a second order differentiator. This implies consequences for phase-visualization applications as will be discussed below.

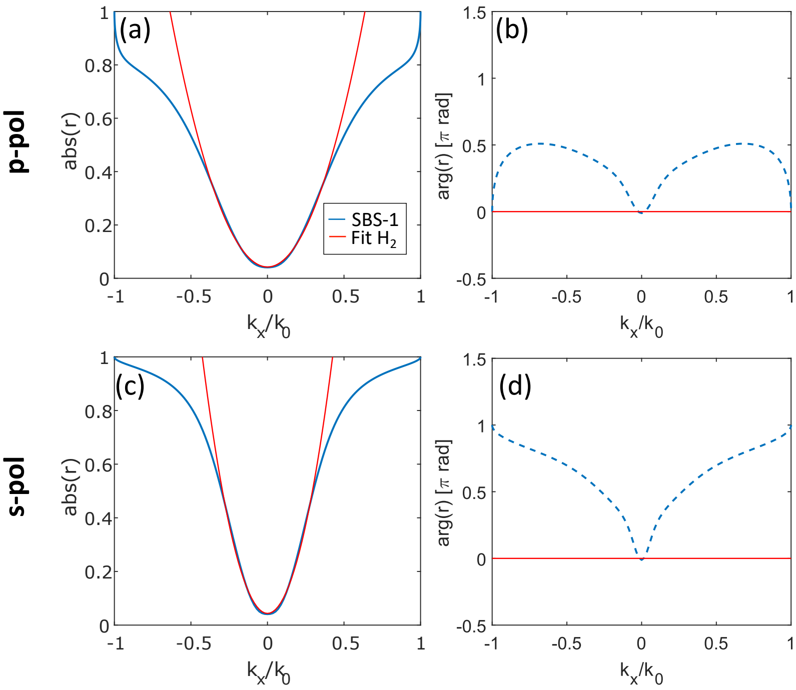

Figure 4.6: Optical transfer function of MIM absorber SBS1 at $\lambda = 631\,\mathrm{nm}$ shown as the amplitude- abs(r) and phase contribution arg(r) of the reflection coefficient r for $p-$ (top row) and $s-$polarization (bottom row) in blue. Fitted optical transfer function H_2 of a second-order differentitor as introduced in eq.(2.44) shown for comparison in red. Fitting parameters provided in table A.2 in the appendix.

4.2.2 Edge enhancement with MIM absorber

Based on the above, spatial frequency filtering of an amplitude image through reflection from the thin film absorber has been investigated numerically . The given wavefield $E(k_x, k_y)$ associated with an image is decomposed into plane wave p- and s-components with $\tilde{E}_p(k_x, k_y)$ and $\tilde{E}_s(k_x, k_y)$ describing their Fourier transforms respectively. Amplitude reflectance for both polarization states is given by $r_p(k_x, k_y)$ and $r_s(k_x, k_y)$, which are calculated from (2.63) as described in the thin-film model in section 2.2 and serve as optical transfer functions here. The p- and s-components of the Fourier spectrum of the reflected wavefield are then given by

$$\tilde{E}_{\mathrm{ref},p}(k_x, k_y) = r_p \tilde{E}_p(k_x, k_y) \tag{4.2}$$

$$\tilde{E}_{\mathrm{ref},s}(k_x, k_y) = r_s \tilde{E}_s(k_x, k_y) \tag{4.3}$$

In this model we neglect cross polarization induced by the image. The reflected fields $E_{\mathrm{ref},p}$ and $E_{\mathrm{ref},s}$ are obtained from inverse Fourier transforming. From the resulting fields the intensity distribution of the reflected field is calculated. The angular sensitivity of the reflectance from the absorber enhances regions in the reflected image dominated by high spatial frequencies, e.g. sharp edges, while regions dominated by low spatial frequencies, i.e. homogeneous areas, will appear darker (*cf.* Chapter 2). Fig.4.7 illustrates the enhancement of edges in an amplitude image reflected from device SBS1. It is apparent that the edges of the figure '2' for reflection at the absorption wavelength (Fig.4.7 (i-k) appear bright compared to homogenous areas, thus demonstrating the edge enhancement capability of the device for p-, s- and unpolarized light. The output intensity for unpolarized light I_{unp} has been calculated as an averaged result of the p- and s-polarized output intensities according to eq.(4.4), neglecting polarization effects induced by the object.

$$I_{\mathrm{unp}} = (E^2_{\mathrm{out},p} + E^2_{\mathrm{out},s})/2 \tag{4.4}$$

At longer (l-n) and shorter (c-e) wavelengths, where the device does not suppress reflection of low spatial frequencies (*cf.* Fig.4.5), the output images do not show enhanced edges in line with expectations. It should be noted that 'ringing-effects' are apparent in the vicinity of the edges in (i-k). These are the result of the nonlinear optical transfer

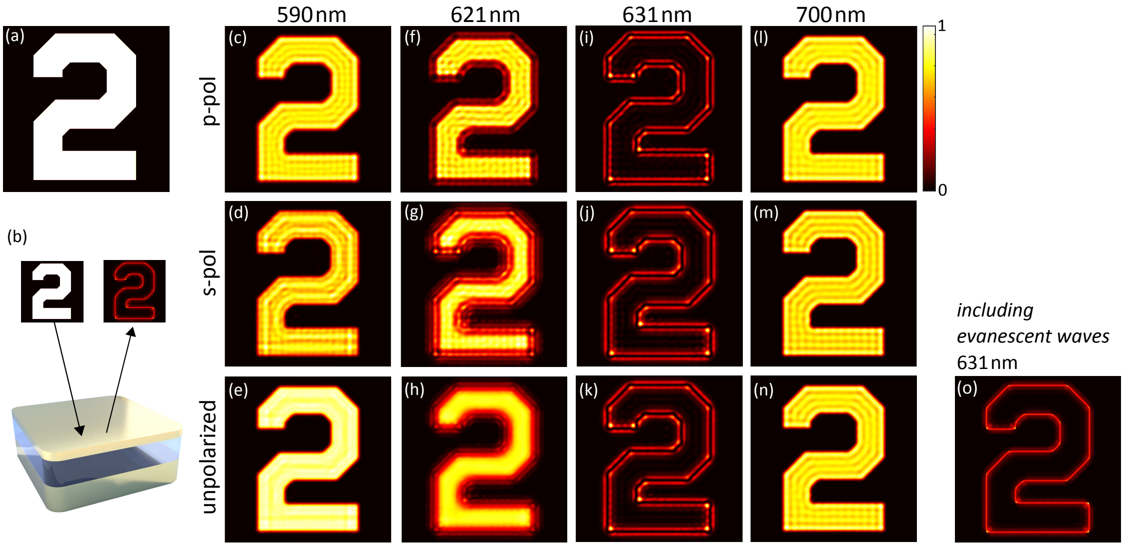

Figure 4.7: Numerical demonstration of edge enhancement in an amplitude image reflected from the thinfilm absorber structure. (a) Amplitude of the original image (b) conceptual illustration of the amplitude image projected onto the surface of the absorber (input) and the image reflected from the absorber (output), normalized intensity of reflected images for p-polarisation (top-row), s-polarisation (middle row) and unpolarized light (bottom row) at wavelengths of 590 nm, 621 nm, 631 nm and 700 nm. The image size is chosen as $15 \times 15\,\mu\text{m}^2$. Spatial frequencies associated with evanescent waves are excluded from the calculation except for (o) shown for comparison. All images are normalized to their brightest pixel.

function of the system as apparent from Fig.4.5 and the filtering of spatial frequencies associated with evanescent waves in order to account for the finite numerical aperture of real imaging systems as discussed previously in section 2.1.4. The effect has been observed in [66] as well. These effects become less apparent for increased image sizes as will be discussed below. At shorter wavelengths in the vicinity of the the absorption wavelength as shown in Fig.4.7(f-h) the absorber enables filtering of higher spatial frequencies thereby acting as a bandpass filter. Here this results in blurring of the images as expected for high-pass spatial frequency filtering.

The edge enhancement capability of the device depends on the spatial frequency content of the image projected onto the thin film stack (*cf.* sections 2.1.4, 2.1.7). For this reason the absolute scaling of the image determines whether its spatial frequency spectrum overlaps with the range of spatial frequencies in which the absorber is able to discriminate between ‘high’ and ‘low’ spatial frequencies to a degree that is reasonably high for detection in experiments. In particular noise and non-complete absorption at normal incidence reduce edge contrast. While for the purpose of demonstration a suitable image size of $15 \times 15\,\mu\text{m}^2$ was chosen for the calculations in Fig.4.7, the device performance changes for different sizes. We demonstrate this by calculating images reflected from the device for varying sizes of the input image as shown in Fig.4.8.

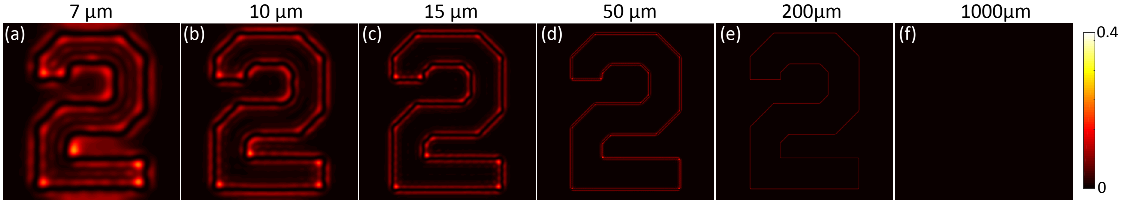

Figure 4.8: Numerical demonstration of edge enhancement in an amplitude image reflected from SBS1 absorber as a function of the absolute image size with decreasing edge intensity as size increases. Original image (a) and normalized intensity of reflected images for unpolarized light and sizes of the original image of (b) $3\,\mu$m, (c) $10\,\mu$m, (d) $100\,\mu$m and (e) $1000\,\mu$m (not visible - contrast diminishes). Normalized intensity given as a fraction of the incident intensity.

For the image under consideration one can observe that clear edge enhancement is performed only for an image scaled to a size larger than approximately $10\,\mu$m (c)(d), while the spatial frequency content for the smaller (b) image does not provide the required overlap with the filtering function of the absorber. Larger images as shown in (e,f) will generate comparably low intensity images for which we conclude that image sizes between approximately $10\,\mu$m and $200\,\mu$m are suitable for experimental confirmation. Due to the relatively low angular sensitivity of the absorber, small objects or demagnified images of larger objects are required to perform spatial frequency filtering using this device. This imposes a limitation on the applicability of the absorber since additional optics for the mapping of the spatial frequency content will be required for object outside of the above deduced scale interval. In section 4.4 an approach to engineer the steepness of the optical transfer function of the device through replacement of the dielectric spacer layer is discussed, which allows to shift the applicability of the approach to different image sizes. In summary correct scaling of the image will be crucial in performing experimental edge detection. However it should be noted that in the case of edges, their sharpness also strongly influences the spatial frequencies contained in the image. Since the sharpness of experimentally used images is hard to determine, the numerically obtained scaling factors from Fig.4.8 can only serve as a guide for experimental measurements. We will discuss this aspect in the experimental section below.

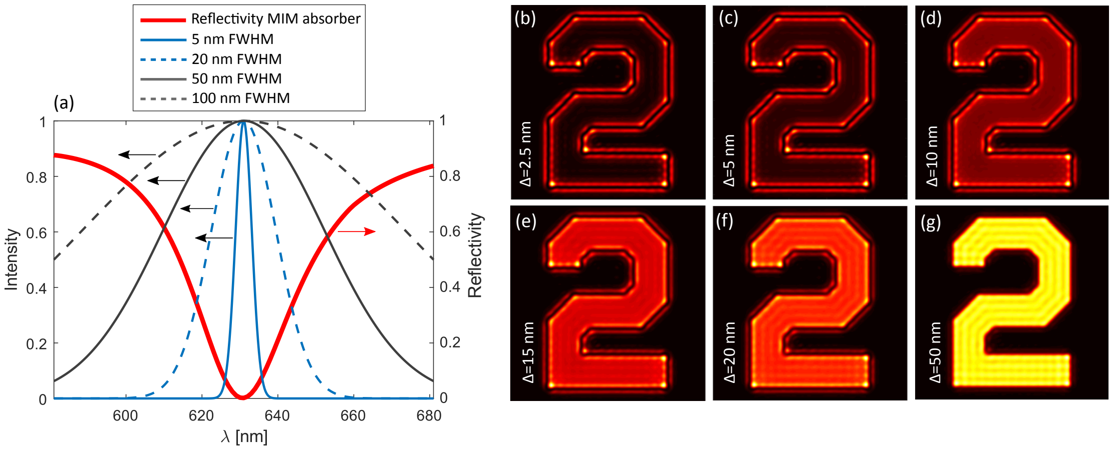

Figure 4.9: Numerical demonstration of the impact of a finite linewidth of the illumination on the edge enhancement capability of the device at the example of the device SBS1 for an image of 15 µm size. (a) Overlap between reflectivity minimum of the absorber SBS1 at normal incidence and illumination spectrum for bandwidths (FWHM) of $\Delta\lambda = 0, 20, 50$ and 100 nm. (b)-(g) averaged intensity of reflected image for a bandwidth of $\Delta\lambda = 2.5$ nm (b), 5 nm (c), 10 nm (d), 15 nm (e), 20 nm (f) and 50 nm (g). All images are normalized to their brightest pixel.

While so far we have assumed monochromatic illumination, experimentally any light source will have a finite bandwidth. It is evident from Fig. 4.5, that the optical transfer function of the device changes for deviations from the absorption wavelength. As far as filtering of low spatial frequencies is concerned, one can observe a decrease in performance for wavelengths deviating from the absorption wavelength $\lambda \neq \lambda_a$. In Fig. 4.9 we numerically demonstrate the impact of a finite bandwidth of the illumination source on the edge enhancement capability of the absorber.

For the wavelength distribution we assume a Gaussian line shape $G(\lambda)$ with line width (FWHM) $\Delta\lambda$ centered on the absorption wavelength λ_a. The results have been calculated from the weighted average of the intensities at $m = 5$ points centered around the central wavelength according to equation (4.5)

$$I_{\text{average}} = \sum_{n=1}^{m} G(\lambda_n) I_{\text{out}}(\lambda_n). \tag{4.5}$$

A decrease in edge enhancement contrast for increasing illumination bandwidth is apparent. While edge enhancement can still be observed for a bandwidth of up to $\Delta\lambda =$ 15 nm (b)-(d), contrast vanishes for larger bandwidths (e)-(g) in this particular case. In experimental measurements it is therefore crucial to minimize the illumination bandwidth in order to maximize image contrast.

4.2.3 MIM absorber for visualization of phase gradients

As outlined in chapter 2 the use of nanophotonic devices for image processing is of particular interest for phase visualization. In order to demonstrate the conversion of a phase-gradient in the incident wavefield into an intensity variation in the reflected image, the reflectance from the absorber for an electric field $E(x,y) = e^{i\phi(x,y)}$ with Gaussian shaped phase distribution $\phi(x,y) = \phi_{\max} \exp\left[-\left(\frac{x}{\sqrt{2}\sigma}\right)^2 - \left(\frac{y}{\sqrt{2}\sigma}\right)^2\right]$ with $\sigma = 1\,\mu\mathrm{m}$ was calculated as shown in Fig.4.10. The calculated intensity distributions are clearly related to the incident phase-distribution demonstrating the ability of the absorber to visualize phase-modulations. Differences between the different polarization states can be mainly seen in the image brightness with $s-$polarized light yielding the highest intensities in agreement with the calculations above. However, in line with the theoretical deduction of section 2.1.5 for systems with a quadractic optical transfer functions, the particular intensity distribution depends on the strength of the input phase gradient. While Fig.4.10(b-d) exhibits intensity maxima in regions of large phase-gradient, this does not hold for smaller maximum phase excursions (e-j). This needs to be pointed out as a limitation of the absorber as a phase-visualization tool since it implies a complex relationship between phase- and intensity distribution after processing.

In summary we have numerically demonstrated the ability of thin-film MIM absorber structures to function as high- and low-pass spatial frequency filters in reflection. Furthermore we demonstrated its all-optical image processing capability at the examples of edge enhancement in an amplitude image and the conversion of a phase gradient in a wavefield into an intensity modulation.

The amplitude contrast of light directed through a biological cell is commonly not sufficient to resolve details associated with its internal structure. To enhance the contrast without adding chemical stains, the phase gradients that arise from the refractive index or thickness modulation across the cell must be converted to intensity variations. Here we investigate the potential of the thin-film absorber to visualize phase gradients of the order of those induced in light directed through red blood cells (*cf.* Fig. 4.11).

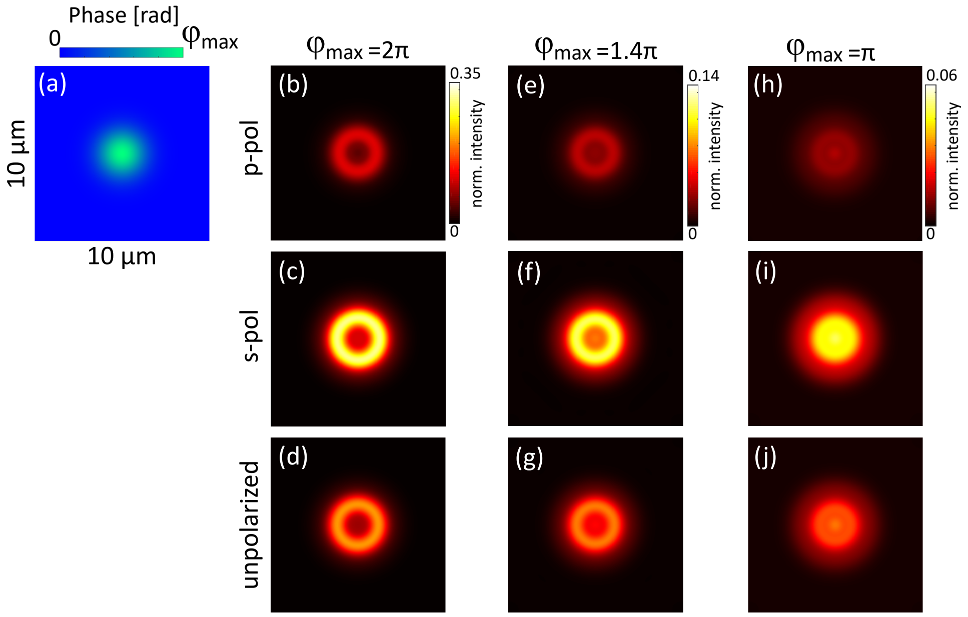

Figure 4.10: Numerical demonstration of conversion of a Gaussian shaped phase-gradient in an incident wavefield (a) into an intensity modulation upon reflection from absorber SBS1. Intensity of the reflected light as a fraction of the incident intensity (b-j) for p-polarization (top row), s-polarization (middle row) and unpolarized light (bottom row) for different maximum phase-excursions $\phi_{\max}$. The image size is $10 \times 10\,\mu$m in all cases.

In our calculations we assume a pure phase object, neglecting refraction and assume parallel light rays passing undeviated through a model of a red blood cell of homogenous refractive index [220] ($n_{\text{cell}} = 1.41$) immersed in water [221] ($n_{\text{water}} = 1.33$) with the rays experiencing a phase shift due to the thickness profile of the cell. Using the obtained phase modulation $\phi(x, y)$ we calculate the reflection from the mirror for an input field $E(x, y) = \exp(i\phi)$. The thickness profile of the red blood cell with a diameter of 7.82μm is calculate from the approximately biconcave shape (Fig. 4.11(a)) of the cell given in [222] with the resulting phase profile shown in Fig. 4.11(b). In the reflected intensity (Fig. 4.11(c)) two dominant bright rings around the steep phase gradient at the outer part of the cell are apparent with the inner part of the cell appearing considerably darker. It should be noted that the resulting complex intensity distribution is a result of the nonlinear transfer function of the absorber as well as the exclusion of evanescent waves in the calculations as discussed for Gaussian shaped phase modulations above. In the calculation shown here we have neglected refraction and the double-passing of the light through the cell that occurs after being reflected from the mirror which will potentially add distortions to the images.

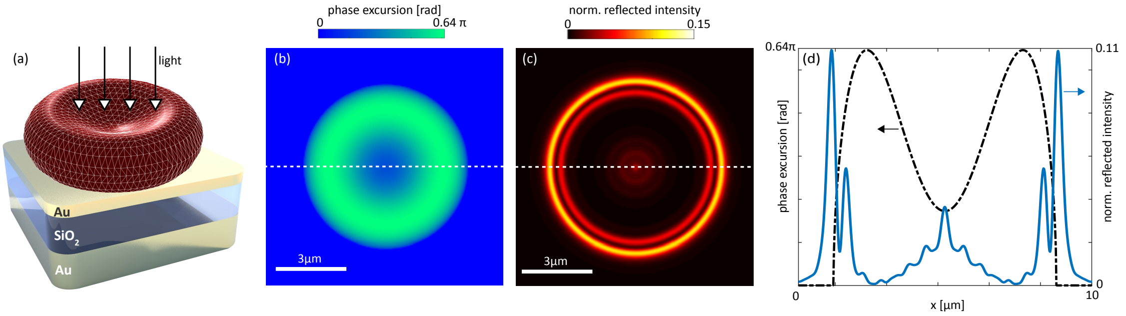

Figure 4.11: Calculated conversion of the phase gradient associated with light of wavelength $\lambda = 631$nm transmitted through a red blood cell into an intensity modulation using the thin-film absorber. (a) Spatial profile used for the model of a red blood cell on top of the thin film absorber (b) corresponding phase modulation $\varphi(x, y)$ and (c) reflected intensity as a fraction of the intensity of the incident field, (d) lineplots of the phase- and intensity modulation along the dashed lines shown in (b),(d).

The results indicate, however, the potential of the absorber to increase imaging contrast for biological cells which are directly placed on top of the mirror. The thin-film absorber, therefore has potential as a simple platform for the development of nanophotonic enabled biological phase imaging applications. Based on these numerical considerations we will now experimentally investigate the applicability and limitations of MIM absorber structures for all-optical information processing.

4.3 Experimental results

The numerical framework outlined above has been utilized to design a range of different thin film near-perfect absorber devices that were subsequently fabricated and characterized.

4.3.1 Fabrication and characterization of MIM absorbers

All devices were fabricated on [100] p-type silicon wafers. A titanium adhesion layer with a thickness of 3 nm was deposited on the wafer at a deposition rate of 0.2 Å/s. Subsequently a 150 nm thick layer of Au was deposited at 0.7 Å/s using an IntlVac NanoChrome II e-beam evaporator. A layer of SiO_2 with varying thickness d_2 was grown on the sample using the Oxford Instruments PLASMALAB 100 PECVD system. Finally a Au film of thickness d_3 was deposited on the SiO_2 layer using e-beam evaporation. In an initial attempt an absorber device with nominal parameters set to d_1 =35 nm and d_2 =150 nm was fabricated, thus lying within the range of parameters predicted as suitable by the numerical calculations above. We will refer to this device as SBS-exp1 in the following. The reflectance from the device was measured for both p- and s-polarization as a function of angle of incidence using a spectrometer (Agilent Cary 7000 UV-Vis-NIR Universal Measuring Spectrometer (UMS) [26]) as schematically illustrated in Fig.4.12 with the results shown in Fig.4.13.

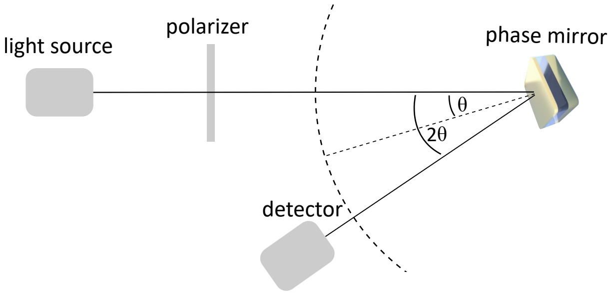

Figure 4.12: Schematic illustration of setup used for angle dependent reflectance measurements uding the Agilent Cary 7000 UV-Vis-NIR Universal Measuring Spectrometer (UMS). The sample is tilted with a step size of $\Delta\theta = 1°$ and specular reflection at an angle of 2θ detected. Reprinted with permission from [60], licensed under a Creative Commons Attribution (CC BY) license.

The design of the spectrometer limits the minimum and maximum measurable angle of incidence to $\theta_{\text{min}} = 6°$ and $\theta_{\text{max}} = 84°$ respectively. The measurements show absorption of approximately 91% of the incident intensity around 662 nm at 6° angle of incidence shifting towards the blue as the angle of incidence increases for both p- and s- polarized light consistent with the numerical results. From this a filtering contrast of $C_s \approx 0.86$ for $p-$ and $C_s \approx 0.85$ for $s-$polarized light is obtained (*cf.* eq.(2.43)). The absorption maximum at near-normal incidence is shifted by approximately 45 nm to towards the red spectral range compared to the numerical prediction ($\lambda_{\text{num}} = 615$ nm) for these nominal parameters. This can be attributed to variations in the dielectric function of silicon dioxide and gold in thin films compared to bulk material. Furthermore an uncertainty of approximately ±10% in deposited film thickness for both thin film fabrication methods contributes to this shift as demonstrated above in Fig. 4.4.

---

[26] Measurements involving the Agilent Cary 7000 UV-Vis-NIR Universal Measuring Spectrometer (UMS) were carried out in colaboration with Prof. Gomez and Dr. Della Gaspera at RMIT University, Melbourne.

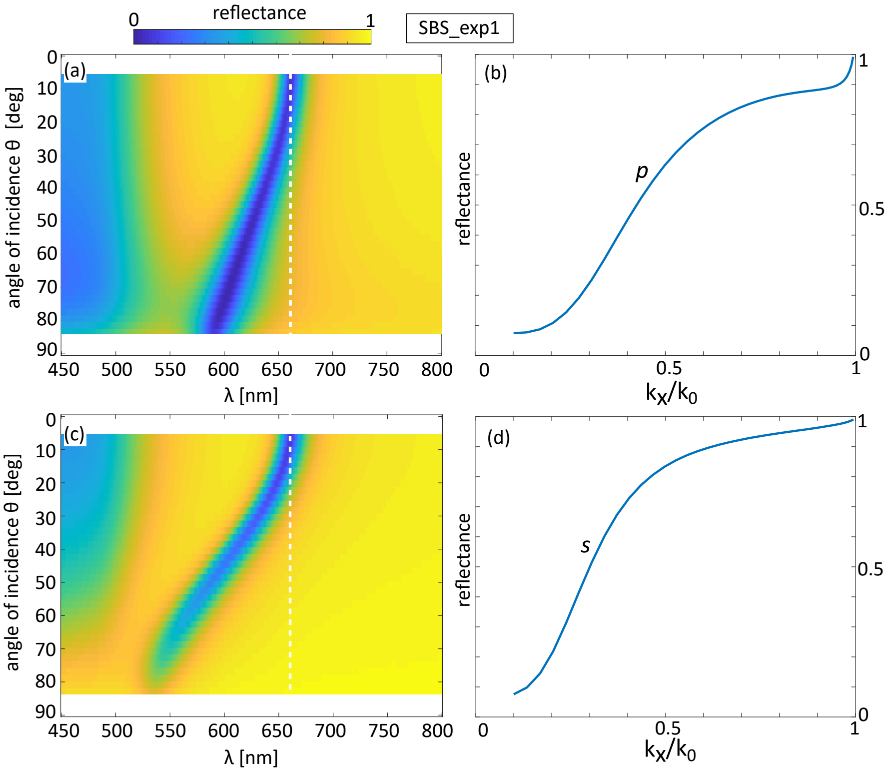

Figure 4.13: (a),(c) Experimentally measured reflectance from device SBS-exp1 as a function of angle of incidence. (b),(d) Reflectance as a function of spatial frequency at the wavelength $\lambda_\mathrm{a} = 662\,\mathrm{nm}$ indicated by dashed lines with $k_\mathrm{x}/k_0 = \sin\theta$.

In order to improve the filtering performance of the device, an absorber with an absorption efficiency at the absorption wavelength under normal incidence as close as possible to unity, i.e. $R(\lambda = \lambda_a, \theta = 0) \approx 0$, is required. Due to the inevitable deviations in layer thicknesses and dielectric functions during the e-beam evaporation and chemical vapor deposition processes, it was decided that a series of devices should be fabricated and the sample with the best performance used for imaging experiments. Five devices with fixed thickness d_3 =31 nm of the covering Au layer and varying thickness d_2 of the $\mathrm{SiO_2}$ spacer layer were fabricated. The Au backmirror and the covering Au layer have been fabricated on all devices in a simultaneous step for which they are assumed to be identical. From this series of devices that with a nominal spacer layer thickness of d_2 =155 nm has been selected for further investigation based on its absorption characteristics shown in Fig.4.14. These reflectance measurements were taken in the same manner as outlined above for the device SBS-exp1.

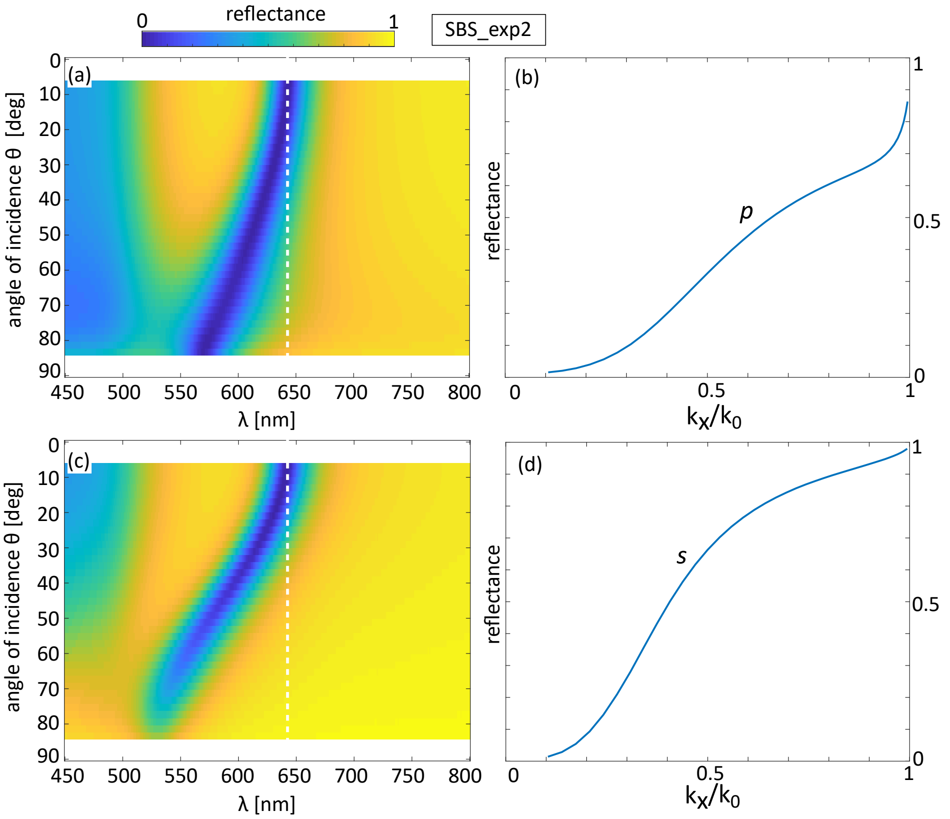

Figure 4.14: (a),(c) Experimentally measured reflection from device SBS-exp2 as a function of angle of incidence. (b),(d) Reflectance as a function of spatial frequency at the wavelength $\lambda_a = 640\,\mathrm{nm}$ indicated by dashed lines with $k_x/k_0 = \sin\theta$. Adapted with permission from [60], licensed under a Creative Commons Attribution (CC BY) license.

We will refer to this second device as 'SBS-exp2' in the following. To streamline presentation, reflection measurements of the remaining devices from this series are shown in the appendix in Fig.A.1, A.2, A.3 and A.4. It is apparent that the absorption wavelength of the absorbers is tuned from 600 nm to 640 nm as the thickness of the spacer layer is increased. The data experimentally confirms the possibility of shifting the operation wavelength of the thin film absorber as an all-optical image processing device as numerically demonstrated above in Fig.4.2. Limitations in setting the operational wavelength of the device arise, however, from the accuracy of the thin-film deposition method and reproducibility of material properties as discussed earlier. For all devices in this series an absorption efficiency above 98.5% was achieved for which the thickness of the superstrate, which influences the absorption efficiency as well (*c.f.* Fig.4.3), was not varied further in this experiment. For experiments that require further improvement of the filtering contrast, variation of this parameter should be included in the experimental optimization process. It should be noted that this could imply significant fabrication time since a separate e-beam evaporation step would be required for each device. These usually take several hours of vacuum pumping and evaporation.

The reflectance from device SBS-exp2 shows that the absorption efficiency of the absorber reaches 98.5% at near-normal ($\theta = 6°$). From this a filtering contrast of $C_s \approx 0.97$ for $p-$ and $s-$polarized light is obtained from the measurements for absorber SBS-exp2. For this reason the filtering contrast between high- and low spatial frequencies is significantly enhanced compared to device SBS-exp1 and device SBS-exp2 is used for all following image processing measurements.

The results from Fig. 4.13 and 4.14 experimentally confirm the capacity of the MIM absorber to filter low spatial frequencies in reflection. In order to demonstrate image processing, a Köhler-illumination setup has been designed as shown in Fig. 4.15. The setup enables projection of demagnified images of an object onto the device.

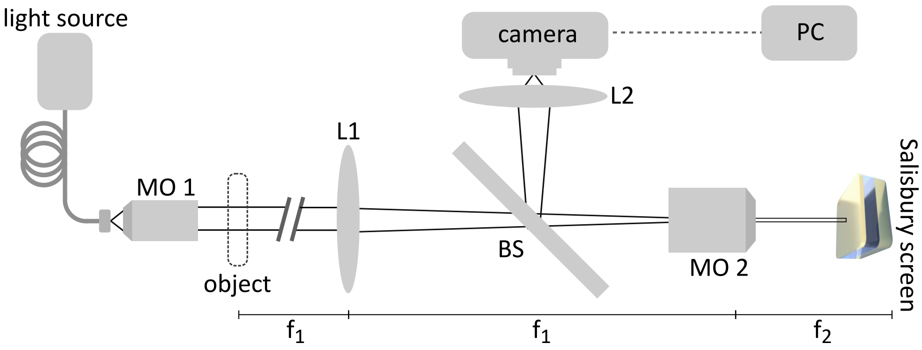

Figure 4.15: Köhler-illumination setup used for demonstration of edge enhancement and phase gradient detection. Spatial frequency mapping through demagnification using the telescope consisting of L1 and MO2. For simplicity the distance between the object and lens L1 is not shown to scale as here indicated by the break sign. Adapted with permission from [60], licensed under a Creative Commons Attribution (CC BY) license.

Unpolarized light from a supercontinuum laser source (Fianium SC-450-2) is passed through a fiber-coupled tunable filter (Fianium Superchrome VIS-FDS-MM) in order to limit the bandwidth to 5 nm. The light is guided to the Köhler-illumination setup using a single mode fiber (Thorlabs SM600) and the output collimated via a NA 0.3 Nikon LU Plan Fluor objective (MO1). The collimated beam is transmitted through an object under investigation. The image is then projected onto the sample surface via a telescope consisting of a $f = 100\,\text{mm}$ lens (Thorlabs LA1509-A) (L1), a beamsplitter (Thorlabs CM1-BS013) and an infinity corrected NA 0.90 Nikon Plan NCG ×100 objective (MO2) with a working distance of 1 mm. This telescope effectively enables 50× demagnification of the image thus broadening its spatial frequency distribution in Fourier space. The light reflected from the absorber device is then imaged onto the camera via lens (L2).

As a proof-of-concept, Fourier plane images in reflection were obtained using this setup with object and lens (L1) removed as shown in Fig. 4.16. The Fourier plane images are consistent with the results from the spectrometer measurements shown in Fig. 4.13. Suppression of low spatial frequencies is evident in Fig. 4.16(c). It should be noted that the results also confirm the ability of the device to filter high spatial frequencies at lower wavelengths and perform bandpass filtering at intermediate wavelengths as apparent in 4.16(b) in line with the numerical results above.

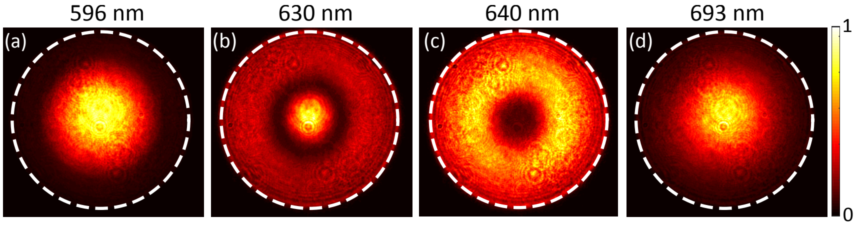

Figure 4.16: Measured Fourier plane images in reflection from absorber SBS-exp2 with central wavelength set to 596 nm (a), 630 nm(b), 640 nm (c) and 693 nm (d) with the dashed lines indicating NA = 0.9. All images are normalized to their brightest pixel. Adapted with permission from [60], licensed under a Creative Commons Attribution (CC BY) license.

4.3.2 Edge enhancement in reflected amplitude images

To demonstrate the spatial frequency filtering capability of the device in an amplitude image, a USAF-1951 resolution test target (Thorlabs R1DS1N) (Fig. 4.17(a)) has been inserted into the setup as the object. The images of the figure '2' reflected from the absorber as a function of wavelength are shown in Fig. 4.17(b)-(l). The results show clearly enhanced edges of the figure '2' in the vicinity of the absorption wavelength of the absorber (Fig. 4.17e-g) which are not observable at shorter (4.17(b), (c)) and longer wavelengths (Fig. 4.17(h),(i)). The bandwidth of the light source of 5 nm reduces the edge enhancement contrast as elucidated above in Fig.4.9 for which the use of a laser system with lower bandwidth would increase the image contrast. Filtering of low spatial frequencies at wavelengths shorter than the absorption wavelength is apparent in Fig. 4.17(d) with a blurred figure '2' compared to the reflected image at wavelengths where spatial filtering is negligible (Fig. 4.17 (b),(h),(i)). To confirm the findings, the experiment was repeated using a different microscope objective (Nikon Plan N 20x NA 0.4) as the MO2 in order to decrease the demagnification to 10×. Fig. 4.17 (j-l) show that at this lower demagnification the image quality is increased but the contrast between the edges and the homogenous areas of the image is too low for edges to be apparent. This is in line with the numerical findings above and confirms the requirement for adequate demagnification or selection of appropriately sized objects. It should be noted that the lower NA of the objective also reduces the spatial frequency content captured by the imaging system for which the results in (b-i) and the results shown in (j-l) are not fully comparable.

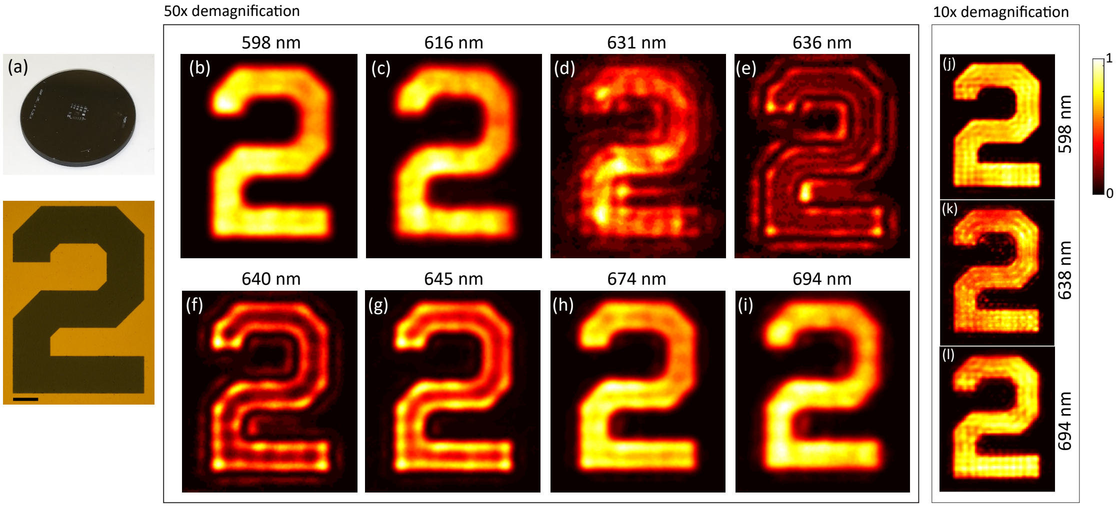

Figure 4.17: Experimental demonstration of edge enhancement in an amplitude image reflected from the thinfilm absorber structure SBS-exp2. (a) USAF resolution test target (top) and microscope image of figure '2' with scalebar 50 μm, (b)-(i) Normalized intensity of reflected images for unpolarized light at wavelengths ranging from 597 nm to 694 nm. (j-l) Images recorded for lower demagnification (10X) exhibiting no edge enhancement. All Images are normalized to the brightest pixel.

The results above experimentally confirm the ability of the absorber to filter low and high spatial frequencies in an amplitude image. The double-ringing around the edges of the figure '2' are a result of the nonlinear transfer function of the screen and the resolution of the sample and imaging system (*cf.* section 2.1.4). The appearance of this effect after spatial-frequency filtering was also observed above in our numerical calculations and experimentally in [66]. In summary, the results experimentally demonstrate for the first time all-optical high- and low pass spatial frequency filtering in an amplitude image using a Salisbury screen type near-perfect absorber.

4.3.3 Visualization of phase gradients in embossed PMMA film

In the following experimental evidence for the capability of the absorber to convert phase gradients in a wavefield into a readily detectable intensity modulation will be provided. We have numerically illustrated this capability for a Gaussian-shaped phase modulation in Fig. 4.10. Experimentally, generating a pure phase gradient, with negligible amplitude modulation, is challenging.

Here we use a PMMA film with a spatially varying thickness profile in the shape of spherical caps (a microlens array - FINLENS Flyeye 80 LPI) as the test sample in the Köhler-illumination setup with a brightfield microscope image shown in Fig. 4.18(a). By immersing the PMMA film in index matching oil (Cargille, $n_{\mathrm{oil}} = 1.518$), scattering of light transmitted through the PMMA film, and thereby the amplitude contrast associated with the thickness modulation, was minimized. As apparent from the resulting brightfield image of the same sample shown in Fig. 4.18(b), the thickness modulation becomes almost invisible except for scattering at the edges of the spherical caps. In a differential interference contrast (DIC) image of the same sample, however, the thickness modulation is clearly visible demonstrating the presence of a near-pure phase modulation.

In Fig. 4.18(e) reflected images of the PMMA film at the absorption wavelength of the absorber device are shown. The central part of the spherical caps, which is associated with low phase gradients, remains dark while the outer parts show increased intensity thereby indicating a steep phase gradient consistent with the differential interference contrast (DIC) image of the sample shown in Fig.4.18(c). At the reference wavelengths shorter (d) and longer (f) than the absorption wavelength of the Salisbury screen, the lens regions appear almost uniform. Remaining bright lines in these images originate from residual scattering at the edges of the spherical caps. The intensity contrast that is generated from the phase-gradient is furthermore emphasized by vertical and horizontal lineplots through the central lens (Fig.4.18(g-i)) as indicated by the blue crosses. In order to reduce noise, these line profiles were averaged over an interval of $\pm 28\,\mu$m around the horizontal (vertical) center of the lens. This result experimentally confirms the ability of the thin film absorber to convert a phase gradient in an incident wavefield into an intensity modulation in the reflected image which can be detected by conventional photodetector technology.

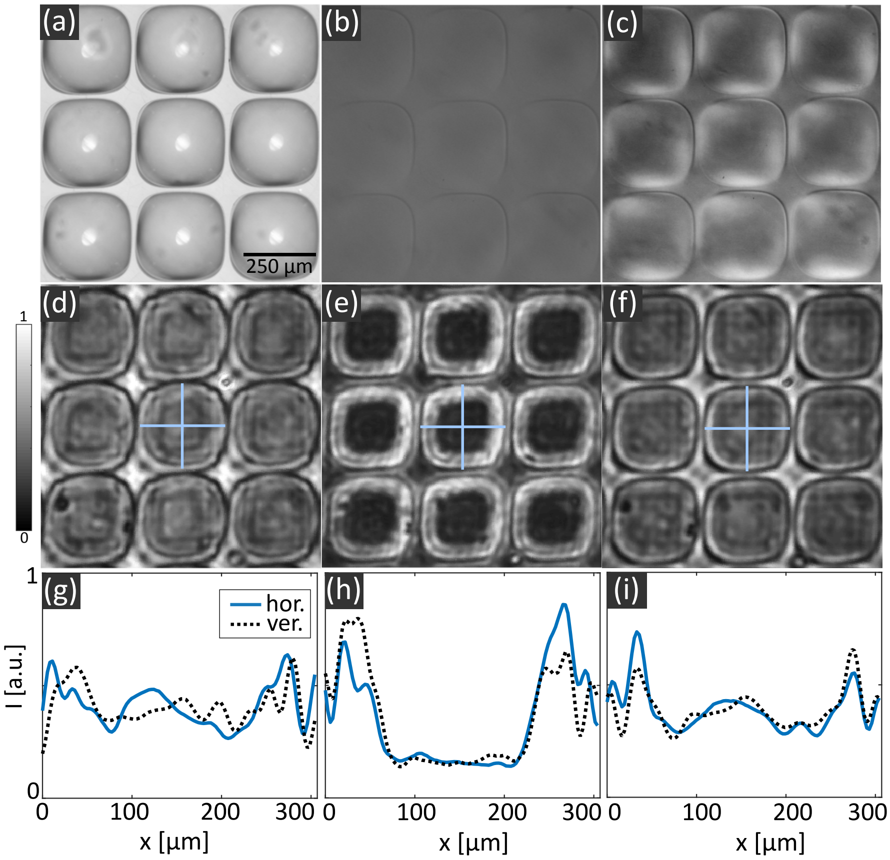

Figure 4.18: Experimental demonstration of phase-gradient visualization using a PMMA film with modulated thickness profile as a test object in the Köhler-illumination setup. Brightfield image of the object (a) without and (b) immersed in index matching oil, (c) differential interference contrast (DIC) image of PMMA film immersed in index matching oil. Images reflected from mirror and corresponding line profile plots through the horizontal and vertical center of the central spherical cap (as indicated by the blue crosses) at 598 nm (d) and (g), 640 nm (e) and (h) and 694 nm (f) and (i). Reprinted with permission from [60], licensed under a Creative Commons Attribution (CC BY) license.

4.3.4 Image enhancement in filamentous algae

As previously discussed, biological cells commonly provide relatively low amplitude contrast but have refractive index and thickness variations corresponding to features within the cell. For this reason visualization of internal cell features without chemical staining requires contrast enhancement based on the phase variations induced by the structure of the cell. As an example of the potential of this method, we investigate a sample of pond-water containing filamentous-algae. The sample was fixed between two coverslips and sealed with clear nail varnish. The filaments of the algae that are investigated here typically consist of chains of cylindrical cells [223]. Fig.4.19 shows the images of the algae reflected from the thin-film absorber SBS-exp2 at central wavelengths of 598 nm, 638 nm and 694 nm. It should be noted that for the presented data all measurements were carried out using an intensity of the incident light below 30 mW/cm^2 ruling out the risk of phototoxicity for common biological cells [224]. The internal structure of the algae filaments is not or only marginally visible in images recorded at the reference wavelengths in Fig.4.19(a) and (c). At 638 nm in Fig.4.19(b), however, increased contrast indicating a typical segmented algae filament becomes apparent. Furthermore increased contrast at this wavelength in other features in the pond water, that are unidentified, is also evident. Limitations in image quality are attributed to scattering by the surrounding water, noise from back reflection of the two cover slips as well as the demagnification of the image through the telescope. Since the biological specimen was obtained from pond water, the scattering and speckle are inevitable but could be reduced in future experiments by using cleaned biological samples. This result is the first experimental indication of the potential of the device to be employed for biological phase-imaging.

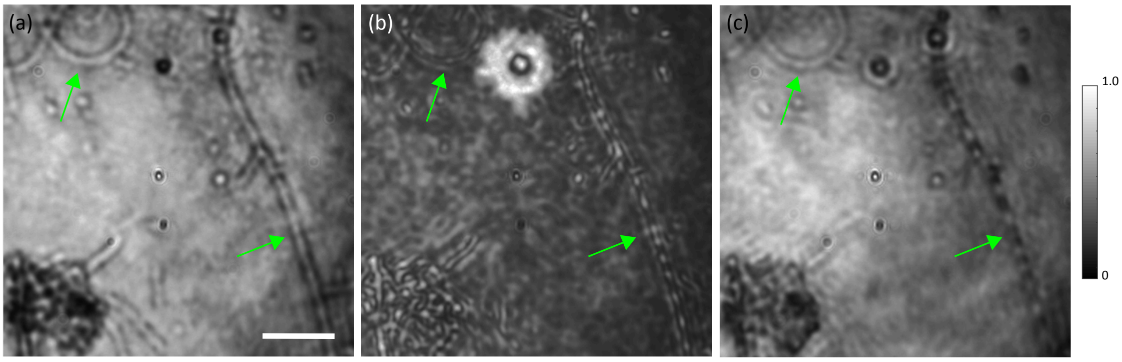

Figure 4.19: Phase imaging of a biological sample using the example of filamentous algae. Images reflected from the mirror at a central wavelength of $\lambda =$ 598 nm (a),638 nm (b)and 694 nm (c), scale bar indicates 250 μm. Reprinted with permission from [60], licensed under a Creative Commons Attribution (CC BY) license.

We propose two ways to increase the resolution of the imaging system. Firstly a better trade-off between the demagnification (i.e. combination of L1 and MO2 in Fig. 4.15) and the spatial frequency mapping could be found for a specific object of interest. While a higher demagnification $\Omega = f_{\mathrm{L1}}/f_{\mathrm{MO2}}$ elevates the spatial frequency content, thereby increasing the contrast between low and high spatial frequencies (*cf.* Fig. 4.8), aberrations in the elements L1, L2 and MO2 become stronger with increasing (de)magnification particularly when operating close to the diffraction limit. Hence, a slightly lower demagnification might be sufficient to generate contrast while maintaining appropriate resolution. A second option is placing the object of interest directly on top of the mirror, thereby avoiding demagnification completely. However, the spatial frequencies generated without demagnification might be too low for specific objects considering the relatively low sensitivity of the Salisbury screen to angle of incidence (*cf.* Fig. 4.14).

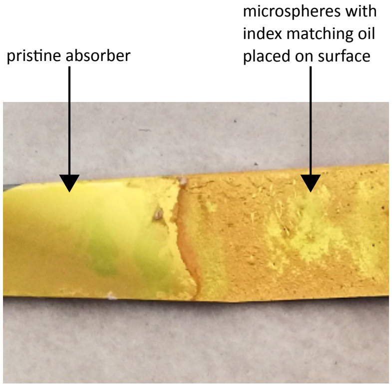

Figure 4.20: Failed attempt at imaging polystyrene microspheres (20 μm diameter) in refractive index matching oil directly placed on the surface of the Au/SiO$_2$/Au absorber. Pristine region of the Salisbury screen *(left)* and regions where microspheres in index matching oil were placed *(right)*.

An initial attempt to place polystyrene microspheres in index matching oil, serving as phase objects, directly on top of the mirror to circumvent the demagnification, destroyed the thin film absorber as show in Fig. 4.20. We attribute this to the low chemical stability of the covering Au layer. It is therefore suggested that an additional optically thin SiO$_2$ protection layer is deposited on top of the absorber in order to increase stability. This involves a process development step to assess the required thickness of the protecting layer that sufficiently improves the stability of the device surface and solves the adhesion issue observed for the semitransparent Au cover layer. As a starting point, a 100 nm thick SiO$_2$ layer is suggested. This does not affect the image processing capacity of the device and should in principle permit phase imaging of objects directly placed on top of the device as discussed for the numerically simulated phase-imaging of red blood cells in Fig. 4.11.

4.4 Summary and Outlook

Inspired by the concept of the Salisbury screen we have reported a simple metal-insulator-metal (MIM) thin-film device that performs high-NA, all-optical 2D spatial frequency filtering on a reflected wave field, with the relevant thickness of the device being less than 200nm thick. This capacity was numerically and experimentally demonstrated using the examples of edge enhancement in a micrometer sized amplitude image and the conversion of a micrometer sized phase gradient into an intensity modulation. The spatial frequency filtering capability of MIM absorbers suggests an avenue for the development of ultra-compact, all-optical information processing devices with application in biological phase imaging. This claim was numerically supported by demonstrating that the absorber holds potential to visualize phase gradients typically arising in light directed through red blood cells. Experimental confirmation of this finding would therefore be an interesting aspect of future research. Here experimentally contrast enhancement in samples of filamentous-algae using the absorber device was demonstrated.

Limitations of the approach were identified in the requirement for micrometer sized images usually associated with demagnification of existing images as well as a spectral bandwidth of the illumination below approximately 10 nm. Furthermore chemical instability issues prevented objects being placed directly on top of the device. Fabrication of a modified device with an additional thin dielectric protection layer could solve this issue. Finally the nonlinear optical transfer function of the device, the finite numerical aperture of real imaging systems as well as the common requirement for demagnification of larger images results in ringing artifacts in the processed images that place limitations on the complexity of images and phase modulations that can be processed.

Potential for an increased steepness of the spatial frequency filtering function of the thin-film absorber lays in a dielectric spacer material with lower refractive index than SiO_2. In order to estimate the limit of this approach, the reflectance as a function of spatial frequency was calculated for a spacer layer of refractive index $n = 1.025$. This unusually low index of refraction corresponds to a synthetic aluminum oxide based dielectric material recently proposed by Zhang et al. [225].

In Fig.4.21 the reflectance of a SiO_2 based device as investigated in this thesis and the lower-refractive index device are compared. The normalized spatial frequency k_x/k_0 at which the reflectance of the absorber reaches 50% can be shifted towards lower frequencies by up to 0.21 for $s-$polarized light, and 0.45 for $p-$polarized light. While an increase in the reflectance is therefore possible, most commonly available dielectrics with $n > 1.025$ would induce a relatively small change within these limits.

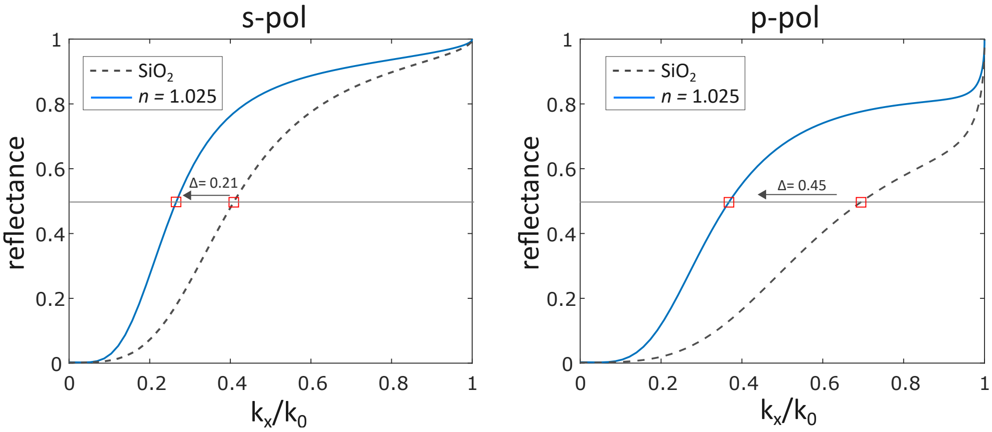

Figure 4.21: Increase of the angular sensitivity of MIM thin-film absorbers through choice of a lower refractive index dielectric material for the spacer layer. Reflectance for (a)s-polarized and (b)p-polarized light as a function of lateral spatial frequency k_x/k_0 for a SiO_2 spacer layer (dashed gray) and a low-index dielectric material with $n = 1.025$ [225] (solid blue).

Furthermore, extensions of the approach inspired by one-dimensional metal-dielectric photonic crystals (MDPhC) [226, 227] with multiple absorption wavelengths could enable all-optical real-time processing of colour images. Finally, for biological applications it is often essential to avoid contact between living cells and metallic surfaces. The absorber architecture could either be modified by adding a covering dielectric layer or by replacing the metallic mirror elements by dielectric Bragg-reflectors as previously demonstrated in [214]. This could make the design fully bio-compatible and enable integration of the entire device into biological tissue. This approach does, however, imply increased fabrication complexity due to a higher number of thin-film layers.

In conclusion, MIM absorbers have potential to be part of next generation all-optical information processing devices within the limits discussed above. However, the fact that they work in reflection and not transmission is an obstacle to easy integration into ultra-compact systems. This issue is addressed and further discussed in chapter 6 where an approach to perform nanophotonics enabled all-optical spatial frequency filtering with transmitting metasurfaces is demonstrated.

Chapter 5

Subradiant modes for Spatial Frequency Filtering

In the previous section we examined unstructured optical thin-films as a platform for analogue optical computation. We will now proceed to investigate nanotextured metasurfaces as introduced in section 2.5 above. In particular, this chapter is concerned with the capacity of nanostructures supporting subradiant modes as previously discussed in section 2.4.3 to perform spatial-frequency filtering on an optical wavefield. The content of this chapter is partially covered in the following journal publication

L. Wesemann, P. Achmari, K. Singh, E. Panchenko, T. D. James, D. E. Gómez, T. J. Davis, and A. Roberts. "Metasurfaces, dark modes, and high NA illumination." *OSA Continuum*, 1(2):727-735, 2018.

5.1 Introduction

Previous work has investigated subradiant resonances of individual nanorod trimers arragened in a triangular configuration as shown in Fig.5.1 [93]. The results demonstrated modal hybridization into plasmonic dark- and bright modes. In particular, a plasmonic dark mode with the dipole moments of the nanorods oriented radially was investigated. It was shown that with decreasing separation of the nanorods the electric dipole mode of the individual nanorods hybridizes and splits into a higher energy dark mode and lower energy bright modes leading to two distinct features in the spectral response of light reflected from the nanostructure. It is specifically the presence of these plasmonic dark modes of radial nanotrimers that carries potential for all-optical, ultra-compact spatial frequency filtering. For this reason nano trimers are a suitable platform for testing subradiant mode excitation for spatial frequency filtering and identifying potential issues.

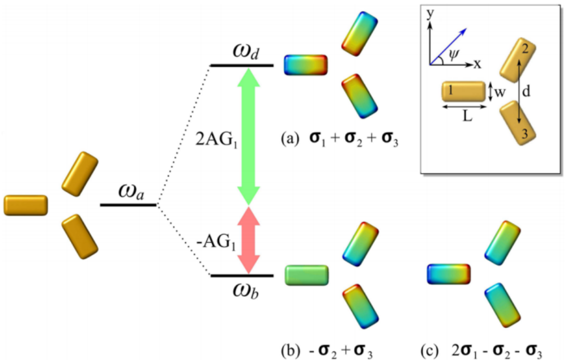

Figure 5.1: Excitation of a subradiant mode and superradiant modes on radial nano rod trimers. Spectral separation of the resonances arises from modal hybridization as a result of coupling between the nano rods as their separation decreases. Figure reprinted with permission from [93][27].

While the excitation of the subradiant mode has been demonstrated experimentally for individual nanotrimers [93], the particular application of the approach to spatial-frequency filtering in images requires arrays of nanotrimers. For this reason the existing research is here extended to investigate the spatial frequency filtering capability and limitations of arrays of plasmonic nanotrimers. In the following we will numerically and experimentally investigate the excitation of subradiant modes of an array of silver nanotrimers. Silver was selected here since it offers sharper plasmonic resonances than for example aluminium in the visible region and does not suffer from intraband transitions at shorter wavelenghts like gold (*c.f.* sections 2.3, 2.4). Optical features will be discussed using the example of a particular device that has been fabricated and permits observation of the relevant characteristics. More general numerical considerations will be presented where required.

---

[27] Reprinted with permission from 'The dark side of plasmonics', D. Gómez, Z. Teo, M. Altissimo, T. Davis, S. Earl, and A. Roberts, *Nano Letters*, vol. 13, no. 8 , pp. 3722−8, 2013. Copyright 2013 American Chemical Society

5.2 Fabrication and characterization of radial trimer metasurfaces

We consider an array of silver rod trimers illuminated by a high-NA objective as schematically shown in Fig.5.2a. A silver nanotrimer metasurface was fabricated using electron beam lithography (EBL). The pattern was written into a bilayer of polymethyl methacrylate (PMMA: 80nm A2 on top of 200nm LMA EL6, baked at 180 degree for 3min after each deposition) resist that was spun onto a microscope glass slide, using an electron beam lithography tool (Vistec EBPG 5000). The sample was then developed in a 3:1 mixture of isopropanol: methylisobutyl. A 40nm thick layer of silver was deposited on the sample through physical vapor deposition on a 2nm adhesion layer of germanium. Lift-off was performed in acetone. In order for the silver nanostructures to be embedded in a near-homogeneous environment that also protects the device from degradation due to exposure to air, an approximately 1 μm thick layer of PMMA was spun onto the sample.

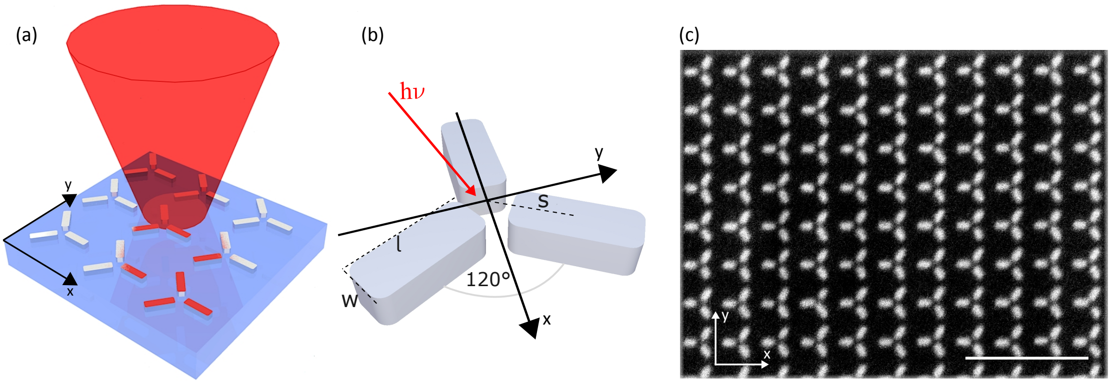

Figure 5.2: Optical metasurface consisting of an array of Ag nanorod trimers. (a) Schematic of nanotrimer array illuminated with a focussed beam (b) individual nanotrimer and geometric parameters rod length l, rod width w and spacing between the center of each rod and the centroid of the configuration s. (c) SEM image of fabricated silver nanotrimer metasurface with scale bar 1 μm. (b,c) Adapted with permission from [61], copyright The Optical Society.

The structure of the sample was investigated using scanning electron beam micrscopy (FEI Nova Nano SEM 430) as introduced in section 3.2.4 in order to obtain information about the actual geometrical parameters of the fabricated structure. Using the software package ImageJ with the thresholding-method, the periodicity p, rod width w, rod length l and the rod spacing (distance from center of rod to center of structure) s were measured at 41 locations in the image and the average was calculated with the standard deviation taken as the error. In the appendix in Fig.A.5 details of the thresholding process are provided. Table 5.1 compares the nominal fabrication values with the values obtained from the SEM image.

parameter	nominal value [nm]	measured value [nm]
p	300	304 ± 9
l	100	104 ± 7
w	40	61 ± 4
s	80	75 ± 5

Table 5.1: Comparison of nominal fabrication parameters and measured gemoetrical paramaters of nanotrimer metasurface from SEM image shown in Fig. 5.2c with uncertainties given as the standard deviation.

5.3 Numerical modelling of subradiant resonances

The metasurface was numerically modeled using the finite element method as implemented in COMSOL Multiphysics 5.3 with the RF module based on the measured parameters given in table 5.1. The array has been modeled using periodic boundary conditions in the lateral (x,y) directions and ports terminating the model on the upper and lower boundary of the model. Linearly polarized electromagnetic waves are launched into the model via the port on the upper boundary of the model. A mesh with a maximum element size of 10 nm was used to resolve the silver nanotrimers where increased simulation accuracy was required. The optical constants for silver were taken from [76] and the array is assumed to be embedded in a homogenous environment of refractive index 1.5. Figure 5.3 shows a plot of the simulated reflectance and transmittance obtained from the S-parameters as a function of wavelength from the metasurface for different polarizations and angles of incidence.

For normally incident light polarized along the x- and y- directions (Fig. 5.3a,b) a broad resonance near 710 nm for x- and 740 nm for y-polarized light is evident in reflection and transmission. Based on the calculated surface-charge distribution shown in the inset, this resonance can be attributed to the excitation of a dipole mode. The polarization sensitivity arises from differences in coupling between the unit cells in the x- and y-directions.

As the angle of incidence is increased, thereby introducing a phase retardation across each unit cell, we expect additional spectral features corresponding to the excitation of dark modes to arise. In the following we will discuss the excitation of different modes with zero net electric dipole moment as well as the impact of lattice effects as a function of angle of incidence in order to obtain insight into the spectral frequency filtering capability of the nanotrimer metasurface. Figure 5.3c,d show the reflectance from and transmission through the metasurface for light incident at an angle of 12.5° for s-polarized light with the transverse component of the wavevector aligned with the x- (c) and y-axes (d) of the array. For both orientations new resonances in the vicinity of 580 nm appear that have not been present for illumination at normal incidence thus suggesting the excitation of a dark mode. The calculated surface charge density shows an azimuthal symmetry confirming the hypothesis that a mode with zero electric dipole moment was excited.

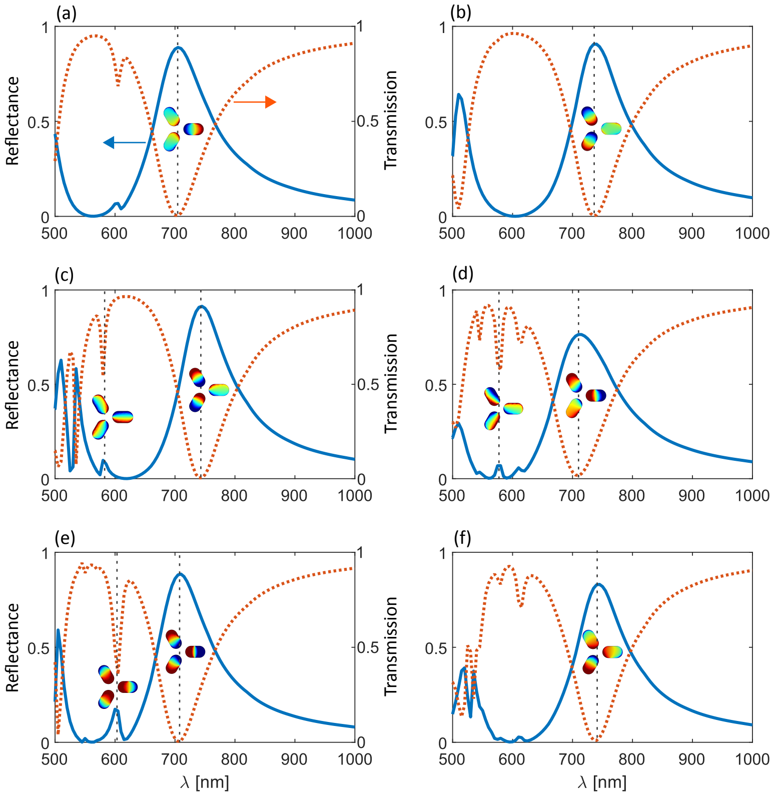

Figure 5.3: Calculated normalized reflectance (solid) and transmittance (dashed) from the metasurface as a function of free-space wavelength for (a) x- and (b) y-polarized, normally incident light. Optical response for light incident at an angle of 12.5° for (c,d) s-polarization and (e,f) p-polarization with the transverse component of the incident wavevector along the x- (c,e) and y- (d,f) direction. Adapted with permission from [61], copyright The Optical Society.

In Fig.5.3e,f the optical response for illumination with p-polarized light incident at the same angle of 12.5° is shown. For this polarization a dark mode near 600 nm with radially oriented dipole moments is excited in the case of illumination with the horizontal component of the wavevector aligned with the x-axis. The mode is however only weakly excited for illumination along the perpendicular direction at a longer wavelength of approximately 610 nm. We attribute this difference to the smaller spacing between elements of adjacing unit cells in y-direction for which we expect increased coupling causing suppression of the dark mode with radial symmetry. Approaches to avoid this suppression of the radial dark mode for excitation in one direction would be choosing an alternative lattice symmetry such as a hexagonal orientation or increasing the lattice periodicity at the cost of reduced power reflectance and the appearance of additional diffraction related artifacts.

It should be noted that weak excitation of the radial dark mode near 600 nm is apparent for illumination at normal incidence in Fig.5.3a which we attribute to near-field excitation caused by the spectral overlap between the dark- and the bright-mode in this case. Finally, several resonances are apparent near 500 nm. These are due to lattice diffraction as well as a dipole mode along the short axis of the nanorods. We will not discuss these features further, but focus on the characteristics of the excitation of the subradiant modes. In summary we have numerically demonstrated the excitation of two different dark modes with radial and azimuthal symmetry on an array of silver nanotrimers. Furthermore we have discussed the suppression of a dark mode on a meta atom due to the arrangement in an array using the example of the radial dark mode.

5.3.1 Angular filtering with radial trimer metasurfaces

Based on the angular sensitivity in the excitation of subradiant modes on nanotrimer arrays identified throughout the analysis of Fig.5.3, we expect to observe characteristic features in Fourier plane images at the corresponding wavelengths in reflection and transmission.

From the previous analysis the suppression of low spatial frequencies for dark mode excitation in reflection is expected in particular, while the suppression of higher spatial frequencies is anticipated for the corresponding Fourier images in transmission. On the other hand a more uniform structure, with a maximum at zero spatial frequency, in the

Fourier plane image is expected for the excitation of bright modes. Below we will discuss the ability of nanotrimer arrays to filter spatial frequencies using calculated Fourier images. These insights will support assessment of their suitability and limitations as ultra compact devices for optical information processing.

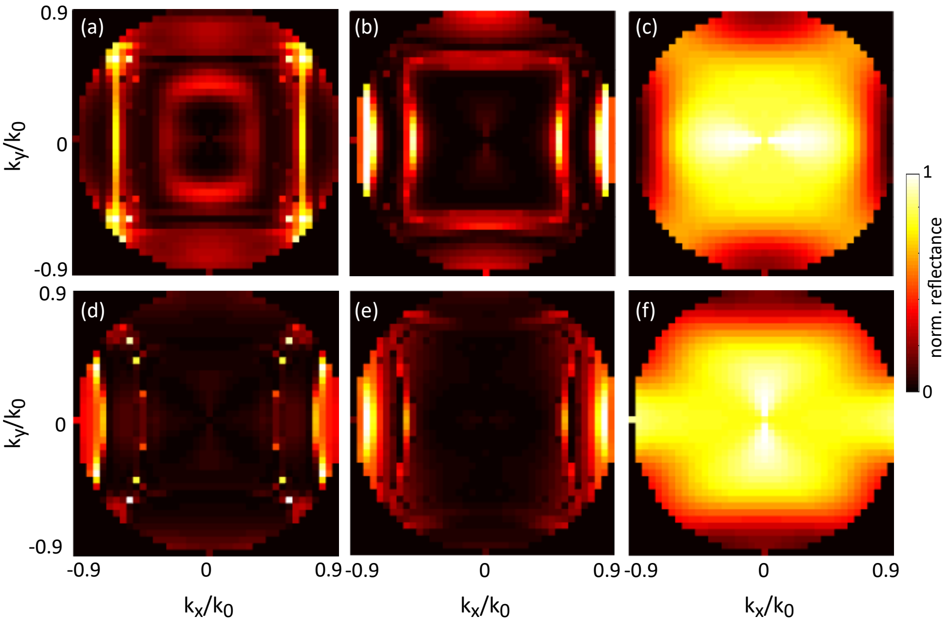

Figure 5.4: Calculated Fourier plane images in reflection for *s*- (top row) and *p*-polarized (bottom row) illumination at wavelengths of 580 nm (a,d), 600 nm (b,e) and 740 nm (c,f). Images normalized to their brightest pixel. Reprinted with permission from [61], copyright The Optical Society.

Figure 5.4 shows calculated Fourier plane images in reflection for *p*- and *s*- polarized light at the wavelengths associated with dark mode excitation (a,b,d,e) and bright mode excitation (c,f). Suppression of low spatial frequencies in reflection is apparent in the Fourier plane images calculated at 580 nm (Fig.5.4a,d) and 600 nm (Fig.5.4b,e) which can be attributed to the excitation of dark modes. At 580 nm one can observe the excitation of a dark mode with azimuthal orientation of the electric dipole moments for *s*-polarized illumination. While the excitation of this mode is largely independent of the direction of the incident wavevector, the excitation of a dark mode with radial symmetry under *p*-polarized illumination at 600 nm is suppressed for wavevectors oriented along the *y*-direction. This is in line with discussions of the suppression of a radial dark mode along this lattice direction. Fourier plane images calculated at 740 nm, corresponding to excitation of the bright mode, show a more uniform structure with no suppression of low spatial

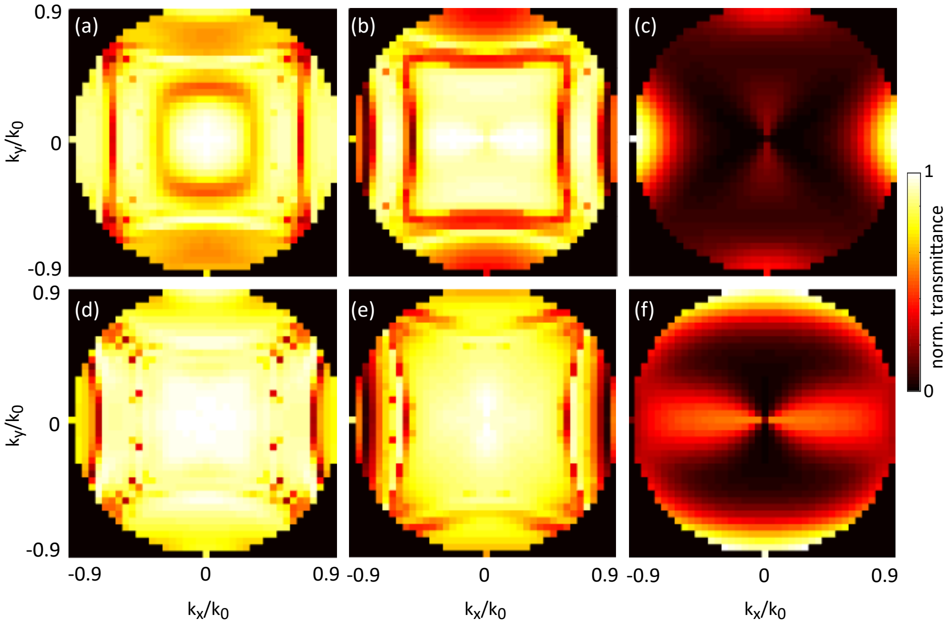

Figure 5.5: Calculated Fourier plane images in transmission for *s*- (top row) and *p*-polarized (bottom row) illumination at wavelengths of 580 nm (a,d), 600 nm (b,e) and 740 nm (c,f). Images normalized to their brightest pixel.

frequencies evident. It should be noted that Fourier plane features at high angles of incidence in Fig.5.4(a,b,d,e) are partly due to lattice diffraction. Owing to the sharp spatial signature of lattice diffraction, the demonstrated Fourier images cannot, however, be explained by their contribution alone. The corresponding calculated Fourier plane images in transmission are shown in Fig.5.5. At the wavelengths associated with excitation of the azimuthal and radial mode (580 nm, 600 nm), the modal features previously discussed for reflection are visible. However, in contrast to that seen in reflection, suppression of higher spatial frequencies is apparent while the metasurface shows strong transmission for normally incident illumination. The Fourier plane images at the excitation wavelength of the bright mode at 740 nm indicate strong suppression of transmission with little spatial dependence. The remaining angular dependence of the bright mode can be attributed to the spectral red shift of the bright mode as the excitation changes from the x-directions to the y-directions as discussed in Fig.5.3. In summary the complex spatial frequency dependance shown in the Fourier plane images in Figures 5.4 and 5.5 arises from the significant difference in coupling strength between unit cells in different directions and the contribution of effects associated with lattice diffraction as previously outlined.

5.3.2 Edge enhancement via subradiant mode excitation

We have numerically demonstrated the ability of nanotrimer arrays to filter low spatial frequencies in a reflected beam for p- and s-polarized illumination. While suppression of higher spatial-frequencies for transmitted light was also demonstrated, we focus on the discussion of low spatial frequency filtering in the following motivated by its application discussed in section 2.1.4. Based on the calculated Fourier plane images discussed above, we numerically demonstrate the image processing capability of the metasurface in the following.

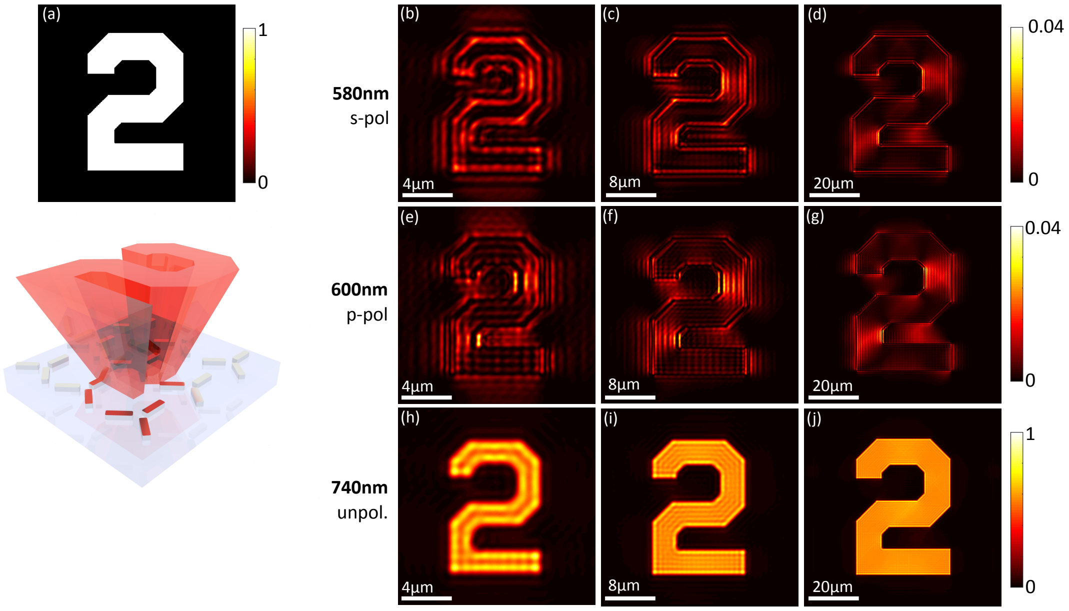

Figure 5.6: Calculated reflectance of an amplitude modulation in the shape of a figure ‘2’ with the intensity image shown in (a) from the radial trimer metasurface at the excitation wavelength of the azimuthal dark mode for s-polarized illumination (b-d), the excitation wavelength of the radial dark mode for p-polarized illumination (e-g) and at the excitation wavelength of the bright mode for unpolarized light (h-j) as a function of image size as indicated by the respective scale bars. Intensities in (b-j) are shown as fraction of the input intensity of the image in (a) for a numerical aperture of NA= 0.9.

The calculated complex reflection coefficients for both polarization states $r_s(k_x, k_y)$ and $r_p(k_x, k_y)$ of the metasurface serve as the optical transfer function and the filtered images are determined as previously in chapter 4 using eq.(2.20). Owing to the time-intense nature of FEM simulations calculation of one Fourier plane image took approximately 20 h thus not permitting calculation of the reflection coefficients with higher resolution. Instead a cubic convolution interpolation, as implemented in MATLAB R2020, was used to smoothen the results of the FEM calculation with the interpolation always passing through all original datapoints. An example of this approach is shown in Fig.A.12 in the appendix. Fig.5.6 shows the calculated reflectance of an amplitude image in the shape of a figure '2' from the metasurface for p- and s- polarized light.

From the images reflected at the dark mode wavelengths at 580 nm for s-polarization and 600 nm for p-polarization, enhanced edges with homogenous areas appearing darker are apparent. The images show, however, strong artifacts, particularly at 600 nm (Fig.5.6(e-g)) which can be attributed to the complexity, particularly the anisotropy, of the optical transfer functions of the radial trimer metasurface (c.f. Fig. 5.4). The degree of distortion strongly limits the complexity of images that can be processed using the radial trimer metasurface. In comparison the images calculated at the bright mode wavelength at 740 nm (Fig.5.6(h-j)) show good fidelity imaging of the object. Remaining artifacts arise from the non-zero angular sensitivity of the bright mode excitation as evident from Fig.5.4(c,f) as well as diffractive effects in the case of the 4 μm image. It should be noted that the intensity of the edge enhanced images at the excitation wavelengths of the dark mode lies below 4% of the incident intensity thereby indicating the risk of a low signal to noise ratio for experimental implementations.

5.3.3 Phase gradient visualization through subradiant modes

In section 2.1.5 the relationship between spatial-frequency filtering and the visualization of phase-gradients was introduced with an emphasis on the the requirements for the optical transfer function. From the investigation of the complex structure observable in the Fourier plane images of the trimer metasurface in Fig.5.4 it is apparent that the structure does not approximate a first- or second-order differentiator. This implied complex artifacts in edge-detection images as seen in Fig.5.6 above. The conversion of phase-modulations into intensity variations is generally more sensitive to the particular shape of the optical transfer function. For this reason phase-visualization with radial trimer metasurfaces can be expected to yield complex intensity patterns. In Fig.5.7 the reflected intensity for an incident wavefield with microscopic Gaussian shaped phase-modulation $E(x,y) = e^{i\phi(x,y)}$ is shown with $\phi(x,y) = \phi_{\max} \exp\big[-\big(\frac{x}{\sqrt{2}\sigma}\big)^2 - \big(\frac{y}{\sqrt{2}\sigma}\big)^2\big]$ for varying values of $\phi_{\max}$ and $\sigma = 5\,\mu$m. The resulting intensity distributions in Fig.5.7(b-i) are related to the incident phase modulation but form complex patterns from which it is not possible to reversely deduce the incident phase modulation precisely. From the investigated numerical data it does not seem possible to tailor the trimer metasurface in a way that yields a clean first- or second-order differentiator. For this reason we will not investigate the capacity of the device to visualize more complex phase gradients. In summary the results indicate strong limitations on the applicability of the device for biological phase imaging.

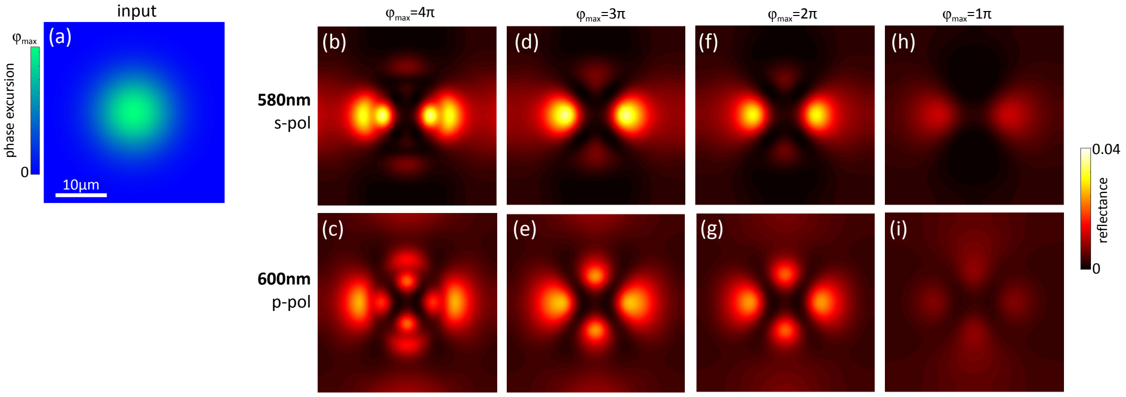

Figure 5.7: Calculated reflectance of a Gaussian shaped microscopic phase modulation (a) with maximum phase excursions of $\phi_{\max} = 4\pi$ (b,c), 3π (d,e), 2π (f,g) and π (h,i) for s-polarized illumination at 580 nm (top row) and p-polarized illumination at 600 nm (bottom row). Intensities are normalized to the Intensity of the input field. All images are calculated for an NA$= 0.9$.

5.3.4 Response to focussed linearly polarized light

So far we have discussed the optical response of the metasurface in terms of p- and s-polarized illumination. However, experimental illumination with linearly polarized light is most accessible. For this reason we use the results from Fig. 5.4 to calculate Fourier plane images for x- and y- polarized light when incident on a lens focusing the light onto the metasurface. References [228] and [229] based on which we derive equations yielding the reflectance $R_x(\sigma_x, \sigma_{xy})$ and $R_y(\sigma_x, \sigma_y)$ when the lens is illuminated with x-or y-polarized light respectively as given in equations (5.2). Here σ_x, σ_y denote normalized spatial frequencies k_x/k_0 and k_y/k_0. A detailled derivation of the equations is given in the appendix in section A.2.2.

$$R_x(\sigma_x,\sigma_y) = \frac{\sigma_x^2 R_p(\sigma_x,\sigma_y) + \sigma_y^2 R_s(\sigma_x,\sigma_y)}{\sigma_x^2 + \sigma_y^2} \tag{5.1}$$

$$R_x(\sigma_x,\sigma_y) = \frac{\sigma_y^2 R_p(\sigma_x,\sigma_y) + \sigma_x^2 R_s(\sigma_x,\sigma_y)}{\sigma_x^2 + \sigma_y^2} \tag{5.2}$$

where R_s and R_p describe the reflectance for s- and p-polarized light. Figure 5.8 shows the calculated Fourier images for x- and y- polarized input illumination at the wavelengths of dark- and bright-mode excitation. We expect significant experimental overlap between the two different dark modes due to their small spectral separation of approximately 20 nm and broadened plasmonic resonances compared to numerical results. For this reason the intensities of the dark modes at 580 nm and 600 nm have been averaged in Fig.5.5.

5.3.5 Spatial frequency filtering with linearly polarized light

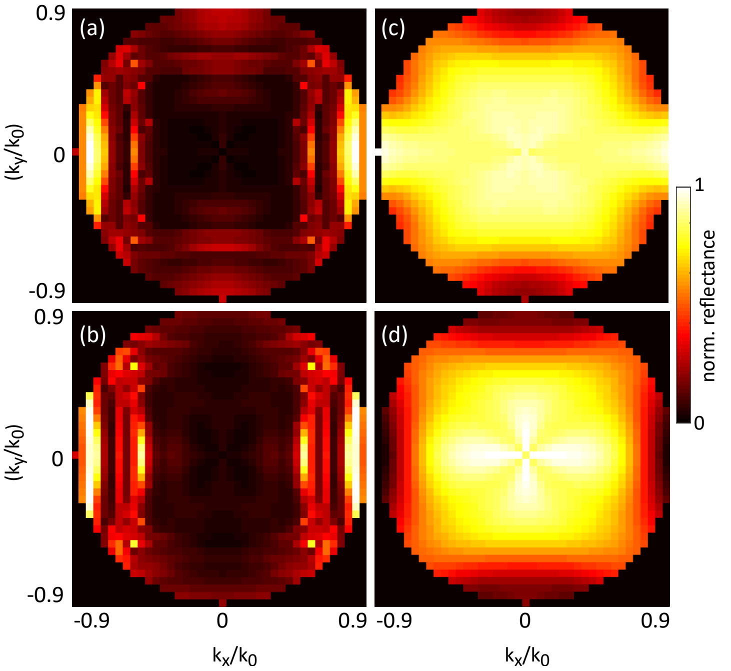

Figure 5.8: Calculated averaged Fourier plane images in reflection for x- (a,c) and y-polarized (b-,d) illumination at the dark- (a,b) and bright-mode (c,d) wavelengths. Images normalized to their brightest pixel. Reprinted with permission from [61], copyright The Optical Society.

Based on the results obtained for s- and p- polarized illumination complex Fourier plane images are expected for x- and y- polarized linear illumination as well. From Figure 5.8a,b we can again observe suppression of low spatial frequencies in reflection as anticipated for dark mode excitation with minor differences in the sensitivity to angle of incidence between x- and y-polarization. The excitation of the bright mode on the other hand shown in Fig.5.8c,d is again associated with strong reflection at low spatial frequencies for both polarizations.

5.4 Experimental results

In the following we will experimentally investigate the excitation of dark modes on the nanotrimer metasurface and evaluate its spatial frequency filtering capability.

5.4.1 Detection of subradiant mode excitation

The reflectance from the metasurface was experimentally measured using the optical setup shown in Fig. 5.9. The light emitted by a tungsten-halogen bulb (Ocean Optics HL-2000)

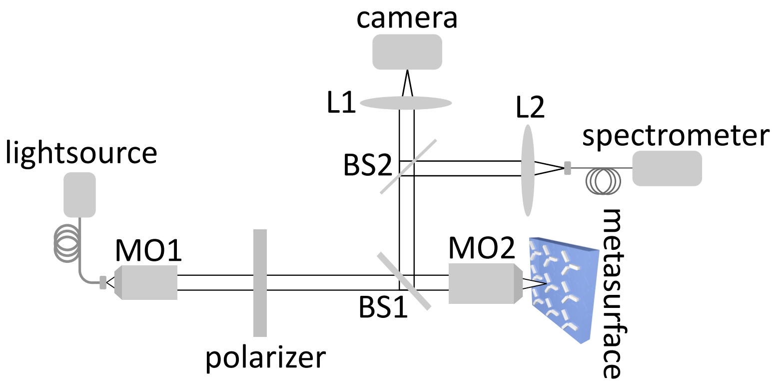

Figure 5.9: Experimental setup for the measurement of reflectance spectra and Fourier plane images in reflection of the radial trimer metasurface. Adapted with permission from [61], copyright The Optical Society.

was collimated by a NA 0.3 Nikon LU Plan Fluor objective and sent through a linear polarizer. Subsequently the light was transmitted through an infinity corrected NA 0.90 Nikon Plan NCG x100 objective to illuminate the metasurface. Due to the high numerical aperture of the illuminating objective, the sample is illuminated with a broad range of incident angles. While the light incident on the NA 0.90 Nikon Plan NCG x100 objective was linearly polarized in either the x- or y-direction, the illumination of the metasurface will consist of a superposition of $s-$ and $p-$ polarized light. The resulting complex incident angular spectrum is described by eq.(5.2) based on [228, 229]. Subsequently the reflected light was guided via a beam splitter (BS1, Thorlabs CM1-BS013) and a thin film beam splitter (BS2, Thorlabs BSW013) to a spectrometer (Ocean Optics QE65000) where reflection spectra were captured. The measured spectra shown below were normalized to spectra obtained from an unpatterned region of the sample.

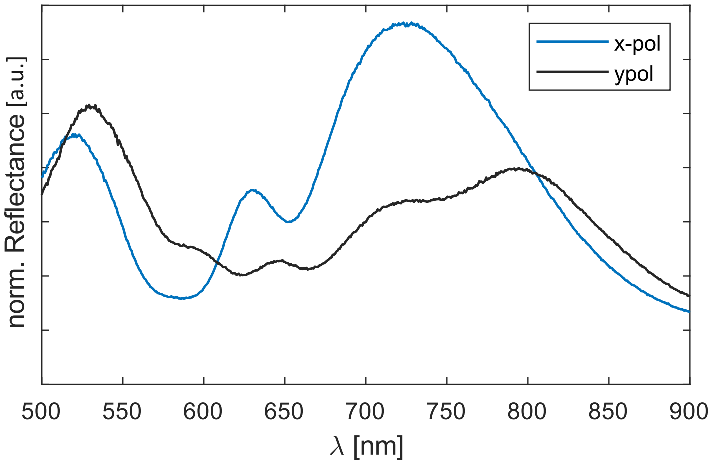

Figure 5.10: Measured reflectance of the radial trimer metasurface for x- (blue) and y-polarized (gray) illumination using an infinity corrected NA 0.90 Nikon Plan NCG x100 objective. Reflectance normalized by reflectance from unpatterned region of the glass substrate. Adapted with permission from [61], copyright The Optical Society.

Figure 5.10 shows the normalized reflectance spectra for x- and y-polarized illumination. For both polarizations two broad peaks at wavelengths longer than 700 nm and near 550 nm are apparent. We can assign these to the excitation of dipole modes along the long and short axis of the trimer rods respectively in line with the numerical results from Fig.5.3. Lattice diffraction also contributes to the peaks around 550 nm. In addition to the dominant dipole resonances, the spectra show weaker features around 630 nm (for x-pol. illumination) as well as near 600 nm and 640 nm (for y-polarized illumination). They appear between the long- and short-axis dipole excitations where dark mode excitation was observed in Fig.5.3. We thus hypothesize that these peaks are associated with the excitation of one or both dark modes identified in the numerical calculations above.

5.4.2 Experimental Fourier plane analysis

In order to test this assumption, Fourier plane images of the metasurface in reflection were recorded. The setup shown in Fig.5.9 was used with the spectrometer beamsplitter (BS2) removed in order to reduce back reflections. The back focal plane of the objective (NA 0.90 Nikon Plan NCG x100) was imaged onto the camera using a $f = 50\,\mathrm{mm}$ lens (Thorlabs LA1131-A). Instead of the halogen lamp light source, a supercontinuum laser source (Fianium Superchrome VISFDS-MM) set to the minimum bandwidth of 10 nm (FWHM) was used to record Fourier plane images as a function of the illumination wavelength.

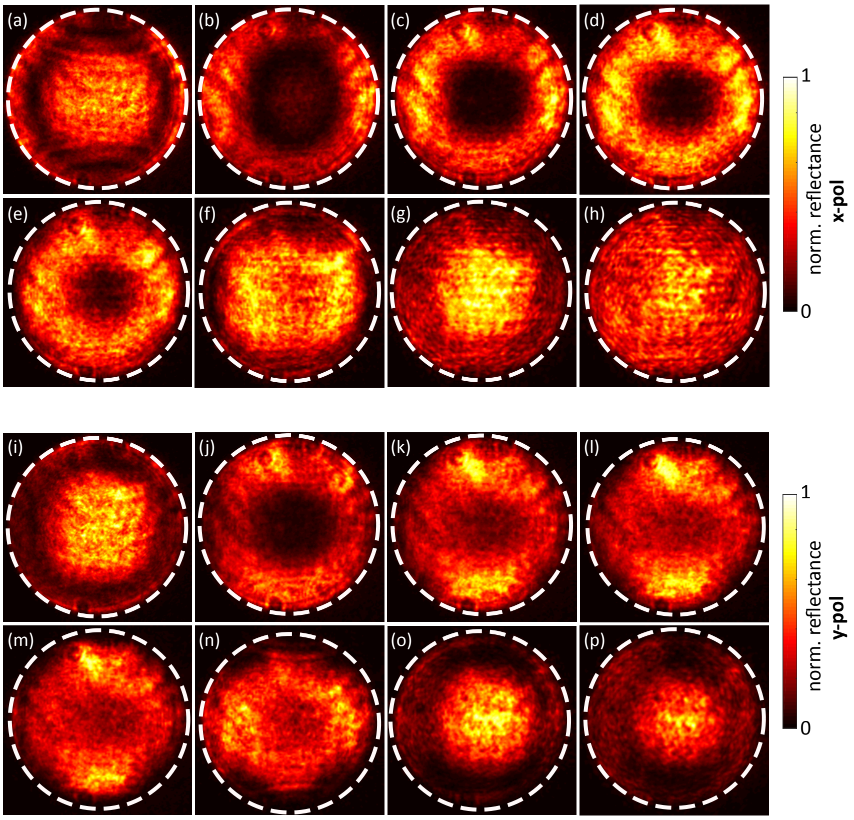

Figure 5.11: Normalized Fourier plane images recorded using x- (a-h) and y-polarized light (i-p) with central wavelengths at 549 nm (a,i) 597 nm (b,j) 616 nm (c,k) 626 nm (d,l) 635 nm (e,m) 654 nm (f,n) 714 nm (g,o) and 741 nm (h,p). All images normalized to their brightest pixel with dashed lines indicating NA= 0.9. Adapted with permission from [61], copyright The Optical Society.

For illumination with x-polarized light (Fig.5.11(a-h)), the Fourier plane images recorded at the wavelengths where we expect dark mode excitation (Fig.5.11(c,d)) show suppressed reflectance at low spatial frequencies in line with the characteristics of subradiant mode excitation seen in Fig.5.4. We attribute residual reflectance at low spatial frequencies at these wavelengths to contributions from the dominant bright mode and background reflections from the glass-air interface. For wavelengths longer than 714 nm (Fig.5.11(g-h)) one can observe a more uniform reflectance with a decrease in reflectance towards higher spatial frequencies in line with the characteristics derived for bright mode excitation. A similar pattern is apparent at wavelengths around 549 nm (Fig.5.11(a)) with additional characteristic diffraction lines confirming the presence of the bright mode with dipoles oriented along the short axis of the nano rods.

Considering illumination with y-polarized light (Fig.5.11(i-p)) at wavelengths associated with the excitation of radiant modes (Fig.5.11(i),(o-p)) a similar pattern as that observed for x-polarized light is apparent with strong reflectance at low spatial frequencies and declining reflectance for higher spatial frequencies. Suppression of low spatial frequencies is evident between approximately 597 nm and 654 nm (Fig.5.11(j-n)) where dark mode excitation was assumed for this polarization based on the spectral measurements from Fig.5.10. The residual reflection at low spatial frequencies is, however, higher for $y-$polarized light than for x-polarized light. Direct identification of the two assumed dark-mode features from the spectral measurements in the Fourier plane measurements was not possible for $y-$polarized light. We attribute the appearance of this double peak to the stronger coupling between unit cells in y-direction than in x-direction as discussed previously.

In summary the analysis of Fourier plane images experimentally confirms the excitation of one or both subradiant modes on the nano trimer metasurface. The results experimentally confirm the ability of the device to suppress reflection at low spatial frequencies at wavelengths associated with subradiant mode excitation. Due to imperfections of the fabricated metasurface and the small spectral separation between both modes, Fig.5.11 does not permit precisely distinguishing between the Fourier plane signatures associated with the excitation of the two different subradiant modes.

5.4.3 Edge enhancement in reflected amplitude images

Given the numerical results (*cf.* Fig.5.6) we expect the device to be able to perform edge enhancement in an amplitude image reflected from the device. The associated measurements are, in principle, equivalent to those performed in chapter 4 where edge enhancement was demonstrated using a Salisbury screen with the system shown in chapter Fig.4.15. Modification of the setup in terms of the telescope system consisting of MO2 and L1 was required due to mechanical limitations which will be discussed further. Previously the Salisbury screen was cut into a small piece and directly mounted into the cage system of the setup itself. This supported the fine alignment of the sample perpendicular to the propagation axis of the incident beam. The nanotrimer metasurface with a total size of about $150 \times 150\,\mu$m on the other hand was fabricated as one of a series of metasurfaces on a microscope glass slide. Mechanical separation of the metasurfaces is, therefore challenging and carries a high risk of damaging the glass substrate. This firstly prohibits mounting the sample direclty into the cage due to the size of the glass slide. Secondly shifting the sample in the x- or y-direction was required in order to project the image onto the desired metasurface. Hence, mounting the sample on a free-standing separate stage was necessary. The alignment precision of the sample in this configuration perpendicular to the propagation axis of the incident beam is limited. This limits the degree to which the image can be demagnified for the purpose of spatial frequency mapping in the telescope system while maintaining focus. This is particularly the case, when micrometer sized images are to be reflected from the sample as it is the case here. For this reason a lower demagnification of the image was selected through the replacement of MO2 by an Olympus Uplan FLN, NA0.75 40x and L1 by 75 mm plano convex LA1608-A thus yielding a demagnification of ≈ 17.

Furthermore a shift of the dark mode feature by approximately 15 nm towards the blue spectral range compared to the results shown in Fig.5.11 was detected when a series of Fourier plane images of the metasurface was recaptured (*cf.* Appendix Fig. A.6). We attribute this to two factors. Firstly a temporal gap of approximately one year lay between the results demonstrated above and the following experimental demonstration of edge enhancement. This temporal gap is believed to have led to degradation of the sample over this time. Specifically oxidation of silver nanorods due to oxygen diffusion through the protective PMMA layer could be the reason. Secondly a conductive coating (30 nm of chromium) had to be deposited on the sample prior to investigation in the SEM after the Fourier measurements in Fig.5.11 had been completed, and was removed subsequently exposing the sample to chromium etchant solution, sulfuric acid and distilled water throughout the process. This chemical treatment can cause slight changes in the dielectric environment resulting in shifts of the plasmonic resonances. While this was outside of the scope of this work, future studies could employ methods such as Energy-dispersive X-ray spectroscopy to detect such chemical changes in the device structure, which would allow further assessment of their longevity.

Figure 5.12(a-d) show Fourier plane images of the metasurface in reflection recorded using the Olympus Uplan FLN, NA0.75 40x Objective at 611 nm and corresponding line plots in the horizontal and vertical direction. For both polarization states the device operates over the entire numerical aperture of the MO with NA= 0.75. The filtering contrast is higher for $x-$ polarized light ($C_s \approx 0.8$, along both directions) than for $y-$polarized light ($C_s \approx 0.5$, along $k_x = 0$) as can be seen from Fig.5.12(b,d). No high-pass filtering along $k_y = 0$ is apparent for $y-$polarized light (Fig.5.12(d)).

In Fig.5.12(e-g) an amplitude image of a micron sized figure '2' reflected from the sample is shown. The result from Fig.5.12(e) confirms the 2D low spatial frequency filtering capability of the structure in reflection for x-polarized illumination. For y-polarized illumination on the other hand (*cf.* Fig.5.12(e)) the filtering capability at this wavelength is observed only weakly and only in the y-direction and with lower contrast, in line with previous findings. For the image reflected from the unpatterned region of the sample, no edge enhancement can be observed.

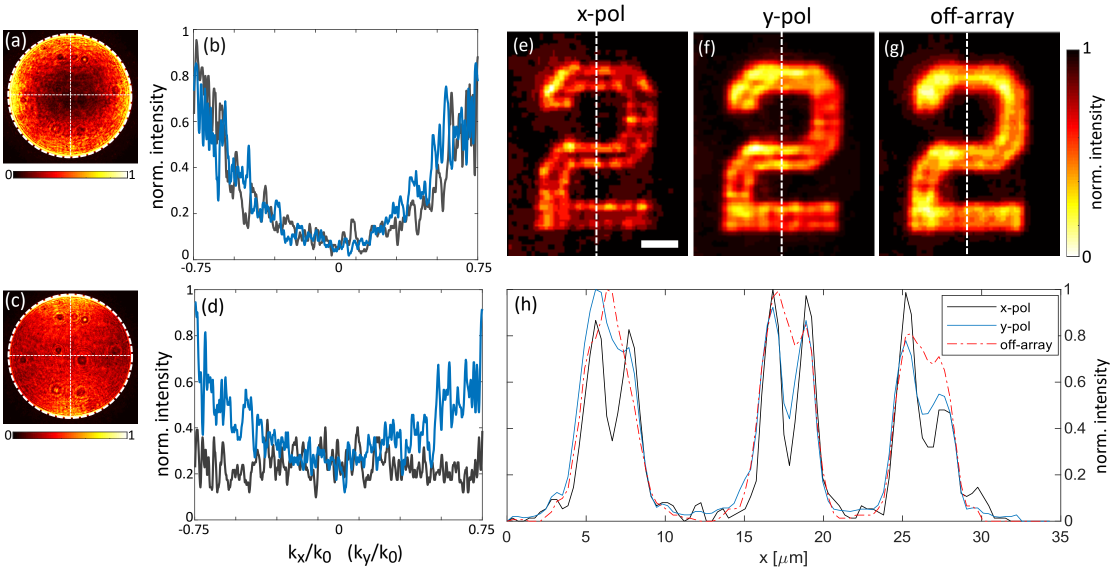

Figure 5.12: Experimental demonstration of edge enhancement of an image reflected from the radial trimer metasurface at λ =611 nm. (a,c) Fourier plane images in reflection for x- and y-polarized light with dashed circles indicating NA= 0.75 and with corresponding line plots shown in (b,d) in vertical (blue) and horizontal direction (gray). Images reflected from the metasurface for x-(e) and y-polarized light (f) with reference of image reflected from unpatterend region of sample under x-polarized illumination (g). Line plot along dashed lines in (e-g) averaged over 4.5 μm for noise reduction. Scalebar is 5 μm.

While experimental Fourier images showed a higher degree of uniformity than their numerical counterpart, significant noise in the Fourier images (Fig. 5.12(a-c) placed limitations on the quality of the obtained reflected images. Additionally a comparably low signal-to-noise ratio of the recorded images further decreased the image quality. This result is in line with the numerical calculations in Fig.5.6 that indicate a maximum contrast of around 5% between the edges and homogenous areas of the image in the reflected intensity. For these reasons the investigation of the device as a spatial frequency filter was concluded at this point and the experimental demonstration of phase-gradient detection, while in principle possible, is outside of the scope of this thesis.

5.5 Summary and Conclusion

In conclusion, we have numerically and experimentally demonstrated the presence of subradiant modes on a plasmonic metasurface. We have numerically identified two different subradiant modes of nanotrimer unit cells and investigated their ability to filter spatial frequencies in reflection and transmission with high numerical aperture. In particular, the suppression of low spatial frequencies in reflection demonstrated in this chapter opens up the potential for the device, or other devices based on similar principles, to perform all-optical edge-detection and conversion of phase gradients in incident wavefields into intensity modulations. Complex polarization dependent effects in Fourier plane images associated with the coupling between unit cells of the metasurface array were identified. These indicate the intriguing possibility of further tuning the array structure of the device to engineer its spatial frequency filtering capabilities. However, lattice effects resulting in anisotropic spatial frequency filtering also place limitations on the flexibility of the plasmonic metasurface as a pathway towards all-optical image processing. In particular, it was discussed that the device does not resemble a first- or second-order differentiator.

The ability of the metasurface to perform edge enhancement in an amplitude image and conversion of a phase gradient into an intensity modulation was numerically demonstrated. In line with expectations the complex optical transfer function of the metasurface caused significant distortions and anisotropies in the filtered images. The visualization of phase-gradients in particular yielded complex intensity distributions from which a reconstruction of the incident phase modulation seems practically impossible. This is in agreement with the complex dynamics governing phase to intensity conversion upon spatial differentiation as discussed in section 2.1.5.

The excitation of subradiant modes on the metasurface was experimentally demonstrated through illumination with a high-NA objective (NA= 0.9). Characteristic signatures of dark mode excitation confirmed the broad conclusions of the numerical results. The quality of the presented data was, however, not good enough to be able to distinguish between details associated with the excitation of different subradiant modes. This is partly attributed to fabrication imperfections that inevitably occur during the process of electron beam lithography. Secondly the bandwidth of the available laser system limits the ability to distinguish between signatures of different subradiant modes due to their small spectral separation and experimentally broadened plasmonic resonances. In future experiments additional spectral filters or a light source with narrower bandwidth could overcome this particular limitation.

Experimentally, edge enhancement in an amplitude image of the size of approximately $20 \times 20\,\mu$m reflected from the metasurface was demonstrated. Due to the polarization dependance, strong contrast could be achieved for polarization of the light incident on the objective polarized along only the x-axis. Finally, the use of subradiant modes on optical metasurfaces was demonstrated to provide an avenue for all-optical, ultracompact spatial frequency filtering. Limitations of the spatial frequency filtering capability of the device were seen. While experimental imaging of phase gradients through subradiant mode excitation will in principle be possible, the previously discussed complexity of the resulting intensity distribution of converted phase-gradients ultimately places strong limitations on the applicability of the device.

While here we have focussed on nanotrimer unit cells, various other nanostructures have been demonstrated to support subradiant resonances including disc ensembles, ring-disc combinations and other rod arrangements [79, 90, 93] (*cf.* section 2.4.3). The capacity of these structures, and potentially combinations of them, to perform all-optical processing of images is yet to be theoretically and experimentally investigated and should be the subject of future research. Investigation of subradiant modes, or bound modes in the continuum (BIC), on dielectric metasurfaces has recently gained increased attention

[230–232]. These modes usually yield sharper resonances and may permit better mode discrimination. Future research could therefore also include subradiant modes on dielectric nanostructures to engineer optical transfer functions [109].

Chapter 6

Resonant Wave Guide Gratings as Spatial Frequency Filters

The previous chapters of this thesis focused on photonic nanostructures enabling spatial frequency filtering in reflection. However, for most applications, particularly biological imaging applications, a device that performs filtering in transmission is essential. Past research has indicated that resonant wave guide gratings (RWG) have characteristics that make them suitable candidates for ultra-compact devices that can perform spatial frequency filtering operations on a transmitted wavefield as reviewed in section 2.6.2 of this thesis. In this chapter we investigate how we can capitalize on the angular filtering capability of RWG's and engineer a device that holds potential for biological imaging applications. Due to the transmitting mode of operation RWGs could be integrated into a generic microscope coverslip in order to optically perform image processing operations using existing microscopy setups. For this reason we will also refer to this device as a metasurface enhanced coverslip (MEC) in the following. A provisional patent application has been filed for the results presented in this chapter under

A. Roberts, T. J. Davis, and L. Wesemann. 'Electromagnetic Filter Device and Method of Use.' *Australian Provisional Patent Application*, Appl. no. 2019904670, in the name of The University of Melbourne, December 2019.

6.1 Introduction

The term resonant waveguide gratings describe a range of resonant nanostructures incorporating subwavelength gratings that support leaky guided modes [164] as introduced in section 2.6.2. Here we confine ourselves to metallic gratings on top of dielectric slab waveguides as depicted in Fig. 6.1.

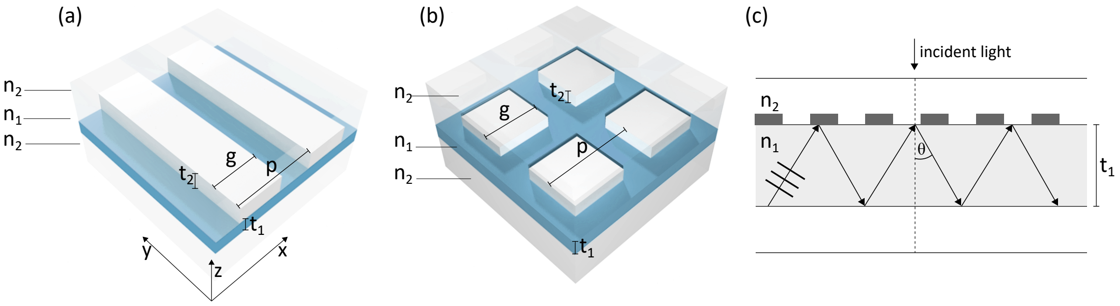

Figure 6.1: Exemplary resonant wave guide grating (RWG) structures with (a) a one-dimensional and (b) a two-dimensional grating on top of a dielectric slab waveguide. The design parameters of the devices are the thickness t_1 and refractive index n_1 of the slab waveguide, the thickness t_2 and dielectric function ϵ_g of the grating material, the width of the grating elements g, the grating period p as well as grating duty cycle g/p and the refractive index of the sub and superstrate n_2. (c) Grating coupler on top of dielectric slab waveguide with made of dielectric materials with refractive indices n_1,n_2 and mode propagation angle θ in the ray picture.

It is well known that a given symmetric slab waveguide (*cf.* Fig.6.1(c)) consisting of a dielectric layer of thickness t_1 and refractive index n_1 between media of lower refractive index $n_2 < n_1$ can support a number of propagating electromagnetic modes at a given frequency $\omega_{\mathrm{cut}} < \omega$ above a cutoff frequency that is specific to the slab waveguide [233]. The transverse electric (TE) and transverse magnetic (TM) modes for a particular waveguide configuration can be determined by solving its characterstic transcendental eigenvalue equations. For a symmetric dielectric slab waveguide these are given for TE and TM modes respectively by

$$\tan(\kappa d) = \frac{\gamma}{\kappa} \tag{6.1}$$

$$\tan(\kappa d) = \left(\frac{n_1}{n_2}\right)\frac{\gamma}{\kappa} \tag{6.2}$$

with $\kappa = \sqrt{n_1^2 k_0^2 - \beta^2}$, $\gamma = -\sqrt{n_2^2 k_0^2 - \beta^2}$, $d = t_1/2$, k_0 the wavenumber and β the propagation constant for the particular mode [234]. For a given propagation constant we can determine the associated propagation angle θ_{mod} of the mode in the ray picture from $\cos(\theta) = \beta/kn_1$. The basic working principle of a RWG is to place a grating on top of this waveguide such that an incident electromagnetic field couples into the waveguide modes.

The simplest model to describe a RWG is to consider its waveguide and grating component independently as discussed in [164]. In this model we can then employ the well known grating equation to determine at which angle of incidence θ_{inc} a given diffraction grating will produce orders with propagation angles that match the propagation angle θ_{mod} of a particular mode of the slab waveguide.

$$\theta_{\text{inc}} = \left| \sin^{-1}\left(\frac{n_2}{n_1} \sin\left(\theta_{\text{mod}}\right) + \frac{m\lambda}{n_1 p} \right) \right| \tag{6.3}$$

As an example we assume a symmetric slab waveguide of thickness $t_1 = 100\,\text{nm}$ and refractive index $n_1 = 2.25$ embedded in a dielectric with refractive index $n_2 = 1.5$. In the wavelength regime considered $\lambda \in [500\,\text{nm}, 750\,\text{nm}]$ the waveguide supports one TE_0 and one TM_0 mode as solved by [235]. In Fig.6.2 the angle of incidence θ_{inc} required for light diffracted by the grating to couple into the waveguide mode is shown as a function of the wavelength λ for three different grating periods p. It is now reasonable to assume that

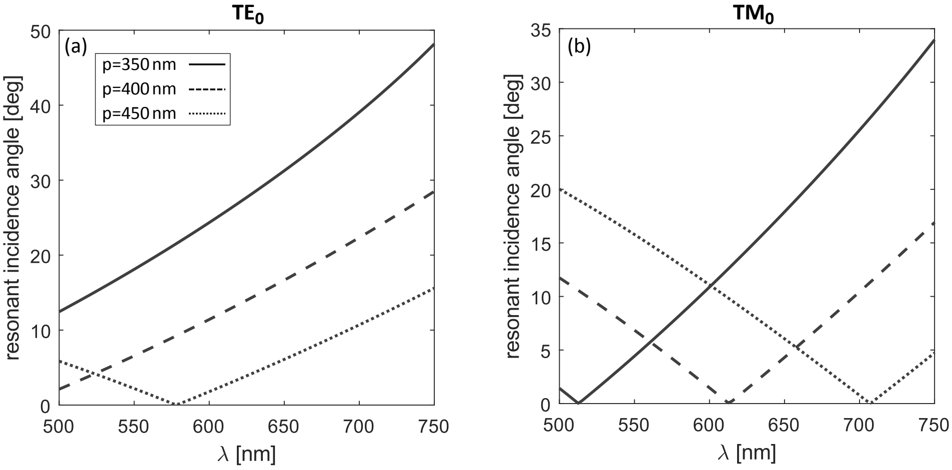

Figure 6.2: Resonance angle θ_{inc} of the RWG as a function of free space wavelength λ for (a) the TE_0 and (b) the TM_0 mode based on the model described in eq.(6.3). Calculated results are shown for gratings of period $p = 350, 400$ and $450\,\text{nm}$.

excitation of a mode will be associated with a fraction of the incident energy travelling in a lateral direction and thus not transmitted through the RWG. For this reason the qualitative considerations above indicate that a RWG should, in principle, enable angular filtering in transmission.

While the above model qualitatively explains the basic working principle of RWGs it has, of course, serious limitations that we now review. First of all the model makes no quantitative statements about reflection and transmission coefficients of the structure. Secondly the assumption that the waveguide and grating component can be treated independently is generally incorrect since the presence of a metallic grating will significantly alter the dispersion properties of the waveguide. Furthermore, the model does not take the specific profile of the grating into account. The grating itself will exhibit resonances, particularly plasmonic resonances in the case of a metallic grating. Finally complex crosstalk between the grating resonances and the waveguide modes will generally be present but is not taken into account.

The utilization of dielectric RWG-type structures as transmitting spatial frequency filters was studied by other authors previously. In the literature review in section 2.6.2 we reviewed the different approaches implementing transmitting one-dimensional [48, 49, 166] and two-dimensional [55] spatial frequency filters. Recently two-dimensional filtering in transmission was for the first time experimentally demonstrated using a dielectric photonic crystal structure [51]. While the studies above are exclusively based on dielectric structures, an approach utilizing a plasmonic grating was demonstrated parallel to our research for the first time [167]. This study by Yang et al. investigates one-dimensional spatial frequency filtering with a gold grating on top of a quartz substrate through the excitation of grating SPP resonances without the addition of the dielectric waveguiding layer. This role is played by the grating itself. The use of plasmonic nanostructures generally implies higher losses than dielectric structures, which can aid in the suppression of light associated with particular spatial frequencies. Here we extend the concept of using plasmonic resonant waveguide gratings for spatial frequency filtering to two-dimensional devices for the first time. Furthermore we investigate the visualization of phase-gradients in a wavefield via transmission through the filter device, which was not included in any of the previous studies above and is one of the major findings of this thesis. Various approaches for numerical modeling of the filter devices were investigated. Golovastikov et al. have derived an analytical method to approximate the complex coupling dynamics between grating and slab waveguide [48] while other authors use full-field simulations such as the FDTD (Finite Difference Time Domain) method [51]. Here we choose another full-field approach, the Finite Element Method, as introduced in section 3.1.1 in order to quantitatively model resonant wave guide gratings as transmitting spatial-frequency filters.

6.2 Numerical modeling of Resonant Waveguide Gratings

In the following section we will numerically investigate the impact of the design parameters of RWG on their spatial frequency filtering capability in transmission. Here we investigate one-dimensional grating structures and also expand the principle to two-dimensional plasmonic gratings enabling high-pass spatial frequency filtering in both directions. We will investigate the particular case of one- and two-dimensional Ag-gratings on high-dielectric index slab waveguides consisting of TiO_2. The resonant wave guide structure was numerically modeled using the finite element method (FEM, *cf.* section 3.1.1) as implemented in COMSOL Multiphysics 5.5 with RF module. The metasurface was modeled using periodic boundary conditions in the transverse direction and port boundary conditions terminating the model at the upper and lower boundary of the model. Electromagnetic waves are launched into the model via the port on the upper boundary of the model. A mesh with a maximum element size of 15 nm was used to resolve the silver patches and the titanium dioxide layer. The mesh was locally adapted where increased spatial meshing was required. The optical properties for silver were taken from [76]. The refractive index of TiO_2 thin-films typically varies substantially due to differences in the chemical stochiometry originating from the specific parameters used in the fabrication process [236, 237]. Throughout this thesis constant evaporation parameters as specified in the experimental part of this chapter were used. Based on spectral reflectance measurements using a Filmmetrics F20 tool a refractive index of $n_{\mathrm{TiO2}}(\lambda = 633\,\mathrm{nm}) = 2.25$ was determined and used as a non-dispersive refractive index for the numerical calculations in the following. This is a typical value for evaporated TiO_2 films as shown in Fig.A.7 in the appendix where reported refractive indices [236, 237] of TiO_2 thin-films are shown for comparison. The reported values are situated between approximately $n = 2.1$ and $n = 2.5$ in the wavelength interval $[500, 750]$nm in line with the results for the sample fabricated here. The array is assumed to be embedded in a homogeneous environment of refractive index $n = 1.5$ simulating a glass substrate and a PMMA superstrate.

6.2.1 Suppression of transmission

In a first step we demonstrate the ability of one- and two-dimensional plasmonic RWG's to suppress transmission at normal incidence using the implemented FEM model. In Fig. 6.3 the transmittance of devices with varying grating periodicity is shown for the electric field polarized along the $y-$ direction with the coordinate system as defined by the inset.

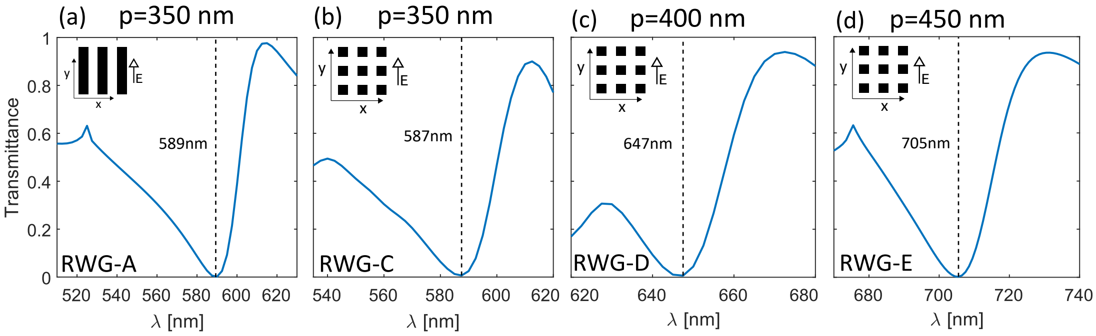

Figure 6.3: Transmittance through resonant wave guide gratings (RWG) with one- and two-dimensional gratings as a function of grating period p and wavelength λ for normally incident light polarized along y-direction as defined by the insets. Shown are the calculated results for devices RWG-A with a one dimensional grating (a), and two-dimensional grating structures RWG-C (b), RWG-D (c) and RWG-E (d) with parameters as summarized in table 6.1.

Strong suppression of transmission at normal incidence in the visible wavelength regime is apparent with the wavelength of minimum transmittance λ_c shifting towards longer wavelengths as the grating period p increases in line with expectations from the qualitative model discussed above. For exemplary one- and two-dimensional gratings with periods of $p = 350\,\text{nm}$, $400\,\text{nm}$ and $450\,\text{nm}$ the transmittance is reduced to below 1% for one- and two-dimensional gratings.

In Fig.6.4(a,e) the excitation of TE and TM waveguide modes at the wavelength of minimum transmission is shown for a RWG device with one-dimensional grating (RWG-A).

Illumination with $s-$polarized light indicates excitation of TE waveguide modes, while illumination with $p-$polarized light excites TM waveguide modes. At oblique incidence (Fig.6.4(b)) the incident light does not couple into the waveguide for which no significant suppression of transmission occurs. For devices with thicker waveguide layers (Fig.6.4(c,d,f)) higher order TE and TM modes are excited for normally incident light.

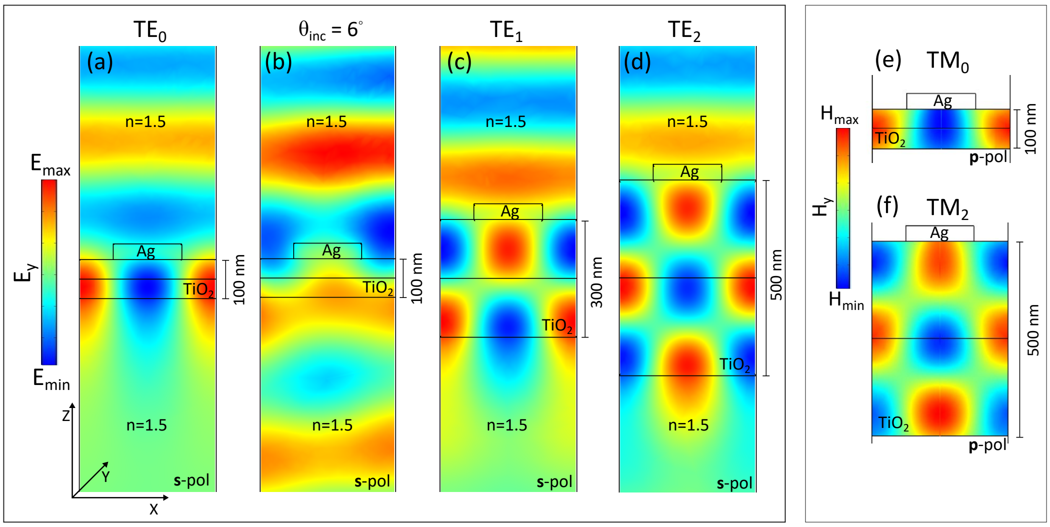

Figure 6.4: Coupling into TE and TM waveguide modes of resonant waveguide grating with period $p = 350\,\text{nm}$ as a function of TiO_2 slab thickness and angle of incidence at $\lambda = 589\,\text{nm}$. (a-d) Shown is the E_y component of the electric field for incident $s-$polarized light with the electric field along $y-$direction. (a) Excitation of TE_0 mode in RWG-A for illumination with normally incident light, (b) At oblique incidence ($\theta = 6°$) no waveguide mode is excited (c,d) Excitation of higher-order TE-modes at normal incidence for increased layer thicknesses of 300 nm and 500 nm. (e,f) Shows H_y component of the magnetic field indicating excitation of TM modes for incident $p-$polarized light with the magnetic field along $y-$direction and waveguide layer thicknesses of 100 nm (RWG-A) and 500 nm.

In the following we will investigate the spatial frequency filtering capability of the devices in transmission. For the purpose of demonstrating the functionality of the devices, suitable parameters were chosen for the calculations in Fig.6.3 based on numerical parameter scans. A detailed description of the the impact of the grating geometry on the spatial frequency filtering performance is given in the appendix in section A.3.2. In summary, the thickness of the waveguide layer was kept constant at a typical value of $t = 100\,\text{nm}$ and variations of the grating duty cycle and grating thickness were investigated with the aim of finding a reasonable compromise between suppression of low spatial frequencies and filtering contrast. The selected parameters are summarized in table 6.1. It should be emphasized that for specific applications other parameters could yield improved performance. However due to the time-intense nature of finite element method simulations, we here proceed with the derived parameters since the resulting performance is sufficient to demonstrate the relevant characteristics of resonant wave guide gratings as transmitting all-optical spatial frequency filters.

ID	type	unit cell	p [nm]	g/p	t_1 [nm]	t_2 [nm]	λ_0 [nm]
RWG-A	1D	beam	350	0.5	100	40	589
RWG-B	1D	beam	400	0.5	100	40	650
RWG-C	2D	square	350	0.6	100	40	587
RWG-D	2D	square	400	0.6	100	40	647
RWG-E	2D	square	450	0.6	100	40	705

Table 6.1: Geometric parameters of resonant wave guide gratings RWG-A,B,C,D and E investigated in the following. Shown for one- and two-dimensional gratings are unit cell type, grating period p, grating duty cycle g/p, thickness of the TiO_2 layer t_1 and the silver grating t_2 and the resulting calculated absorption wavelength λ_0.

6.2.2 Spatial Frequency Filtering

After suitable parameters for the resonant waveguide gratings were found above, the following section is concerned with determining the two dimensional optical transfer function of the devices. Initially we will investigate the properties of one-dimensional gratings (device RWG-A and B) followed by a discussion of two-dimensional structures (devices RWG-C,D,E). In the following we will refer to the characteristics of the filter functions, namely contrast C_s and numerical aperture NA, as introduced in section 2.1.7.

6.2.2.1 One-dimensional resonant wave-guide gratings

Fig.6.5 shows calculated Fourier plane images for device RWG-A. For p- as well as s-polarization broad suppression of transmission is apparent along $k_x = 0$ with the exception of increased transmission in the vicinity of $k_y = 0.4$. For the resonant waveguide gratings investigated in this chapter cross-polarization can be neglected for which it is not included in the following calculations. For the perpendicular direction along $k_y = 0$ a steep increase in transmission with an NA$= 0.05$ and contrast $C_s = 0.999$ is apparent for s-polarized light. For p-polarized light the structure exhibits a broader suppression of transmission with an NA $= 0.20$. Hence, the one-dimensional grating structure acts as a polarization dependent and directional high-pass spatial frequency filter. This indicates potential for ultra-compact image processing approaches that are optically switchable through the choice of the polarization state.

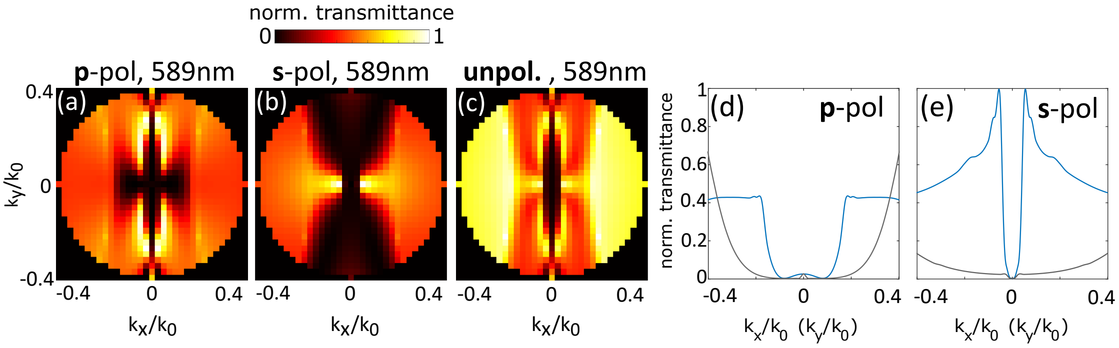

Figure 6.5: Fourier plane images in transmission of resonant waveguide grating with a one-dimensional grating (RWG-A) with period $p = 350\,\text{nm}$ at wavelength $\lambda = 589\,\text{nm}$ for p-polarization (a), s-polarization (b) and unpolarized light (c). Images are normalized to their brightest pixel. Lineplots through $k_x = 0$ (gray) and $k_y = 0$ (blue) in (d,e) respectively.

Calculation of the Fourier plane images (*cf.* Fig.6.5 and Fig.6.7) is computationally intense and took on average 20 h per Fourier plane image using the available high-performance computer with specifications as described in section 3.1.1. A higher resolution was thus not achievable with reasonable computation time. For the image processing calculations the transfer functions were smoothened via cubic-spline interpolation. An example of a Fourier plane image with increased resolution and the corresponding low-resolution counterpart is shown in the appendix in Fig.A.12.

As discussed in the introduction to this thesis, for edge detection the suppression of low spatial frequencies is usually sufficient in order to highlight edges and suppress the intensity in homogenous image parts. However, for phase visualization, the particular mathematical operation represented by the optical transfer function has a major impact on the resulting intensity distribution. In Fig.6.6 we investigate the amplitude $|t| = \text{abs}(t)$

and phase component $\varphi = \arg(t)$ of the optical transfer function $t(k_x, k_y) = |t|e^{i\varphi}$ of device RWG-A for s-polarized light along the filtering direction of the device (along $k_y = 0$), that was here calculated with increased resolution for the relevant interval.

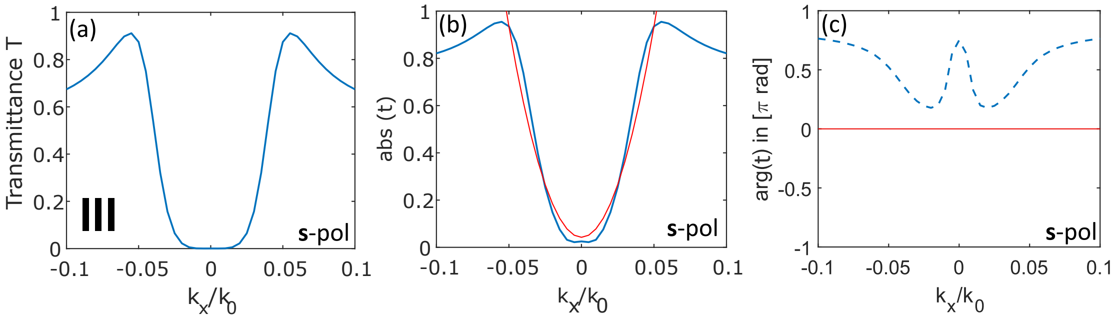

Figure 6.6: Comparison between the one-dimensional resonant wave guide grating RWG-A and a second order differentiator for s-polarization. Calculated results for the magnitude (b) and phase (c) of the transmission coefficient of device RWG-A at $\lambda = 589\,\text{nm}$ along $k_y = 0$ shown in blue with the respective fit of $H = a_1(k_x/k_0)^2 + a_2$, determined over the NA of each filter function, shown in red. Fitting parameters a_1, a_2 provided in table A.2 in the appendix. Transmittance $T = |t|^2$ shown in (a) for reference.

The amplitude coefficient of the device shows a near-quadratic dependence on spatial frequency for which the optical transfer function of a second-order differentiatior (*cf.* fundamentals, sections 2.1.4 and 2.1.7) was fitted to the calculated result for device RWG-A. A second-order differentiator exhibits a quadratic dependence of the amplitude transfer function $|t|$ on the spatial frequency and a flat phase-transfer function φ. Here we fit the function given in eq.(2.44) over the NA of the transfer function corresponding to an operation proportional to a second-order differentiation with an amplitude offset. The result is shown in red in Fig.6.6(b,c). The fitting parameters are summarized in table A.2 in the appendix. It is apparent that there is good agreement between the calculated and fitted amplitude transfer function while the phase transfer function shows considerable deviation. These deviations have implications for artifacts in phase-visualization applications using one-dimensional resonant wave guide gratings as will be discussed further below in section 6.2.4.

6.2.2.2 Two-dimensional resonant wave-guide gratings

While for specific applications one-dimensional spatial-frequency filtering can be required, two-dimensional filtering is generally desirable. In the following we will investigate the capability of two-dimensional resonant wave-guide gratings as introduced in Fig.6.1(b) using the examples of devices RWG-C,D,E. For many applications it is desirable for the optical transfer function to be isotropic, i.e. show a high degree of rotational symmetry. We calculate the Fourier plane images in transmission for the three grating periods investigated throughout the optimization process above at their respective absorption wavelengths λ_c with the results shown in Fig.6.7. All three grating structures show strong suppression of low spatial frequencies with increased transmission at higher spatial frequencies in all directions.

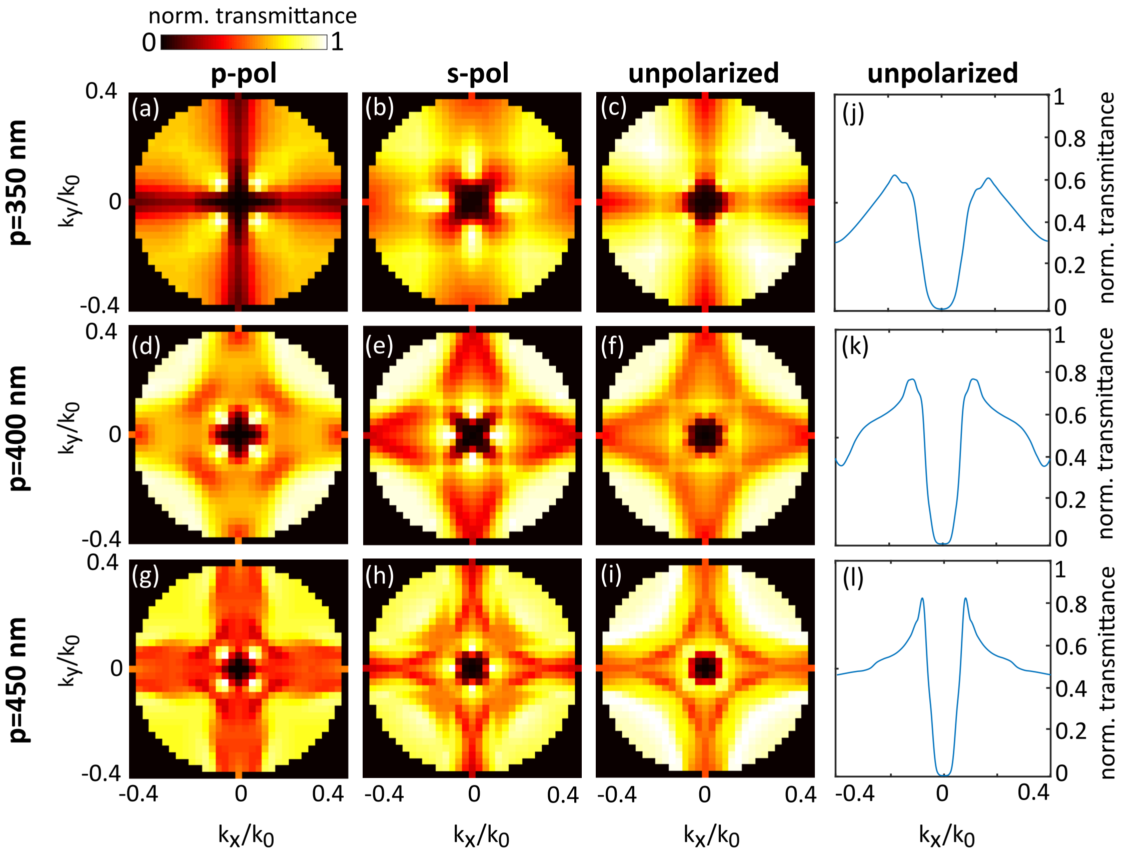

Figure 6.7: Fourier plane images in transmission of two-dimensional resonant waveguide gratings at their respective absorption wavelength λ_c. Results shown for RWG-B (a-c), RWG-C (d-f) and RWG-D (g-i) and p-polarization (first column), s-polarization (second column) and unpolarized light (third column). Line-plots through $k_y = 0$, and equivalently $k_x = 0$, for unpolarized light are shown in (j-l). Fourier plane images are normalized to their brightest pixel.

The transmittance exhibits a reasonable degree of rotational symmetry, particularly for unpolarized light. For s-polarized light a steeper increase in transmittance is apparent along $k_x = 0$ or equivalently along $k_y = 0$ compared to the diagonal direction along $k_y = -k_x$ and $k_y = k_x$. The numerical aperture of the filter function decreases from NA= 0.175 to NA= 0.075 as the grating period is increased from $p = 350\,\mathrm{nm}$ to $p = 450\,\mathrm{nm}$. This will, for example, result in slightly different processing of images of a particular size between the three devices. The filtering contrast of the devices is calculated to be $C_s = 0.954$ (RWG-C), $C_s = 0.979$ (RWG-D) and $C_s = 0.993$ (RWG-E) along $k_x = 0$ or equivalently $k_y = 0$. In summary the results numerically demonstrate the potential of two-dimensional resonant waveguide gratings for bi-directional high-pass filtering of spatial frequencies using unpolarized light.

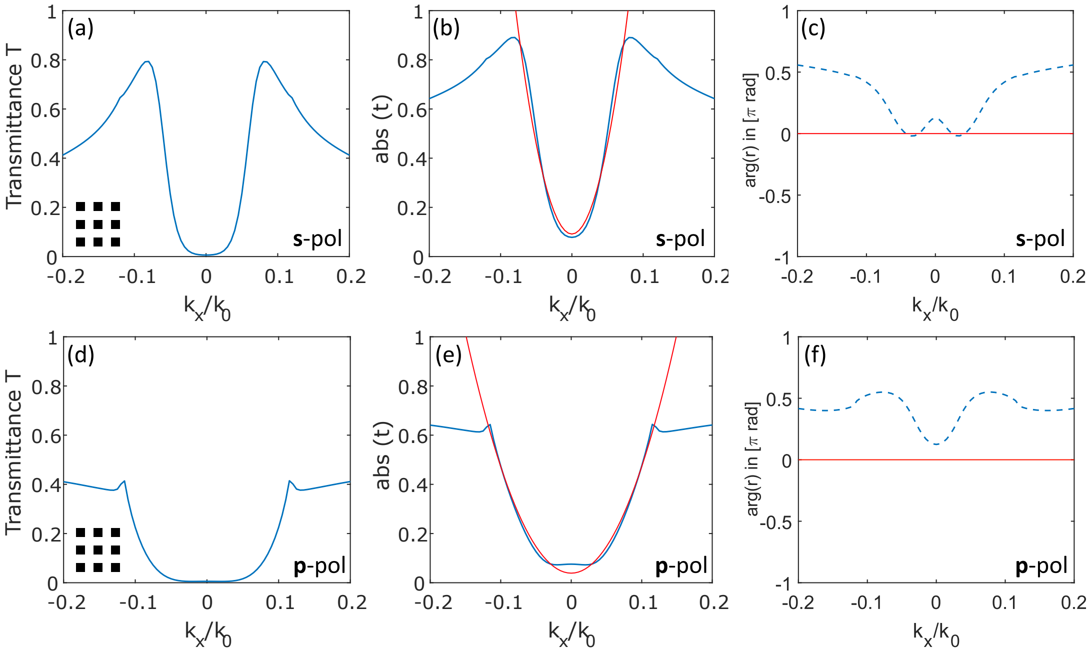

Figure 6.8: Comparison between the two-dimensional resonant wave guide grating RWG-C and a second order differentiator for s- (a-c) and p-polarization (d-f). Calculated results for the magnitude (b,e) and phase (c,f) of the transmission coefficient of device RWG-C at $\lambda = 647\,\mathrm{nm}$ along $k_y = 0$ shown in blue with the respective fit of $H = a_1(k_x/k_0)^2 + a_2$, determined over the NA of each filter function, shown in red. Fitting parameters a_1, a_2 provided in table A.2 in the appendix. Transmittance $T = |t|^2$ shown in (a,d) for reference.

As for the one-dimensional grating RWC-A above, we here again investigate the similarity between the two-dimensional resonant waveguide gratings and a second-order differentiator with the optical transfer function calculated with higher resolution within the relevant interval. Using the example of device RWG-D ($p = 400\,\mathrm{nm}$) its amplitude- and phase-transfer function along $k_y = 0$, or equivalently $k_x = 0$ for symmetry reasons, are shown in Fig.6.8(b,c) and (e,f) for $s-$ and $p-$polarized light respectively. The quadratic transfer function provided in eq.(2.44) was again fitted to the calculated amplitude- and phase transfer function with the result shown in red in Fig.6.8 with the fitting parameters provided in table A.2 in the appendix. It is apparent that, similar to the one-dimensional grating discussed earlier, the amplitude transfer function closely resembles a quadratic transfer function while considerable discrepancies can be seen in the phase-transfer function. The deviations of the optical transfer function from the transfer function of an ideal second-order differentiator implies possible artifacts in two-dimensional edge-enhancement and particularly phase-visualization applications as will be discussed in section 6.2.4.

6.2.3 Edge enhancement

Based on the spatial-frequency filtering characteristics of the resonant wave guide gratings described above we will numerically demonstrate edge enhancement in transmitted amplitude images in the following. Initially we will briefly demonstrate directional, polarization dependent edge detection using devices with one-dimensional grating structures. With the focus of this chapter on two-dimensional operations, we subsequently investigate edge-enhancement using two-dimensional grating structures in more detail.

6.2.3.1 One-dimensional edge-detection

The Fourier plane analysis from Fig.6.5 indicates potential for one-dimensional resonant wave-guide gratings to perform edge-enhancement in one spatial direction. In Fig.6.9 images of a figure ‘2’ as shown in Fig.6.9(a) transmitted through device RWG-A are shown as a function of the polarization state. For s-polarized light (Fig.6.9(b)) enhanced edges are apparent along the x-direction with perpendicular edges remaining dark. In line with the calculated Fourier plane images only modest edge enhancement for p-polarized light is apparent (Fig.6.9(c)). For unpolarized light (Fig.6.9(c)) the resulting image shows edge enhancement along the x-direction although with reduced suppression of the low-spatial frequency content of the image compared to the result for s-polarized light. As previously discussed in section 2.1.4 ringing effects are due to the numerical aperture as well as the non-linearity and non-isotropy of the optical transfer function. In summary the results demonstrate that one-dimensional RWGs carry potential for directional edge detection in transmitted amplitude images.

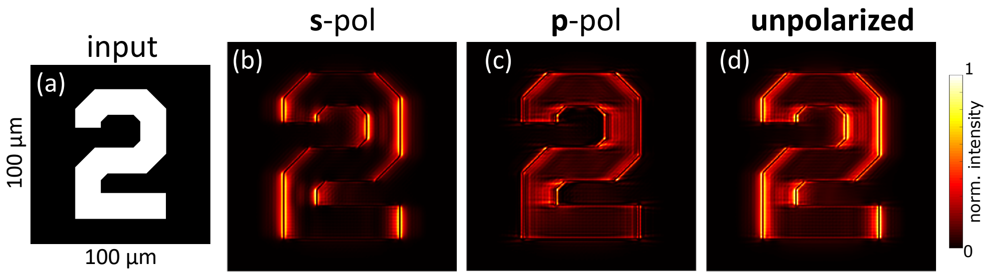

Figure 6.9: Numerical demonstration of one-dimensional and polarization dependent edge enhancement in an amplitude image (a) with the transmitted images shown in (b-d) for device RWG-A at $\lambda = 589\,\text{nm}$. Output intensity is shown for s-polarization (b), p-polarization (c) and unpolarized light (average of $p-$ and $s-$ contribution) (d). All results are calculated for a numerical aperture of NA=0.4 and normalized to their brightest pixel.

6.2.3.2 Two-dimensional edge-detection

Below we numerically demonstrate two-dimensional edge enhancement upon transmission through resonant waveguide gratings with devices RWC-C,D and E. The resulting images for p-, s- and unpolarized light are shown in Fig.6.10. For a fixed image size of $100\,\mu\text{m} \times 100\,\mu\text{m}$ the transmitted images clearly show enhanced edges for all polarizations with the homogenous areas of the input appearing dark. Minor differences between the resulting images are the result of the complex details observable in the Fourier plane images of the devices RWG-C,D and E in Fig. 6.7. In summary the results demonstrate that RWG have the potential to all-optically perform edge detection on amplitude images in two dimensions. The impact of the scale of features on the processed images will be discussed in the following.

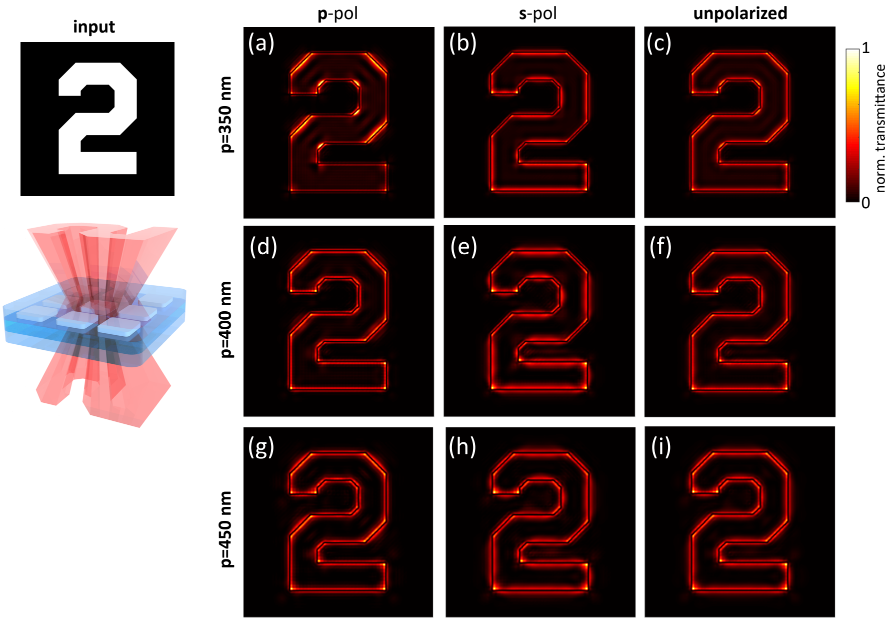

Figure 6.10: Numerical demonstration of edge enhancement in an amplitude image (input) with the transmitted images shown in (a-i) for devices RWG-C,D and E with grating periods of $p = 350\,\text{nm}$ at $\lambda = 587\,\text{nm}$ (a-c), $p = 400\,\text{nm}$ at $\lambda = 645\,\text{nm}$ (d-f) and $p = 450\,\text{nm}$ at $\lambda = 705\,\text{nm}$ (g-i). Output intensity is shown for p-polarization (first column), s-polarization (second column) and unpolarized light (third column). Image size is $100\,\mu\text{m} \times 100\,\mu\text{m}$ and all results are calculated for a numerical aperture of NA$= 0.4$. All images are normalized to their brightest pixel.

6.2.3.3 Scaling effects on edge enhancement

Using the example of a device RWG-D processed images are shown for image sizes ranging from $25\,\mu\text{m}$ to $500\,\mu\text{m}$ at a numerical aperture of NA$= 0.4$ in Fig.6.11. In line with expectations edge contrast and image brightness reduce with increasing image size. For larger images the impact of ringing effects around the edges is less dominant. For image sizes below approximately $50\,\mu\text{m}$ edge enhancement contrast disappears due to image blurring. The numerical results provide a rough estimate for a suitable image size for experimental applications betwen $50\,\mu\text{m}$ to $200\,\mu\text{m}$ in order to compensate for potential noise and deviations from the theoretical optical transfer function particularly in terms of the degree of suppression of low-spatial frequency content. The dependence on adequate choice of the images and the appearance of ringing effects places limitations on the type of images and processing resolutions that can be processed with the device. We will discuss potential pathways to improve this at the end of this chapter.

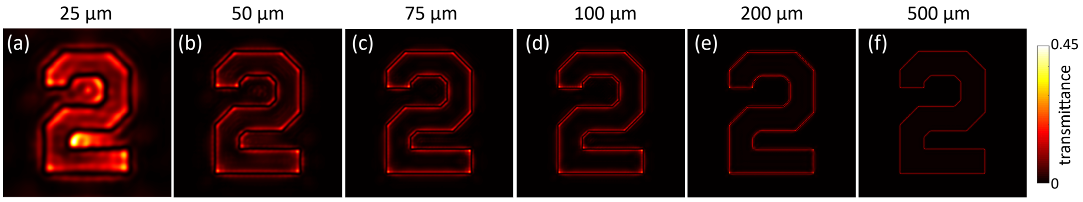

Figure 6.11: Numerical demonstration of edge enhancement in an amplitude image transmitted through RWC-C at $\lambda = 647\,\text{nm}$ as a function of absolute image size ranging from $25\,\mu\text{m}$ to $500\,\mu\text{m}$. All intensities are given as the fraction of the input intensity.

6.2.4 Detection of phase gradients

As discussed in the introduction in section 2.1.5 the conversion of phase-gradients in a wave field into intensity modulations can be achieved through high-pass spatial frequency filtering. While ideally a first-order differentiator is sought, the resonant wave-guide gratings under consideration roughly resemble second-order differentiators in one (RWG-A) and two dimensions (RWG-C,D,E) for normally incident light. At the end of the numerical part of this chapter we also discuss pathways to utilize plasmonic RWGs as near-first order differentiators at oblique incidence. However, operation at normal incidence is preferable for integration into compact imaging systems for which we here focus on phase visualization in normally incident wave fields. In the following we will demonstrate phase-visualization numerically for one- and two-dimensional resonant waveguide gratings. With regard to potential applications of the structure, this section relates to the potential of the structures to visualize phase gradients in biological cells placed on top of the device. In a first step we investigate the conversion of a Gaussian shaped phase modulation.

6.2.4.1 One-dimensional phase visualization

Fig.6.12(b-c) shows the intensity distribution obtained upon transmission of a wavefield exhibiting a Gaussian shaped phase modulation with maximum phase excursion $\varphi_{\text{max}} = 2\pi$ as shown in Fig.6.12(a) through device RWG-A. For s-polarized and unpolarized light intensity maxima are located at the slopes of the phase excursion along $y = 0$ while negligible intensity modulation is apparent in the perpendicular direction in line with the Fourier plane images discussed in Fig.6.5(b,c). However, as discussed in the introduction to this thesis in section 2.1.5 phase visualization with a second-order differentiator implies artifacts in resulting intensity distributions and only highlights region of steep gradients where the phase gradient can be considered linear. Resulting artifacts can therefore be assigned to the quadratic nature of the transfer function of the RWG and its non-constant phase contribution as discussed in Fig.6.6. For p-polarized light a more complex intensity distribution emerges as a result of the strongly nonlinear and anisotropic optical transfer function of the device as apparent from the Fourier plane image in Fig.6.5(a) rendering the device non-suitable for phase-gradient detection in this case.

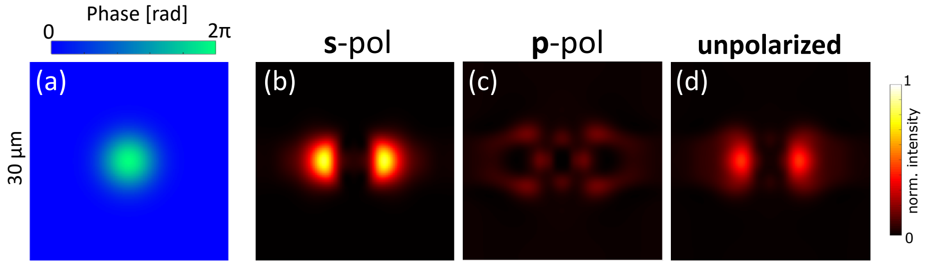

Figure 6.12: Numerical demonstration of directional detection of a Gaussian shaped phase gradient (a) upon transmission through a resonant waveguide grating with one-dimensional grating (RWG-A) with period $p = 350\,\text{nm}$ at $\lambda = 589\,\text{nm}$ for s-polarized (b), p-polarized (c) and unpolarized light (d). Image size is $30\,\mu\text{m} \times 30\,\mu\text{m}$. All intensities are given as fraction of the input intensity.

6.2.4.2 Two-dimensional phase visualization

Following visualization of transmitted phase gradients in one direction, we will now extend the considerations to visualization of phase gradients using two-dimensional resonant wave guide gratings. Fig.6.13 shows the intensity distribution obtained for a Gaussian shaped phase modulation with varying maximum phase φ_{max} excursion transmitted through device RWG-D at its resonance wavelength $\lambda = 647\,\text{nm}$. It is apparent that the transmitted intensity distributions in Fig. 6.13 (b-e) are related to the two-dimensional phase modulation in Fig. 6.13(a). However, as discussed for one-dimensional gratings above, the quadratic nature of the transfer function of the device and its non-constant phase contribution as shown in Fig.6.8 (c,f) result in a complex intensity distribution. In line with expectations for a second order differentiator higher maximum phase excursion (i.e. $\varphi_{\text{max}} = 3\pi, 4\pi$), leading to near-linear phase-gradients at the slopes of the Gaussian excursion, result in intensity maxima at regions of steepest phase gradient while for lower maximum phase excursion (i.e. $\varphi_{\max} = 2\pi, 1\pi$) the complexity of the resulting intensity increases. While a phase excursion of $\varphi_{\max} = 3\pi$ (Fig. 6.13 (e-g)) results in a characteristic ring around the rising and falling edges of the Gaussian phase excursion, weaker phase modulations show intensity maxima at the maxima of the phase modulation as shown for example in Fig.6.13(h-j).

In summary, phase visualization using one- and two-dimensional resonant waveguide gratings was demonstrated numerically. The limitation of the approach lies in the nonlinearity of the optical transfer function which places limitations on the phase-gradients that can be visualized in a useful way. Possible pathways for linearization of the optical transfer functions of resonant waveguide gratings will be discussed at the end of this chapter.

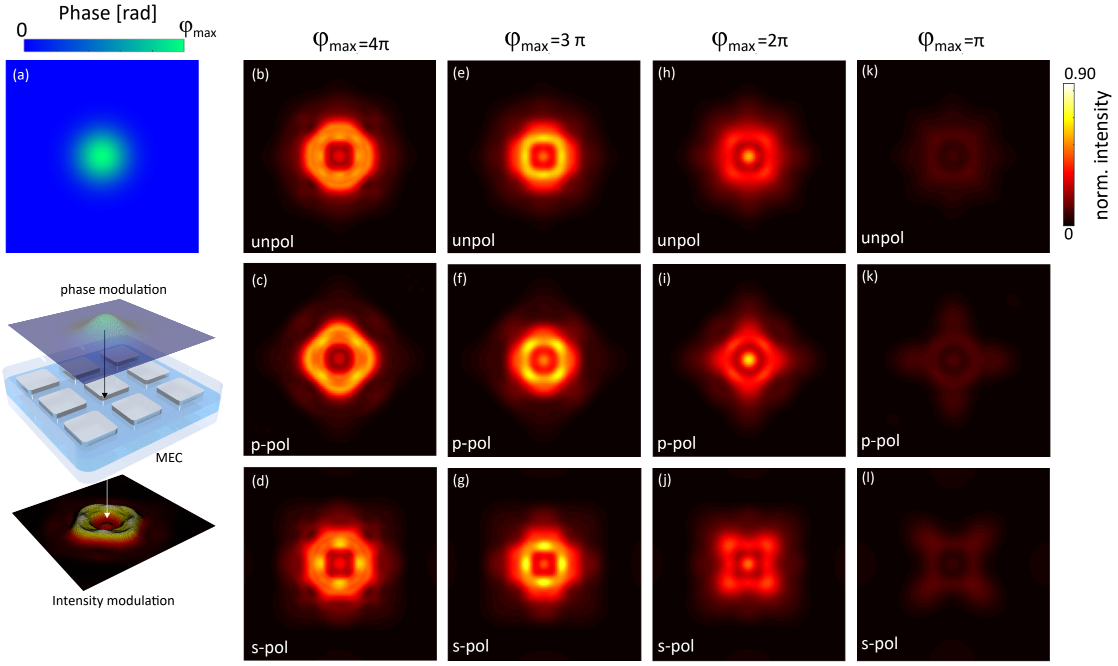

Figure 6.13: Numerical demonstration of conversion of a Gaussian shaped phase gradient (a) into an intensity modulation upon transmission through a MEC with period $p = 400\,\mathrm{nm}$ at $\lambda = 647\,\mathrm{nm}$ (RWG-D) as a function of maximum phase excursion for unpolarized (first row), p-polarized (second row) and s-polarized light (third row). Image size is $30\,\mu\mathrm{m} \times 30\,\mu\mathrm{m}$. All intensities are normalized to the input intensity.

6.2.4.3 Visualization of phase-gradients in red blood cells

In chapter 4 we have used a model of a red blood cell as described in [222] to investigate the conversion of the phase-modulation arising from its thickness profile as shown in

Fig.6.14(b) into intensity variations. Here we reuse this model to evaluate whether the phase gradients arising from red-blood cells immersed in water and placed on top of the device can be visualized in transmitted light as illustrated in Fig.6.14(a). The resulting intensity is shown in Fig.6.14(c-e) with minor differences for p-, s- and unpolarized light. While the emerging intensity pattern is clearly related to the phase-modulation of the red blood cell, regions of maximum intensity again do not coincide with locations of steepest phase gradient due to the nonlinearity of the optical transfer function of the device as discussed above. The results, however, indicate the potential of resonant wave guide gratings to visualize microscopic phase gradients as typically associated with light transmission through biological cells.

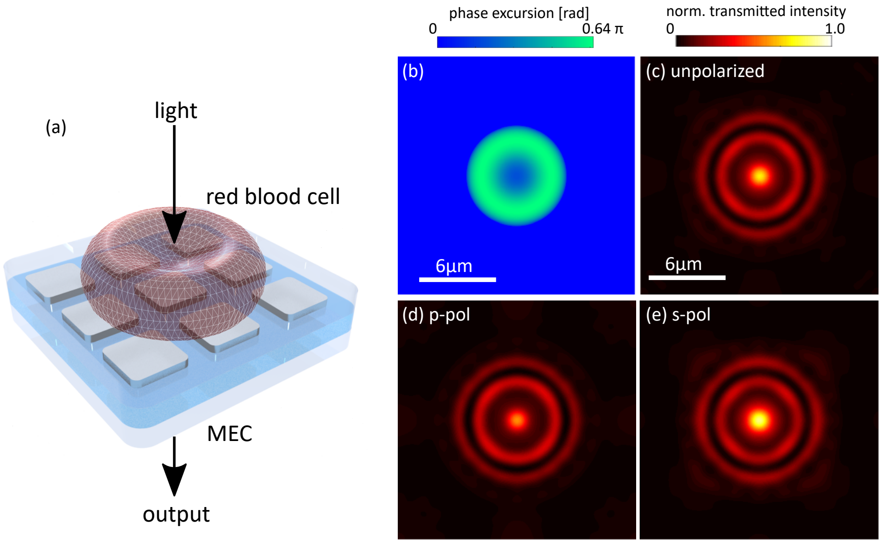

Figure 6.14: Calculated conversion of the phase gradient associated with light of wavelength $\lambda = 647$nm transmitted through a red blood cell into an intensity modulation using the MEC with period $p = 400\,\text{nm}$ (RWG-D) as shown in (a). (b) phase modulation $\varphi(x, y)$ associated with a red blood cell and (c-e) transmitted intensity as a fraction of the incident intensity for unpolarized light and light with p- and s-polarization.

6.2.5 Tilted operation of filter device

The operation of resonant waveguide gratings at a tilt-angle carries potential to expand the functionality of the devices as discussed in the following. Firstly, we have so far investigated operation of the devices at their resonance wavelength for normally incident light. However for this mode of operation, the unavailability of a light source at this wavelength or the requirement for operation at a particular wavelength can limit the versatility of the spatial frequency filter. In Fig.6.15(a) the transmittance as a function of normalized spatial frequency is shown for the one-dimensional grating device RWG-A (*cf.* table 6.1), which operates at $\lambda = 589\,\text{nm}$ for normally incident light. By operation at off-resonance wavelength the coupling condition changes thereby effectively shifting the suppression of transmitted light towards higher spatial frequencies. This is shown for the examples of $\lambda = 615\,\text{nm}$ and $\lambda = 633\,\text{nm}$ (HeNe laser line). Tilting the filter device along the axis parallel to the grating lines as indicated in Fig.6.15(b) by 4.9° or 8.9° respectively, suppression of low spatial frequency content can be achieved at these wavelengths for $s-$polarized light. In experimental situations, however, tilting the sample can represent a challenge owing to geometrical constraints for example when the sample is placed between microscope objectives with short focal lengths. It should be noted that for tilted operation and $p-$polarized light a different tilt angle is required (*cf.* Fig.6.15(a)) for which suppression of low spatial frequency content with unpolarized light is no longer possible in this configuration. The resulting Fourier plane image for tilted operation at $\lambda = 615\,\text{nm}$ is shown in Fig.6.15(c) indicating high-pass spatial frequency filtering with a numerical aperture of approximately NA=0.2.

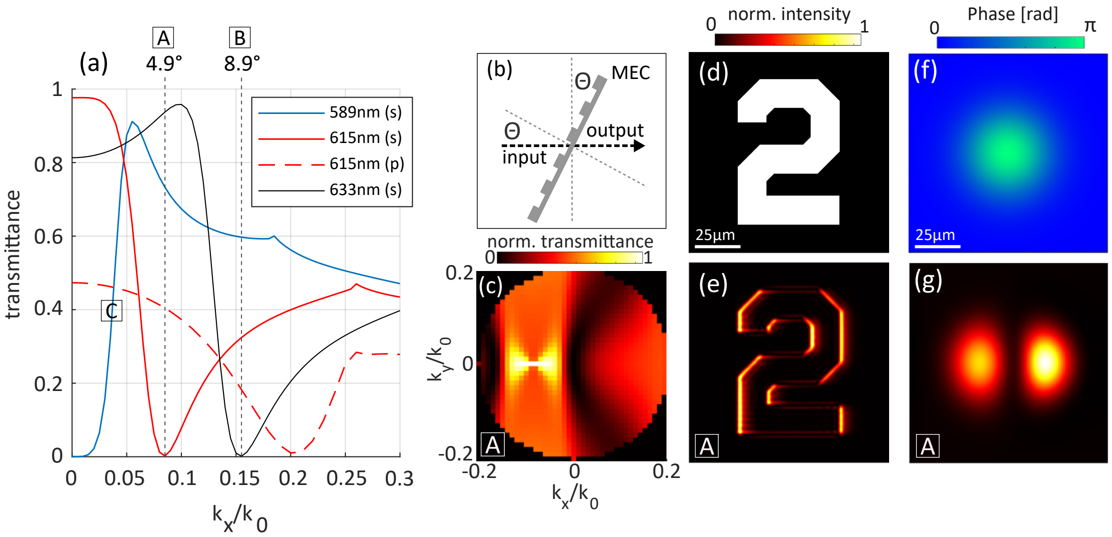

Figure 6.15: Numerical demonstration of tilted operation of device RWG-A. (a) Suppression of transmission as a function of wavelength λ and normalized spatial frequency k_x/k_0 for $s-$ and $p-$polarization. (b) Schematic of tilted operation of the filter device. (c) Fourier plane image for operation at $\lambda = 615\,\text{nm}$ at a tilt of $\theta = 4.9°$ for s-polarization (config. [A]). (d,e) Edge detection in an amplitude image transmitted through the device for config. [A], (f,g) Visualization of Gaussian shaped phase-modulation for a wavefield transmitted through the device in config. [A].

Following the previous investigations above, this enables us to utilize device RWG-A to perform one-dimensional edge detection on a transmitted amplitude image for $s-$polarized light at $\lambda = 615\,\text{nm}$ as calculated in Fig.6.15(d,e). Furthermore visualization of a Gaussian shaped phase modulation in this configuration is numerically demonstrated in Fig.6.15(f,g). The transmitted wavefield clearly indicates intensity maxima at the slopes of the Gaussian phase modulation with asymmetries in the intensity arising from the anisotropy of the transmittance for tilted operation as apparent from Fig.6.15(a,c).

Secondly, operation at a tilt angle enable the introduction of an asymmetry in the optical transfer function as previously investigated, for example in Roberts et al. [57] and Bykov et al. [49]. In Fig.6.16 the magnitude and phase of the optical transfer function of device RWG-A are shown for tilted operation. Due to the near-linear magnititude in the vicinity of $k_x/k_0 = 0$ (*cf.* Fig.6.16(a)) and the abrupt phase-shift (*cf.* Fig.6.16(b)) the device roughly approximates a first order-differentiator.

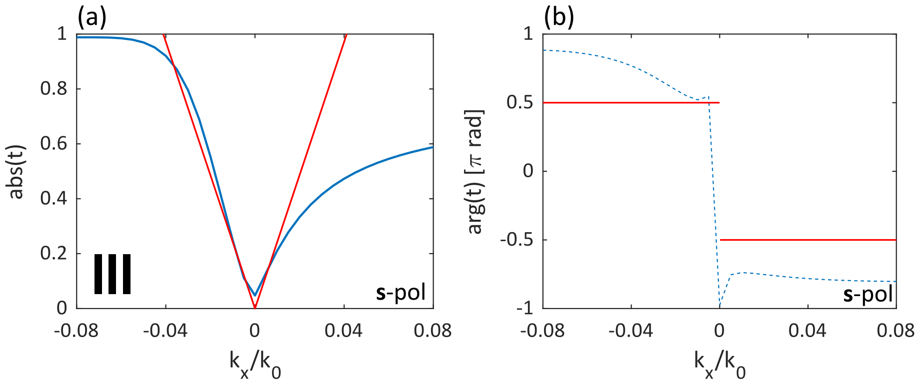

Figure 6.16: Numerical demonstration of asymmetric optical transfer function for tilted operation of resonant waveguide grating RWG-A. Shown in blue are the magnitude (a) and phase (b) of the transmission coefficient as a function of normalized spatial frequency for operation at $\lambda = 615\,\text{nm}$ at a tilt of $\theta = 4.9°$ for s-polarization. For comparison a transfer function proportional to a first-order differentiator with transfer function $H = a_1 i(\frac{k_x}{k_0})$ is shown in red for $a_1 = -23.4$.

However, further research on the device parameters is required to engineer an optical transfer function that provides a closer approximation of a first-order differentiator. In the summary of this thesis in chapter 7 we discuss potential pathways for more efficient numerical design that could allow precise reverse engineering resonant waveguide gratings to a desired optical transfer function.

A second way of operating a filter device at a tilt-angle is to operate at the absorption wavelength for normal incidence and tilting the device by a small angle of approximately 1 to 3° in order to off-set the optical transfer function as indicated in Fig.6.15(a) (configuration [C]). In this configuration an asymmetric, near linear amplitude transfer function is obtained within a narrow spatial frequency range around the offset as shown in Fig. 6.17. We will demonstrate this in the experimental part of this chapter for device RWG-B (*cf.* table 6.1) instead of device RWG-A due to the failure of a laser system that occured during the experiments. For this reason the results below are shown for RWG-A and RWG-B.

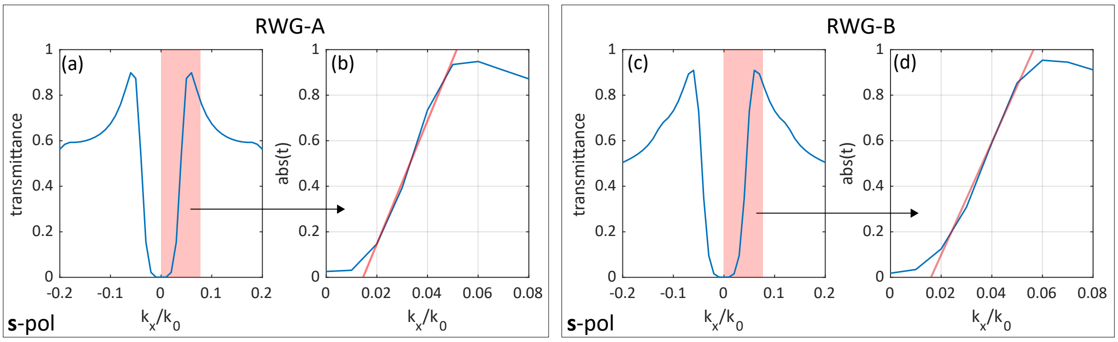

Figure 6.17: Accessing asymmetric region of transfer function of RWG-A and RWG-B by sample titling at resonance wavelength for normal incidence and $s-$polarization. Transmittance $|t|^2$ (a,c) and amplitude contribution to optical transfer function $|t|$ (b,d) at $\lambda = 589\,\mathrm{nm}$ (RWG-A) and $\lambda = 650\,\mathrm{nm}$ (RWG-B). Shown in red are linear fits within the interval $(0.02 \leq k_x/k_0 \leq 0.05)$.

This mode of operation is useful in particular to discriminate between positive and negative phase gradients which become visible in the intensity image. In Fig.6.18 the intensity obtained for transmission of a wavefield with a phase modulation in the shape of a red blood cell as described in [222] and introduced earlier in this chapter is shown. Due to the narrow spatial frequency range in which the amplitude transfer function is near-linear, we here consider a spatially expanded version of this model as indicated by the scalebar in Fig.6.18(a). It is apparent that for both RWG-A and RWG-B the obtained intensity contrast originating from the incident phase-modulation exhibits an asymmetry that can be adjusted by tuning the tilt-angle of the device in this configuration which creates a 3D pseudo visual relief effect. This offers the intriguing opportunity to use the filter device as an adjustable phase-visualization device as we will demonstrate experimentally in section 6.3.5.

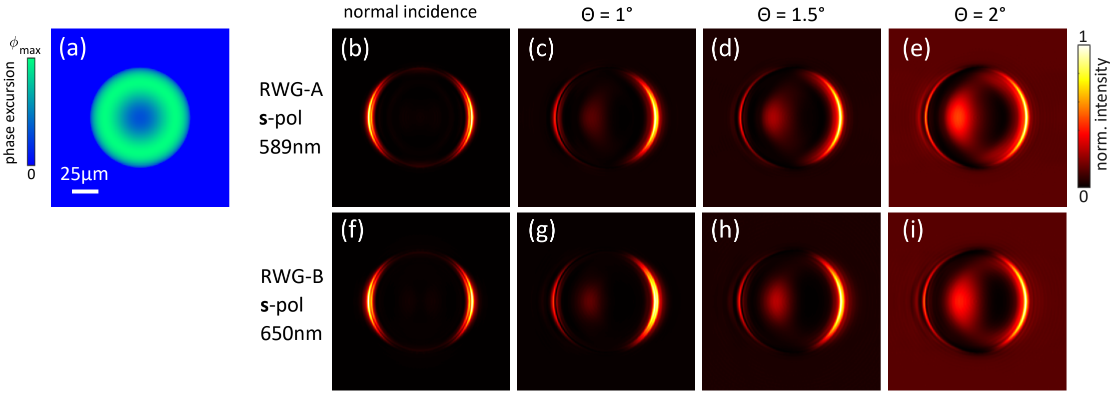

Figure 6.18: Numerical demonstration of visualization of phase-modulation in the shape of a spatially expanded red blood cell for a maximum phase excursion $\phi_{\text{max}} = 2\pi$ (a) for tilted operation of RWG-A (b-e) and RWG-B (f-i) at angles ranging from $\theta = 0°$ to $3°$ for $s-$ polarized light at the respective resonance wavelengths of the devices as indicated. All images normalized to their brightest pixel.

6.3 Experimental Results

The numerical calculations above served to demonstrate the potential of plasmonic resonant waveguide gratings for one- and two-dimensional spatial frequency filtering in transmission. In the following corresponding experimental confirmation will be demonstrated for the first time.

6.3.1 Fabrication of MEC devices

A series of MEC devices corresponding to the devices investigated numerically above was fabricated using electron beam lithography (EBL). A 100 nm thick layer of TiO_2 was deposited on top of a 4-inch glass wafer by physical vapor deposition at a deposition rate of 0.5 Å/s (Intlvac Nanochrome II). The metasurface pattern was written into a single layer of polymethyl methacrylate resist (PMMA: 280nm A4, baked at 180°C for 3 min after deposition) that was spun onto the sample, using an electron beam lithography tool (Vistec EBPG 5000). The nominal geometric parameters used for the inscription are summarized in table 6.1. The sample was developed in a 3:1 mixture of isopropanol: methylisobutyl. Subsequently a 40 nm thick layer of silver was deposited on the sample through physical vapor deposition on a 2 nm adhesion layer of chromium. In order for the silver array to be embedded in a near-homogenous environment that protects it from degradation due to exposure to air, a 750 nm thick layer of PMMA has been spun onto the sample and was baked at 180°C for 3 min. Scanning electron beam microscopy (FEI Nova Nano SEM 430) was used to image samples[28] fabricated using the above process as shown in Fig.6.7. The images indicate a successful fabrication process although irregularities are apparent in the grating elements which can impact the device performance as well as the operational wavelength as discussed below. These defects are attributed to insufficient adhesion between the Ag nanostructures and the TiO_2 layer. Using the software package FIJI in ImageJ an average of the actual grating period p and duty cycle g/p of the grating were determined in order to quantify the deviation. The results are summarized in table A.1 in the appendix and show a slight increase in average grating periods and duty cycles which we attribute to charge diffusion effects during the EBL lithography step.

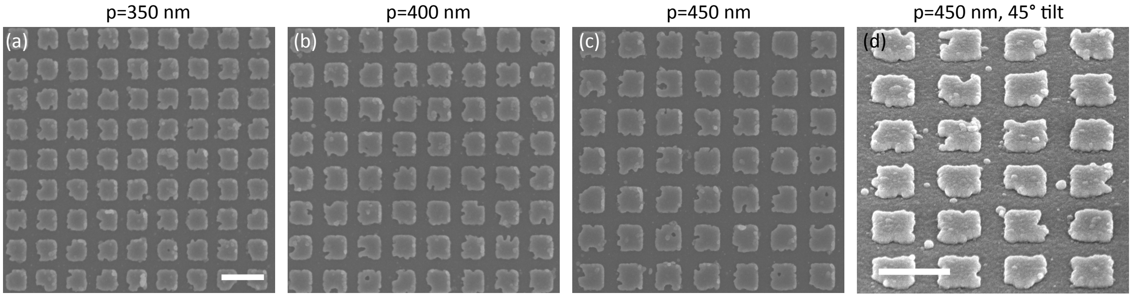

Figure 6.19: Representative SEM images metasurfaces consisting of two-dimensional Ag gratings on a 100 nm TiO_2 layer. Nominal grating periods are $p = 350$ nm (a), 400 nm (b) and 450 nm (c). The grating duty cycle is set to $g/p = 60\%$. A SEM capture of the metasurface shown in (b) tilted to 45° is shown in (d). Scale bars are 500 nm.

6.3.2 Fourier plane analysis in transmission

The devices were subsequently characterized regarding their transmission characteristics. In the following we will initially experimentally confirm suppression of low spatial frequencies along one direction using one-dimensional gratings before we proceed to two-dimensional resonant waveguide devices. Fourier plane images in transmission are recorded using the setup shown in Fig.6.20. Unpolarized light from a supercontinuum

---

[28] Due to the laboratory closures associated with Covid19 these SEM image are of a representative sample fabricated through an identical process. SEM captures of one-dimensional gratings were not available in this dataset.

laser source (Fianium SC-450-2) is spectrally filtered with a fiber-coupled tunable filter (Fianium Superchrome VIS-FDS-MM) and then guided to the setup through a single mode fiber (Thorlabs SM600) where the beam is collimated using a Nikon LU PLAN Fluor 5X 0.3NA objective (MO1). The collimated beam is transmitted through a beamsplitter (CCM1-BS013) and focussed by a Nikon LU PLAN 20X 0.40NA objective (MO2). The sample is placed in the focal point of MO2 and the transmitted beam collimated with an Olympus PLAN N 20X 0.4NA objective (MO3). Subsequently the beam is focused onto camera 2 (Thorlabs DCC1545M) using an $f = 50\,\mathrm{mm}$ lens where Fourier plane images in transmission are recorded. In this setup camera 1 (Thorlabs DCC1545M) is used only to monitor the position on the glass sample.

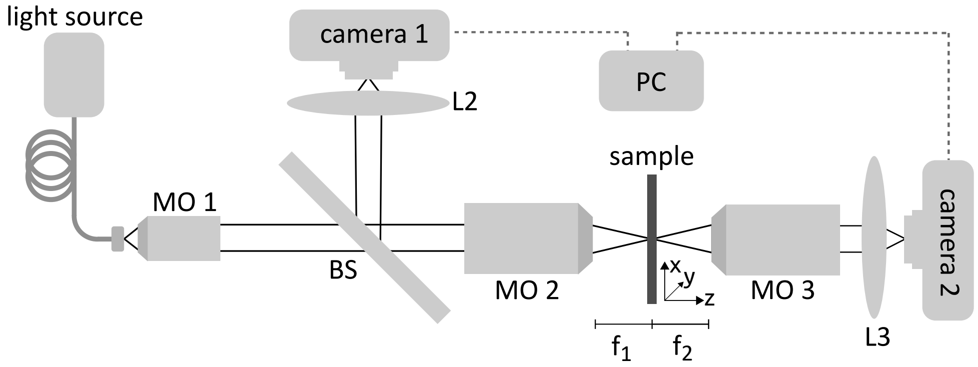

Figure 6.20: Setup used for the characterization of the angular transmission spectrum of the MEC. Fourier plane images are recorded by placing the metasurface in the focal point of MO2 and MO3.

6.3.2.1 One dimensional gratings

Fourier plane images in transmission were obtained for a device with a one dimensional grating with grating period $p = 350\,\mathrm{nm}$ (metasurface RWG-A). The data was recorded using the setup depicted in Fig.6.20 with an additional linear polarizer (Thorlabs LPVIS050-MP2) introduced between MO1 and the beamsplitter. The resulting images are shown in Fig.6.21.

In the following evaluation the bars of the grating are oriented along the y-direction as indicated in Fig.6.21(b,c). At the absorption wavelength $\lambda = 579\,\mathrm{nm}$ of the device broad suppression of low spatial frequencies over the entire range $-0.4 < k_y/k_0 < 0.4$ along $k_x = 0$ is apparent for unpolarized light, x-polarized light and y-polarized light as can be seen in Fig.6.21(a-c) and the corresponding lineplots in Fig.6.21(g-i). In the perpendicular direction, along $k_y = 0$, the Fourier plane images indicate suppression of low spatial frequencies with significantly increased transmission at higher spatial frequencies. For unpolarized and y-polarized light a steep increase in the transmission is apparent (Fig.6.21(a,b)) with an NA$\approx$ 0.09 of the filtering function. The filtering contrast is slightly higher for y-polarized ($C_s \approx 0.8$) than for unpolarized light ($C_s \approx 0.6$). While for x-polarized light transmission also increases at higher spatial frequencies (Fig.6.21(c)), broader suppression of low spatial frequencies is apparent with the width of the filtering function given by NA$\approx$ 0.19. An increased NA of the filtering function is also apparent for unpolarized light at wavelengths in the vicinity of the absorption wavelength as, for example, shown in Fig.6.21(e).

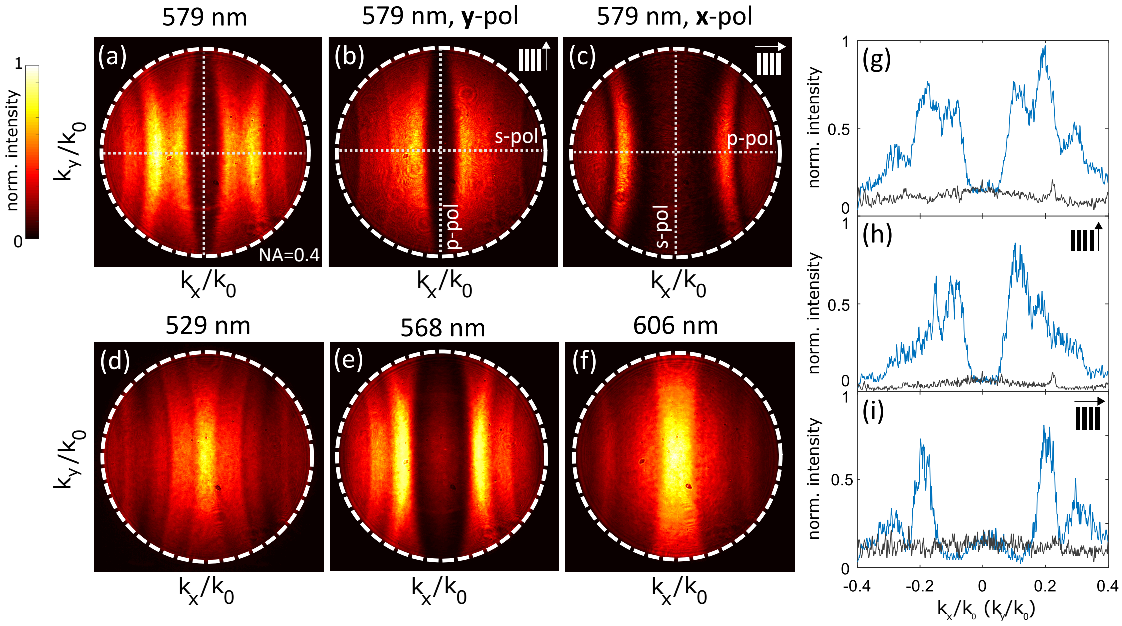

Figure 6.21: Experimental Fourier plane images in transmission of a 1D grating metasurfaces (RWG-A) for a nominal grating period of $p = 350$ nm as function of central wavelength and polarization state (a-f). Corresponding lineplots along $k_x = 0$ and $k_y = 0$ in (a-c) are shown in (g-i) respectively. The linear polarization is set as indicated in the insets. All images are normalized to their brightest pixel.

At wavelengths significantly shorter (Fig.6.21(d)) or longer (Fig.6.21(e)) than the resonance wavelength, the device acts as a low-pass spatial frequency filter. The findings confirm the results presented in the numerical part of this chapter albeit showing reduced experimental filtering contrast which we attribute to deviations in the fabricated grating geometry (*cf.* SEM analysis) and the bandwidth of the supercontinuum laser source increasing transmission of normally incident light. The results experimentally confirm that one-dimensional plasmonic resonant wave guide gratings enable polarization dependent spatial frequency filtering along one spatial direction with potential for polarization switchable devices. This switching capability could be enabled by adding an adjustable polarizer to the device. It must be acknowledged that this could imply bulk-optical components or mechanical parts unless realized through opto-electrically switchable polarizers.

6.3.2.2 Two dimensional gratings

Using the setup shown in Fig. 6.20 Fourier plane images in transmission were recorded for devices with two-dimensional gratings structures as a function of central wavelength with the spectral filter set to its minimum bandwidth of 5 nm. The results are shown in Fig. 6.22. It is apparent that transmission of low spatial frequencies is suppressed at the absorption wavelength of each device (Fig. 6.22(c,h,m)). At longer and shorter wavelengths suppression of transmission occurs at higher angles of incidence in line with expectations. While details in the measured Fourier plane images at higher spatial frequencies deviate from the results observed in the calculations (*cf.* Fig. 6.7), suppression of low spatial frequencies occurs at wavelengths that are consistent with the calculations. We attribute deviations and a minor shift of the absorption wavelengths by approximately $\Delta\lambda = 20\,\mathrm{nm}$ towards the blue spectral region compared to the numerical result to the deviations in geometric parameters of the grating discussed above based on SEM images of the structures and variations in the dielectric functions of silver and TiO_2. A decrease in the NA of the filter function from NA$\approx$ 0.17 (RWG-C, Fig.6.22(e)) to NA$\approx$ 0.08 (RWG-E, Fig.6.22(k)) is apparent from the lineplots as the grating period increases in line with the numerical results in Fig.6.7. All three devices exhibit a similar filtering contrast of $C_s \approx 0.6$ (RWG-C), $C_s \approx 0.6$ (RWG-D) and $C_s \approx 0.5$ (RWG-E). Significantly reduced filtering contrast compared to simulated devices can be attributed to imperfections in the grating structures (*cf.* SEM analysis) leading to a significant amount of normally incident light to be transmitted as well as the bandwidth of the supercontinuum light source. The presented results demonstrate the spectral tunability of the operational wavelength of two dimensional resonant waveguide gratings as spatial frequency filters over a range of $\Delta\lambda = 114\,\mathrm{nm}$ within the visible spectrum through device design.

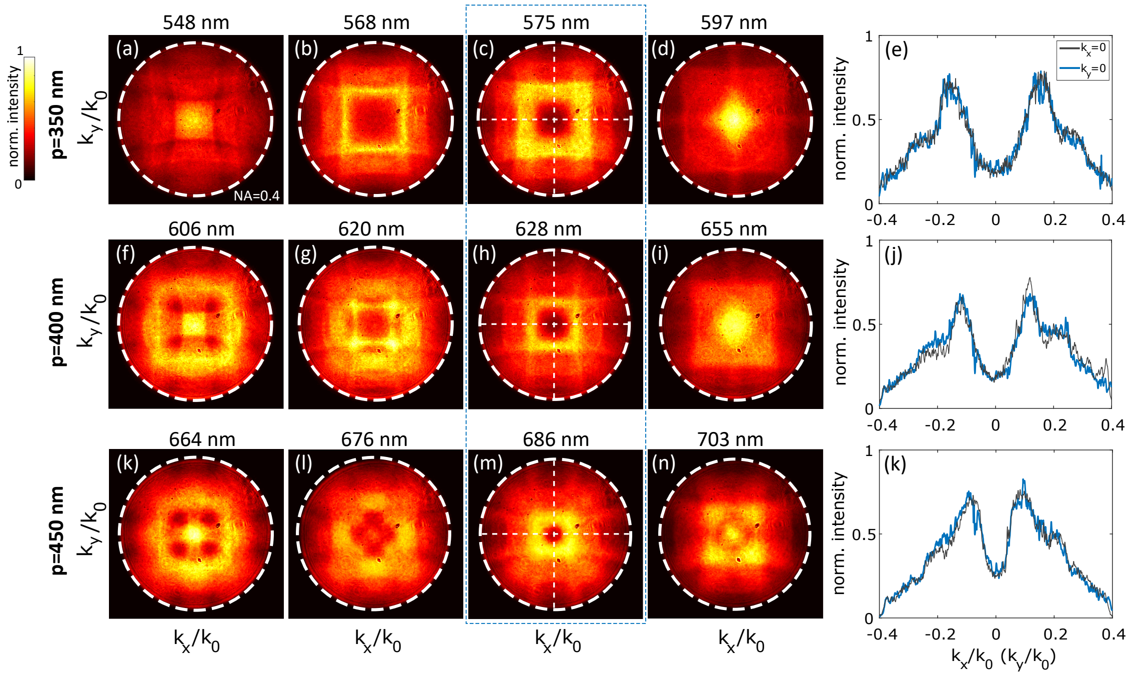

Figure 6.22: Experimental Fourier plane images in transmission of 2D grating metasurfaces for nominal grating periods of $p = 350\,\text{nm}$ (RWG-B) (a-d), 400 nm (RWG-C) (f-i) and 450 nm (RWG-D) (k-n) with corresponding lineplots along $k_x = 0$ and $k_y = 0$ in (e),(j),(k). Images are recorded using the setup introduced in Fig. 6.20 for an illumination bandwidth of $\Delta\lambda = 5\,\text{nm}$. All images are normalized to their brightest pixel.

The numerical results in the previous section indicated a weak dependence of the optical transfer function on the polarization state for two dimensional gratings as apparent from Fig.6.7(a,b). As an example Fourier plane measurements with an additional linear polarizer (Thorlabs LPVIS050-MP2) in the beam path after MO1 and before the beamsplitter in Fig.6.23 were obtained of the grating with a period of $p = 350\,\text{nm}$ (RWG-B). Shown are the Fourier plane image for light linearly polarized in the x- and y-directions with the grating aligned with the coordinate system as indicated by the inset. The Fourier plane images show suppression of low spatial frequencies with minor directional differences. The lineplot along the dashed lines in Fig.6.23(a) is depicted in Fig.6.23(c). In this image the lineplot along $k_x = 0$ corresponds to p-polarized light while the lineplot along $k_y = 0$ corresponds to s-polarized light. The graphs indicate a steeper transfer function for s-polarized light (NA≈0.12) than for p-polarized light (NA≈0.18) along the respective directions in line with numerical expectations. In summary, the investigated two dimensional resonant waveguide gratings enable isotropic filtering of low spatial frequency content for unpolarized light whereas linearly polarized light introduces a difference in the NA of the filter function.

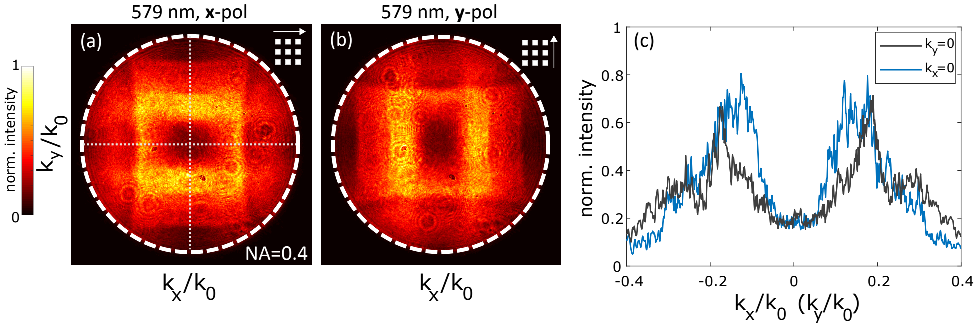

Figure 6.23: Polarization dependence of the optical transfer function of resonant waveguide gratings with two-dimensional gratings. Shown are experimental Fourier plane images in transmission of a metasurfaces RWG-B with nominal grating period $p = 350\,\text{nm}$ (a,b) with linearly polarized incident light as indicated by the inset. All images are normalized to their brightest pixel. Lineplots along $k_x = 0$ and $k_y = 0$ as indicated by the dashed lines are shown in (c).

6.3.3 Edge enhancement in transmitted amplitude images

Following the demonstration of spatial frequency filtering in transmission we will now investigate the application of resonant waveguide gratings to perform edge detection in transmitted amplitude images. In chapters 4 and 5, demagnified images were projected onto the devices under consideration in order to expand the spatial frequency content of the images thereby compensating for the high NA of the MIM absorber structures. The resonant wave guide gratings investigated here operate within a smaller NA < 0.2 and do not require elevation of the spatial frequency content of the images on the available resolution test target (Thorlabs R1DS1N) through demagnification.

We thus choose a different approach here and place an amplitude mask directly onto the device. We use a transmission setup as illustrated in Fig.6.24. The setup is established on a Nikon Ti-80i inverted microscope. Unpolarized light from the supercontinuum laser source is spectrally filtered by the fiber-coupled tunable filter and then guided to the setup through a single mode fiber (Thorlabs SM600) where it is collimated with a Nikon LU PLAN Fluor 5X 0.3NA objective (MO1). The collimated beam is incidident onto the mask sitting on the metasurface and the transmitted field collected by a Nikon LU PLAN 20X 0.40NA objective (MO2). Subsequently the transmitted light is imaged onto a camera placed at the output port of the microscope via the tube lens of the microscope (L). In the following, we will first experimentally demonstrate switchable directional edge detection using one-dimensional gratings (RWG-A) before we proceed to isotropic edge detection using the two dimensional grating structures (RWG-C,D,E).

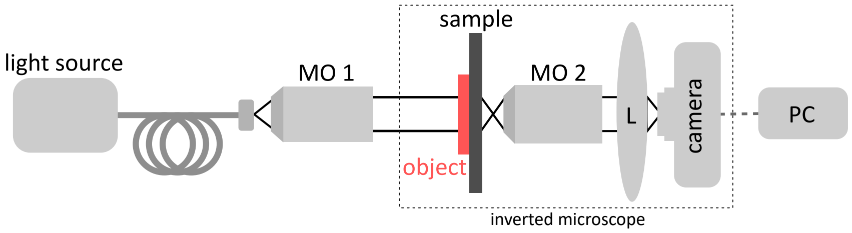

Figure 6.24: Setup built on Nikon Ti-80i inverted microscope used for the experimental demonstration of edge enhancement and contrast enhancement in biological samples in transmission. The object (resolution test target) is placed directly on top of the sample and the transmitted field is imaged onto a camera.

6.3.3.1 Polarization dependent directional edge detection

As an amplitude object we here again use a figure '2' from a negative USAF-1951 resolution test target (Thorlabs R1DS1N) (Fig.4.17(a)). With the Fourier plane images in Fig.6.21 indicating directional and polarization dependent filtering of spatial frequencies we here exploit this capability of one dimensional resonant waveguide gratings to demonstrate polarization switchable edge detection along one spatial direction. We use the example of the previously investigated one-dimensional grating with a period of $p = 350\,\text{nm}$ (RWG-A). Using the setup shown in Fig.6.24, with an additional linear polarization filter (Thorlabs LPVIS050-MP2) inserted into the beam path between MO1 and the mask, transmitted images were recorded as a function of the wavelength and polarization direction as shown in Figure 6.25. For unpolarized light and y-polarized light at the absorption wavelength $\lambda = 579\,\text{nm}$ (Fig.6.25(b,c)) clearly enhanced edges along the x-direction are visible while no edge enhancement is apparent in the perpendicular y-direction. Increased suppression of low spatial frequencies for y-polarized light compared to unpolarized light is apparent from the lineplots in Fig.6.25 (g,h) along the dashed lines in Fig.6.25(b,c). For x-polarized light no enhanced edges along either x- or y-direction can be detected as apparent from Fig.6.25(d) and the corresponding lineplot in Fig.6.25(i). Complete absence of enhanced edges even in the x-direction in this case can be attributed to the increased NA of the filtering function and the broad suppression of low spatial frequencies for x-polarization.

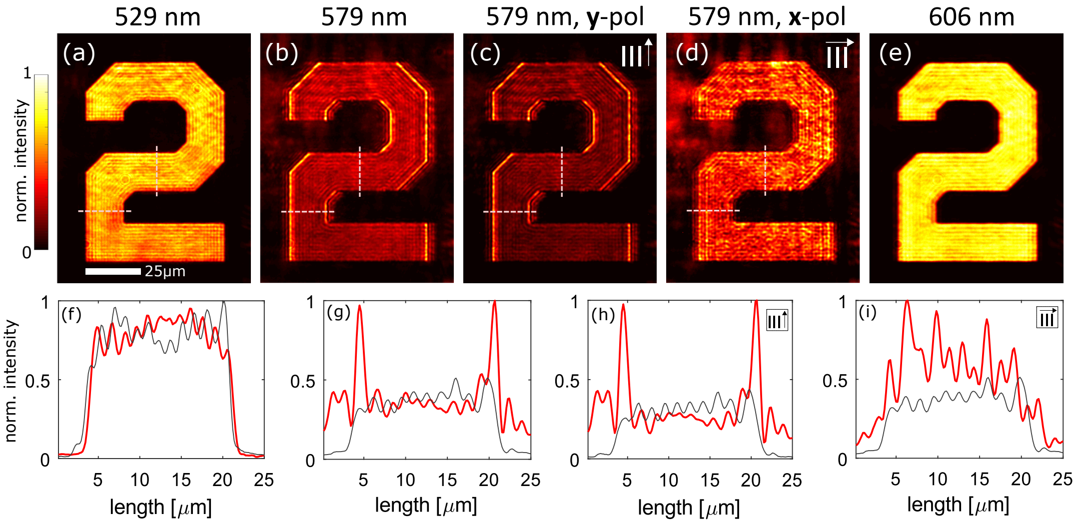

Figure 6.25: Experimental demonstration of directional edge enhancement in amplitude images transmitted through a 1D grating (RWG-A) with orientation of the grating along the y-axis as indicated by the insets. Resulting Intensity at the resonance wavelength of the grating $\lambda = 579\,\mathrm{nm}$ is shown in (b-d) for unpolarized light (b), vertically polarized light (c) and horizontally polarized light (d). Reference images transmitted at off-resonance wavelenghts are shown in (a) and (e) with the respective wavelengths as indicated. All images are normalized to their brightest pixel. Lineplots along the dashed lines in the images in (a-d) are shown in (f-i) respectively with each pair of lineplots normalized to their highest value. The red and gray curves shows the lineplots in horizontal and vertical direction respectively.

The results are consistent with the corresponding Fourier plane images for this device and experimentally confirm the directional edge detection capability for this device that can be switched on and off through choice of the polarization state. Remaining transmission of low spatial frequencies is consistent with the previously recorded Fourier plane images and could be improved by further decreasing the device transmission for near-zero spatial frequencies. Additionally, background noise from reflections at the mask-sample interface and sample-air interface reduce the image quality. This is particularly evident at the resonance wavelength (Fig.6.25(b-d)) where the signal to noise ratio is lower than at the reference wavelengths.

6.3.3.2 Two dimensional edge detection

In order to demonstrate two-dimensional edge-detection in tranmission, the measurement is repeated for a device with a two-dimensional grating structure (RWG-C). In Figure 6.26 the transmitted images are shown for a smaller (a-c) and larger (e-g) version of the image as indicated by the respective scale bars. At the absorption wavelength $\lambda = 575\,\text{nm}$ clearly enhanced edges with suppressed transmission in homogeneous areas are apparent in the images in Fig.6.26(b) and (f). In the reference images transmitted at $\lambda = 548\,\text{nm}$ (Fig.6.26(a,e)) and $\lambda = 606\,\text{nm}$ (Fig.6.26(c,g)) no edge enhancement is apparent consistent with the previously recorded Fourier images at these wavlengths (Fig.6.22(a,d)). Lineplots shown in Fig.6.26(d) and (h) compare the results for the resonant and off-resonant cases for both image sizes along the dashed lines in Fig.6.26(b,c) and (f,g) respectively. Comparing the edge enhancement of the smaller (Fig.6.26(a-c)) and larger image (Fig.6.26(e-g)) narrower edges in relation to the total image size are apparent in the larger image in line with numerical calculations shown in Fig.6.10. It should be noted that ringing artifacts are apparent around the image at the resonance due to the spatial frequency filtering

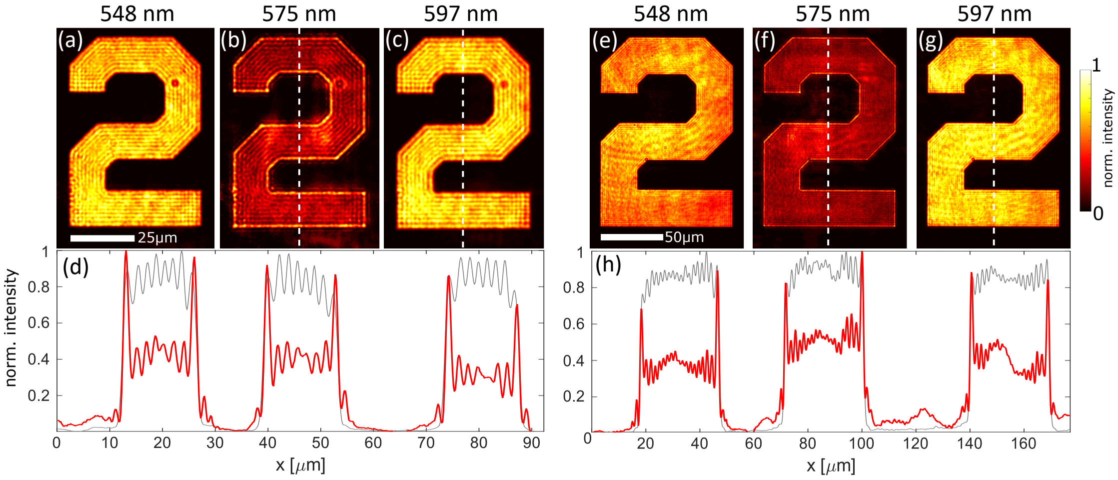

Figure 6.26: Experimental demonstration of 2D edge enhancement in amplitude images of a figure '2' transmitted through device RWG-C. Images were recorded at the resonance wavelength of the metasurface $\lambda = 575\,\text{nm}$ (b,f) as well as off-resonance for reference in (a,c) and (e,g) with wavelengths as indicated. Shown are the results for a smaller (a-c) and larger image (e-g) as indicated by the respective scale bars. Lineplots along the dashed lines in (b,c) normalized to their maximum value are shown in (d) and along the dashed lines in (f,g) are shown in (h) with the edge enhanced image in red and the reference in gray.

as well as the nonlinear transfer function of the device as discussed in previous chapters (*cf.* section 2.1.4). The interface reflections again contribute to background noise in this image (*cf.* Fig.6.26(b,f)). In summary, the results demonstrate metasurface enabled two-dimensional edge detection in transmission in the visible spectral range.

6.3.4 Contrast enhancement in images of biological samples

The relevance of the presented work for biological imaging applications was discussed in the introduction of this thesis and in the numerical section of this chapter. Here we experimentally demonstrate contrast enhancement in an image of onion epidermis in water directly placed on top of the metasurface and covered by a microscope coverslip. In order to protect the sample, the onion epidermis was placed on the back side of the glass substrate and illuminated using the setup shown in Fig.6.24 with light incident from the TiO_2 side in contrast to previous experiments where the metasurfaces were illuminated from the Ag side. Operation in the inverse direction retains low spatial filtering capability of the device as demonstrated by measured Fourier plane images for backside illumination shown in the Appendix in Fig.A.11. In order to capture a larger part of the onion epidermis, MO2 in the setup was replaced by a Nikon LU PLan 10x 0.3NA microscope objective. Figure 6.25 shows the transmitted images for the onion epidermis on and off the metasurface as a function of the illumination wavelength. At the absorption wavelength of $\lambda = 575\,\text{nm}$ suppression of transmission in the interior of

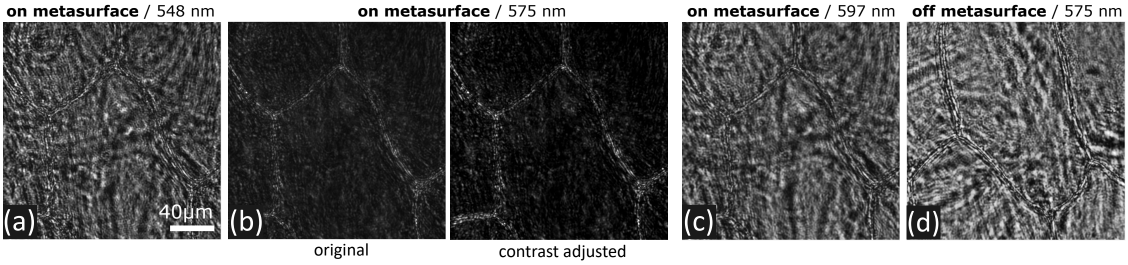

Figure 6.27: Experimental demonstration of contrast enhancement in an image of onion epidermis in water placed on the backside of device RWG-B to protect the sample. For backside illumination through a 2D array with nominal grating period $p = 350\,\text{nm}$ the measured intensity distribution at the resonance wavelength $\lambda = 575\,\text{nm}$ is shown in (b) with the measured image (left) and a version with digitally adjusted contrast for clarity (right). Off-resonance references are shown in (a,c) recorded at the indicated wavelengths, (d) onion epidermis placed on top of an unpatterned region of the sample and illuminated at $\lambda = 575\,\text{nm}$.

the cell and increased intensity along the cell boundaries is apparent. In contrast, at the reference wavelengths of $\lambda = 548\,\text{nm}$ and $\lambda = 597\,\text{nm}$ the images do not show this contrast enhancement. Figure 6.25(d) shows a reference image of the onion epidermis placed on an unpatterned region of the sample and illuminated at the resonance wavelength of $\lambda = 575\,\text{nm}$ confirming the contrast enhancement is due to the presence of the metasurface in Fig.6.25(b). Speckle apparent in all images originates from reflections between the glass interfaces of the RWG and the microscope coverslip as well as scattering within the onion epidermis which, owing the coherence of the light source, reduces the image quality. In summary the result confirms the potential of the structure for contrast enhancement in biological imaging. However, improvements in filtering contrast and strategies for the reduction of speckle will be required to optimize the performance of the approach.

6.3.5 Phase-visualization using spatial light modulator

In this section the experimental visualization of phase-gradients using metasurface enhaced coverslip (MEC) devices is demonstrated as investigated numerically in section 6.2. In the final stages of this research, a spatial light modulator (SLM) device (Holoeye Pluto 2 VIS014) became available and was used here to generate wavefields with phase modulations. The device consists of a 1920×1080 pixel liquid crystal on silicon display with a pixel size of $8\,\mu\text{m}$. The device is calibrated such that it enables imparting a pixel-by-pixel programmable phase shift between $[0, 2\pi]$ onto a reflected wavefield as will be discussed further below. Owing to the failure of the supercontinuum laser source used in previous experiments, a replacement laser was employed for the experiments presented in the following. We use a fiber coupled Fabry-Perot laser diode (Thorlabs S1FC635) operating at a fixed wavelength of $\lambda = 637\,\text{nm}$ with a bandwidth of $1\,\text{nm}$ (FWHM). While this laser system does not permit tuning of the operational wavelength, it offers a lower bandwidth than the previously used supercontinuum system that reached minimum bandwidth of $5\,\text{nm}$ (FWHM). This contributes to increased filtering contrast but limits the selection of resonant waveguide gratings that can be used as will be discussed further below. It is, however, a much cheaper and safer source of light than the class 4 supercontinuum source which demonstrates the potential of the devices to be used with simple laser systems.

Here we use a setup as illustrated in Fig.6.28. Unpolarized light from the benchtop laser system (Thorlabs S1FC635) is guided to the setup through a single mode fiber (Thorlabs

SM600) where the beam is collimated using a Nikon LU PLAN Fluor 5X 0.3NA objective (MO1) and linearly polarized (Thorlabs LPVIS050-MP2) along the operational direction of the SLM (corresponding to the y-axis of sample) and projected onto the spatial light modulator to modulate the phase. The reflected field is then demagnified through a telescope consisting of a $f = 150\,\mathrm{mm}$ lens (Thorlabs-LA1433-A) (L1) and a micropscope objective (Nikon UPlanFl 20x 0.5NA) (MO2) and the phase-image projected onto the MEC sample. The transmitted light is collected using a microscope objective (MO3), and through a $f = 50\,\mathrm{mm}$ lens (Thorlabs LA1131-A) (L3) projected onto a camera (Thorlabs DCC1545M).

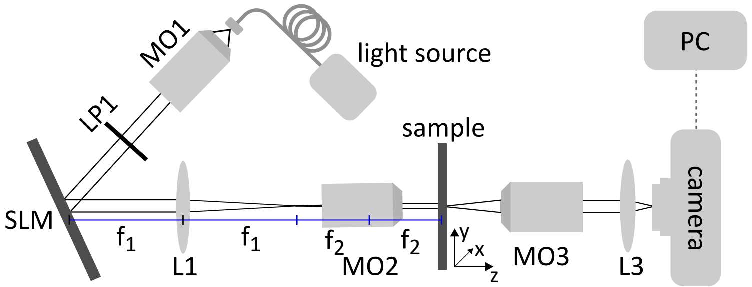

Figure 6.28: Experimental setup for the generation and detection of phase-gradients upon transmission through resonant wave guide gratings using a spatial light modulator (SLM). The SLM device is operated at an angle of 13.5°.

Here we use a MEC device consisting of a one-dimensional resonant waveguide grating with period $p = 400\,\mathrm{nm}$ with fabrication parameters of device RWG-B (*cf.* table 6.1) which operates at the wavelength of the available laser source as demonstrated in Fig.6.29(a,b) through experimentally measured Fourier plane images. The results are in line with the previously investigated one-dimensional grating device RWG-A that operated at a lower wavelength (*cf.* section 6.3.2.1). In the following we operate the device with $y-$polarized light which enables high-spatial frequency filtering along the $x-$direction as apparent from the lineplot in Fig.6.29(c) with a filtering contrast of $C_s \approx 0.9$. As discussed in section 6.2.5, a slight tilt of the device enables shifting the optical transfer function as indicated for the amplitude transfer function in Fig.6.29(d) in the interval $(0.02 \leq k_x/k_0 \leq 0.05)$ corresponding to a tilt of $\theta = 1° - 3°$. We will exploit this below to adjust the optical transfer function of the MEC device to process phase images.

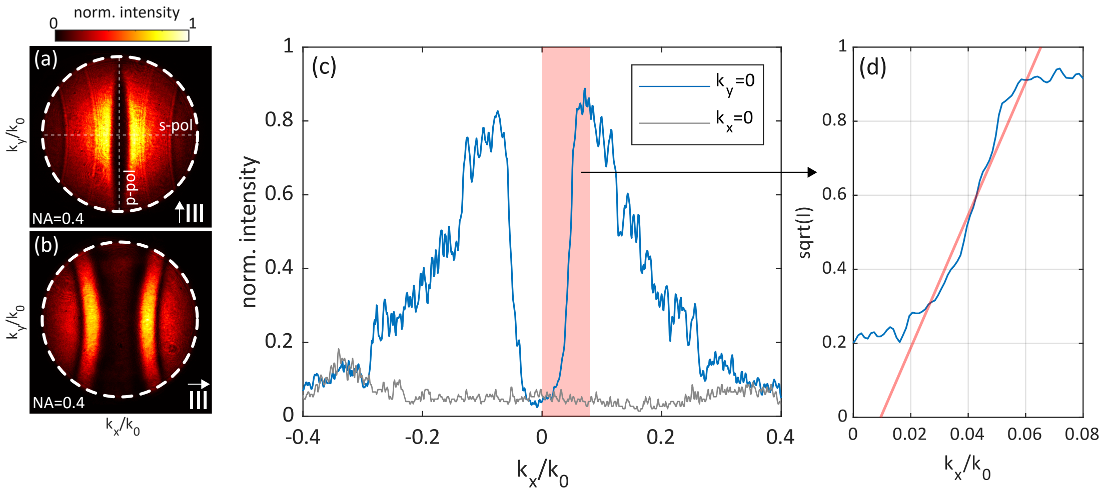

Figure 6.29: Measured Fourier plane images of device RWG-B using Thorlabs S1FC635 laser source at $\lambda = 637\,\text{nm}$ for (a) y- and (b) x-polarized light. (c) Corresponding lineplot of intensity for y-polarized illumination along $k_x = 0$ and $k_y = 0$. (d)Asymmetric, near-linear region of amplitude transfer function as indicated by linear fit in red for interval interval $(0.02 \leq k_x/k_0 \leq 0.05)$ accessible through tilt of sample by approximately $\theta = 1°$ to $3°$.

We use the setup shown in Fig.6.28 with the MEC characterized in Fig.6.29 (RWG-B) to perform experimental visualization of phase-gradients in the following. Here we choose a phase-modulation in the shape of an expanded red blood cell (Fig.6.30(a)) numerically investigated in section 6.2.5. The SLM is configured to linearly map grayscale values in the interval $[1, 256]$ to phase-shifts in the interval $[0, 2\pi]$ in a wavefield reflected from the SLM at the operational wavelength. The intensity distribution of the wavefield transmitted through the MEC device is shown for normal incidence in Fig.6.30(g) with the reference for transmission through an unpatterned region of the sample shown in Fig.6.30(l). While the phase-modulation is almost invisible in the reference image, clear intensity maxima are visible at the edges of the cell for transmission through the MEC with strong suppression of transmission in other parts of the image. This result is in line with the numerical result for this configuration shown in Fig.6.30(b) and represents the first experimental demonstration of phase visualization with a resonant wave-guide grating. However, the resulting image is dominated by the intensity maxima resulting from the edges of the cell model and does not permit insight into the gradual phase-modulations characteristic of the wavefield.

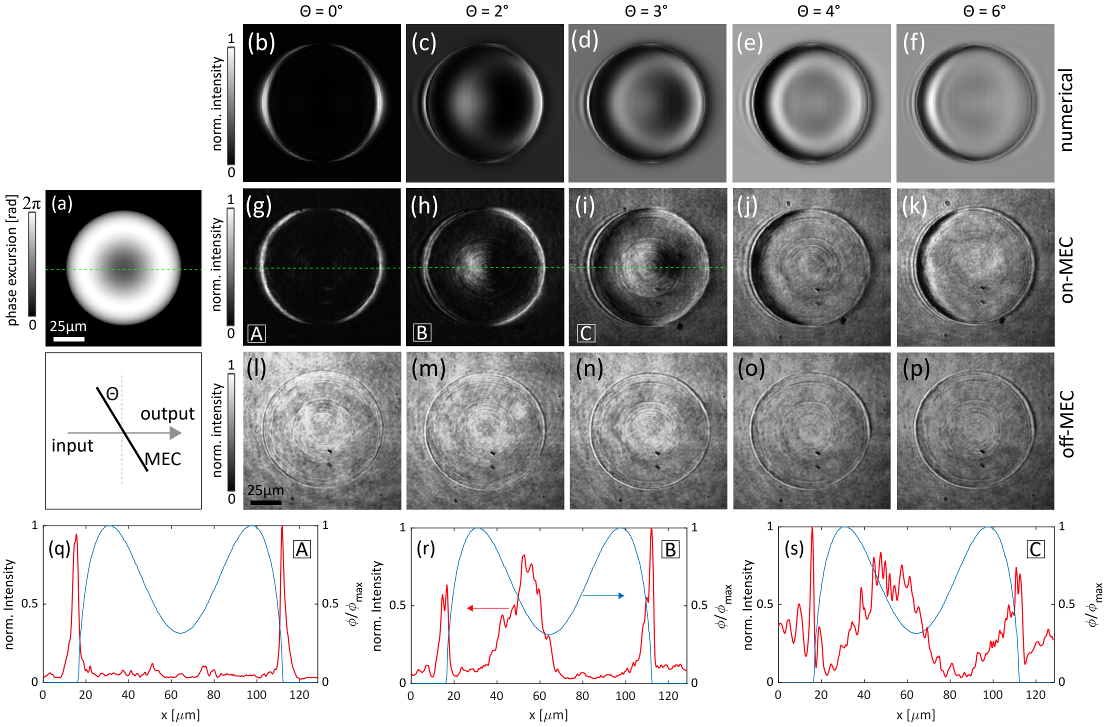

Figure 6.30: Experimental visualization of a phase-gradient associated with a sized-up model of a red blood cell as shown in (a) with maximum phase excursion $\phi_{\max} = 2\pi$. Here MEC device RWG-B is used for y-polarized light at $\lambda = 637\,\mathrm{nm}$ using the Thorlabs S1FC635 benchtop laser. Calculated intensity distribution upon transmission as a function of the tilt angle of the sample θ shown in (b-f) with experimental equivalents shown in (g-k). (l-p) Reference images for transmission of the phase-image through an unpatterened region of the sample for all tilt-angles. Lineplots through $y = 0$ for (g,h,i) shown in (q,r,s) respectively.

As discussed above in section 6.2.5, we can tilt the sample in order to offset the optical transfer function. This is shown in Fig.6.30(h-k) for a tilt angle between 2° and 6° experimentally with respective numerical results shown in Fig.6.30(c-f). Reference results for transmission through an unpatterned region of the sample are shown in Fig.6.30(m-p) respectively. It is apparent that the phase-profile of the cell model becomes visible as a pseudo 3D image for tilted operation. The experimental results are consistent with the numerical calculations that were obtained using the transfer function shown in Fig.6.17. In particular for tilt angles of $\theta = 2°$ (Fig.6.30(h)) and $\theta = 3°$ (Fig.6.30(i)) the phase-variation becomes apparent. These represent the first experimental demonstration of visualization of non-abrupt phase gradients in a wavefield with a transmitting optical metasurface and confirm the enormous potential of metasurface enabled phase-visualization.

6.4 Summary and Conclusion

In this chapter plasmonic resonant waveguide gratings were investigated as ultra compact and transmitting optical spatial frequency filters. The approach exploits the angular sensitivity in the coupling of incident light to modes supported by the resonant waveguide grating. In particular one- and two dimensional subwavelength silver gratings on TiO_2 slab wave guides were studied.

The first part of this chapter was concerned with the numerical modeling of the structure using the finite element method (FEM). The spatial frequency filtering ability of the structure was simulated and suitable geometric parameters for high filtering contrast determined. It was demonstrated for the first time that two dimensional plasmonic resonant waveguide gratings enable near-isotropic two-dimensional filtering of low spatial frequencies with unpolarized and linearly polarized light. Through choice of the grating period, suppression of low spatial frequency content was achieved at different wavelengths in the visible spectrum. Furthermore it was shown that one dimensional gratings enable filtering of the Fourier content of a wavefield in the direction perpendicular to the grating lines. Strong sensitivity with regard to the polarization direction was determined offering potential for optically switchable object plane filters. Through numerical examples, edge detection in transmitted micrometre sized amplitude images and conversion of phase gradients in transmitted wavefields into corresponding intensity distributions was demonstrated. Limitations of the structure due to its nonlinear transfer function were discussed. These contribute to ringing effects in amplitude images and can cause complex intensity distributions upon transmission of wavefields with phase gradients. Finally, operation of the devices at a tilt angle was investigated and demonstrated to enable shifting the wavelength at which suppression of low-spatial frequencies occurs. It was discussed that this also enables the generation of asymmetric optical transfer functions. It was numerically demonstrated that this enables the investigated devices to approximate first-order differentiators and carries potential to operate the devices at an offset angle for asymmetric phase-gradient visualization.

A series of resonant waveguide gratings with the determined device parameters was fabricated through electron beam evaporation of TiO_2 layers and a subsequent electron beam lithography (EBL) process. Fourier plane images of the metasurfaces in transmission were recorded confirming the numerically determined spatial frequency filtering characteristics for one- and two-dimensional grating structures. From SEM analysis random defects were apparent in the grating structures. These are attributed to insufficient adhesion between the Ag patches and the underlying TiO_2 layer. Future research could further investigate how such random defects in the grating structure affect the device performance. Further fabrication process optimization should also be part of future research in order to eliminate the apparent imperfections of the structure and thereby enhance the device performance. In particular the adhesion of the silver nanostructures to the TiO_2 layer could be improved through variation of the adhesion layer material and thicknesses. Following the Fourier analysis, suppression of spatial frequencies in transmitted amplitude images was demonstrated. Two dimensional edge enhancement as well as switchable directional edge enhancement were demonstrated for micrometer sized images directly placed on top of the metasurface. Contrast enhancement in an image of onion epidermis placed on top of the device was demonstrated proving the potential of the approach for biological imaging applications.

Finally, experimental visualization of phase-gradients generated by a spatial light modulator (SLM) upon transmission through a one-dimensional resonant waveguide grating was demonstrated in the last part of this chapter. Furthermore, it was experimentally confirmed that introduction of an asymmetry in the optical transfer function through tilt of the sample can be exploitet to enable asymmetric visualization of the phase profile in the incident wavefield to create a pseudo 3D image. These result are a central achievement of this thesis and represent the first demonstration of phase-gradient visualization using a transmitting metasurface and confirm the great potential of the devices for biological imaging applications. A promising aspect of future research is therefore the visualization of phase-gradients in live biological cells using the MEC devices investigated in this thesis. We will discuss this further in the general summary and outlook of this thesis.

In addition to this, modification of the grating unit cell of the devices offers a substantial additional degree of freedom to tailor the optical transfer function of the structures. While here we have considered lines and squares, more complex, potentially asymmetric, unit cells with suitable resonances are a possible extension of the structure. The focus of this thesis was to specifically enable image processing in the visible regime, since it is most interesting to most biological applications. Future research could include devices for near-IR processing which is of particular interest for data processing in telecommunication and in addition simplifies prototyping due to larger unit cells compared to those designed for operation at visible wavelengths.

While the prototyping of the presented devices was achieved through a time intensive electron-beam lithography process, alternative fabrication methods could enable large area and high-throughput fabrication. This will be a crucial step in the transition of the investigated structures to applicable devices. Specifically, nanoimprint techniques offer sufficient resolution for the type of structures investigated in this chapter. An issue with imprinting of the structure, that we are aware of, is that accessing the high-index layer during the imprint step is challenging but approaches to overcome this are currently under development in our research group. Developing a suitable nanoimprint fabrication process should therefor be considered for future research. In summary the results presented in this chapter demonstrate the significant potential of plasmonic resonant wave guide gratings as ultra-compact image processing facilitators in transmission.

Chapter 7

Thesis Summary and Outlook

The primary goal of this thesis was to further our understanding of ultra-compact all-optical image processing in general, and to develop specific implementation approaches utilizing nanophotonic structures. In particular the application of the devices developed during this project to edge-detection and phase-imaging, including biological image processing, were a central aim of this research. This chapter summarizes the outcomes of this work and suggests potential extensions and further research based on the investigated image processing approaches.

7.1 Summary of Research Outcomes

The research presented in this thesis demonstrates important steps toward the understanding and development of the next generation of all-optical information processing devices with subwavelength footprint. A detailed summary and outlook on future research of each part of this thesis was included at the end of the respective chapter and we will only summarize and draw connections between the major achievements here.

The first part of this thesis was concerned with establishing the theoretical framework necessary to describe all-optical information processing in general and its application to object- rather than Fourier-plane systems. Subsequently, the implementation of compact object-plane systems through nanophotonic approaches was discussed. The confluence of Fourier optics and spatial analogue optical computation on the one hand, and plasmonic resonances, optical metasurfaces as well as thin-film systems on the other hand formed the framework for the research discussed here. Based on this approach three fundamentally different methods for nanophotonic image processing were investigated with the major achievements summarized below:

- Demonstration of spatial frequency filtering in reflection through metal-insulator-metal (MIM) thin-film absorbers with subwavelength thickness.
  ⟶ ([60], chapter 4).
- Investigation of the angular sensitivity in the excitation of subradiant modes (SRM) on plasmonic metasurfaces and their potential and limitations for all-optical image processing in reflection.
  ⟶ ([61], chapter 5)
- Modeling and fabrication of plasmonic resonant waveguide gratings (RWG) with the capacity to perform high-pass spatial frequency filtering on transmitted wavefields.
  ⟶ ([62], chapter 6).
- Performing numerical and experimental edge detection on amplitude images through MIM absorbers, SRM excitation and via RWGs.
  ⟶ ([60, 63], chapters 4-6)
- Numerically and experimentally demonstrating MIM absorbers and RWGs as ultracompact devices for the visualization of phase-gradients in incident wavefields upond reflection and transmission respectively.
  ⟶ ([60], chapters 4 and 6).
- Application of MIM absorber and RWGs to perform experimental contrast enhancement in images of biological samples.
  ⟶ ([60], sections 4.3.4 and 6.3.4).

7.2 Future Work and Outlook

In the following potential extensions of the presented research will be discussed in detail for each topic of this thesis separately before we concluded with a broader outlook on future developments of nanophotonic information processing.

7.2.1 Algorithmic Metasurface Design

The angular filtering capability of plasmonic metasurfaces was investigated in this thesis. Owing to the computationally intense nature of FEM calculations, our ability to adapt the geometry of the metasurfaces in order to tailor their optical transfer function is currently limited. A promising next step would be exploiting computationally efficient semi-analytical approaches for nanoparticle interactions [57, 93, 238, 239] coupled with an iterative optimization algorithm. This could potentially be implemented using machine-learning as proposed for inverse metasurface design [240, 241] and serve as a starting point for further analysis through FEM calculations.

7.2.2 Switchable Filter Devices

The devices investigated in this thesis have static optical transfer functions and operate at a fixed wavelength. Extending the properties of these devices by adding dynamically switchable characteristics carries vast potential for their integration in complex information processing systems. Approaches to realize this include phase-change materials like chalcogenide glasses, transition metal oxides and liquid crystals. Also graphene or elastomers that react to external voltages, heatflow and an applied magnetic field have been considered [32, 100]. Approaches based on reconfigurable metasurfaces in which the geometry of the resonators changes as a result of the application of a DC external field represent further potential gateways to switching functionality [242]. Replacing one or several elements in the approaches investigated in this thesis with reconfigurable materials is a promising pathway towards versatile optical information processing devices.

7.2.3 Spatio-Temporal Information Processing

In this thesis we have studied analogue optical computation in the spatial domain while a large body of research focuses on performing computation on the temporal shape of light pulses. The investigated approaches include for example semiconductor processors [146, 149], optical fiber based systems [147, 148, 151], photonic crystals [150] and resonant grating structures [243] among others. Golastikov et al. have proposed simultaneous spatial-and temporal computation of optical wavefields upon transmission through resonant diffraction gratings [244]. The above research indicates potential for waveguide grating structures, similar to the devices investigated in this thesis, to perform spatio-temporal processing of transmitted wavefields.

7.2.4 Wavefront Sensing and Recovery

Wavefront sensing describes the detection and quantification of phase aberations of optical wavefronts. It is an essential tool in various scientific and technical fields including astronomy [245, 246] and ocular diagnostics [247]. Astronomical telescopes that observe light originating from stars need to take disturbances introduced by atmospheric turbulences into account. These manifest themselves in wavefront aberrations that need to be detected using wavefront sensors, and usually subsequently corrected using adaptive optical elements such as deformable mirrors. In ocular diagnostics on the other hand wavefront aberrations carry important information about the quality of the lens of the eye and also find application in optical coherence tomography (OCT) for high resolution imaging of the retina. Typical approaches in these fields involve Shack-Hartmann (SH) sensing and interferometric approaches as reviewed in chapter 3 of [248]. These solutions either require post-processing (SH) or are based on bulk-optical components in the case of interferometric approaches. The object-plane phase-sensing approaches investigated in this thesis carry potential to develop novel compact solutions for all-optical real-time sensing of wavefront aberations in these fields and should be considered in future research.

7.2.5 Biological Applications

In the introduction to this thesis we stated the relevance of visualization of phase gradients in wavefields for biological applications, in particular the characterization of internal cell structures with low amplitude contrast [249]. The visualization of changes in red-blood cells for example is crucial in the detection of medical conditions such as sickle disease as well as infectious diseases like malaria [250]. Furthermore we discussed the unavailability of compact phase-imaging solutions that do not require computational postprocessing or exogenous contrast agents. The research in this thesis has provided a proof-of-concept demonstration for biological image processing using MIM absorbers and plasmonic RWGs indicating significant potential for application in live-cell and tissue imaging. Owing to their operation in transmission, RWGs in particular carry vast potential to serve as metasurface-enhanced microscope coverslips enabling real-time manipulation of the images of biological samples directly placed on its surface. Further employing the structures investigated in this thesis for edge-detection and phase-imaging of biological cells would therefore be a major step towards the transition from proof-of-concept to applicable biomedical devices. Future versions of the developed systems could potentially also enable quantitative phase imaging (QPI) approaches. These comprise techniques that enable precise quantification of phase shifts induced by a specimen and is an essential tool for quantitative research on physiological processes of living cells [20, 251]. Such methods would also enable the detection of quantitative 3D-data describing the spatial profile of a given biological specimen. To achieve this quantitative 3D imaging, direct mapping between obtained intensity in filtered images and spatial frequency in the original wavefield will be crucial. This can for example be achieved through a device with an asymmetric, linear optical transfer function.

Nanophotonic systems with angular sensitivity could also be employed to enhance existing optical imaging technology. Fluorescence microscopy is a widely employed method in cellular biology and relies on labeling elements of a cell with quantum dots or other fluorescent molecules [252–254]. Gaining control over the angular emission patterns of fluorophores has advantages in terms of energy efficiency and selectivity in molecular applications. Exploiting plasmonic resonances to achieve this goal has received considerable attention [255–258]. The angular filtering ability arising from plasmonic metasurfaces and thin-film devices as investigated in this thesis could be exploited to manipulate or enhance the directional emission of quantum dots and other fluorescent molecules and should be considered in future research.

7.2.6 Mobile Imaging Devices

Ultra-compact image processing systems could in the future be integrated into mobile devices. While the current versions of the investigated nanophotonic filters still require optical components such as microscope objectives for the magnification or demagnification of images, compound optical devices that incorporate flat optical lenses could eliminate this requirement and realize ultra-compact systems that perform the imaging and image-processing step. This has previously been demonstrated by Zhou et al. [51]. A major application in this field is low-cost, mobile medical imaging equipment. In remote regions of developing countries, conventional imaging technology is often unavailable for medical diagnostics which is regarded as major cause for the high morbidity rate of infectious diseases such as malaria [259]. Innovative solutions that enable existing camera technology in smartphones to serve as medical diagnostic tools have recently gained attention [260–262]. Integration of meta-optical image processing devices with the recording, processing and connectivity features of smartphones, is therefore a promising pathway to make live-saving technology available to millions of people.

7.2.7 Optical Security Features

Finally, in addition to imaging applications the visible effects inherent in many optical metasurface- and thin-film designs open up perspectives for optical security features. The trade of counterfeit goods is today ranked among the top two profitable markets for criminal organizations worldwide making up approximately 39% of illegal profits. It is second only to global drug trafficking [263, 264]. The range of affected goods spans from apparel through mechanical and electronic components and currencies. Apart from the severe hazards that low-quality counterfeit goods such as pharmaceuticals pose to customers, remarkable economic losses are incurred every year [263]. This situation implies a direct demand for optical security features that enable efficient differentiation between genuine and counterfeit versions of a merchandise. On one hand such security features need to be easy to use throughout supply chains and by customers, as well as easy and cost efficient to fabricate. On the other hand, their fabrication needs to be largely inaccessible to counterfeiters [263]. Optical metasurfaces are promising candidates for next generation optical security features fulfilling these conditions [136, 265]. Angular sensitive features, which do not rely on conventional diffraction gratings but rather on phase-sensitive nanophotonic devices as investigated in this thesis, could pave the way towards a new class of optical anti-counterfeit labels.

7.3 Conclusion

This thesis has contributed to the development of all-optical information processing platforms with the capacity to be integrated into next generation ultra-compact imaging systems. Suggestions for extensions of the presented research as discussed above are promising pathways to enable the transition from the proofs-of-concept demonstrated here to scientific and industrial applications including biomedical imaging.

Bibliography

[1] D. L. Hoffmann, C. D. Standish, M. García-Diez, P. B. Pettitt, J. A. Milton, J. Zilhão, J. J. Alcolea-González, P. Cantalejo-Duarte, H. Collado, R. De Balbín, *et al.*, "U-Th dating of carbonate crusts reveals Neandertal origin of Iberian cave art," *Science*, vol. 359, no. 6378, pp. 912–915, 2018.

[2] W. Burger, M. J. Burge, M. J. Burge, and M. J. Burge, *Principles of Digital Image Processing.* Springer, 2009.

[3] P. J. Hutzler, "Spatial frequency filtering and its application to microscopy," *Applied Optics*, vol. 16, no. 8, pp. 2264–2272, 1977.

[4] A. Barty, K. Nugent, D. Paganin, and A. Roberts, "Quantitative optical phase microscopy," *Optics Letters*, vol. 23, no. 11, pp. 817–819, 1998.

[5] F. Zernike, "Phase contrast, a new method for the microscopic observation of transparent objects," *Physica*, 1942.

[6] B. Abbey, K. A. Nugent, G. J. Williams, J. N. Clark, A. G. Peele, M. A. Pfeifer, M. De Jonge, and I. McNulty, "Keyhole coherent diffractive imaging," *Nature Physics*, vol. 4, no. 5, pp. 394–398, 2008.

[7] D. B. Murphy, *Fundamentals of Light Microscopy and Electronic Imaging.* John Wiley & Sons, 2002.

[8] E. Panchenko, J. J. Cadusch, T. D. James, and A. Roberts, "Plasmonic metasurface-enabled differential photodetectors for broadband optical polarization characterization," *ACS Photonics*, vol. 3, no. 10, pp. 1833–1839, 2016.

[9] I. Pitas, *Digital Image Processing Algorithms and Applications.* John Wiley & Sons, 2000.

[10] B. C. Reed, J. F. Brown, D. VanderZee, T. R. Loveland, J. W. Merchant, and D. O. Ohlen, "Measuring phenological variability from satellite imagery," *Journal of Vegetation Science*, vol. 5, no. 5, pp. 703–714, 1994.

[11] S. L. Ozesmi and M. E. Bauer, "Satellite remote sensing of wetlands," *Wetlands Ecology and Management*, vol. 10, no. 5, pp. 381–402, 2002.

[12] R. V. Martin, "Satellite remote sensing of surface air quality," *Atmospheric Environment*, vol. 42, no. 34, pp. 7823–7843, 2008.

[13] D. J. Rogers, S. E. Randolph, R. W. Snow, and S. I. Hay, "Satellite imagery in the study and forecast of malaria," *Nature*, vol. 415, no. 6872, pp. 710–715, 2002.

[14] S. Wolfert, L. Ge, C. Verdouw, and M.-J. Bogaardt, "Big data in smart farming–a review," *Agricultural Systems*, vol. 153, pp. 69–80, 2017.

[15] J. G. A. Barbedo, "Digital image processing techniques for detecting, quantifying and classifying plant diseases," *SpringerPlus*, vol. 2, no. 1, p. 660, 2013.

[16] V. Bolón-Canedo, N. Sánchez-Maroño, and A. Alonso-Betanzos, "Recent advances and emerging challenges of feature selection in the context of big data," *Knowledge-Based Systems*, vol. 86, pp. 33–45, 2015.

[17] J. Bouwmeester and J. Guo, "Survey of worldwide pico-and nanosatellite missions, distributions and subsystem technology," *Acta Astronautica*, vol. 67, no. 7-8, pp. 854–862, 2010.

[18] C. Reddy, T. J. Beveridge, J. A. Breznak, and G. Marzluf, *Methods for general and molecular microbiology.* American Society for Microbiology Press, 2007.

[19] A. Diaspro, *Optical fluorescence microscopy: From the spectral to the nano dimension.* Springer Science & Business Media, 2010.

[20] Y. Park, C. Depeursinge, and G. Popescu, "Quantitative phase imaging in biomedicine," *Nature Photonics*, vol. 12, no. 10, pp. 578–589, 2018.

[21] L. Cutrona, E. Leith, C. Palermo, and L. Porcello, "Optical data processing and filtering systems," *IRE Transactions on Information Theory*, vol. 6, no. 3, pp. 386–400, 1960.

[22] J. W. Goodman, *Introduction to Fourier optics.* Roberts and Company Publishers, 2005.

[23] B. C. Platt and R. Shack, "History and principles of Shack-Hartmann wavefront sensing," *Journal of Refractive Surgery*, vol. 17, no. 5, pp. S573–S577, 2001.

[24] D. R. Solli and B. Jalali, "Analog optical computing," *Nature Photonics*, vol. 9, no. 11, p. 704, 2015.

[25] C. M. Soukoulis and M. Wegener, "Past achievements and future challenges in the development of three-dimensional photonic metamaterials," *Nature Photonics*, vol. 5, no. 9, pp. 523–530, 2011.

[26] E. Plum, J. Zhou, J. Dong, V. Fedotov, T. Koschny, C. Soukoulis, and N. Zheludev, "Metamaterial with negative index due to chirality," *Physical Review B*, vol. 79, no. 3, p. 035407, 2009.

[27] N. Landy, S. Sajuyigbe, J. J. Mock, D. R. Smith, and W. J. Padilla, "Perfect metamaterial absorber," *Physical Review Letters*, vol. 100, no. 20, p. 207402, 2008.

[28] M. Decker, R. Zhao, C. Soukoulis, S. Linden, and M. Wegener, "Twisted split-ring-resonator photonic metamaterial with huge optical activity," *Optics Letters*, vol. 35, no. 10, pp. 1593–1595, 2010.

[29] N. Meinzer, W. L. Barnes, and I. R. Hooper, "Plasmonic meta-atoms and metasurfaces," *Nature Photonics*, vol. 8, no. 12, p. 889, 2014.

[30] P. Genevet, F. Capasso, F. Aieta, M. Khorasaninejad, and R. Devlin, "Recent advances in planar optics: from plasmonic to dielectric metasurfaces," *Optica*, vol. 4, no. 1, pp. 139–152, 2017.

[31] S. M. Kamali, E. Arbabi, A. Arbabi, and A. Faraon, "A review of dielectric optical metasurfaces for wavefront control," *Nanophotonics*, vol. 7, no. 6, pp. 1041–1068, 2018.

[32] A. V. Kildishev, A. Boltasseva, and V. M. Shalaev, "Planar photonics with metasurfaces," *Science*, vol. 339, no. 6125, p. 1232009, 2013.

[33] P. R. West, J. L. Stewart, A. V. Kildishev, V. M. Shalaev, V. V. Shkunov, F. Strohkendl, Y. A. Zakharenkov, R. K. Dodds, and R. Byren, "All-dielectric subwavelength metasurface focusing lens," *Optics Express*, vol. 22, no. 21, pp. 26212–26221, 2014.

[34] A. Arbabi, Y. Horie, A. J. Ball, M. Bagheri, and A. Faraon, “Subwavelength-thick lenses with high numerical apertures and large efficiency based on high-contrast transmitarrays,” *Nature Communications*, vol. 6, no. 1, pp. 1–6, 2015.

[35] L. Huang, X. Chen, H. Muhlenbernd, G. Li, B. Bai, Q. Tan, G. Jin, T. Zentgraf, and S. Zhang, “Dispersionless phase discontinuities for controlling light propagation,” *Nano Letters*, vol. 12, no. 11, pp. 5750–5755, 2012.

[36] N. Yu, F. Aieta, P. Genevet, M. A. Kats, Z. Gaburro, and F. Capasso, “A broadband, background-free quarter-wave plate based on plasmonic metasurfaces,” *Nano Letters*, vol. 12, no. 12, pp. 6328–6333, 2012.

[37] B. Walther, C. Helgert, C. Rockstuhl, F. Setzpfandt, F. Eilenberger, E.-B. Kley, F. Lederer, A. Tünnermann, and T. Pertsch, “Spatial and spectral light shaping with metamaterials,” *Advanced Materials*, vol. 24, no. 47, pp. 6300–6304, 2012.

[38] J. Lin, P. Genevet, M. A. Kats, N. Antoniou, and F. Capasso, “Nanostructured holograms for broadband manipulation of vector beams,” *Nano Letters*, vol. 13, no. 9, pp. 4269–4274, 2013.

[39] A. Silva, F. Monticone, G. Castaldi, V. Galdi, A. Alù, and N. Engheta, “Performing mathematical operations with metamaterials,” *Science*, vol. 343, no. 6167, pp. 160–163, 2014.

[40] S. K. Case, “Fourier processing in the object plane,” *Optics Letters*, vol. 4, no. 9, pp. 286–288, 1979.

[41] G. Molesini, “Fourier processing with phase-reflection gratings,” *Optics Letters*, vol. 8, no. 9, pp. 465–467, 1983.

[42] G. Molesini and F. Quercioli, “Interference filters as Fourier processors,” *Applied Optics*, vol. 20, no. 11, pp. 1893–1893, 1981.

[43] L. L. Doskolovich, D. A. Bykov, E. A. Bezus, and V. A. Soifer, “Spatial differentiation of optical beams using phase-shifted Bragg grating,” *Optics Letters*, vol. 39, pp. 1278–1281, 2014.

[44] D. A. Bykov, L. L. Doskolovich, E. A. Bezus, and V. A. Soifer, “Optical computation of the Laplace operator using phase-shifted Bragg grating,” *Optics Express*, vol. 22, no. 21, pp. 25084–25092, 2014.

[45] T. Zhu, Y. Zhou, Y. Lou, H. Ye, M. Qiu, Z. Ruan, and S. Fan, “Plasmonic computing of spatial differentiation,” *Nature Communications*, vol. 8, no. 1, pp. 1–6, 2017.

[46] A. Youssefi, F. Zangeneh-Nejad, S. Abdollahramezani, and A. Khavasi, “Analog computing by Brewster effect,” *Optics Letters*, vol. 41, no. 15, pp. 3467–3470, 2016.

[47] T. Zhu, Y. Lou, Y. Zhou, J. Zhang, J. Huang, Y. Li, H. Luo, S. Wen, S. Zhu, Q. Gong, *et al.*, “Generalized spatial differentiation from the spin hall effect of light and its application in image processing of edge detection,” *Physical Review Applied*, vol. 11, no. 3, p. 034043, 2019.

[48] N. V. Golovastikov, D. A. Bykov, and L. L. Doskolovich, “Resonant diffraction gratings for spatial differentiation of optical beams,” *Quantum Electronics*, vol. 44, no. 10, p. 984, 2014.

[49] D. A. Bykov, L. L. Doskolovich, A. A. Morozov, V. V. Podlipnov, E. A. Bezus, P. Verma, and V. A. Soifer, “First-order optical spatial differentiator based on a guided-mode resonant grating,” *Optics Express*, vol. 26, no. 8, pp. 10997–11006, 2018.

[50] C. Guo, M. Xiao, M. Minkov, Y. Shi, and S. Fan, “Photonic crystal slab laplace operator for image differentiation,” *Optica*, vol. 5, no. 3, pp. 251–256, 2018.

[51] Y. Zhou, H. Zheng, I. I. Kravchenko, and J. Valentine, “Flat optics for image differentiation,” *Nature Photonics*, vol. 14, no. 5, pp. 316–323, 2020.

[52] T. Davis, K. Vernon, and G. D. of Physics, “A plasmonic “ac Wheatstone bridge” circuit for high-sensitivity phase measurement and single-molecule detection,” *Journal of Applied Physics*, 2009.

[53] A. Roberts, T. J. Davis, and D. E. Gomez, “Dark mode metasurfaces: sensing optical phase difference with subradiant modes and Fano resonances,” *Journal of the Optical Society of America B*, vol. 34, no. 7, pp. D95–D100, 2017.

[54] W. Wu, W. Jiang, J. Yang, S. Gong, and Y. Ma, “Multilayered analog optical differentiating device: performance analysis on structural parameters,” *Optics Letters*, vol. 42, pp. 5270–5273, 2017.

[55] A. Saba, M. R. Tavakol, P. Karimi-Khoozani, and A. Khavasi, "Two-dimensional edge detection by guided mode resonant metasurface," *IEEE Photonics Technology Letters*, vol. 30, no. 9, pp. 853–856, 2018.

[56] H. Kwon, D. Sounas, A. Cordaro, A. Polman, and A. Alù, "Nonlocal metasurfaces for optical signal processing," *Physical Review Letters*, vol. 121, no. 17, p. 173004, 2018.

[57] A. Roberts, D. E. Gómez, and T. J. Davis, "Optical image processing with metasurface dark modes," *Journal of the Optical Society of America A*, vol. 35, no. 9, pp. 1575–1584, 2018.

[58] Y. Hwang and T. J. Davis, "Optical metasurfaces for subwavelength difference operations," *Applied Physics Letters*, vol. 109, no. 18, p. 181101, 2016.

[59] B. Vohnsen and D. Valente, "Surface-plasmon-based wavefront sensing," *Optica*, vol. 2, no. 12, pp. 1024–1027, 2015.

[60] L. Wesemann, E. Panchenko, K. Singh, E. Della Gaspera, D. E. Gómez, T. J. Davis, and A. Roberts, "Selective near-perfect absorbing mirror as a spatial frequency filter for optical image processing," *APL Photonics*, vol. 4, no. 10, p. 100801, 2019.

[61] L. Wesemann, P. Achmari, K. Singh, E. Panchenko, T. D. James, D. E. Gómez, T. J. Davis, and A. Roberts, "Metasurfaces, dark modes, and high NA illumination," *OSA Continuum*, vol. 1, no. 2, pp. 727–735, 2018.

[62] A. Roberts, J. T. Davis, and L. Wesemann, "Electromagnetic filter device and method of use," 2019. In the name of The University of Melbourne, Australian Provisional Patent, Application No. 2019904670.

[63] L. Wesemann, E. Panchenko, K. Singh, D. E. Gomez, T. J. Davis, and A. Roberts, "Plasmonic metasurfaces for optical information processing," in *SPIE Micro + Nano Materials, Devices, and Applications 2019* (M. C. Simpson and S. Juodkazis, eds.), vol. 11201, pp. 18 – 19, International Society for Optics and Photonics, SPIE, 2019.

[64] C.-C. Tseng, S.-C. Pei, and S.-C. Hsia, "Computation of fractional derivatives using Fourier transform and digital FIR differentiator," *Signal Processing*, vol. 80, no. 1, pp. 151–159, 2000.

[65] E. Hewitt and R. E. Hewitt, "The Gibbs-Wilbraham phenomenon: an episode in Fourier analysis," *Archive for history of Exact Sciences*, vol. 21, no. 2, pp. 129–160, 1979.

[66] A. Cordaro, H. Kwon, D. Sounas, A. F. Koenderink, A. Alù, and A. Polman, "High-index dielectric metasurfaces performing mathematical operations," *Nano Letters*, vol. 19, no. 12, pp. 8418–8423, 2019.

[67] A. K. Cherri and M. A. Karim, "Optical symbolic substitution: edge detection using prewitt, sobel, and roberts operators," *Applied Optics*, vol. 28, no. 21, pp. 4644–4648, 1989.

[68] R. C. Anderson and S. Lewis, "Flow visualization by dark central ground interferometry," *Applied Optics*, vol. 24, no. 22, pp. 3687–3687, 1985.

[69] H. Taylor and J. Waldram, "Improvements in the Schlieren method," *Journal of Scientific Instruments*, vol. 10, no. 12, p. 378, 1933.

[70] G. S. Settles, *Schlieren and Shadowgraph Techniques: Visualizing Penomena in Transparent Media.* Springer Science & Business Media, 2012.

[71] "Nobel prize 1953 - Frits Zernike." `https://www.nobelprize.org/prizes/physics/1953/summary/`. Accessed: 2020-06-22.

[72] S. E. Umbaugh, *Digital Image Processing and Analysis: Human and Computer Vision Applications with CVIPtools.* CRC press, 2010.

[73] A. Pors, M. G. Nielsen, and S. I. Bozhevolnyi, "Analog computing using reflective plasmonic metasurfaces," *Nano Letters*, vol. 15, no. 1, pp. 791–797, 2015.

[74] H. A. Macleod and H. A. Macleod, *Thin-film Optical Filters.* CRC press, 2010.

[75] S. A. Maier, *Plasmonics: Fundamentals and Applications.* Springer, 2007.

[76] P. B. Johnson and R.-W. Christy, "Optical constants of the noble metals," *Physical Review B*, vol. 6, no. 12, p. 4370, 1972.

[77] W. L. Barnes, A. Dereux, and T. W. Ebbesen, "Surface plasmon subwavelength optics," *Nature*, vol. 424, no. 6950, pp. 824–830, 2003.

[78] M. D. Malinsky, K. L. Kelly, G. C. Schatz, and R. P. Van Duyne, “Chain length dependence and sensing capabilities of the localized surface plasmon resonance of silver nanoparticles chemically modified with alkanethiol self-assembled monolayers,” *Journal of the American Chemical Society*, vol. 123, no. 7, pp. 1471–1482, 2001.

[79] F. Hao, P. Nordlander, Y. Sonnefraud, P. Dorpe, and S. A. Maier, “Tunability of subradiant dipolar and Fano-Type plasmon resonances in metallic Ring/Disk cavities: Implications for nanoscale optical sensing,” *ACS Nano*, vol. 3, no. 3, pp. 643–652, 2009.

[80] M. Lippitz, M. A. van Dijk, and M. Orrit, “Third-harmonic generation from single gold nanoparticles,” *Nano Letters*, vol. 5, no. 4, pp. 799–802, 2005.

[81] L. J. Sherry, S.-H. Chang, G. C. Schatz, R. P. Van Duyne, B. J. Wiley, and Y. Xia, “Localized surface plasmon resonance spectroscopy of single silver nanocubes,” *Nano Letters*, vol. 5, no. 10, pp. 2034–2038, 2005.

[82] S. Link and M. A. El-Sayed, “Spectral properties and relaxation dynamics of surface plasmon electronic oscillations in gold and silver nanodots and nanorods,” *The Journal of Physical Chemistry B*, vol. 103, no. 40, pp. 8410–8426, 1999.

[83] I. Pastoriza-Santos and L. M. Liz-Marzán, “Synthesis of silver nanoprisms in DMF,” *Nano Letters*, vol. 2, no. 8, pp. 903–905, 2002.

[84] S. Oldenburg, R. Averitt, S. Westcott, and N. Halas, “Nanoengineering of optical resonances,” *Chemical Physics Letters*, vol. 288, no. 2-4, pp. 243–247, 1998.

[85] J. Aizpurua, P. Hanarp, D. Sutherland, M. Käll, G. W. Bryant, and F. G. De Abajo, “Optical properties of gold nanorings,” *Physical Review Letters*, vol. 90, no. 5, p. 057401, 2003.

[86] S. A. M. Anatoly V. Zayats, *Active Plasmonics and Tuneable Plasmonic Metamaterials*. Wiley, 2013.

[87] E. Prodan, C. Radloff, N. J. Halas, and P. Nordlander, “A hybridization model for the plasmon response of complex nanostructures,” *Science*, vol. 302, no. 5644, pp. 419–422, 2003.

[88] P. Nordlander, C. Oubre, E. Prodan, K. Li, and M. Stockman, “Plasmon hybridization in nanoparticle dimers,” *Nano Letters*, vol. 4, no. 5, pp. 899–903, 2004.

[89] H. Wang, Y. Wu, B. Lassiter, C. L. Nehl, J. H. Hafner, P. Nordlander, and N. J. Halas, “Symmetry breaking in individual plasmonic nanoparticles,” *Proceedings of the National Academy of Sciences*, vol. 103, no. 29, pp. 10856–10860, 2006.

[90] J. Alegret, T. Rindzevicius, T. Pakizeh, Y. Alaverdyan, L. Gunnarsson, and M. Kall, “Plasmonic properties of silver trimers with trigonal symmetry fabricated by electron-beam lithography,” *The Journal of Physical Chemistry C*, vol. 112, no. 37, pp. 14313–14317, 2008.

[91] C. W. Hsu, B. Zhen, A. D. Stone, J. D. Joannopoulos, and M. Soljačić, “Bound states in the continuum,” *Nature Reviews Materials*, vol. 1, no. 9, pp. 1–13, 2016.

[92] D. Marinica, A. Borisov, and S. Shabanov, “Bound states in the continuum in photonics,” *Physical Review Letters*, vol. 100, no. 18, p. 183902, 2008.

[93] D. Gómez, Z. Teo, M. Altissimo, T. Davis, S. Earl, and A. Roberts, “The dark side of plasmonics,” *Nano Letters*, vol. 13, no. 8, pp. 3722–3728, 2013.

[94] P. Achmari, “Characterisation of sub-radiant modes of metasurfaces,” Master’s thesis, The University of Melbourne, School of Physics, 2016.

[95] A. L. Koh, K. Bao, I. Khan, W. E. Smith, G. Kothleitner, P. Nordlander, S. A. Maier, and D. W. McComb, “Electron energy-loss spectroscopy (EELS) of surface plasmons in single silver nanoparticles and dimers: influence of beam damage and mapping of dark modes,” *ACS nano*, vol. 3, no. 10, pp. 3015–3022, 2009.

[96] S.-C. Yang, H. Kobori, C.-L. He, M.-H. Lin, H.-Y. Chen, C. Li, M. Kanehara, T. Teranishi, and S. Gwo, “Plasmon hybridization in individual gold nanocrystal dimers: direct observation of bright and dark modes,” *Nano Letters*, vol. 10, no. 2, pp. 632–637, 2010.

[97] W. Zhou and T. W. Odom, “Tunable subradiant lattice plasmons by out-of-plane dipolar interactions,” *Nature Nanotechnology*, vol. 6, no. 7, pp. 423–427, 2011.

[98] G. Volpe, S. Cherukulappurath, R. Juanola Parramon, G. Molina-Terriza, and R. Quidant, “Controlling the optical near field of nanoantennas with spatial phase-shaped beams,” *Nano Letters*, vol. 9, no. 10, pp. 3608–3611, 2009.

[99] A. Yanai, M. Grajower, G. M. Lerman, M. Hentschel, H. Giessen, and U. Levy, "Near- and far-field properties of plasmonic oligomers under radially and azimuthally polarized light excitation.," *ACS Nano*, vol. 8, no. 5, pp. 4969–74, 2014.

[100] N. Yu and F. Capasso, "Flat optics with designer metasurfaces," *Nature Materials*, vol. 13, no. 2, pp. 139–150, 2014.

[101] J. Imbrock, L. Wesemann, S. Kroesen, M. Ayoub, and C. Denz, "Waveguide-integrated three-dimensional quasi-phase-matching structures," *Optica*, vol. 7, no. 1, pp. 28–34, 2020.

[102] Y. Lee, S.-J. Kim, H. Park, and B. Lee, "Metamaterials and metasurfaces for sensor applications," *Sensors*, vol. 17, no. 8, p. 1726, 2017.

[103] L. Novotny, "Effective wavelength scaling for optical antennas," *Physical Review Letters*, vol. 98, no. 26, p. 266802, 2007.

[104] F. Falcone, T. Lopetegi, M. Laso, J. Baena, J. Bonache, M. Beruete, R. Marqués, F. Martín, and M. Sorolla, "Babinet principle applied to the design of metasurfaces and metamaterials," *Physical Review Letters*, vol. 93, no. 19, p. 197401, 2004.

[105] N. Yu, P. Genevet, M. A. Kats, F. Aieta, J. Tetienne, F. Capasso, and Z. Gaburro, "Light propagation with phase discontinuities: Generalized laws of reflection and refraction," *Science*, vol. 334, no. 6054, pp. 333–337, 2011.

[106] A. E. Nikolaenko, F. De Angelis, S. A. Boden, N. Papasimakis, P. Ashburn, E. Di Fabrizio, and N. I. Zheludev, "Carbon nanotubes in a photonic metamaterial," *Physical Review Letters*, vol. 104, no. 15, p. 153902, 2010.

[107] A. Arbabi, R. M. Briggs, Y. Horie, M. Bagheri, and A. Faraon, "Efficient dielectric metasurface collimating lenses for mid-infrared quantum cascade lasers," *Optics Express*, vol. 23, no. 26, pp. 33310–33317, 2015.

[108] M. Khorasaninejad, W. T. Chen, R. C. Devlin, J. Oh, A. Y. Zhu, and F. Capasso, "Metalenses at visible wavelengths: Diffraction-limited focusing and subwavelength resolution imaging," *Science*, vol. 352, no. 6290, pp. 1190–1194, 2016.

[109] A. Arbabi, Y. Horie, M. Bagheri, and A. Faraon, "Dielectric metasurfaces for complete control of phase and polarization with subwavelength spatial resolution and high transmission," *Nature Nanotechnology*, vol. 10, no. 11, p. 937, 2015.

[110] A. E. Minovich, A. E. Miroshnichenko, A. Y. Bykov, T. V. Murzina, D. N. Neshev, and Y. S. Kivshar, “Functional and nonlinear optical metasurfaces,” *Laser & Photonics Reviews*, vol. 9, no. 2, pp. 195–213, 2015.

[111] A. Pors and S. I. Bozhevolnyi, “Plasmonic metasurfaces for efficient phase control in reflection,” *Optics Express*, vol. 21, no. 22, pp. 27438–27451, 2013.

[112] S. Sun, K.-Y. Yang, C.-M. Wang, T.-K. Juan, W. T. Chen, C. Y. Liao, Q. He, S. Xiao, W.-T. Kung, G.-Y. Guo, *et al.*, “High-efficiency broadband anomalous reflection by gradient meta-surfaces,” *Nano Letters*, vol. 12, no. 12, pp. 6223–6229, 2012.

[113] P. Lalanne and P. Chavel, “Metalenses at visible wavelengths: past, present, perspectives,” *Laser & Photonics Reviews*, vol. 11, no. 3, p. 1600295, 2017.

[114] R. Paniagua-Dominguez, Y. F. Yu, E. Khaidarov, S. Choi, V. Leong, R. M. Bakker, X. Liang, Y. H. Fu, V. Valuckas, L. A. Krivitsky, *et al.*, “A metalens with a near-unity numerical aperture,” *Nano Letters*, vol. 18, no. 3, pp. 2124–2132, 2018.

[115] M. Mutlu, A. E. Akosman, G. Kurt, M. Gokkavas, and E. Ozbay, “Experimental realization of a high-contrast grating based broadband quarter-wave plate,” *Optics Express*, vol. 20, no. 25, pp. 27966–27973, 2012.

[116] X. Ni, S. Ishii, A. V. Kildishev, and V. M. Shalaev, “Ultra-thin, planar, babinet-inverted plasmonic metalenses,” *Light: Science & Applications*, vol. 2, no. 4, pp. e72–e72, 2013.

[117] P. Genevet, N. Yu, F. Aieta, J. Lin, M. A. Kats, R. Blanchard, M. O. Scully, Z. Gaburro, and F. Capasso, “Ultra-thin plasmonic optical vortex plate based on phase discontinuities,” *Applied Physics Letters*, vol. 100, no. 1, p. 013101, 2012.

[118] E. Karimi, S. A. Schulz, I. De Leon, H. Qassim, J. Upham, and R. W. Boyd, “Generating optical orbital angular momentum at visible wavelengths using a plasmonic metasurface,” *Light: Science & Applications*, vol. 3, no. 5, pp. e167–e167, 2014.

[119] X. Ni, A. V. Kildishev, and V. M. Shalaev, “Metasurface holograms for visible light,” *Nature Communications*, vol. 4, no. 1, pp. 1–6, 2013.

[120] B. Wang, F. Dong, Q.-T. Li, D. Yang, C. Sun, J. Chen, Z. Song, L. Xu, W. Chu, Y.-F. Xiao, *et al.*, “Visible-frequency dielectric metasurfaces for multiwavelength

achromatic and highly dispersive holograms," *Nano Letters*, vol. 16, no. 8, pp. 5235–5240, 2016.

[121] L. Wang, S. Kruk, H. Tang, T. Li, I. Kravchenko, D. N. Neshev, and Y. S. Kivshar, "Grayscale transparent metasurface holograms," *Optica*, vol. 3, no. 12, pp. 1504–1505, 2016.

[122] X. Zhang, J. Jin, Y. Wang, M. Pu, X. Li, Z. Zhao, P. Gao, C. Wang, and X. Luo, "Metasurface-based broadband hologram with high tolerance to fabrication errors," *Scientific Reports*, vol. 6, p. 19856, 2016.

[123] T. D. James, P. Mulvaney, and A. Roberts, "The plasmonic pixel: large area, wide gamut color reproduction using aluminum nanostructures," *Nano Letters*, vol. 16, no. 6, pp. 3817–3823, 2016.

[124] E. Panchenko, L. Wesemann, D. E. Gómez, T. D. James, T. J. Davis, and A. Roberts, "Ultracompact camera pixel with integrated plasmonic color filters," *Advanced Optical Materials*, vol. 7, no. 23, p. 1900893, 2019.

[125] T. Vo-Dinh, "Surface-enhanced raman spectroscopy using metallic nanostructures," *TrAC Trends in Analytical Chemistry*, vol. 17, no. 8-9, pp. 557–582, 1998.

[126] M. Moskovits, "Surface-enhanced raman spectroscopy: a brief retrospective," *Journal of Raman Spectroscopy*, vol. 36, no. 6-7, pp. 485–496, 2005.

[127] S. J. Lee, Z. Guan, H. Xu, and M. Moskovits, "Surface-enhanced raman spectroscopy and nanogeometry: The plasmonic origin of SERS," *The Journal of Physical Chemistry C*, vol. 111, no. 49, pp. 17985–17988, 2007.

[128] C. Andreou, R. Mirsafavi, M. Moskovits, and C. D. Meinhart, "Detection of low concentrations of ampicillin in milk," *Analyst*, vol. 140, no. 15, pp. 5003–5005, 2015.

[129] K. Kneipp, A. S. Haka, H. Kneipp, K. Badizadegan, N. Yoshizawa, C. Boone, K. E. Shafer-Peltier, J. T. Motz, R. R. Dasari, and M. S. Feld, "Surface-enhanced raman spectroscopy in single living cells using gold nanoparticles," *Applied Spectroscopy*, vol. 56, no. 2, pp. 150–154, 2002.

[130] S. Ayas, H. Guner, B. Turker, O. O. Ekiz, F. Dirisaglik, A. K. Okyay, and A. Dana, "Raman enhancement on a broadband meta-surface," *ACS nano*, vol. 6, no. 8, pp. 6852–6861, 2012.

[131] S. Romano, G. Zito, S. Manago, G. Calafiore, E. Penzo, S. Cabrini, A. C. De Luca, and V. Mocella, "Surface-enhanced raman and fluorescence spectroscopy with an all-dielectric metasurface," *The Journal of Physical Chemistry C*, vol. 122, no. 34, pp. 19738–19745, 2018.

[132] S. Yokogawa, S. P. Burgos, and H. A. Atwater, "Plasmonic color filters for cmos image sensor applications," *Nano Letters*, vol. 12, no. 8, pp. 4349–4354, 2012.

[133] Y. S. Do, J. H. Park, B. Y. Hwang, S.-M. Lee, B.-K. Ju, and K. C. Choi, "Plasmonic color filter and its fabrication for large-area applications," *Advanced Optical Materials*, vol. 1, no. 2, pp. 133–138, 2013.

[134] A. S. Roberts, A. Pors, O. Albrektsen, and S. I. Bozhevolnyi, "Subwavelength plasmonic color printing protected for ambient use," *Nano Letters*, vol. 14, no. 2, pp. 783–787, 2014.

[135] S. J. Tan, L. Zhang, D. Zhu, X. M. Goh, Y. M. Wang, K. Kumar, C.-W. Qiu, and J. K. Yang, "Plasmonic color palettes for photorealistic printing with aluminum nanostructures," *Nano Letters*, vol. 14, no. 7, pp. 4023–4029, 2014.

[136] F. Cheng, J. Gao, T. S. Luk, and X. Yang, "Structural color printing based on plasmonic metasurfaces of perfect light absorption," *Scientific Reports*, vol. 5, p. 11045, 2015.

[137] A. Kristensen, J. K. Yang, S. I. Bozhevolnyi, S. Link, P. Nordlander, N. J. Halas, and N. A. Mortensen, "Plasmonic colour generation," *Nature Reviews Materials*, vol. 2, no. 1, pp. 1–14, 2016.

[138] V. Vashistha, G. Vaidya, R. S. Hegde, A. E. Serebryannikov, N. Bonod, and M. Krawczyk, "All-dielectric metasurfaces based on cross-shaped resonators for color pixels with extended gamut," *ACS Photonics*, vol. 4, no. 5, pp. 1076–1082, 2017.

[139] L. Shang, W. Zhang, K. Xu, and Y. Zhao, "Bio-inspired intelligent structural color materials," *Materials Horizons*, vol. 6, no. 5, pp. 945–958, 2019.

[140] J. S. Clausen, E. Højlund-Nielsen, A. B. Christiansen, S. Yazdi, M. Grajower, H. Taha, U. Levy, A. Kristensen, and N. A. Mortensen, "Plasmonic metasurfaces for coloration of plastic consumer products," *Nano Letters*, vol. 14, no. 8, pp. 4499–4504, 2014.

[141] Y. Zhan, K. Wu, C. Zhang, S. Wu, and X. Li, “Infrared hot-carrier photodetection based on planar perfect absorber,” *Optics Letters*, vol. 40, no. 18, pp. 4261–4264, 2015.

[142] Y. Tian, F. P. García de Arquer, C.-T. Dinh, G. Favraud, M. Bonifazi, J. Li, M. Liu, X. Zhang, X. Zheng, M. G. Kibria, *et al.*, “Enhanced solar-to-hydrogen generation with broadband epsilon-near-zero nanostructured photocatalysts,” *Advanced Materials*, vol. 29, no. 27, p. 1701165, 2017.

[143] C. Ng, L. Wesemann, E. Panchenko, J. Song, T. J. Davis, A. Roberts, and D. E. Gómez, “Plasmonic near-complete optical absorption and its applications,” *Advanced Optical Materials*, vol. 7, no. 14, p. 1801660, 2019.

[144] T. Chung, S.-Y. Lee, E. Y. Song, H. Chun, and B. Lee, “Plasmonic nanostructures for nano-scale bio-sensing,” *Sensors*, vol. 11, no. 11, pp. 10907–10929, 2011.

[145] W. Xie and S. Schlücker, “Rationally designed multifunctional plasmonic nanostructures for surface-enhanced raman spectroscopy: a review,” *Reports on Progress in Physics*, vol. 77, no. 11, p. 116502, 2014.

[146] W. Liu, M. Li, R. S. Guzzon, E. J. Norberg, J. S. Parker, M. Lu, L. A. Coldren, and J. Yao, “A fully reconfigurable photonic integrated signal processor,” *Nature Photonics*, vol. 10, no. 3, pp. 190–195, 2016.

[147] M. Li, H.-S. Jeong, J. Azaña, and T.-J. Ahn, “25-Terahertz-bandwidth all-optical temporal differentiator,” *Optics Express*, vol. 20, no. 27, pp. 28273–28280, 2012.

[148] R. Slavík, Y. Park, N. Ayotte, S. Doucet, T.-J. Ahn, S. LaRochelle, and J. Azaña, “Photonic temporal integrator for all-optical computing,” *Optics Express*, vol. 16, no. 22, pp. 18202–18214, 2008.

[149] S. Tan, Z. Wu, L. Lei, S. Hu, J. Dong, and X. Zhang, “All-optical computation system for solving differential equations based on optical intensity differentiator,” *Optics Express*, vol. 21, no. 6, pp. 7008–7013, 2013.

[150] N. L. Kazanskiy, P. G. Serafimovich, and S. N. Khonina, “Use of photonic crystal cavities for temporal differentiation of optical signals,” *Optics Letters*, vol. 38, no. 7, pp. 1149–1151, 2013.

[151] L. M. Rivas, S. Boudreau, Y. Park, R. Slavík, S. LaRochelle, A. Carballar, and J. Azaña, "Experimental demonstration of ultrafast all-fiber high-order photonic temporal differentiators," *Optics Letters*, vol. 34, no. 12, pp. 1792–1794, 2009.

[152] N. Liu, M. Mesch, T. Weiss, M. Hentschel, and H. Giessen, "Infrared perfect absorber and its application as plasmonic sensor," *Nano Letters*, vol. 10, no. 7, pp. 2342–2348, 2010.

[153] Z. Fang, Y.-R. Zhen, L. Fan, X. Zhu, and P. Nordlander, "Tunable wide-angle plasmonic perfect absorber at visible frequencies," *Physical Review B*, vol. 85, no. 24, p. 245401, 2012.

[154] N. V. Golovastikov, D. A. Bykov, L. L. Doskolovich, and E. A. Bezus, "Spatial optical integrator based on phase-shifted bragg gratings," *Optics Communications*, vol. 338, pp. 457–460, 2015.

[155] A. Othonos, "Fiber bragg gratings," *Review of scientific instruments*, vol. 68, no. 12, pp. 4309–4341, 1997.

[156] R. Kashyap, *Fiber Bragg Gratings.* Academic press, 2009.

[157] M. Li, H. Li, and Y. Painchaud, "Multi-channel notch filter based on a phase-shifted phase-only-sampled fiber bragg grating," *Optics Express*, vol. 16, no. 23, pp. 19388–19394, 2008.

[158] N. K. Berger, B. Levit, B. Fischer, M. Kulishov, D. V. Plant, and J. Azaña, "Temporal differentiation of optical signals using a phase-shifted fiber bragg grating," *Optics Express*, vol. 15, no. 2, pp. 371–381, 2007.

[159] F. Zangeneh-Nejad and A. Khavasi, "Spatial integration by a dielectric slab and its planar graphene-based counterpart," *Optics Letters*, vol. 42, no. 10, pp. 1954–1957, 2017.

[160] F. Zangeneh-Nejad, A. Khavasi, and B. Rejaei, "Analog optical computing by half-wavelength slabs," *Optics Communications*, vol. 407, pp. 338–343, 2018.

[161] Z. Ruan, "Spatial mode control of surface plasmon polariton excitation with gain medium: from spatial differentiator to integrator," *Optics Letters*, vol. 40, no. 4, pp. 601–604, 2015.

[162] Y. Fang, Y. Lou, and Z. Ruan, “On-grating graphene surface plasmons enabling spatial differentiation in the terahertz region,” *Optics Letters*, vol. 42, pp. 3840–3843, OCT 1 2017.

[163] K. Y. Bliokh, F. J. Rodríguez-Fortuño, F. Nori, and A. V. Zayats, “Spin–orbit interactions of light,” *Nature Photonics*, vol. 9, no. 12, p. 796, 2015.

[164] G. Quaranta, G. Basset, O. J. Martin, and B. Gallinet, “Recent advances in resonant waveguide gratings,” *Laser & Photonics Reviews*, vol. 12, no. 9, p. 1800017, 2018.

[165] Y. Fang and Z. Ruan, “Optical spatial differentiator for a synthetic three-dimensional optical field,” *Optics letters*, vol. 43, no. 23, pp. 5893–5896, 2018.

[166] Z. Dong, J. Si, X. Yu, and X. Deng, “Optical spatial differentiator based on subwavelength high-contrast gratings,” *Applied Physics Letters*, vol. 112, p. 181102, 2018.

[167] W. Yang, X. Yu, J. Zhang, and X. Deng, “Plasmonic transmitted optical differentiator based on the subwavelength gold gratings,” *Optics Letters*, vol. 45, no. 8, pp. 2295–2298, 2020.

[168] N. M. Mojarad and M. Agio, “Tailoring the excitation of localized surface plasmon-polariton resonances by focusing radially-polarized beams,” *Optics Express*, vol. 17, no. 1, pp. 117–122, 2009.

[169] P. Nordlander, “The dark side of the ring,” *Nature Nanotechnology*, vol. 8, no. 2, pp. 76–77, 2013.

[170] Y. Hwang, T. J. Davis, J. Lin, and X.-C. Yuan, “Plasmonic circuit for second-order spatial differentiation at the subwavelength scale,” *Optics Express*, vol. 26, no. 6, pp. 7368–7375, 2018.

[171] T. Davis, F. Eftekhari, D. Gómez, and A. Roberts, “Metasurfaces with asymmetric optical transfer functions for optical signal processing,” *Physical Review Letters*, vol. 123, no. 1, p. 013901, 2019.

[172] K. Busch, M. Koenig, and J. Niegemann, “Discontinuous Galerkin methods in nanophotonics,” *Laser & Photonics Reviews*, vol. 5, no. 6, pp. 773–809, 2011.

[173] B. Gallinet, J. Butet, and O. J. Martin, "Numerical methods for nanophotonics: standard problems and future challenges," *Laser & Photonics Reviews*, vol. 9, no. 6, pp. 577–603, 2015.

[174] P. bai Zhou, *Numerical Analysis of Electromagnetic Fields.* Springer-Verlag Berlin Heidelberg New York, 1993.

[175] A. Taflove and S. C. Hagness, *Computational electrodynamics: the finite-difference time-domain method.* Artech house, 2005.

[176] M. Moharam and T. Gaylord, "Rigorous coupled-wave analysis of planar-grating diffraction," *Journal of the Optical Society of America*, vol. 71, no. 7, pp. 811–818, 1981.

[177] M. Moharam, E. B. Grann, D. A. Pommet, and T. Gaylord, "Formulation for stable and efficient implementation of the rigorous coupled-wave analysis of binary gratings," *Journal of the Optical Society of America A*, vol. 12, no. 5, pp. 1068–1076, 1995.

[178] T. Grosges, A. Vial, and D. Barchiesi, "Models of near-field spectroscopic studies: comparison between finite-element and finite-difference methods," *Optics Express*, vol. 13, no. 21, pp. 8483–8497, 2005.

[179] J. Smajic, C. Hafner, L. Raguin, K. Tavzarashvili, and M. Mishrikey, "Comparison of numerical methods for the analysis of plasmonic structures," *Journal of Computational and Theoretical Nanoscience*, vol. 6, no. 3, pp. 763–774, 2009.

[180] M. E. Solano, M. Faryad, A. Lakhtakia, and P. B. Monk, "Comparison of rigorous coupled-wave approach and finite element method for photovoltaic devices with periodically corrugated metallic backreflector," *Journal of the Optical Society of America A*, vol. 31, no. 10, pp. 2275–2284, 2014.

[181] C. M. Dissanayake, M. Premaratne, I. D. Rukhlenko, and G. P. Agrawal, "FDTD modeling of anisotropic nonlinear optical phenomena in silicon waveguides," *Optics Express*, vol. 18, no. 20, pp. 21427–21448, 2010.

[182] M. Fujii, C. Koos, C. Poulton, J. Leuthold, and W. Freude, "Nonlinear FDTD analysis and experimental verification of four-wave mixing in InGaAsP-InP racetrack

microresonators," *IEEE Photonics Technology Letters*, vol. 18, no. 2, pp. 361–363, 2006.

[183] Z. Lin, T. Alcorn, M. Loncar, S. G. Johnson, and A. W. Rodriguez, "High-efficiency degenerate four-wave mixing in triply resonant nanobeam cavities," *Physical Review A*, vol. 89, no. 5, p. 053839, 2014.

[184] O. C. Zienkiewicz, R. L. Taylor, P. Nithiarasu, and J. Zhu, *The finite element method*, vol. 3. McGraw-hill London, 1977.

[185] P. G. Ciarlet, *The Finite Element Method for Elliptic Problems*, vol. 40. Siam, 2002.

[186] J.-M. Jin, *The Finite Element Method in Electromagnetics.* John Wiley & Sons, 2015.

[187] "COMSOL official website." `https://www.comsol.com/`. Accessed: 2020-02-27.

[188] K. S. Harsha, *Principles of Vapor Deposition of Thin Films.* Elsevier, 2005.

[189] N. Xu and S. E. Huq, "Novel cold cathode materials and applications," *Materials Science and Engineering: R: Reports*, vol. 48, no. 2-5, pp. 47–189, 2005.

[190] A. C. Jones and M. L. Hitchman, *Chemical Vapour Deposition: Precursors, Processes and Applications.* Royal society of chemistry, 2009.

[191] C. E. Morosanu, *Thin Films by Chemical Vapour Deposition*, vol. 7. Elsevier, 2016.

[192] O. Gabriel, S. Kirner, M. Klick, B. Stannowski, and R. Schlatmann, "Plasma monitoring and pecvd process control in thin film silicon-based solar cell manufacturing," *EPJ Photovoltaics*, vol. 5, p. 55202, 2014.

[193] K. Choy, "Chemical vapour deposition of coatings," *Progress in Materials Science*, vol. 48, no. 2, pp. 57–170, 2003.

[194] G. S. Tompa, "Plasma enhanced chemical vapor deposition system," Sept. 18 2001. US Patent 6,289,842.

[195] K. Seshan, *Handbook of Thin Film Deposition.* William Andrew, 2001.

[196] D. M. Tennant, "Progress and issues in e-beam and other top down nanolithography," *Journal of Vacuum Science & Technology A: Vacuum, Surfaces, and Films*, vol. 31, no. 5, p. 050813, 2013.

[197] H.-H. Hsiao, C. H. Chu, and D. P. Tsai, “Fundamentals and applications of metasurfaces,” *Small Methods*, vol. 1, no. 4, p. 1600064, 2017.

[198] C. S. Wu, Y. Makiuchi, and C. Chen, *High-energy Electron Beam Lithography for Nanoscale Fabrication.* InTech Europe: Rijeka, Croatia, 2010.

[199] H. Pfeiffer, “Variable spot shaping for electron-beam lithography,” *Journal of Vacuum Science and Technology*, vol. 15, no. 3, pp. 887–890, 1978.

[200] “BEAMER - electron- and laser-beam lithography software.” `https://www.genisys-gmbh.com/beamer.html`. Accessed: 2019-06-16.

[201] S. L. Flegler and S. L. Flegler, *Scanning & Transmission Electron Microscopy.* Oxford University Press, 1997.

[202] W. Zhou, R. Apkarian, Z. L. Wang, and D. Joy, “Fundamentals of scanning electron microscopy (SEM),” in *Scanning Microscopy For Nanotechnology*, pp. 1–40, Springer, 2006.

[203] “Hitachi launches world’s highest resolution FE-SEM.” `http://www.nanotech-now.com/news.cgi?story_id=42612`. Accessed: 2019-12-11.

[204] L. Reimer, *Scanning Electron Microscopy: Physics of Image Formation and Microanalysis*, vol. 45. Springer, 2013.

[205] M. Tare, O. R. Puli, S. M. Oros, and A. Singh, “Drosophila adult eye model to teach scanning electron microscopy in an undergraduate cell biology laboratory,” *Drosophila Information Service*, vol. 92, 2009.

[206] W. W. Salisbury, “Absorbent body for electromagnetic waves,” *US Patent 2599944A*, 1952.

[207] H. Shin, M. F. Yanik, S. Fan, R. Zia, and M. L. Brongersma, “Omnidirectional resonance in a metal–dielectric–metal geometry,” *Applied Physics Letters*, vol. 84, no. 22, pp. 4421–4423, 2004.

[208] S. Shu, Z. Li, and Y. Y. Li, “Triple-layer fabry-perot absorber with near-perfect absorption in visible and near-infrared regime,” *Optics express*, vol. 21, no. 21, pp. 25307–25315, 2013.

[209] M. Yan, “Metal–insulator–metal light absorber: a continuous structure,” *Journal of Optics*, vol. 15, no. 2, p. 025006, 2013.

[210] Y. Cui, Y. He, Y. Jin, F. Ding, L. Yang, Y. Ye, S. Zhong, Y. Lin, and S. He, “Plasmonic and metamaterial structures as electromagnetic absorbers,” *Laser & Photonics Reviews*, vol. 8, no. 4, pp. 495–520, 2014.

[211] H.-T. Chen, “Interference theory of metamaterial perfect absorbers,” *Optics express*, vol. 20, no. 7, pp. 7165–7172, 2012.

[212] B. J. Lee and Z. Zhang, “Design and fabrication of planar multilayer structures with coherent thermal emission characteristics,” *Journal of Applied Physics*, vol. 100, no. 6, p. 063529, 2006.

[213] Z. Li, S. Butun, and K. Aydin, “Large-area, lithography-free super absorbers and color filters at visible frequencies using ultrathin metallic films,” *ACS Photonics*, vol. 2, no. 2, pp. 183–188, 2015.

[214] J. R. Tischler, M. S. Bradley, and V. Bulović, “Critically coupled resonators in vertical geometry using a planar mirror and a 5 nm thick absorbing film,” *Optics letters*, vol. 31, no. 13, pp. 2045–2047, 2006.

[215] W. Streyer, S. Law, G. Rooney, T. Jacobs, and D. Wasserman, “Strong absorption and selective emission from engineered metals with dielectric coatings,” *Optics express*, vol. 21, no. 7, pp. 9113–9122, 2013.

[216] M. A. Kats, R. Blanchard, P. Genevet, and F. Capasso, “Nanometre optical coatings based on strong interference effects in highly absorbing media,” *Nature Materials*, vol. 12, no. 1, p. 20, 2013.

[217] I. Malitson, “Interspecimen comparison of the refractive index of fused silica,” *Journal of the Optical Society of America*, vol. 55, no. 10, pp. 1205–1209, 1965.

[218] P.-z. Yang, L.-m. Liu, J.-h. Mo, and W. Yang, “Characterization of PECVD grown porous SiO2 thin films with potential application in an uncooled infrared detector,” *Semiconductor Science and Technology*, vol. 25, no. 4, p. 045017, 2010.

[219] D. I. Yakubovsky, A. V. Arsenin, Y. V. Stebunov, D. Y. Fedyanin, and V. S. Volkov, “Optical constants and structural properties of thin gold films,” *Optics Express*, vol. 25, no. 21, pp. 25574–25587, 2017.

[220] M. Kinnunen, A. Kauppila, A. Karmenyan, and R. Myllylä, “Effect of the size and shape of a red blood cell on elastic light scattering properties at the single-cell level,” *Biomedical Optics Express*, vol. 2, no. 7, pp. 1803–1814, 2011.

[221] G. M. Hale and M. R. Querry, “Optical constants of water in the 200-nm to 200-μm wavelength region,” *Applied Optics*, vol. 12, no. 3, pp. 555–563, 1973.

[222] E. Evans and Y.-C. Fung, “Improved measurements of the erythrocyte geometry,” *Microvascular Research*, vol. 4, no. 4, pp. 335–347, 1972.

[223] M. Johnson, S. Shivkumar, and L. Berlowitz-Tarrant, “Structure and properties of filamentous green algae,” *Materials Science and Engineering: B*, vol. 38, no. 1-2, pp. 103–108, 1996.

[224] S. Wäldchen, J. Lehmann, T. Klein, S. Van De Linde, and M. Sauer, “Light-induced cell damage in live-cell super-resolution microscopy,” *Scientific Reports*, vol. 5, p. 15348, 2015.

[225] X. A. Zhang, A. Bagal, E. C. Dandley, J. Zhao, C. J. Oldham, B.-I. Wu, G. N. Parsons, and C.-H. Chang, “Ordered 3d thin-shell nanolattice materials with near-unity refractive indices,” *Advanced Functional Materials*, vol. 25, no. 42, pp. 6644–6649, 2015.

[226] J. Yu, Y. Shen, X. Liu, R. Fu, J. Zi, and Z. Zhu, “Absorption in one-dimensional metallic–dielectric photonic crystals,” *Journal of Physics: Condensed Matter*, vol. 16, no. 7, p. L51, 2004.

[227] J. Dong, G. Liang, Y. Chen, and H. Wang, “Robust absorption broadband in one-dimensional metallic-dielectric quasi-periodic structure,” *Optics express*, vol. 14, no. 5, pp. 2014–2020, 2006.

[228] M. Mansuripur, “Distribution of light at and near the focus of high-numerical-aperture objectives,” *Journal of the Optical Society of America A*, vol. 3, no. 12, pp. 2086–2093, 1986.

[229] M. Mansuripur, “Distribution of light at and near the focus of high-numerical-aperture objectives: erratum certain computational aspects of vector diffraction problems: erratum,” *Journal of the Optical Society of America A*, vol. 10, no. 2, pp. 382–383, 1993.

[230] K. Fan, I. V. Shadrivov, and W. J. Padilla, "Dynamic bound states in the continuum," *Optica*, vol. 6, no. 2, pp. 169–173, 2019.

[231] A. S. Kupriianov, Y. Xu, A. Sayanskiy, V. Dmitriev, Y. S. Kivshar, and V. R. Tuz, "Metasurface engineering through bound states in the continuum," *Physical Review Applied*, vol. 12, no. 1, p. 014024, 2019.

[232] K. Koshelev, A. Bogdanov, and Y. Kivshar, "Meta-optics and bound states in the continuum," *Science Bulletin*, vol. 64, no. 12, pp. 836–842, 2019.

[233] K. Okamoto, *Fundamentals of Optical Waveguides.* Academic press, 2006.

[234] R. Alferness, W. Burns, J. Donelly, I. Kaminow, H. Kogelnik, F. Leonberger, A. Milton, T. Tamir, and R. Tucker, *Guided-Wave Optoelectronics*, vol. 26. Springer Science & Business Media, 2013.

[235] "Mode solver for dielectric multilayer slab waveguides." `https://www.computational-photonics.eu/oms.html`. Accessed: 2020-04-03.

[236] T. Siefke, S. Kroker, K. Pfeiffer, O. Puffky, K. Dietrich, D. Franta, I. Ohlídal, A. Szeghalmi, E.-B. Kley, and A. Tünnermann, "Materials pushing the application limits of wire grid polarizers further into the deep ultraviolet spectral range," *Advanced Optical Materials*, vol. 4, no. 11, pp. 1780–1786, 2016.

[237] S. Sarkar, V. Gupta, M. Kumar, J. Schubert, P. T. Probst, J. Joseph, and T. A. Konig, "Hybridized guided-mode resonances via colloidal plasmonic self-assembled grating," *ACS Applied Materials & Interfaces*, vol. 11, no. 14, pp. 13752–13760, 2019.

[238] T. Davis, D. Gómez, and K. Vernon, "Simple model for the hybridization of surface plasmon resonances in metallic nanoparticles," *Nano Letters*, vol. 10, no. 7, pp. 2618–2625, 2010.

[239] T. Davis and D. Gómez, "Colloquium: an algebraic model of localized surface plasmons and their interactions," *Reviews of Modern Physics*, vol. 89, no. 1, p. 011003, 2017.

[240] Z. Liu, D. Zhu, S. P. Rodrigues, K.-T. Lee, and W. Cai, "Generative model for the inverse design of metasurfaces," *Nano Letters*, vol. 18, no. 10, pp. 6570–6576, 2018.

[241] S. Jafar-Zanjani, S. Inampudi, and H. Mosallaei, “Adaptive genetic algorithm for optical metasurfaces design,” *Scientific Reports*, vol. 8, no. 1, pp. 1–16, 2018.

[242] N. I. Zheludev and Y. S. Kivshar, “From metamaterials to metadevices,” *Nature Materials*, vol. 11, no. 11, pp. 917–924, 2012.

[243] D. A. Bykov, L. L. Doskolovich, and V. A. Soifer, “Temporal differentiation of optical signals using resonant gratings,” *Optics Letters*, vol. 36, no. 17, pp. 3509–3511, 2011.

[244] N. Golovastikov, D. Bykov, L. Doskolovich, and V. Soifer, “Spatiotemporal optical pulse transformation by a resonant diffraction grating,” *Journal of Experimental and Theoretical Physics*, vol. 121, no. 5, pp. 785–792, 2015.

[245] G. Rousset, J. Fontanella, P. Kern, P. Gigan, and F. Rigaut, “First diffraction-limited astronomical images with adaptive optics,” *Astronomy and Astrophysics*, vol. 230, pp. L29–L32, 1990.

[246] M. G. Löfdahl and G. Scharmer, “Wavefront sensing and image restoration from focused and defocused solar images.,” *Astronomy and Astrophysics Supplement Series*, vol. 107, pp. 243–264, 1994.

[247] F. Carones, “Diagnostic use of ocular wavefront sensing.,” *Ophthalmology Clinics of North America*, vol. 17, no. 2, pp. 129–33, 2004.

[248] J. Porter, H. Queener, J. Lin, K. Thorn, and A. A. Awwal, *Adaptive Optics for Vision Science: Principles, Practices, Design, and Applications*, vol. 171. John Wiley & Sons, 2006.

[249] E. Holden, A. Tárnok, and G. Popescu, “Quantitative phase imaging for label-free cytometry,” *Cytometry Part A*, vol. 91, no. 5, pp. 407–411, 2017.

[250] G. Popescu, Y. Park, W. Choi, R. R. Dasari, M. S. Feld, and K. Badizadegan, “Imaging red blood cell dynamics by quantitative phase microscopy,” *Blood Cells, Molecules, and Diseases*, vol. 41, no. 1, pp. 10–16, 2008.

[251] T. A. Zangle and M. A. Teitell, “Live-cell mass profiling: an emerging approach in quantitative biophysics,” *Nature Methods*, vol. 11, no. 12, p. 1221, 2014.

[252] J. W. Lichtman and J.-A. Conchello, "Fluorescence microscopy," *Nature Methods*, vol. 2, no. 12, pp. 910–919, 2005.

[253] X. Michalet, F. F. Pinaud, L. A. Bentolila, J. M. Tsay, S. Doose, J. J. Li, G. Sundaresan, A. Wu, S. Gambhir, and S. Weiss, "Quantum dots for live cells, in vivo imaging, and diagnostics," *Science*, vol. 307, no. 5709, pp. 538–544, 2005.

[254] J. K. Jaiswal, E. R. Goldman, H. Mattoussi, and S. M. Simon, "Use of quantum dots for live cell imaging," *Nature Methods*, vol. 1, no. 1, p. 73, 2004.

[255] J. Malicka, I. Gryczynski, Z. Gryczynski, and J. R. Lakowicz, "Dna hybridization using surface plasmon-coupled emission," *Analytical Chemistry*, vol. 75, no. 23, pp. 6629–6633, 2003.

[256] I. Gryczynski, J. Malicka, Z. Gryczynski, and J. R. Lakowicz, "Surface plasmon-coupled emission with gold films," *The Journal of Physical Chemistry B*, vol. 108, no. 33, pp. 12568–12574, 2004.

[257] H. Aouani, O. Mahboub, E. Devaux, H. Rigneault, T. W. Ebbesen, and J. Wenger, "Plasmonic antennas for directional sorting of fluorescence emission," *Nano Letters*, vol. 11, no. 6, pp. 2400–2406, 2011.

[258] G. Lozano, D. J. Louwers, S. R. Rodríguez, S. Murai, O. T. Jansen, M. A. Verschuuren, and J. G. Rivas, "Plasmonics for solid-state lighting: enhanced excitation and directional emission of highly efficient light sources," *Light: Science & Applications*, vol. 2, no. 5, pp. e66–e66, 2013.

[259] N. R. Council *et al.*, *Optics and Photonics: Essential Technologies for our Nation*. National Academies Press, 2013.

[260] S. A. Lee and C. Yang, "A smartphone-based chip-scale microscope using ambient illumination," *Lab on a Chip*, vol. 14, no. 16, pp. 3056–3063, 2014.

[261] X. Meng, H. Huang, K. Yan, X. Tian, W. Yu, H. Cui, Y. Kong, L. Xue, C. Liu, and S. Wang, "Smartphone based hand-held quantitative phase microscope using the transport of intensity equation method," *Lab on a Chip*, vol. 17, no. 1, pp. 104–109, 2017.

[262] B. K. Goud, D. Shinde, D. Udupa, C. M. Krishna, K. D. Rao, and N. Sahoo, "Low cost digital holographic microscope for 3-D cell imaging by integrating smartphone and DVD optical head," *Optics and Lasers in Engineering*, vol. 114, pp. 1–6, 2019.

[263] A. F. Smith and S. E. Skrabalak, "Metal nanomaterials for optical anti-counterfeit labels," *Journal of Materials Chemistry C*, vol. 5, no. 13, pp. 3207–3215, 2017.

[264] F. Schneider, "The financial flows of transnational crime and tax fraud in OECD countries: what do we (not) know?," *Public Finance Review*, vol. 41, no. 5, pp. 677–707, 2013.

[265] X. Zang, F. Dong, F. Yue, C. Zhang, L. Xu, Z. Song, M. Chen, P.-Y. Chen, G. S. Buller, Y. Zhu, *et al.*, "Polarization encoded color image embedded in a dielectric metasurface," *Advanced Materials*, vol. 30, no. 21, p. 1707499, 2018.

Appendix

A.1 Metal-Insulator-Metal absorber

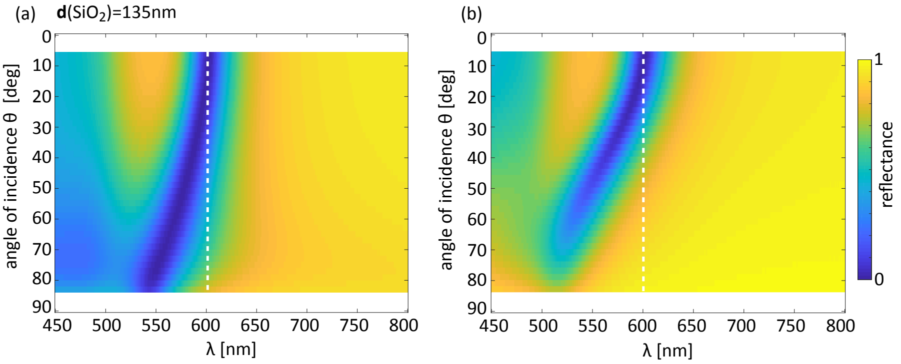

Figure A.1: Experimentally measured reflection from a Salisbury screen consisting of a 135 nm thick SiO_2 layer on a Au base covered with a semitransparent layer of gold with thickness 31 nm as a function of angle of incidence for p-polarization (a) and s-polarization (b). The device shows maximum absorption in reflection at$\lambda = 600\,\text{nm}$.

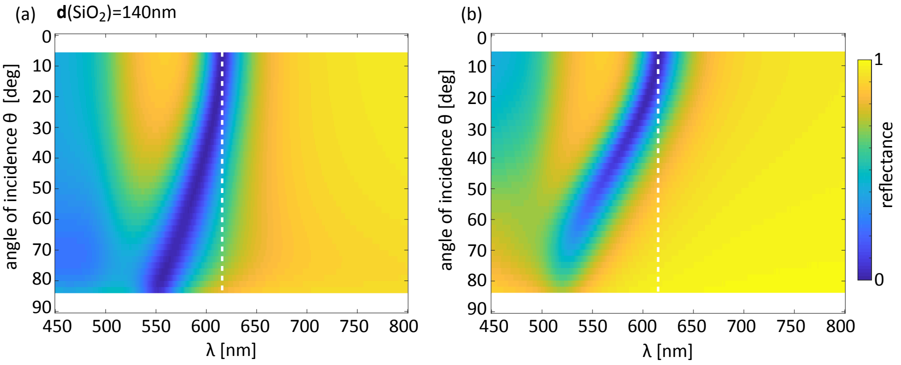

Figure A.2: Experimentally measured reflection from a Salisbury screen consisting of a 140 nm thick SiO_2 layer on a Au base covered with a semitransparent layer of gold with thickness 31 nm as a function of angle of incidence for p-polarization (a) and s-polarization (b). The device shows maximum absorption in reflection at$\lambda = 614\,\text{nm}$.

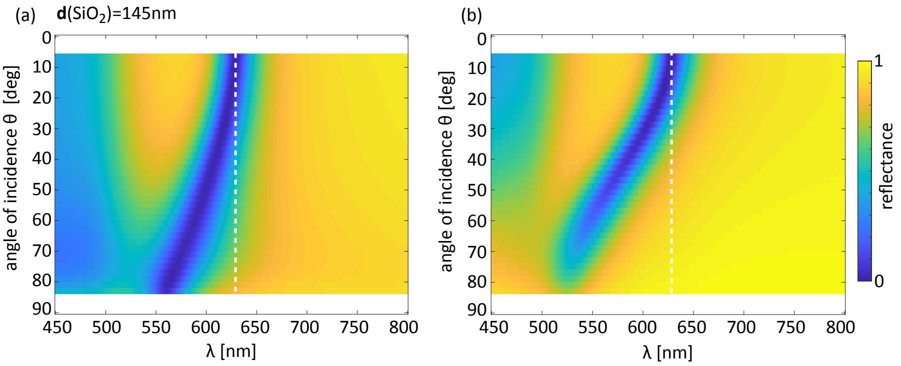

Figure A.3: Experimentally measured reflection from a Salisbury screen consisting of a 145 nm thick SiO_2 layer on a Au base covered with a semitransparent layer of gold with thickness 31 nm as a function of angle of incidence for p-polarization (a) and s-polarization (b). The device shows maximum absorption in reflection at$\lambda = 627\,\text{nm}$.

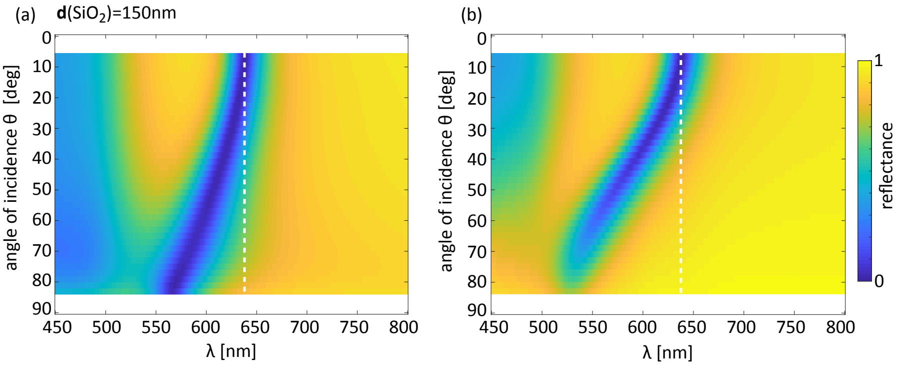

Figure A.4: Experimentally measured reflection from a Salisbury screen consisting of a 150 nm thick SiO_2 layer on a Au base covered with a semitransparent layer of gold with thickness 31 nm as a function of angle of incidence for p-polarization (a) and s-polarization (b). The device shows maximum absorption in reflection at$\lambda = 636\,\text{nm}$.

A.2 Subradiant mode excitation

A.2.1 Analysis of SEM image

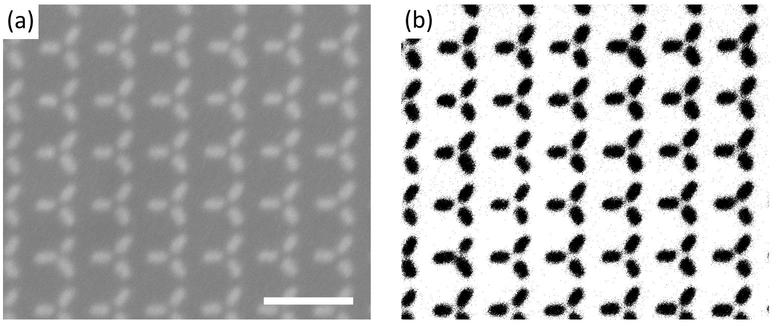

Figure A.5: SEM analysis of radial trimer metasurface, (a) Section of raw SEM image of radial trimer metasurface and (b) result of thresholding method using ImageJ software with pixel value threshold pts= 152/255 for determination of geometric parameters of fabricated sample. Scalebar is 500 nm.

A.2.2 Metasurface response to focused linearly polarized light

In [228, 229] an expression is given for the $p-$ and $s-$polarized field components of a focused linearly polarized beam as a function of spatial frequency. Based on this we here derive an expression that relates the reflectance R_p, R_s from the radial trimer metasurface for purely $p-$ and $s-$ polarized light to its reflectance for focussed linearly polarzied light R_x, R_y. For the following deduction we will denote normalized spatial frequencies with $\sigma = \mathbf{k}/k_0$ and $\sigma_x = k_x/k_0$, $\sigma_y = k_y/k_0$ respectively. We assume a linearly polarized plane wave with wavevector $\sigma = (0, 0, 1)$ along $z-$direction, amplitude E_0 and polarization along $x-$direction. If this beam is deflected, for example by a lens, such that the resulting beam has a wavevector $\sigma* = (\sigma_x, \sigma_y, (1 - \sigma_x^2 - \sigma_y^2)^{1/2})$ the authors of [228] show that the $p-$ and $s-$ polarized components of the deflected beam are given by

$$\tilde{E}_s(\sigma_x, \sigma_y) = E_0|\sigma_y|/\sqrt{(\sigma_x^2 + \sigma_y^2)} \tag{A.1}$$

$$\tilde{E}_p(\sigma_x, \sigma_y) = E_0|\sigma_x|/\sqrt{(\sigma_x^2 + \sigma_y^2)}. \tag{A.2}$$

At this stage the plane wave is incident on the metasurface. The reflection from the metasurface for $s-$ and $p-$polarized light is known from the optical transfer functions r_s

and r_p respectively. From this we obtain the reflected fields as

$$\tilde{E}_{s,\mathrm{ref}} = r_s \tilde{E}_s \tag{A.3}$$

$$\tilde{E}_{p,\mathrm{ref}} = r_p \tilde{E}_p \tag{A.4}$$

The total intensity as a function of spatial-frequency for $x-$polarized light I_x is then given by

$$I_x(\sigma_x, \sigma_y) = a|\tilde{E}_{s,\mathrm{ref}}(\sigma_x, \sigma_y)|^2 + a|\tilde{E}_{p,\mathrm{ref}}(\sigma_x, \sigma_y)|^2 \tag{A.5}$$

$$= \frac{aE_0^2(r_s^2\sigma_y^2 + r_p^2\sigma_x^2)}{\sigma_x^2 + \sigma_y^2} \tag{A.6}$$

$$= \frac{aE_0^2(R_s\sigma_y^2 + R_p\sigma_x^2)}{\sigma_x^2 + \sigma_y^2} \tag{A.7}$$

Where $a = c^2\epsilon_0^2/4$. From this follows with $R_x = I_x/I_0$ where I_0 is the intensity of the incident beam

$$R_x(\sigma_x, \sigma_y) = \frac{R_s\sigma_y^2 + R_p\sigma_x^2}{\sigma_x^2 + \sigma_y^2}. \tag{A.8}$$

Repeating the above derivation for an incident wave polarized along $y-$direction then yields the reflectance for focused $y-$polarized beams

$$R_y(\sigma_x, \sigma_y) = \frac{R_p\sigma_y^2 + R_s\sigma_x^2}{\sigma_x^2 + \sigma_y^2}. \tag{A.9}$$

We employ these equations in chapter 5 to derive Fourier plane images for focused linearly polarized light incident on the radial trimer metasurface.

A.2.3 Fourier plane images

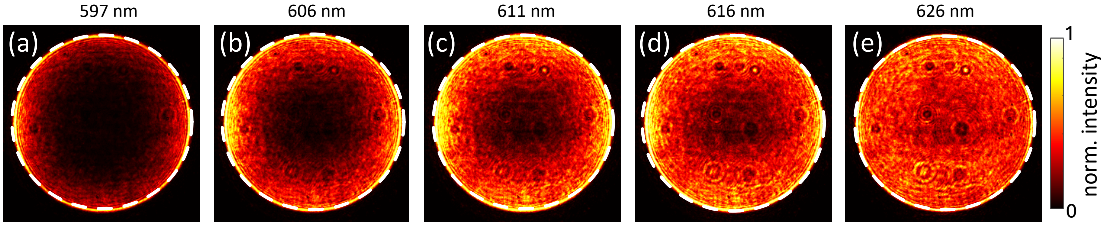

Figure A.6: Recapture of experimentally measured Fourier plane images of radial trimer metasurface prior to performing edge detection experiment. Images recorded using an Olympus Uplan FLN, NA0.75 40× microscope objective. Dashed lines indicate NA=0.75.

A.3 Resonant Waveguide Gratings

A.3.1 Refractive index of TiO_2 thin-films.

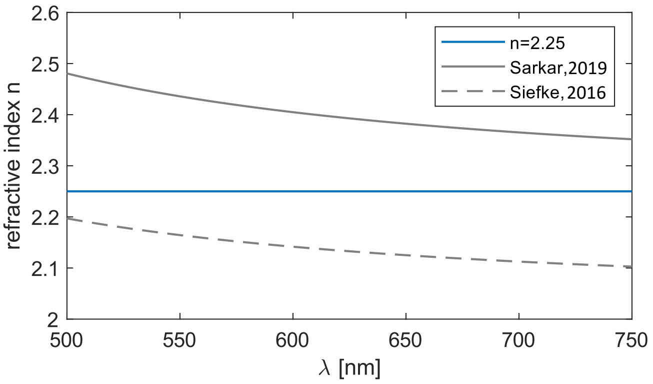

Figure A.7: Comparison of literature values of refractive index for thin films of TiO_2 with value $n = 2.25$ as measured through spectral reflectance and used for numerical calculations in this thesis. Shown are the literature values from [236] (Siefke,2016) and [237] (Sarkar,2019).

A.3.2 Design of grating parameters

FEM simulations were employed to find suitable parameters for the fabrication of metallic resonant wave guide gratings as transmitting high-pass spatial frequency filters. In the following the impact of variations in the geometric parameters of the grating structure as introduced in chapter 6 will be discussed. The thickness of the underlying TiO_2

waveguide layer is kept constant at $t_1 = 100\,\mathrm{nm}$ as previously chosen and we focus on the variation of the grating parameters in order to reduce the parameter space. Further device optimization could also take variations of the wave guide layer thickness into account.

Initially we will review the transmission characteristics of devices with one-dimensional plasmonic gratings before we proceed to two dimensional grating structures.

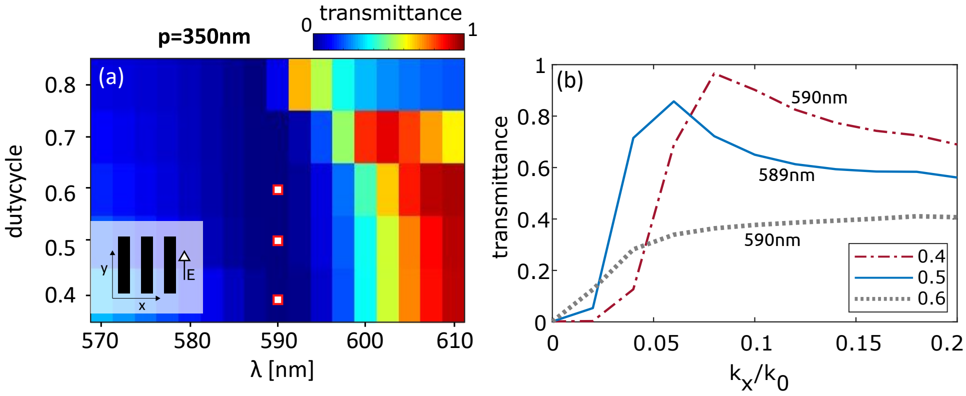

Figure A.8: (a) Transmittance of a Ag RWG for normally incident light, linearly polarized along the y-direction as a function of grating duty cycle and wavelength for one-dimensional grating with a period of $p = 350\,\mathrm{nm}$ and grating thickness of $t_2 = 40\,\mathrm{nm}$. (b) Transmittance of s-polarized light as a function of spatial frequency at the respective transmittance minimum (red squares) with the lateral component of the wavevector along the x-direction.

Fig.A.8 shows the transmission of a device with one dimensional grating as a function of the angle of incidence for varying values of the grating duty cycle g/p and a grating period of $p = 350\,\mathrm{nm}$. It is evident that the transmittance increases for higher spatial frequencies rendering the grating a high-pass spatial frequency filter. A grating duty cycle $g/p \leq 0.5$ results in increased filtering contrast compared to higher duty cycles as exemplary shown for duty cycles of 0.4, 0.5 and 0.6 in A.8(b). It should be noted that Fig.A.8 considers s-polarized light with the lateral component of the wavevector along x-direction as indicated by the inset. This polarization and direction of tilt is the preferred optical configuration for high-pass spatial-frequency filtering with one-dimensional gratings.

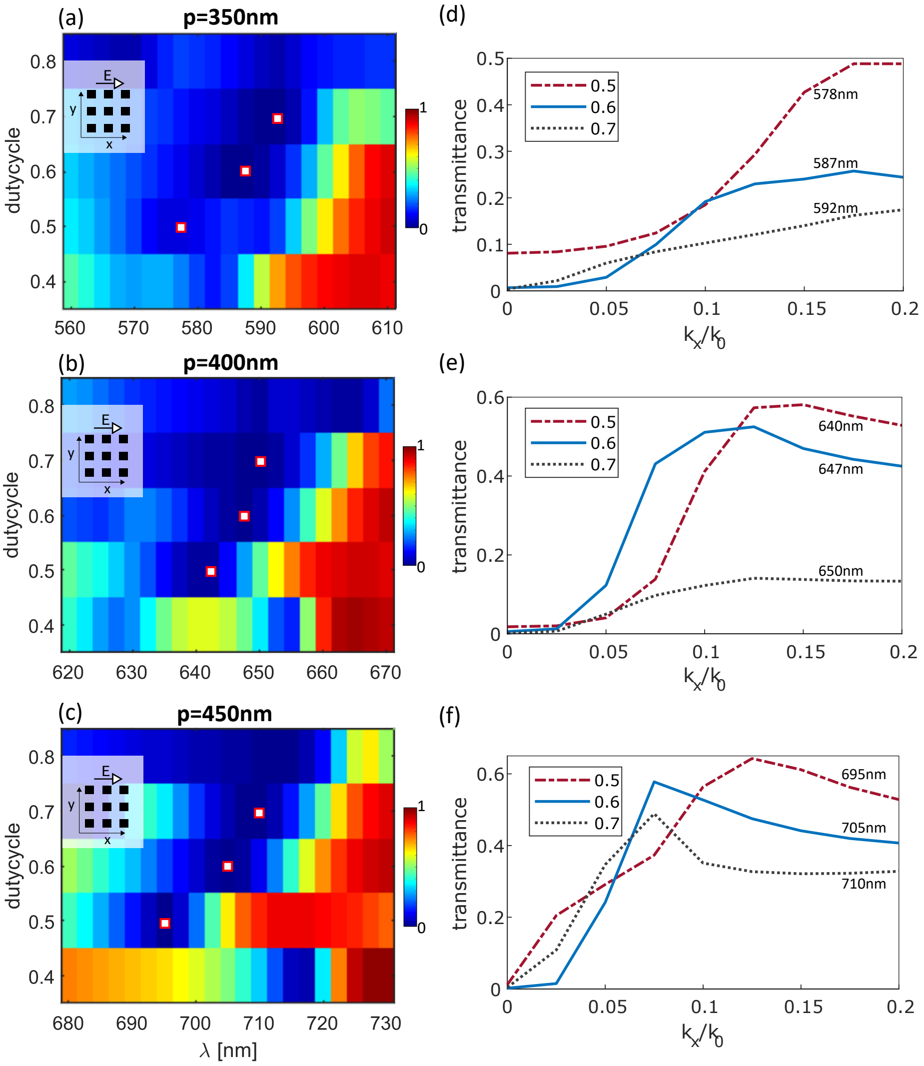

Figure A.9: Transmittance of a Ag RWG for normally incident light, linearly polarized along the x-direction as a function of grating duty cycle and wavelength for two-dimensional gratings with periods of (a) $p = 350\,\text{nm}$, (b) $p = 400\,\text{nm}$ and (c) $p = 450\,\text{nm}$. The grating thickness is $t_2 = 40\,\text{nm}$. Transmittance of unpolarized light (average of $p-$ and $s-$polarized component) as a function of spatial frequency at the respective transmittance minimum (red squares) for each grating (d-f) with the lateral component of the wavevector along the x-direction.

While tailoring of the NA of the filter function and the filtering contrast is possible via choice of similar parameters, here we proceed with a grating duty cycle of $g/p = 0.5$ for further considerations. Since the grating thickness can not be varied between structures fabricated on a single sample owed to the associated evaporation step, we choose a thickness of $t = 40\,\text{nm}$ here. This value is optimized for two dimensional structures as discussed further below and also yiels reasonable results for one-dimensional structures.

Fig.A.9 shows the transmission of devices with two-dimensional grating structure as a function of the angle of incidence for varying values of the grating duty cycle g/p and grating periods of $p = 350\,\text{nm}$, 400 nm and 450 nm. Two-dimensional resonant waveguide gratings enable spatial-frequency filtering in both directions with a near isotropic optical transfer function for unpolarized light as is discussed in more detail through Fourier plane analysis in section 6.2.2. For this reason we aim to find suitable parameters to implement a high-pass spatial frequency filter for unpolarized light. For all values of the grating duty cycle the transmittance increases for increasing spatial frequencies thus also confirming the high-pass spatial frequency filtering cability for devies with two-dimensional gratings. Here we choose a grating duty cycle of $g/p = 0.6$ for two-dimensional grating structures.

Throughout the presented optimization process we have not yet varied the grating thickness but kept it constant at a typical value of 40 nm with the resulting devices providing strong suppression of transmission at normal incidence and reasonable angular filtering contrast as quantified above. Fig.A.10 shows the impact of the grating thickness on the absorption wavelength and angular filter function of devices with two-dimensional grating structures of exemplary grating period $p = 400\,\text{nm}$. A slight shift of the absorption wavelength within a range of $\Delta\lambda = 10\,\text{nm}$ is apparent. The grating thickness has a minor impact on the NA and contrast of the filtering function within the considered range ($20\,\text{nm} \leq t \leq 60\,\text{nm}$) as shown in Fig.A.10(b). Here we choose a universal value for the grating thickness of $t_2 = 40\,\text{nm}$ for all structures discussed in chapter 6.

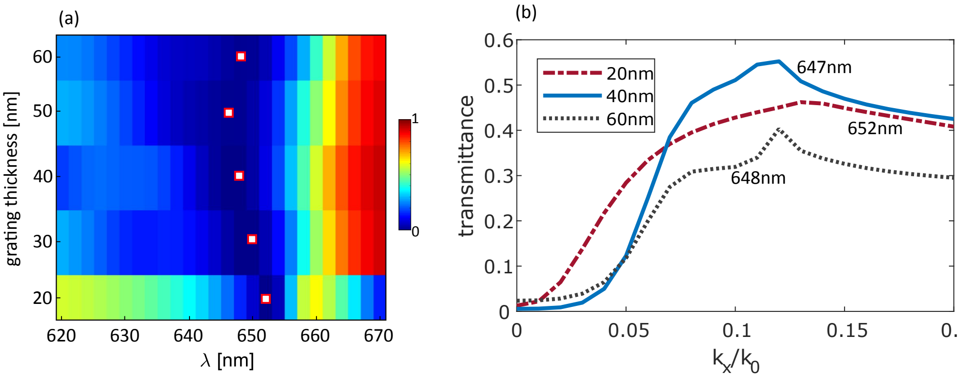

Figure A.10: Transmittance through a Ag RWG with two-dimensional grating for unpolarized light as a function of (a) the wavelength λ and grating thickness t and (b) the lateral normalized spatial-frequency k_x/k_0 (b) for varying grating thicknesses t for a grating period of $p = 400\,\text{nm}$. The grating dutycycle is set to $g/p = 0.6$ in all calculations.

While for the filtering application considered here the resulting device performance is sufficient and due to the time consuming nature of FEM simulations we conclude the optimization process at this stage, further iterative optimization involving the thickness of the waveguide layer and shape of the unit cell of the grating might lead to improved performance for particular applications.

A.3.3 SEM analysis of fabricated Ag gratings

p	p (fab)	duty cycle	duty cycle (fab)
350	352±9	0.6	0.66±0.04
400	406±5	0.6	0.67±0.03
450	456±7	0.6	0.67±0.03

Table A.1: Nominal and experimentally measured (-*fab*) grating parameters of two-dimensional resonant waveguide gratings using the ImajeJ software package. Shown are the grating period p and the duty cycle g/p.

A.3.4 Backside illumination

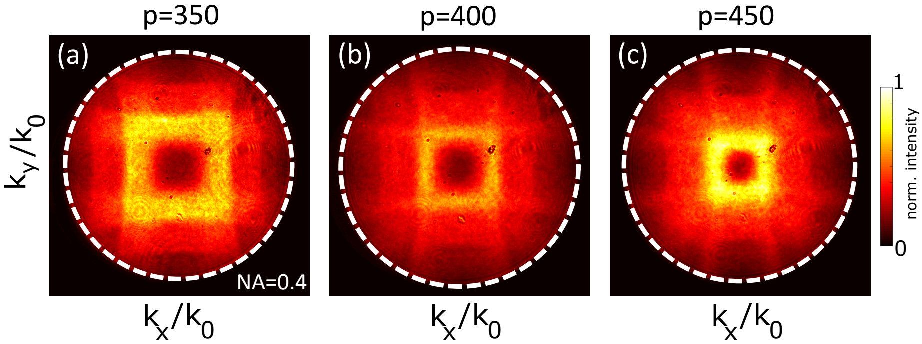

Figure A.11: Experimental Fourier plane images in transmission through RWG-B at $\lambda_c = 575\,\text{nm}$ (a), RWG-C at $\lambda_c = 628\,\text{nm}$ (b) and RWG-D at $\lambda_c = 686\,\text{nm}$ (c) for illumination from the Ag-side of the sample at the respective absorption wavelengths λ_c of the structures. Images are recorded using the setup introduced in Fig. 6.20 for an illumination bandwidth of $\Delta\lambda = 5\,\text{nm}$. All images are normalized to their brightest pixel.

A.3.5 Interpolation of Fourier plane images

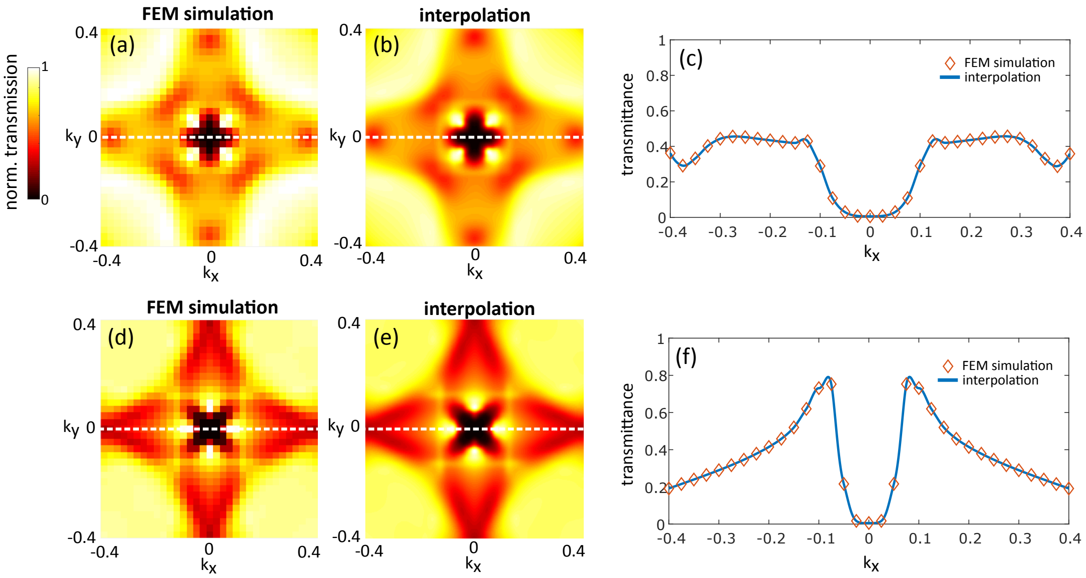

Figure A.12: Cubic interpolation of optical transfer function in order to increase smoothness of simulated data. Here we consider the example of a MEC device with a 40 nm thick silver grating of period $p = 400\,\text{nm}$ and duty cycle 60% on top of a 100 nm thick TiO_2 layer. The transmittance as a function of spatial frequencies was obtained from FEM simulations for p- and s-polarized light as shown in (a) and (d). The result of the cubic interpolation is shown in (b) and (e) with lineplots through $k_y = 0$ confirming the validity of the interpolation.

A.4 Fitting parameters

type	ID	lambda [nm]	polarization	note	a1	a2	NA
MIM	SBS1	631	*s*-pol	isotropic	5.3	0.043	0.3
MIM	SBS1	631	*p*-pol	isotropic	2.4	0.043	0.4
RWG (1D)	RWG-A	589	*s*-pol	along ky=0	356.7	0.042	0.055
RWG (2D)	RWG-C	647	*p*-pol	along ky=0	43.3	0.034	0.115
RWG (2D)	RWG-C	647	*s*-pol	along ky=0	146.4	0.091	0.080

Table A.2: Summary of fitting parameters for second-order differentiatiors using the optical transfer function of MIM absorbers and metallic resonant waveguide gratings as investigated in this thesis.